Universidade Federal do Espírito Santo

Programa de Pós-Graduação em Astrofísica, Cosmologia e Gravitação

Pushing the boundaries of modern cosmology: physics beyond the Copernican principle

David F. Camarena Torres

Thesis submitted as part of the requirements for the degree of
Doctor of Philosophy in Astronomy & Physics

Supervisor: Prof. Valerio Marra
UFES

Co-supervisor: Prof. Luca Amendola
Heidelberg

2022

Universidade Federal do Espírito Santo
Centro de Ciências Exatas
Programa de Pós-Graduação em Astrofísica, Cosmologia e Gravitação

Pushing the boundaries of modern cosmology: physics beyond the Copernican principle

David F. Camarena Torres

A presente tese "*Pushing the boundaries of modern cosmology: physics beyond the Copernican principle*" foi submetida por *David F. Camarena Torres* ao PPGCosmo, tendo sido apresentada e aprovada no ano de 2022 como parte dos requisitos para a obtenção do título de Doutor em Astronomia e Física.

Comissão avaliadora:

Prof. Dr. Valerio Marra (UFES/PPGCosmo), orientador, presidente da banca,
Prof. Dr. Luca Amendola (Ruprecht-Karls-Universität Heidelberg/PPGCosmo), co-orientador,
Prof. Dr. Chris Clarkson (Queen Mary University of London), examinador externo,
Prof. Dr. Domenico Sapone (Universidad de Chile), examinador externo,
Prof. Dr. Oliver F. Piattella (Università degli Studi dell'Insubria/PPGCosmo), examinador externo.

To José Alejandro Camarena Bermeo
Your memory will carry on

Abstract

The standard paradigm of modern cosmology relies on a set of fundamental assumptions that simplify and make possible the modeling of the Universe. Among these critical hypotheses, there is the presumption that we do not occupy a special place in the Universe, the so-called Copernican principle. The assumption of this principle constrains the degrees of freedom allowed by the theory, and, in particular, within the framework of the General Theory of Relativity, leads to a spatially homogeneous and isotropic space-time. Here, we present a program to observationally test the Copernican principle and study the cosmological applications of inhomogeneous cosmologies. Under the assumption of a spherically inhomogeneous extension of the standard model and using the latest cosmological data, we test the Copernican principle by placing constraints on radial deviations of the spatially homogeneous and isotropic space-time. We also forecast the precision with which future surveys, such as DES, Euclid and LSST, will be able to test the Copernican principle and test their ability to detect any possible violations. Furthermore, we investigate if a local void could explain away the 5σ discrepancy between the early and late times determinations of the Hubble constant. Our goal is to take the first steps to extend the boundary of the standard paradigm of modern cosmology, and, in particular, to develop a suitable framework for the development of physics beyond the Copernican principle.

Keywords: theoretical cosmology – observational cosmology – large-scale structure of Universe – Hubble constant

Resumo

O paradigma padrão da cosmologia moderna baseia-se em um conjunto de pressupostos fundamentais que simplificam e possibilitam a modelagem do Universo. Entre essas hipóteses críticas, está a presunção de que não ocupamos um lugar especial no Universo, o chamado princípio Copernicano. A suposição deste princípio restringe os graus de liberdade permitidos pela teoria e, em particular, no âmbito da Teoria Geral da Relatividade, conduz a um espaço-tempo espacialmente homogêneo e isotrópico. Aqui, apresentamos um programa para testar observacionalmente o princípio Copernicano e estudar as implicações cosmológicas dos modelos cosmológicos não homogêneas. Sob a suposição de uma extensão esfericamente não homogênea do modelo padrão e usando os dados cosmológicos mais recentes, testamos o princípio Copernicano colocando restrições nos desvios radiais do espaço-tempo espacialmente homogêneo e isotrópico. Também prevemos a precisão com que os levantamentos futuros de dados, como DES, Euclid e LSST, poderão testar o princípio Copernicano e testar sua capacidade de detectar possíveis violações. Além disso, investigamos se um vazio local poderia explicar a discrepância 5σ entre as determinações em tempos primordiais e tempos tardios da constante de Hubble. Nosso objetivo é dar os primeiros passos em direção à extensão da fronteira do paradigma padrão da cosmologia moderna e, em particular, apontamos a desenvolver uma estrutura adequada para o desenvolvimento da física além do princípio Copernicano.

Palavras chaves: cosmologia teórica – cosmologia observacional – estrutura em grande escala do universo – constante de Hubble

List of Papers

During my PhD, I have performed research in cosmology, focusing on topics related to inhomogeneous cosmology, the Hubble problem, and data analysis. This has led me to publish several papers in different scientific journals. Here, I list the papers that are included in this thesis.

Publication on the Copernican principle

I have published four papers about the Copernican principle and the cosmological implications of assuming it. Among these, I have led the projects: CP Paper I, CP Paper II, and CP Paper III. On the other hand, I have contributed to BEHOMO Paper I by providing the analytical predictions of the ΛLTB model, producing figures, and critically reviewing the different versions of the manuscript.

CP Paper I

David Camarena, Valerio Marra, Ziad Sakr & Chris Clarkson, *The Copernican principle in light of the latest cosmological data*,
Mon. Not. Roy. Astron. Soc. 509 (2021) 1, 1291-1302 [`arXiv:2107.02296`]

CP Paper II

David Camarena, Valerio Marra, Ziad Sakr & Chris Clarkson, *A void in the Hubble tension? The end of the line for the Hubble bubble*,
[`arXiv:2205.05422`]

CP Paper III

Euclid collaboration: **David Camarena** *et al.*, *Euclid: Testing the Copernican principle with next-generation surveys*,
[`arXiv:2207.09995`]

BEHOMO Paper I

Valerio Marra, Tiago Castro, **David Camarena**, Stefano Borgani, Antonio Ragagnin *The BEHOMO project: ΛLTB N-body simulations*,
A&A 2022, DOI: 10.1051/0004-6361/202243539 [`arXiv:2203.04009`]

Publication on the Hubble tension

I have published four papers about the Hubble tension. Among these, I have led the projects: H0 Paper I, H0 Paper II, and H0 Paper III. I contributed to Alestas et al. [8] by performing the cosmological analysis, discussing the results, and assisting and reviewing the different versions of the manuscript.

H0 Paper I

David Camarena & Valerio Marra, *Local determination of the Hubble constant and the deceleration parameter*,
Phys. Rev. Res. 2 (2020) 1, 013028 [`arXiv:1906.11814`]

H0 Paper II

David Camarena & Valerio Marra, *A new method to build the (inverse) distance ladder*,
Mon. Not. Roy. Astron. Soc. 495 (2020) 3, 2630-2644 [`arXiv:1910.14125`]

H0 Paper III

David Camarena & Valerio Marra, *On the use of the local prior on the absolute magnitude of Type Ia supernovae in cosmological inference*,
Mon. Not. Roy. Astron. Soc. 504 (2021), 5164-5171 [`arXiv:2101.08641`]

Alestas et al. [8]

George Alestas, **David Camarena**, Eleonora Di Valentino, Lavrentios Kazantzidis, Valerio Marra, Savvas Nesseris & Leandros Perivolaropoulos, *Late-transition versus smooth $H(z)$-deformation models for the resolution of the Hubble crisis*,
Phys. Rev. D 105, 063538 (2022) [`arXiv:2110.04336`]

Publication from scientific collaborations

Thanks to my research on the Hubble tension, I was kindly invited to sign the Snowmass 2021 letters: Intertwined I, Intertwined II, Intertwined III, and Intertwined IV. I was also invited to contribute to the Snowmass 2022 review Cosmology intertwined, specifically to Section VII. After joining the Theory Working Group of the Euclid consortium as an external collaborator, I have contributed to the publication of Euclid I. I have participated in the discussion of the results and elaboration of Section 5.1 of this paper as also providing the theoretical predictions for the fiducial wCDM and ΛLTB models.

Intertwined I

Eleonora Di Valentino *et al.* (incl. **David Camarena**), *Snowmass2021 - Letter of interest cosmology intertwined I: Perspectives for the next decade*,
Astropart. Phys. 131 (2021) 102606 [`arXiv:2008.11283`]

Intertwined II

Eleonora Di Valentino *et al.* (incl. **David Camarena**), *Snowmass2021 - Letter of interest cosmology intertwined II: The hubble constant tension*,
Astropart. Phys. 131 (2021) 102605 [`arXiv:2008.11284`]

Intertwined III

Eleonora Di Valentino *et al.* (incl. **David Camarena**), *Cosmology intertwined III: $f\sigma_8$ and S_8*,
Astropart. Phys. 131 (2021) 102604 [`arXiv:2008.11285`]

Intertwined IV

Eleonora Di Valentino *et al.* (incl. **David Camarena**), *Snowmass2021 - Letter of interest cosmology intertwined IV: The age of the universe and its curvature*,
Astropart. Phys. 131 (2021) 102607 [`arXiv:2008.11286`]

Cosmology intertwined

Elcio Abdalla *et al.* (incl. **David Camarena**), *Cosmology intertwined: A review of the particle physics, astrophysics, and cosmology associated with the cosmological tensions and anomalies*,
JHEAp 34 (2022) 49-211 [arXiv:2203.06142]

Euclid I

Euclid collaboration: Savvas Nesseris *et al.* (incl. **David Camarena**), *Euclid: Forecast constraints on consistency tests of the ΛCDM model*,
Astron. Astrophys. 660 (2022) A67 [arXiv:2110.11421]

Acknowledgments / Agradecimentos

I would like to thanks Prof. Dr. Valerio Marra, my supervisor, for all the supporting and guidance during my PhD. I also want to thank Prof. Dr. Luca Amendola, my co-advisor, for his very warm welcome to his group in Heidelberg. As well as for his support during my stay visit to the ITP Heidelberg and his willingness to help me.

I would like to thank the CAPES foundation for funding my PhD's scholarship and my stay in Heidelberg, Germany.

Contents

Introduction

The human being seems to be in a never-ending quest to answer profound questions about life, the Universe, and everything. Although such questions indubitably fit in the metaphysical and philosophical subject, some of them relate to the scientific study of the Universe, i.e., cosmology. Indeed, given its comprehensive architecture, modern cosmology surpasses the frontiers of natural science to meet the metaphysical and philosophical playground — following the reasoning exposed by Ellis et al. [15], cosmology has both narrow and broad aims. While, on the one hand, it shares some of its aspects with other branches of physics, for instance as an explanatory theory that aims to explain several phenomena of our cosmos, on the other hand, it can provide a starting point to research the aforementioned philosophical issues.

This fundamental relation between philosophy and cosmology has also influenced the reasoning of cosmologists. We can not deny that the profound philosophical questions about our existence have played a crucial point in the hypotheses contemplated and promoted by cosmologists. More explicitly, these fundamental metaphysical and philosophical issues have grounded the foundations of the standard paradigm of modern cosmology [15]. Indeed, the current standard framework of modern cosmology has been established by a set of fundamental assumptions, principles, and hypotheses that reduce the number of degrees of freedom needed to model our Universe. Thanks to the fundamental assumptions of modern cosmology, cosmologists have made a terrific advance in the developing of a scientific theory of the Universe.

On the other hand, the existence of theoretical problems not yet resolved and discrepancies between different cosmological observations could point to a breakdown of the standard paradigm. Among those issues faced by modern cosmology, the Hubble tension stands out. This tension indicates a $\sim 5\sigma$ disagreement between physics at late and early times. Such discrepancy can be illustrated if one considers the value of the Hubble constant inferred from the analysis of CMB data, $H_0 = 67.27 \pm 0.60$ km s^{-1} Mpc^{-1} [16], and the latest local determination of the Hubble constant, $H_0 = 73.04 \pm 1.04$ km s^{-1} Mpc^{-1}, obtained through the cosmic distance ladder [17].

In light of this, testing the fundamental assumptions of modern cosmology is crucial to put on more solid ground the foundations of the standard paradigm. In this thesis, we explore physics beyond the standard paradigm by relaxing the assumption of the Copernican principle, the notion that we are not placed in a special place in the Universe. By assuming an inhomogeneous extension of the standard Λ Cold Dark Matter model, we aim to study physics beyond the assumption of homogeneity. To provide the first steps toward an extension of the boundaries of the current paradigm of modern cosmology, we propose and develop a suitable program to study, analyze, and interpret cosmological and astrophysical data in inhomogeneous space-times.

This thesis is organized as follows. In Chapter 2, we shall present the empirical and theoretical foundations of the standard paradigm of modern cosmology. We primarily focus on revising the Copernican principle and introducing the standard cosmological model. Then, in Chapter 3 we will discuss some of the problems faced by the standard paradigm. Our discussion will focus on problems that relate to the foundations of the standard paradigm, in particular, such relevant to the assumption of the Copernican principle. Cosmological models beyond the hypothesis of cosmic homogeneity will be given in Chapter 4. In such a Chapter, we shall also discuss the Lemaître-Tolman-Bondi metric and its application in cosmology. In addition, a spherically symmetric inhomogeneous model with a cosmological constant, i.e., the LLTB model. Results of the different analyses performed here will be displayed and discussed in Chapter 5. Finally, we shall conclude in Chapter 6.

To nurture the discussion presented in this thesis, besides the main Chapters, the present work includes three Appendixes. In particular, in Appendix A we describe the demarginalization technique used to obtain the underlying calibration of supernovae given by the Cepheid and geometrical distances. Appendix B presents, on the other hand, a complementary analysis used to assess the impact of low-ℓ Planck data in the test of the Copernican principle. Lastly, we present in Appendix C a re-scaling technique used to create mock catalogs with non-standard fiducial models.

In this thesis, we adopt natural units such that $c = 1$, where c is the speed of light in the vacuum. Additionally, we use the subscript "0" to denote the present-day value of a given quantity. On the other hand, in Chapters 2 and 3 the derivative with respect to the cosmic time will be denoted by a dot, but, from Chapter 4 and on we will use a dot to denote the partial derivative with respect to the time coordinate and a prime to denote the partial derivative with respect the radial coordinate.

The standard paradigm of modern cosmology

In this Chapter, we will briefly revise the foundations of the standard paradigm of modern cosmology. We shall report some of the empirical evidence and the theoretical assumptions used to ground a scientific theory of the Universe. We will start introducing a fundamental concept of observational cosmology, the redshift. Later, the Hubble-Lemaître law, Cosmic Microwave Background, primordial abundances of the light elements, and cosmic acceleration will be discussed. We will then focus on revisiting the theory of gravity assumed by the standard paradigm: the General Theory of Relativity. After this, a discussion of the assumption of an isotropic and homogeneous Universe will take place. The principal aim of such a discussion is to introduce the Friedmann-Lemaître-Roberson Walker metric, the Copernican principle, and their relation with cosmological observations. We shall close the present chapter by presenting the standard model of cosmology, i.e., the cosmological constant Λ and Cold Dark Matter model (hereafter, the ΛCDM model). Basic concepts of the background evolution and perturbations theory will be reviewed.

2.1. Empirical foundations

Different observations have influenced our perception of the Universe, even leading us in some cases to modify and postulate new theoretical models. This shows that the groundwork of modern cosmology not only relies on theoretical studies but also on a set of empirical evidence that has molded a phenomenological approach to the Universe. Here, we will examine some of the empirical evidence exploited to set up the foundations of the standard paradigm of modern cosmology. We will focus our attention on the evidence that will later become relevant and valuable to the development of this work.

2.1.1. The redshift

Even when we are limited to observing the Universe from our particular position, i.e., Earth, cosmologists have been able to assemble an accurate and sophisticated program to probe the nature of our Universe. One of the fundamental pieces of this program — observational cosmology — is the redshift.

As explained below, the redshift, related to the expansion of the Universe, can be evaluated through the radiation emitted by the different cosmological structures. Indeed, the expansion of the Universe stretches the light emitted by a source. Consequently, the radiation is observed at a wavelength λ_o large than the emitted one λ_e. This stretching of the observed electromagnetic radiation is quantified through the redshift

$$z \equiv \frac{\lambda_o}{\lambda_e} - 1\,. \tag{2.1}$$

2.1.2. The Hubble-Lemaître law

The Hubble-Lemaitre law constitutes the first and most direct observational evidence that we live in an expanding Universe.[1] It establishes that the radial velocity, v, of an object away from us, for instance a galaxy, is directly proportional to its physical distance, d. More precisely, it states the empirical relation

$$v = H_0\, d\,. \tag{2.2}$$

with H_0, the so-called Hubble constant, being the constant of proportionality. The Hubble constant, H_0, whose units are given in km s^{-1}Mpc^{-1}, is occasionally presented in its normalized and dimensionless form defined as $h \equiv H_0/100$ km s^{-1}Mpc^{-1}.

Hubble used Equation (2.2), observations coming from the 100-inch Hooker telescope and published radial velocities, to determine for the first time the rate of the expansion of the Universe. Although its measurements were rather imprecise — he obtained an expansion rate of $H_0 =$ 500 km s^{-1}Mpc^{-1} [19] — this first determination of the Hubble constant was fundamental in the development of observational cosmology. As it will be discussed later, in Section 3.5.1, direct observational methods used to measure the value of the Hubble constant are deeply inspired by the Hubble-Lemaitre law.

2.1.3. Cosmic Microwave Background

To explain the expansion of the Universe, the standard paradigm of modern cosmology adopts the Big Bang hypothesis, the conception that the Universe was born in an extremely dense and hot state. Besides illustrating how the Universe expanded from an initial state of high density and temperature, the models stemming from the Big Bang theory also predict the existence of the Cosmic Microwave Background (hereafter, CMB). Such a prediction was for the first time derived in 1948, when Ralph Alpher, Robert Herman, and George Gamov applied the Big Bang theory to establish a mechanism capable of predicting the abundance of light elements in the Universes [20]. The existence of the CMB was not confirmed until 1965 when Penzias and Wilson identified a 3.5 K persistent signal in measurements provided by the 20-foot horn-reflector antenna [21].

This serendipitous discovery made by Penzias and Wilson quickly became one of the empirical pillars of modern cosmology, providing important support to the hypothesis of a Big Bang cosmology. Luckily for us, the discovery of the CMB was not limited to being a historical fact but also opened a window to test cosmological models — the CMB temperature and polarization fluctuations provide us with one of the most important and accurate observables in cosmology. The first NASA's satellite dedicated to cosmology, COBE, helped not only set an early program to observationally study the CMB but also provided several sturdy constraints on the Cosmic Infrared Background [22]. Some of the primary results provided by COBE more than two decades ago are still relevant, e.g., the measurements of the CMB temperature and the amplitude of y-distortion. Considerable improvements came by the hand of the WMAP satellite, which stood out for providing a few percent constraints on the six parameters of the standard

[1] In order to acknowledge the contributions made by Georges Lemaître to the scientific theory of the expansion of the Universe [18], the International Astronomical Union (IAU) recommended in 2018 to rename the so-called Hubble law as the Hubble–Lemaître law.

model, consequently determining the age of the Universe to be 13.77 billion years to within a half percent [23]. Ultimately, using CMB data coming from the Planck mission [24], we have been not only capable of constraining several cosmological parameters with an astonishing precision but also testing fundamental assumptions about our Universe. Indeed, observations from Planck point to a statistically significant agreement between the fluctuations in the temperature of the photons released at the last scattering surface and an isotropic Universe [25, 26]. The latter will be better discussed in Section 2.3.3. Figure 2.1 shows a comparison between the resolution attained by COBE, WMAP, and Planck missions.

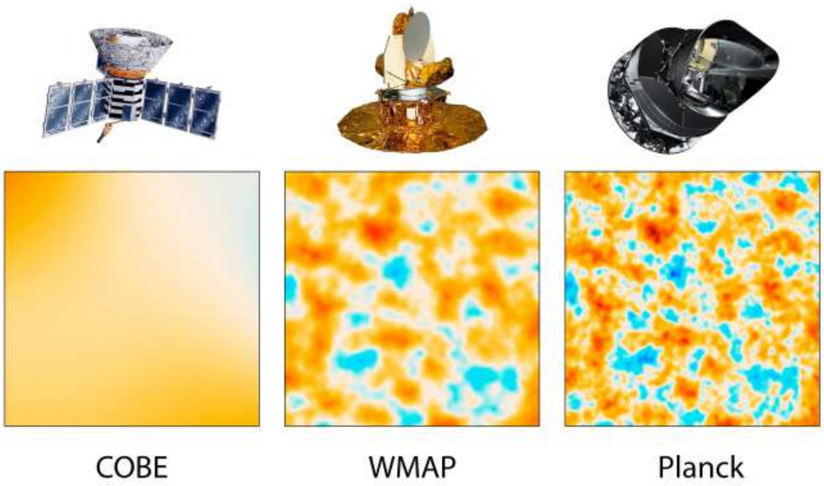

Figure 2.1.: Resolutions on CMB temperature maps as attained by the COBE, WMAP, and Planck missions. While the first NASA cosmological satellite measured the CMB fluctuations with a 7° resolution, WMAP observed the temperature fluctuations with a resolution of 0.3°. Planck satellite achieved unprecedented precision by detection fluctuations at the 0.07° scale. Figure from https://photojournal.jpl.nasa.gov/catalog/PIA16874.

2.1.4. Primordial abundances of light elements

Along with constraints coming from CMB, the Big Bang Nucleosynthesis (hereafter, BBN) theory provides accurate predictions for the abundance of deuterium, ^{3}He, ^{4}He, and ^{7}Li. Overall, observational constraints on the abundance of such elements are consistent with theoretical predictions and provide important empirical support for Big Bang cosmology. As shown in Figure 2.2, the standard paradigm of modern cosmology predicts the abundance of light elements as a function of the baryon-to-photon ratio η. The mismatch between observations and theory, exhibited in the bottom panel of Figure 2.2, for the abundance of ^{7}Li is the so-called Lithium problem. This problem will be discussed in Section 3.1.

2.1.5. Cosmic acceleration

Observations coming from the light curves of the Type Ia Supernovae (hereafter, SNe) led to the discovery of the accelerating expansion of the Universe. By analyzing the luminosity distance-redshift relationship of SNe, two independent research groups, led by Adam Riess and Saul Perlmutter, concluded that the universe was not only expanding but also accelerating [28, 29].

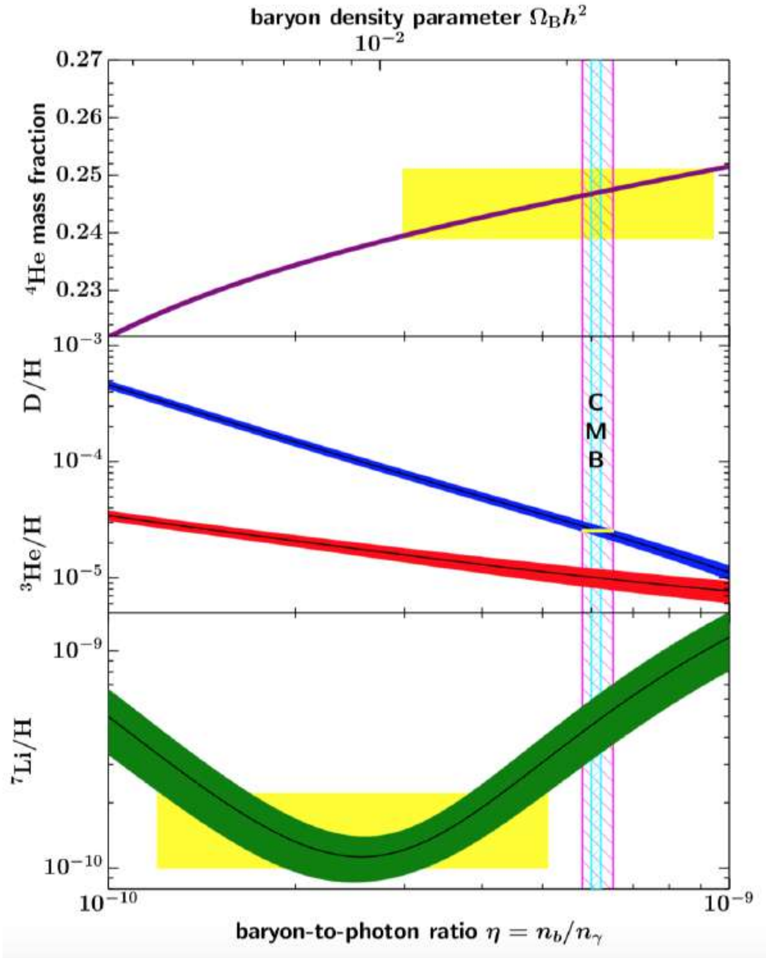

Figure 2.2.: Abundances of light elements as a function of the baryon-to-photon ratio, η. The light blue vertical band shows the CMB constraint on the η at 95% confidence level, while the purple vertical band indicates the constraint at 95% confidence level from BBN D+^{4}He concordance ranges. On the other hand, the yellow boxes illustrate the observed light elements abundances. Although, BBN accurately predicts the ^{4}He abundance, it is easy to note that there exists a disagreement between the observation and theoretical prediction on the abundance of ^{7}Li. Figure from Zyla et al. [27].

This finding produced an enormous change in the paradigm of cosmology and led cosmologists to postulate the existence of a mysterious component with negative pressure capable to drive the accelerated expansion of the Universe: the dark energy — a key ingredient of the standard cosmological paradigm.

It is important to emphasize that the interpretation of an accelerating Universe is given within the framework of the standard paradigm, particularly under the assumption of the Friedmann-Lemaître-Roberson-Walker metric. Thus, the dimming of SNe's luminosity does not truly constitute direct evidence of cosmic acceleration. This is particularly noticeable once we demonstrate that an inhomogeneous space-time, for instance, a Lemaître-Tolman-Bondi metric, can mimic the cosmic acceleration by means of spatial gradients without invoking a dark energy component, see Section 4.1.3.

Albeit, it is also important to highlight that cosmic acceleration is not only supported by the luminosity of SNe. A plethora of cosmological data sets are in agreement with an accelerating Universe and, in particular, with the standard paradigm — the existence of a mysterious dark energy component.[2] In contrast, alternative explanations tend to fail in explaining further cosmological data. This reveals robust evidence in favor of cosmic acceleration. We would like to close this Section by stressing that the paragraph above does not intend to argue in favor of a non-accelerating Universe but rather expose a circular problem of modern cosmology: a theoretical framework is needed to interpret the data, and the data is needed to test the theoretical framework.

2.2. The General Relativity framework

Historically associated with the birth of modern cosmology, the General Theory of Relativity (hereafter, GR), introduced in 1915, is a cornerstone of modern cosmology. Its appearance grounded the theoretical basis of a scientific theory of the Universe. Thanks to Einstein's theory of gravity, we have been able to set a theoretical framework suitable for studying different aspects of the Universe. Using this framework, cosmologists have proposed and promoted a wealth of models to describe the Universe. Although we can not confidently state that GR is the correct theory of gravity, cosmological models relying on Einstein's theory can accurately describe a plethora of cosmological observations.

The generalization of Special Relativity led Einstein to propose a theory of gravity whose mathematical foundations relies on differential geometry. Intricate and rigorous mathematical definitions swamp and constitute the formal framework of Einstein's theory of gravity. However, despite this complexity, physicists have assigned a beautiful, simplistic, and sharp interpretation to the GR: the presence of matter disturbs the space-time geometry and, in turn, the geometry of the space-time determines the matter's dynamics. This interpretation usually stems from the main result of GR:

$$R_{\mu\nu} - \frac{1}{2} R g_{\mu\nu} = 8\pi G T_{\mu\nu}\,, \tag{2.3}$$

the so-called Einstein field equations (hereafter, EFE). Equation (2.3) make clear the relation between matter and the geometry of the space-time. The matter field, represented by the energy-momentum tensor $T_{\mu\nu}$, tells space-time how to curve, and space-time, left-hand side of above equation, tells matter how to move. Note that the geometrical side of Einstein equation can be recast using the Einstein tensor, $G_{\mu\nu}$, such that $G_{\mu\nu} \equiv R_{\mu\nu} - \frac{1}{2} R g_{\mu\nu}$.

The EFE equations are highly nonlinear, mainly because of the complex definition of the Ricci tensor and scalar. Thus, Einstein's equations do not possess a general solution. Thus, if we aim to build up cosmological models, assumptions that simplify the solution of Equation (2.3) will be needed. Such assumptions will typically limit the geometry of the space-time, the left-hand side of EFE, or the matter content of the Universe, the right-hand side of EFE. The standard paradigm of cosmology will assume the so-called Cosmological principle to fix the left-hand side of EFE. We will discuss this assumption and its cosmological consequences in the following Section.

2.3. A spatially isotropic and homogeneous Universe

The standard paradigm of modern cosmology relies on a series of fundamental hypotheses that establish a theoretical and empirical framework needed to interpret cosmological data and model

[2] Typical observational probes of cosmic acceleration are thoroughly discussed in the review presented by Weinberg et al. [30].

our Universe. Such assumptions typically reduce the degrees of freedom needed to describe our Universe and simplify the approach required to build up cosmological models. Among these founding hypotheses, there is the Cosmological principle.

The Cosmological principle, the notion that the Universe is both spatially isotropic and homogeneous at sufficiently large scales, was initially introduced by Einstein to reduce the complexity of the EFE if one considers an arbitrary distribution of matter. As discussed by Coles and Lucchin [31], Einstein's motivations were based mainly on the Mach's principle; Einstein believed that to develop a theoretical science of cosmology was necessary to assume the simplicity of the global structure of the Universe to later derive a similar simplicity in the local behavior of matter. The latter formulation motivated Bondi and Roxburgh [32] to formulate the Perfect Cosmological principle, version in which the Universe is not only spatially homogeneous but space–time is homogeneous, and, consequently, consistent with the a idea of a steady-state Universe.

The Cosmological principle constrains the geometry of the space-time, unavoidably leading to the Friedmann-Lemaître-Roberson-Walker metric. It is important to highlight that although cosmologists still seem to agree with Einstein's initial rationale, our motivations for assuming a spatially homogeneous and isotropic Universe are not necessarily related to the Mach's principle. Empirical evidence in favor of spatial isotropy is often used together with the so-called Copernican principle to argue in favor of the cosmological principle. In this Section, we will revise the relation between the Copernican principle and the assumption of a spatially homogeneous and isotropic space-time. We will start our discussion by introducing the Friedmann-Lemaître-Roberson-Walker metric (hereafter, FLRW metric). Later, the Copernican principle will be defined and discussed. Finally, we will close this Section by reviewing some routes that can be taken to obtain the FLRW metric, having the Copernican principle as a starting point.

2.3.1. The Friedmann-Lemaître-Roberson-Walker metric

By invoking the Cosmological principle, cosmologists have made a tremendous advance in the understanding of the Universe. Such a principle not only allows us to simplify the models of GR but also allows us to understand the whole Universe even though we are only able to collect data from our position. The specific form of the metric is the principle's fundamental mathematical repercussion.

The symmetries established by the Cosmological principle can be translated to the mathematical language using the theory of symmetric spaces [see Chapter 13 of 33]. Thus, it is possible to demonstrate that a spatially homogeneous and isotropic Universe correspond to a space-time with a maximally symmetric subspace. This reduces the metric to follow the FLRW metric:

$$ds^2 = -dt^2 + a^2(t)\left[\frac{dr^2}{1-kr^2} + r^2 d\theta^2 + r^2 \sin^2\theta d\phi^2\right], \tag{2.4}$$

where $a(t)$ is the scalar factor and k is the curvature of the maximally symmetric sub-space. The time dependence of the scalar factor is included to account for the expansion of the Universe, while the curvature of the metric will constrain the geometry of the subspace such that

$$k = \begin{cases} +|k| & \text{spherical sub-space,} \\ 0 & \text{Euclidean sub-space,} \\ -|k| & \text{hyperbolic sub-space.} \end{cases} \tag{2.5}$$

It is worth mentioning that is always possible to find a coordinate transformation that transforms metrics with the same symmetries, scalar curvature, and numbers of negative and positive eigenvalues. That is, in a Universe in which the Cosmological principle is valid, the space-time will be well-described by the FLRW metric.

2.3.2. The Copernican principle

The Copernican principle proposes the hypothesis that we do not occupy a special place in the Universe; we are merely typical observers. Equivalent, there are no special parts of the Universe, and statistically, all regions of the Universe look the same. As explained in the following Section, when associated with isotropy, the Copernican hypothesis implies a homogeneous Universe and, consequently, can be interpreted as a weak version of the Cosmological principle.

Since we live in a lumpy universe that deviates on small scales from the FLRW metric, in the real world, the Copernican hypothesis also implies that when inhomogeneities at small scales are smoothed out, the Universe turns out homogeneous. This means that the assumption of the Copernican principle implicitly introduces the existence of a cosmic homogeneity scale. There have been numerous attempts to establish this scale through observation. For instance, galaxies and quasars surveys have been analyzed by using number count techniques. The results of such analyses have led us to determine the presence of a cosmic homogeneity scale with a range around 70 — 150 Mpc [34, 35, 36].

2.3.3. Routes to the FLRW metric

According to the standard paradigm of modern cosmology, we can accurately model the Universe through the FLRW metric (and its perturbations). Although this postulate is indeed a consequence of assuming the Cosmological principle, it is also true that the assumption of the FLRW can be also observationally argued if one relies on the observed isotropy and the Copernican hypothesis. In conjunction with observables, the Copernican principle is capable of constraining the geometry of the space-time to be spatially isotropic and homogeneous. This latter becomes noticeable if one considers the Ehlers-Geren-Sachs theorem (hereafter, EGS theorem) and its different extensions.

In 1968, Ehlers, Geren, and Sachs proved that if the matter content of the Universe is a perfectly isotropic radiation fluid then the space-time is static or FLRW [37]. This statement, dubbed the EGS theorem, was one of the first attempts to prove the FLRW metric via observations. An alternative interpretation of this theorem states that if we observe a perfectly isotropic CMB radiation, then the space-time in our region must be conformally stationary [38]. Given that the Copernican principle limits us to be typical observers, space-time should be conformally stationary at every point resulting in an FLRW space-time. This theorem constitutes a powerful proof that cosmological observations, hand in hand with the Copernican principle, can constrain the geometry of space-time to follow the FLRW metric.

Although this theorem is an important result to cosmologists, one should keep in mind that, due to its unrealistic assumptions, the EGS can not be applied to the real world — in its original form, the EGS theorem does only consider radiation as the source of the gravitation field. To overcome these limitations, several extensions of the EGS theorem were proposed. Most of these proposals include dark energy and matter as components of the Universe [39, 40, 41, 42, 43, 44, 45], nevertheless, such improved versions can not be applied to our cosmos either. The main reason is that the CMB radiation is not perfectly isotropic but rather almost isotropic. In this context, the almost-EGS theorem was proposed [see 42, 46, 47, 48, 49, for instance] as a plausible approximation to the real world.[3] In contrast to the latter, it has been also claimed that the almost-EGS theorem needs further assumptions to be consistent with our CMB observations [50].

Through this thesis, we embrace the almost-EGS theorem to relate the CMB isotropy and

[3]Note that the almost-EGS theorem leads to an almost FLRW space-time, whose covariant definition is lacking [38]

Copernican principle to the FLRW metric. This includes the assumption that the gradients of the very low multipoles of the CMB power spectrum are small compared to their amplitude. Finally, it is important to highlight that there exist other ways to arrive at the FLRW metric using as the principal assumption the Copernican principle [see 38, for a further discussion].

2.4. The standard cosmological model

In this Section, we will introduce the standard cosmological model: the ΛCDM model.[4] Our discussion will focus on reviewing some of the basic concepts of the background evolution and the theory of perturbations of ΛCDM. We shall also revise some of the concepts that will be necessary for a fruitful discussion of the results presented in this thesis.

2.4.1. Friedmann equations and the cosmic inventory

The assumption of spatial homogeneity and isotropy also limits the energy-momentum tensor. Given the special geometry of the FRLW metric, Equation (2.4), the energy flux across the spatial-surface, T^{0j}, the momentum density, T^{0i}, and the shear stress, T^{ij}, of the energy-momentum tensor are expected to be zero, where $i, j = 1, 2, 3$ and $i \neq j$ for the shear stress. This means that the right-hand side of the Einstein equations should describe a perfect fluid, a fluid whose viscosity and conductivity are zero. The energy-momentum tensor for a perfect fluid follows:

$$T_{\mu\nu} = (\rho + p)\, U_\mu U_\nu + p g_{\mu\nu} \,, \tag{2.6}$$

where U_μ is the four-velocity of fluid, p is the pressure, and ρ the energy density. The EFE then give the Friedmann equations

$$H^2 = \frac{8\pi G}{3}\rho - \frac{k}{a^2} \,, \tag{2.7}$$

$$\frac{\ddot{a}}{a} = -\frac{4\pi G}{3}\left(\rho + 3p\right) \,, \tag{2.8}$$

where $H \equiv \dot{a}/a$ is the Hubble parameter with units of km s^{-1} Mpc^{-1}, and G is the universal gravitational constant. Equations (2.7) and (2.8) are also called the first Friedmann equation and acceleration equation, respectively. Note that the sign of $(\rho + 3p)$, the right-hand side of the Equation (2.8), will determine whether the Universe is accelerating or decelerating.

To solve the above equations is necessary to introduce a relation between the energy density and pressure with the scalar factor. This relation will be provided by the law of conservation of energy, which, in its covariant form, corresponds to the conservation of the energy-momentum tensor. In GR, Bianchi identities and Equation (2.3) guarantee

$$\nabla_\mu T^{\mu\nu} = 0 \,, \tag{2.9}$$

where ∇_μ is the covariant derivative which includes the connections or Christoffel symbols of the metric. In addition, upon the assumption of a barotropic equation of state (hereafter, EoS)

[4] We use the expression *standard paradigm* to refer to the theoretical and empirical concepts that constitute the standard framework of modern cosmology. On the other hand, we use the expression *standard model* to describe the set of the most accepted theoretical definition used to build up a framework suitable for the understanding of cosmology.

in which the energy density and the pressure related through $p = w\rho$, with w being the EoS parameter, the continuity equation is obtained:

$$\dot{\rho} + 3H(1+w)\rho = 0\,. \tag{2.10}$$

In order to explain the accelerated expansion of the Universe it is necessary a component whose EoS parameter obeys $w < -1/3$, see Equation (2.8).

Using Equation (2.7), we can define the energy density that is necessary to obtain a spatially flat Universe, this is the critical density

$$\rho_{cri} \equiv \frac{3H^2}{8\pi G}\,.$$

Considering this last definition, we can recast the energy density parameter such that

$$\Omega \equiv \frac{\rho}{\rho_{cri}} = \frac{8\pi G}{3H^2}\rho\,, \tag{2.11}$$

and consequently the first Friedmann equation follows the closure equation:

$$1 = \Omega + \Omega_k\,, \tag{2.12}$$

where $\Omega_k \equiv -\frac{k}{a^2H^2}$ and Ω are called the density parameters. Since the Universe is filled with more than one material component, ρ is the total energy density, i.e., it contains the contribution of all the material species such that $\rho \equiv \sum_i \rho_i$, where i labels a particular specie. Note that the same applies for the pressure p and the density parameter Ω. In what follows, we briefly revise the matter components of the ΛCDM model.

2.4.1.1. Matter

The non-relativistic matter sector of the standard cosmological model is composed of baryons and cold dark matter. We dub baryons all the non-relativistic particles described by the Standard Model of particle physics and denominate as cold dark matter the non-relativistic species that only interacts gravitationally with the other components of the Universe.

The non-relativistic matter species, or simply matter, is expected to have a negligible pressure such that the EoS parameter obeys $w_m \ll 1$. Pragmatically, the EoS is usually set to $w_m = 0$. Due to conservation of energy and momentum

$$\begin{aligned} \dot{\rho_m} &= -3\frac{\dot{a}}{a}\rho_m\,, \\ \rho_m(a) &= \rho_{m0}a^{-3}\,, \end{aligned} \tag{2.13}$$

or using the density parameter:

$$\begin{aligned} \rho_m(a) =& \frac{3H_0^2}{8\pi G}\Omega_{m0}a^{-3}\;, \\ \Omega_m(a) =& \frac{\Omega_{m0}a^{-3}}{E^2(a)}\;, \end{aligned} \tag{2.14}$$

where the subscript m refers to matter and $E(a) \equiv H(a)/H_0$ is the normalized Hubble parameter. Note that $\Omega_m = \Omega_b + \Omega_c$, where subscripts b and c represent baryons and cold dark matter, respectively.

The result obtained from the conservation of the energy-momentum tensor, i.e., Equation (2.13), can be intuitively interpreted. The energy density is roughly speaking defined as the total energy in a unit of volume, where the latter is proportional to a^3. Therefore, in a scenario where the species have constant energy, due to the expansion of the Universe, the energy density is expected to decrease as $\rho \propto a^{-3}$.

2.4.1.2. Radiation

Relativistic species shape the radiation, which, in the standard model, corresponds to photons and massless neutrinos. Note that although neutrino flavor oscillations suggest the existence of massive neutrinos, neutrinos are often approximated as massless.

Relativistic matter species have a EoS parameter $w_r = 1/3$, which according to the conservation of energy and momentum gives:

$$
\begin{aligned}
\dot{\rho_r} &= -4\frac{\dot{a}}{a}\rho_r \,, \\
\rho_r(a) &= \rho_{r0}a^{-4} \,,
\end{aligned}
\tag{2.15}
$$

or using the density parameter:

$$
\begin{aligned}
\rho_r(a) &= \frac{3H_0^2}{8\pi G}\Omega_{r0}a^{-4} \,, \\
\Omega_r(a) &= \frac{\Omega_{r0}a^{-4}}{E^2(a)} \,,
\end{aligned}
\tag{2.16}
$$

where the subscript r refers to radiation. Ω_r accounts for the contributions of photons and massless neutrinos. Even though the aforementioned relativistic species are expected to evolve at the same rate, a^{-4}, the energy density of them differs due to their intrinsic definitions. While photons will follow the Bose-Einstein distribution, the Standard Model neutrinos will be described by the Fermi–Dirac statistics. Thus, the density parameters of the massless neutrino and photos will be related through [51]

$$
\Omega_\nu = \frac{7}{8}\frac{N_{\rm eff}}{2}\left(\frac{4}{11}\right)^{4/3}\Omega_\gamma \,,
$$

where the subscripts ν and γ represent the neutrinos and photons, respectively, and $N_{\rm eff}$, the effective families of neutrinos. Ultimately, because of this

$$
\Omega_{r0} = \Omega_{\gamma 0}\left[1 + \frac{7}{8}\frac{N_{\rm eff}}{2}\left(\frac{4}{11}\right)^{4/3}\right] . \tag{2.17}
$$

In contrast to the non-relativistic matter, $\rho_m(a)$, radiation, $\rho_r(a)$, possesses an extra a^{-1}. This additional scale factor in Equation (2.15) comes from the fact that due to the expansion the energy of a photon decays with a^{-1}. It is important to highlight that here, we refer to the relic radiation, that is, photons and neutrinos formed in the baryogenesis. For a revision of the astrophysical radiation released during the structures formation see [52].

2.4.1.3. Cosmological constant

In 1917, Einstein introduced the cosmological constant, Λ, to make the field equations of GR compatible with his vision of a static and finite Universe [53]. However, the presence of instabilities in this kind of model demonstrated that the cosmological constant does not satisfactory explain a static and finite Universe [54]. Nowadays, the role of Λ is not to model a static universe but rather an accelerated expanding universe. Thanks to its negative pressure, a Universe dominated by the cosmological constant satisfies $w < -1/3$ and ergo explains the accelerated expansion of the universe, $\ddot{a} > 0$, see Equation (2.8).

Similar to matter and radiation, the cosmological constant can be included in the Einstein equations as a component of a perfect fluid such that the energy-momentum tensor is

$$T^{\Lambda}_{\mu\nu} = -\frac{\Lambda}{8\pi G} g_{\mu\nu} \,, \tag{2.18}$$

and, consequently, the cosmological constant energy density and pressure follow

$$\rho_\Lambda = \frac{\Lambda}{8\pi G} \,, \tag{2.19}$$

$$p_\Lambda = -\frac{\Lambda}{8\pi G} \,. \tag{2.20}$$

This means, that the density parameter results

$$\Omega_\Lambda = \frac{\Omega_{\Lambda 0}}{E^2(a)} \,, \tag{2.21}$$

where $\Omega_{\Lambda 0} = \Lambda/3H_0^2$. On the other hand, in contrast to the other species of the standard cosmological model, the cosmological constant can be also interpreted as an intrinsic constant of Einstein theory that can be introduced in Equation (2.3) by modifying the fundamental action of GR. In such a case, the field equations can be reshape as

$$R_{\mu\nu} - \frac{1}{2} R g_{\mu\nu} + \Lambda g_{\mu\nu} = 8\pi G T_{\mu\nu} \,. \tag{2.22}$$

The cosmological constant is often associated with the vacuum energy of the Universe, since its EoS parameter matches $w_\Lambda = -1$, as seen from Equations (2.19) and (2.20). Independently of considering or not the cosmological constant as an intrinsic constant of the Einstein's theory of gravity, the presence of Λ is a fundamental piece on the standard paradigm of cosmology. For the sake of convenience, we will adopt the EFE as expressed in Equation (2.22).

2.4.2. The background evolution

2.4.2.1. Stages of the Universe

The evolution of the scale factor affects the way different species contribute to the total energy of the Universe. For instance, at early times when $a \to 0$, the contribution of radiation will be more important than the contribution of matter or the cosmological constant. Analogously, at late-times where $a \to 1$, Λ is expected to dominate the total energy of our Universe. These features become more evident if one uses Equations (2.14), (2.16) and (2.21) to recast the Friedmann equations as

$$E(z) = \left[\Omega_{m0}(1+z)^3 + \Omega_{r0}(1+z)^4 + \Omega_{\Lambda 0}\right]^{1/2} \,, \tag{2.23}$$

$$q(z) = \frac{1}{2}\left[(1+w_m)\,\Omega_m(z) + (1+w_r)\,\Omega_r(z) + (1+w_\Lambda)\,\Omega_\Lambda(z)\right] \,, \tag{2.24}$$

where the redshift and scale factor are related by $a = 1/(1+z)$, and $q \equiv -\ddot{a}a/\dot{a}^2$ is the deceleration parameter.

From Equation Equation (2.23), it is easy to infer that the background evolution of the ΛCDM scenario will consist of three different epochs: a radiation-dominated era, a matter-dominated era, and a dark energy-dominated era. Strictly speaking, there exists an additional stage at early times. This stage, dubbed inflation, occurs before the radiation-dominated epoch and represents another accelerating epoch of the Universe [see 55, for a thoroughly review of inflation]. Figure 2.3 shows the three mentioned stages of the Universe by showing how the density parameter of the different species evolves with the scale factor (left panel). We also display the evolution of the deceleration parameter (right panel). At early times, the radiation dominates the dynamic of the background yielding to a Universe with decelerated expansion, i.e. $q > 0$ (light orange area). Subsequently, because of the expansion, the matter becomes more important and starts to dominate at redshifts lower than $z_{\rm eq}$ (purple area), with $z_{\rm eq}$ being the redshift of the epoch of matter-radiation equality, i.e., $\Omega_m(z_{\rm eq}) = \Omega_r(z_{\rm eq})$. Eventually the density of matter and radiation dilutes conducing to a dark energy-dominated Universe (white area) whose accelerating expansion is explained by the current value of the decelerating parameter $q_0 \approx -0.55$.

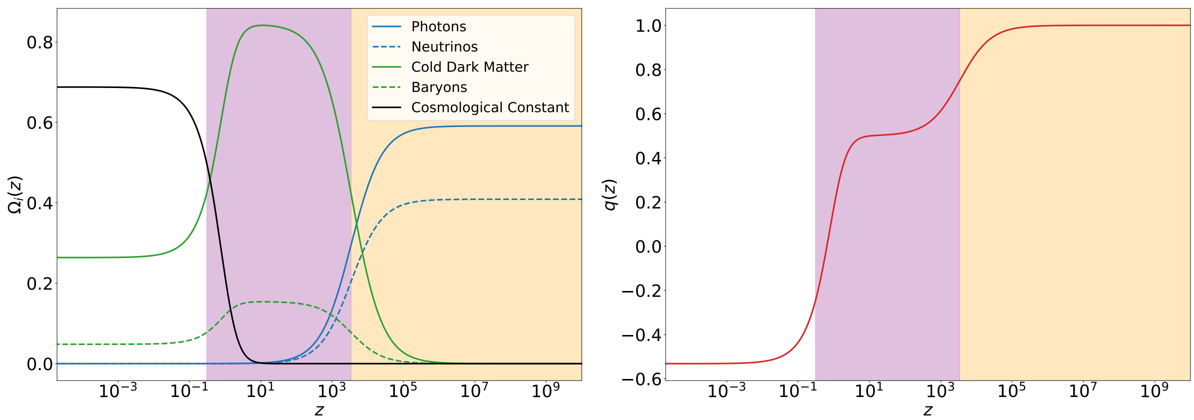

Figure 2.3.: Density parameters of the different species of the ΛCDM model (left panel) and the deceleration parameter (right panel) as a function of the redshift. From the evolution of Ω_i is easily to deduce the three stages of the Universe: the radiation-dominated era (light orange area), the matter-dominated era (purple area), and the dark energy-dominated era (white area).

2.4.2.2. Cosmological distances

Establishing a fundamental relationship between redshift and cosmological distances is a key issue in cosmology. Since, in principle, it is not possible to predict a generic definition of cosmological distances that can be applied to any cosmological model, we are rather limited to computing the cosmological distances according to our cosmological model.[5] Within the standard paradigm and the FLRW assumption, there exist two ways of computing cosmological distances: taking into account or not the expansion of the Universe. The second class of functions are the dubbed comoving distances. Meanwhile, the former are the so-called proper or physical distances.

[5] Approximate definitions of model-independent cosmological distances can be constructed using expansions in series of functions. [see 56, and references therein].

From the FLRW line element, Equation (2.4), its clear that the radial comoving distance obeys

$$D_c = \int_0^r \frac{\mathrm{d}r'}{\sqrt{1-kr'^2}}\,,$$
$$= \begin{cases} \frac{D_H}{\sqrt{\Omega_{k0}}}\sinh[\sqrt{\Omega_{k0}}\frac{r}{D_H}]\,, & \text{for } \Omega_{k0} > 0\,, \\ r\,, & \text{for } \Omega_{k0} = 0\,, \\ \frac{D_H}{\sqrt{|\Omega_{k0}|}}\sin[\sqrt{|\Omega_{k0}|}\frac{r}{D_H}]\,, & \text{for } \Omega_{k0} < 0\,, \end{cases} \tag{2.25}$$

where we have defined the quantities $\Omega_{k0} \equiv -kD_H^2$, $\chi \equiv r/D_H$ and $D_H \equiv 1/H_0$. Additionally, as radiation follows null geodesics, $\mathrm{d}s^2 = 0$, it is

$$r = \int_t^{t_0} \frac{\mathrm{d}t'}{a(t')} = D_H \int_0^z \frac{\mathrm{d}z'}{E(z')}\,,$$

with $E(z)$ being the normalized Hubble rate introduced above. Analogous to the later, we can define the comoving distance travelled by a sound wave of speed c_s from the initial singularity, $z \to +\infty$, to a particular redshift, z, as

$$r_s = \int_z^{+\infty} \frac{c_s dz'}{H(z')}\,. \tag{2.26}$$

This is the so-called comoving sound horizon. Finally, the proper distance, D_C, will be obtained by taking into account the effect of the expansion of the Universe, this is

$$D_p \equiv a(z)D_c = \frac{D_c}{(1+z)}\,. \tag{2.27}$$

On the other hand, we can also define the luminosity and angular distances. The former is important to study standard candles, while the latter to study standard rules. The luminosity and angular distances are defined by

$$D_L = (1+z)D_c\,, \tag{2.28}$$
$$D_A = \frac{D_c}{(1+z)}\,, \tag{2.29}$$

respectively. Note that the luminosity and angular distances follows the Etherington's distance-duality, such that $D_L = (1+z)^2 D_A$. This relation have been demonstrated to be valid if the photon number is conserved and gravity is described by a metric theory [57].

2.4.3. A lumpy Universe

2.4.3.1. Cosmological perturbations

By embracing the assumption of a homogeneous and isotropic Universe, we have established the necessary starting point for the development of modern cosmology. However, we can not deny that we live in a lumpy Universe — our cosmos features large-scale structures, such as galaxies, galaxy clusters, voids, and filaments. Thereby, a comprehensive cosmological model has to go beyond the aforementioned symmetrical assumptions. Mathematically, to account for the undeniable inhomogeneities of the Universe and trace the emergence and evolution of large-scale structures, it is necessary to include deviations from the FLRW metric. Such deviations can be studied via perturbation theory, and, more explicitly, through perturbed FLRW models.

The theory of perturbations is compatible with the theoretical framework settled by GR and can be used not only to trace the growth of perturbations in our Universe but also to study other phenomena, e.g., gravitational waves. Here, we apply the theory of perturbations to the EFE. We start by defining the general perturbed metric, $g_{\mu\nu}$, that can be decomposed as

$$g_{\mu\nu} = \overline{g}_{\mu\nu} + \delta g_{\mu\nu} \,, \tag{2.30}$$

where $\delta g_{\mu\nu}$ is the small deviation, provided by the perturbations, and $\overline{g}_{\mu\nu}$ is the background metric, i.e., the FLRW metric. We then use Equation (2.30) to recast the Einstein's equations, such that at first order we have:

$$\delta G_{\mu\nu} \equiv \delta R_{\mu\nu} - \frac{1}{2}\delta g_{\mu\nu}\overline{R} - \frac{1}{2}g_{\mu\nu}\delta R = 8\pi G \delta T_{\mu\nu} \,, \tag{2.31}$$

where is $\overline{R}$ is the background Ricci scalar.

As mentioned before, it is necessary to develop a perturbed FLRW model if one aims to assess the perturbations around our spatial homogeneous and isotropic Universe. Similar to the case of the background evolution, the first step to constructing this kind of model is to define the metric, i.e., $\delta g_{\mu\nu}$. However, before proposing a strict definition of $\delta g_{\mu\nu}$, it is important to discuss one of the subtleties of Equation (2.30). Given that the background and perturbed metric are not defined in the same manifold, the relationship established in (2.30) is only well-defined if a map between the manifold of $\overline{g}_{\mu\nu}$ and $\delta g_{\mu\nu}$ is defined. Since there is no single way to define such a map, there will be no exclusive definition of cosmological perturbations. This problem, well-known as the gauge problem, can be overcome if one defines gauge-invariant quantities; that is, quantities that do not depend on the map. Here, we will not discuss the gauge problem and its implications in detail, but rather point out some of the gauge-invariant quantities introduced.

We define the perturbed metric, $\delta g_{\mu\nu}$, by imposing the Newtonian gauge [58]:

$$ds^2 = a^2\left(\eta\right)\left\{-\left[1+2\Psi\left(\eta,\vec{x}\right)\right]d\eta^2 + \left[1+2\Phi\left(\eta,\vec{x}\right)\right]\delta_{ij}dx^i dx^j\right\} \,, \tag{2.32}$$

where Ψ and Φ are scalars field and we have introduced the conformal time defined as $\eta = \int dt/a$. For the sake of the simplicity, hereafter, we will drop the arguments $(\eta, \vec{x})$ on the perturbed quantities Ψ, Φ, and derived. Given that neither vector nor tensor perturbations are included in the Newtonian gauge, the potentials Ψ and Φ coincide with the gauge-invariant Bardeen's potentials [59]. Thus, we can conveniently rewrite the left-hand side of Equation (2.31) as

$$\delta G^0{}_0 = 2a^{-2}\left[3\mathcal{H}\left(\mathcal{H}\Psi - \Phi'\right) + \nabla^2\Phi\right] \,, \tag{2.33}$$

$$\delta G^0{}_i = 2a^{-2}\partial_i\left(\Phi' - \mathcal{H}\Psi\right) \,, \tag{2.34}$$

$$\begin{aligned}\delta G^i{}_j = {}& 2a^{-2}\left[\left(\mathcal{H}^2 + 2\mathcal{H}'\right)\Psi + \mathcal{H}\Psi' - \Phi'' - 2\mathcal{H}\Phi'\right]\delta^i{}_j \\ &+ a^{-2}\left[\nabla^2\left(\Psi+\Phi\right)\delta^i{}_j - \partial^i\partial_j\left(\Psi+\Phi\right)\right] \,,\end{aligned} \tag{2.35}$$

where $\mathcal{H} \equiv \frac{a'}{a} = aH$ is the Hubble parameter in conformal time. On the other hand, the perturbed energy-momentum tensor is

$$\delta T^\mu_\nu = \left[\left(1+c_s^2\right)U^\mu U_\nu + c_s^2\delta^\mu{}_\nu\right]\delta\rho + \left(1+w\right)\left(\delta U^\mu U_\nu + U^\mu\delta U_\nu\right)\rho \,, \tag{2.36}$$

where we have defined the density contrast, velocity divergence, and sound speed as

$$\delta \equiv \frac{\delta\rho}{\rho}\,, \tag{2.37}$$

$$\theta \equiv \partial_i v^i\,, \tag{2.38}$$

$$c_s^2 \equiv \frac{\delta p}{\delta\rho}\,, \tag{2.39}$$

respectively. Note that the peculiar velocity, $v^i = dx^i/d\eta$, comes from the four-velocity definition

$$U^\mu = \left[\frac{1}{a}\left(1-\Psi\right), \frac{v^i}{a}\right]\,. \tag{2.40}$$

Expanding Equation (2.36), we can determinate the perturbed components of the energy-momentum tensor, where

$$\delta T^0_{\ 0} = -\delta\rho\,, \tag{2.41}$$

$$\delta T^0_{\ i} = \left(1+w\right)\rho v^i\,, \tag{2.42}$$

$$\delta T^i_{\ j} = c_s^2 \delta^i_{\ j}\ \delta\rho\,. \tag{2.43}$$

Since both sides of the perturbed Einstein equation are determined, see Equations (2.33) to (2.35) and (2.41) to (2.43), we can compute a set of equations that will govern the dynamics of the perturbations:

$$3\mathcal{H}\left(\mathcal{H}\Psi - \Phi'\right) + \nabla^2\Phi = 4\pi G a^2 \rho\delta\,, \tag{2.44}$$

$$\nabla^2\left(\Phi' - \mathcal{H}\Psi\right) = -4\pi G a^2\left(1+w\right)\rho\theta\,, \tag{2.45}$$

$$\Psi + \Phi = 0\,, \tag{2.46}$$

$$\Phi'' + 2\mathcal{H}\Phi' - \mathcal{H}\Psi' - \left(\mathcal{H}^2 + 2\mathcal{H}'\right)\Psi = -4\pi G a^2 c_s^2 \rho\delta\,. \tag{2.47}$$

Each of the above equations has a particular role in the evolution of the FLRW perturbations. For instance, the relativistic Poisson equation, Equation (2.44), will be important to assess the evolution of perturbations at all times, directly relating the matter distribution to the gravitational potentials, and the anisotropic-stress equation, Equation (2.46), will be especially relevant at early times, where photons and neutrinos feature quadrupole moments [60].

2.4.3.2. Summary statistics

To obtain particular solutions of Equations (2.44) and (2.47) initial conditions are necessary. The theory of inflation predicts such initial conditions and assigns them a quantum origin. Thanks to this, cosmological perturbations will turn out to be stochastic in nature — initial conditions as predicted by inflation are probability distributions and not functions. From the theoretical point of view, this means that we are incapable of predicting the inhomogeneous distribution of matter around the Universe.

Even if one assumes that is possible to provide deterministic particular solutions to the perturbed EFE, the information contained in those would be useless by itself. The main reason: it is observationally impossible to determinate $\delta(\eta, \vec{x})$. From our position in space-time, we are limited to measure quantities at t_0, hence, it will turn out impossible to measure $\delta(\eta, \vec{x})$ at any other time.

In spite of everything mentioned, the study of cosmological perturbations continues to be fundamental for the understanding of large-scale structures. Their stochastic nature does not prevent us from using them in the analysis of cosmological models but rather offers us the opportunity to apply descriptive statistics to condensate the information contained in the cosmological perturbations. From the pragmatical point of view, we can take advantage of the stochastic nature of cosmological perturbations.

Within the standard paradigm of modern cosmology, cosmological perturbations are assumed to be well-represented by stochastic Gaussian field. This implies that the relevant summary statistics of $\delta(\eta, \vec{k})$ are the mean and the variance. Additionally, if one assumes the mean to be zero, the leftover statistics will be the variance, which is defined by [31]

$$\left\langle \tilde{\delta}(\eta, \vec{k}_1)\tilde{\delta}(\eta, \vec{k}_2) \right\rangle = P(k_1, z)\delta^D(\vec{k}_1 + \vec{k}_2)\,, \tag{2.48}$$

where $P(k, z)$ is the so-called the power spectrum, δ^D is the Dira delta function, and we have used the Fourier transform of the density contrast

$$\tilde{\delta}(\eta, \vec{k}) = \frac{1}{(2\pi)^3} \int \mathrm{d}x^3 e^{-\vec{k}\cdot\vec{x}} \delta(\eta, \vec{x})\,, \tag{2.49}$$

Note that the isotropy assumed by the standard paradigm is reflected in the definition of the power spectrum, which depends on the magnitude k but not the $\hat{k} \equiv \vec{k}/k$. We want to conclude this Chapter o by highlighting that formally, the operator $\langle\rangle$ denotes the ensemble average, however, it is pragmatically applied as a spatial average. The difference between the spatial and ensemble averages will yield the known cosmic variance.

Problems of the standard paradigm

Due to its great ability to accurately explain various cosmological observations, the ΛCDM model is also known as the concordance model [see Fig. 15 in 61]. However, despite its surprising success, the ΛCDM model faces several theoretical and observational challenges. The fine-tuning problem [62], the coincidence problem [63], the Lithium problem [64], the CMB anomalies [65], and tensions in cosmological parameters, e.g., H_0 and σ_8 [Cosmology intertwined] are only some examples. Here we shall review some of the problems of the standard paradigm of modern cosmology. We will mainly focus on revisiting the ones that relate to the fundamental assumptions of modern cosmology, in particular, those related to the Copernican Principle.

3.1. The lithium problem

As discussed in Section 2.1.4, the BBN theory provides accurate predictions about the abundance of deuterium, ^{3}He, ^{4}He, and ^{7}Li. Although such predictions provide important support for the standard paradigm, the mismatch between the measurements and the theoretical prediction of ^{7}Li abundance could signal the breakdown of the standard BBN. Indeed, the theoretical value predicted by the BBN theory, $^7\mathrm{Li/H} \times 10^{10} = 5.623 \pm 0.247$ [66], is about 3.5 times larger than the observational constraint, $^7\mathrm{Li/H} \times 10^{10} = 1.6 \pm 0.3$ [27]. This discrepancy of about $4 - 5\sigma$ could be attributed to yet unknown astrophysical or nuclear systematics, nevertheless, this missing abundance of Lithium could be a hint to the existence of new physics.

Different cosmological solutions have been proposed to the Lithium problem. For instance, Clara and Martins [67] showed that a variation on the fundamental constants could accommodate the ^{7}Li abundance to the observed value without affecting the abundance of ^{3}He. A similar proposal was presented in [68], where the variation on the fundamental constants also impacts the Hubble tension problem.[1] The Lithium problem has also been studied in the context of the Copernican Principle. Inhomogeneous cosmological models could explain the Lithium problem through a baryon-to-photon ratio that varies with the scale [70]. Many other alternatives have been proposed to explain the discordance in the Lithium abundance [see 71, for an interesting revision of this problem].

3.2. CMB anomalies

Although the ΛCDM framework provides an accurate picture of the CMB observations, several statistical anomalies have been detected in the CMB data. Most of these anomalies, whose significance typically reaches out the $2 - 3\sigma$, arise at the the largest observable angular scales,

[1] A simultaneous solution to the Hubble and Lithium problem was also pursued by Alcaniz et al. [69].

approximately $\gtrsim 60°$. The source of such anomalies is still unknown and they could indicate a violation of the fundamental assumptions of the standard paradigm. Of particular interest here are the cold spot, the variation in cosmological parameters over the sky, and the Planck internal anomalies.

3.2.1. The cold spot

First found in the WMAP [72] data, and later confirmed by the Planck mission [25, 26], the cold spot is a large-scale region of the CMB map with a lower temperature than the average — the mean temperature of the cold spot is about $\sim 100\mu K$ lower than the CMB background temperature. With a diameter of about $10°$ and galactic coordinates corresponding to $l, b \approx 209°, -57°$, the cold spot is inconsistent with some of the fundamental hypotheses of modern cosmology. For instance, it disagrees with the assumption that cosmological perturbations are Gaussian fields [73, 74, 75, 76]. Additionally, it could point out to a breakdown of the assumption of spatial homogeneity [77].[2] In 2015, a supervoid aligned with the cold spot was detected [84]. Such superstructure, dubbed Eridanus supervoid, has been proposed as a promising explanation for the cold spot anomaly [85].

3.2.2. Variation in cosmological parameters over the sky

The variation of the cosmological parameters in the sky has been used to test the symmetries imposed by the Cosmological Principle [see 86, 87, 88, 89, 90, for instance]. The test about the isotropic assumption has been remarkable, as it has revealed important deviations of the isotropy established by the FLRW metric. For example, Fosalba and Gaztanaga [91] have found a directional dependence of the cosmological parameters across the sky in the Planck map. According to their study, the dependence across the sky is strongly inconsistent with the isotropy established by the Cosmological principle — they claimed a probability of $\sim 10^{-9}$ for this finding. Similarly, Yeung and Chu [88] found a directional dependence of the cosmological parameters on the Planck data. Such directional dependence features a Bayes factor that strongly disfavors an isotropic FLRW Universe.

3.2.3. Planck internal anomalies

Planck analysis of the temperature and polarization CMB power spectrum found a shift in the cosmological parameters when constraints coming from $\ell \lesssim 800$ and $\ell \gtrsim 800$ are compared [92, 93, 94]. While Planck collaboration argues that this slight discordance of $\leq 2\sigma$ between high and low multipoles is driven by the "low-ℓ" deficit found in $\ell < 30$, this mismatch could be a hint for the existence of new physics at large scales or the presence of systematics in low multipoles.

On the other hand, introduced as a phenomenological parametrization, the lens parameter $A_{\rm lens}$ as constrained by the CMB power spectrum displays a $\sim 2\sigma$ discordance with the ΛCDM paradigm. Planck constraints give $A_{\rm lens} = 1.180 \pm 0.065$ [16], while the ΛCDM model predicts $A_{\rm lens} = 1$. The lens parameter is strongly correlated with the mild tension detected between the low and high multipoles; an excess of lens $A_{\rm lens} > 1$ reduces the shift in the cosmological parameters [94]. As in the case of the high and low multipoles discrepancy, in the absence of systematics, the preference for $A_{\rm lens} > 1$ could be a hint of the existence of physics beyond the standard paradigm.

[2] Given that supervoids have been also considered as possible solutions to the cold spot [78, 79, 80, 81], this problem could be related to the anomalous strong integrated Sachs-Wolfe signal observed for supervoids and superclusters [82, 83].

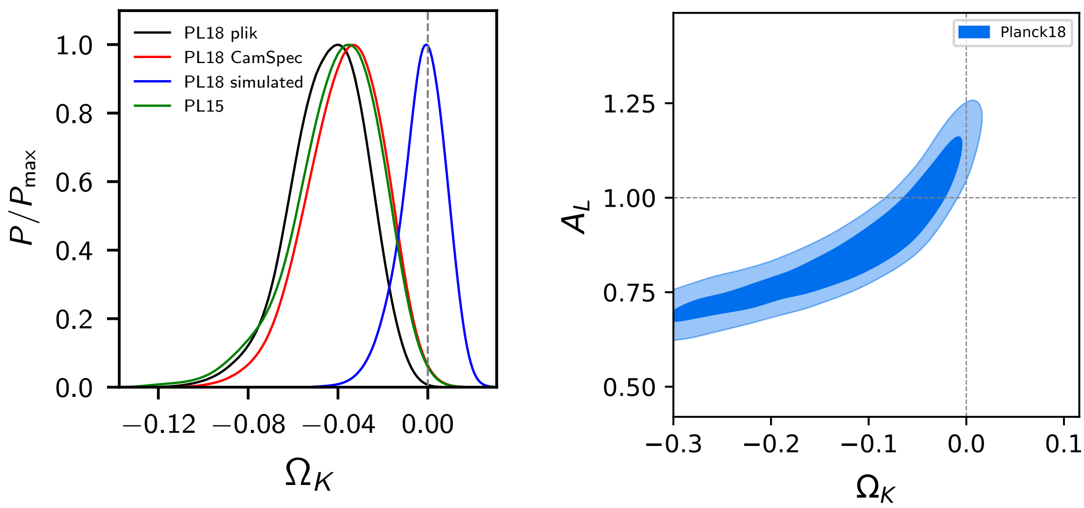

Figure 3.1.: Left panel: 1d posteriors on the curvature parameter obtained from the analysis of real and simulated Planck data. The main analysis of Planck constrains a closed Universe, $\Omega_{k0} < 0$, at more than 3σ. Right panel: 68% and 95% confidence level constraints on Ω_{k0} and $A_{\rm lens}$ from the analysis of Planck 2018 data. It is straightforward to note that Ω_{k0} is strongly correlated with $A_{\rm lens}$. In particular, a slightly closed Universe can mimic the excess of lens, and, ergo, solves the internals anomalies found in Planck CMB data. Figure from Di Valentino et al. [95].

Although these internal anomalies could be produced by statistical fluctuations, one could argue in favor of cosmological models with non-trivial curvature. For instance, Di Valentino et al. [95] argue that, since Planck temperature and polarization data exhibit a $> 3\sigma$ preference for a closed Universe, the internal anomalies found in the Planck data could be cured by an FLRW curvature $\Omega_{k0} < 0$, see Figure Figure 3.1. Di Valentino et al. [95] emphasize that although this closed Universe-scenario can explain the Planck anomalies, it exacerbates the H_0 and S_8 tensions, and further, it is in strong disagreement with other data, e.g., BAO. Finally, the authors claim that the confirmation of a closed Universe would lead to a crisis in cosmology. We would like to highlight that Efstathiou and Gratton [96] have argued that the evidence for a closed Universe found by Di Valentino et al. [95] is prior- and Likelihood-dependent.

In apparent contradiction with the analysis presented in [95], Bose and Lombriser [97] argue that the A_L anomaly and the Hubble and large-scale structure tensions can be cured by an open and hotter Universe. Although the correlation between the CMB temperature and the curvature of the Universe, see Figure 3.2, is discussed in an empirical context, the authors suggest that such changes in the curvature and CMB temperature could be sourced by an inhomogeneous Universe. In Section 5.4, we will use a ΛLTB model to explore this scenario.

3.3. Cosmic dipoles

The amplitude of the temperature fluctuations in the CMB shows, overall, a good agreement with the assumption of an FLRW cosmology, mainly because fluctuations are very small. Yet, this does not apply to the dipole of the CMB temperature.

The amplitude of the CMB dipole ($\ell = 1$), as determined from the CMB data, is at least 10^2

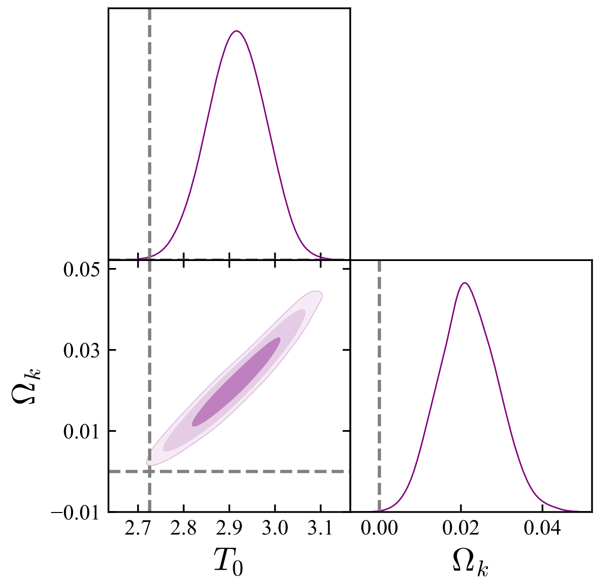

Figure 3.2.: 68% and 95% confidence level constraints on Ω_{k0} and T_0, the CMB temperature, from the analysis of Planck 2018 data under the assumption of a phenomenological extension of the ΛCDM model. Changes on the curvature and CMB temperature leads to solve several tensions. According to the authors, the strong correlation between Ω_{k0} and T_0 could be justified by an inhomogeneous model. Figure from Bose and Lombriser [97].

times bigger than the fluctuations found in higher multipoles, in particular, Planck provides an dipole's amplitude of 3.36208 ± 0.00099 mK [98]. Within the standard paradigm, the motion of the Earth relative to the Hubble flow (or CMB rest-frame) is assumed to be responsible of the high amplitude of the dipole. Indeed, under such an assumption, the Planck collaboration has constrained our relative velocity to be $v = 369.82 \pm 0.11$ km/s with a direction that point in the $l, b \approx 264.0216°, 48.253°$ galactic coordinates. Nonetheless, the dipole could contain a non-kinetic contribution intrinsic to the CMB. The amplitude of the latter could either corroborate or refute the isotropy hypothesis. Although a precise measurement of the intrinsic dipole's amplitude has not yet been achieved, by measuring the Doppler- and aberration-like couplings in the CMB, Ferreira and Quartin [99] have imposed an upper bound limit on the intrinsic dipole: 3.7 mK at a 95% confidence level.

Besides the CMB dipole, more cosmic dipoles have been also detected in other surveys [see Table III and Figure 22 in 100]. Some of these dipoles point in the same direction as the CMB dipole, while others have various directional dependences, and there is no evident pattern in these observations. Given that they feature different amplitudes, cosmological dipoles could hint at a violation of the Cosmological principle. For instance, Secrest et al. [101] have recently claimed that the hypothesis of a merely kinematical dipole in radio galaxies surveys [102] and quasars data [103] consistent with the CMB dipole can be rejected at more than 5σ, see also [104]. In contrast, Darling [105] has claimed the opposite: the sky distribution and brightness of extragalactic radio sources are consistent with the CMB dipole in direction and velocity.

Cosmic dipoles have also been exploited to constrain anisotropic cosmologies and possible deviations of the Copernican principle. Inhomogeneous Cosmological models that include anisotropic degrees of freedom, typically by assuming an off-center observer, can provide a non-perturbation explanation of the CMB dipole [106]. On the other hand, typical voids of Gpc size are constrained by the SNe data and CMB dipole to have an observer within the $\sim 0.5\%$ of the radius of the void [107]. Qualitatively similar results have been found in [108, 109, 110]. Finally, according to Biswas et al. [111], non-Copernican models with a slightly off-center observer would provide a natural explanation for the so-called dark flow observed in CMB data [112, 113, 114].

3.4. The S8 tension

It is remarkable how observations have led us to place tight constraints on cosmological parameters and, indirectly, on other fundamental branches of physics. We can confidently state that observations have played, and still playing, a crucial role in the development of modern cosmology. However, in an era marked by high precision in cosmological observations, understanding the source of the errors that surround our data is a pivotal point of the cosmological program. This becomes crucial if we bring into the discussion the Hubble (next Section) and S8 tensions, which, in the absence of unknown systematics errors, could prove the existence of physics beyond the standard model.

The analysis of the temperature and polarization power spectrum of the CMB led us to constrain the $S_8 \equiv \sigma_8(\Omega_{m0}/0.3)^{0.5}$ parameter to be $S_8 = 0.834 \pm 0.016$ [16]. Cosmological analyses of late time data related to weak lensing, galaxy clustering, and cluster counts, on the other hand, prefer lower values of the same parameter. For instance, KiDS-1000 analysis of cosmic shear data points to $S_8 = 0.759^{+0.024}_{-0.021}$ [115], while the 3×2 pt correlation analysis of DES Y3 data yields $S_8 = 0.776 \pm 0.017$ [116]. These constraints reveal a $\sim 3\sigma$ discrepancy between the late and early times observations. [3] Given its mild significance, this tension could be sourced either by statistical fluctuations or unidentified systematic errors. Moreover, the large-scale structure tension could also point to the presence of new physics, indeed, the S_8 tension has been used as a new window to test deviations and extensions of the cosmological standard model, see Cosmology intertwined and references therein.

3.5. The Hubble crisis

Similarly to the S8 tension, the Hubble tension also indicates a disagreement between physics at late and early times. On the one hand, under the assumption of the ΛCDM model, the latest and primary CMB data constrains the expansion rate of the Universe to $H_0 = 67.27 \pm 0.60$ km s^{-1} Mpc^{-1} [16]. While on the other hand, the most recent model-independent analysis of the cosmic distance ladder constrains the Hubble constant to be $H_0 = 73.04 \pm 1.04$ km s^{-1} Mpc^{-1} [17]. Given its high statistical significance of $\sim 5\sigma$, the disagreement between these measurements has been labeled modern cosmology's greatest challenge. Analogous to the case of the S_8 tension, this disagreement is not exclusive to the above-mentioned measurements but, instead, systematically appears if one compares late and early time determinations of the Hubble constant.[4] Figure 3.3 shows several indirect and direct measurements of H_0 at early and late times, respectively. We would like to highlight that among the Cepheids-SNe-based measurements, our determination

[3]This mismatch it is not exclusive to the aforementioned surveys, but instead it arises as a tension between the early and late times measurements of S_8. See Figure 21 and Table II of [100] for a extensive review of the lastest measurements of S_8.

[4]The tension can reach the $\sim 6\sigma$ level if an optimistic H_0 estimate, deduced by the combination of 23 direct measurements, is considered [118].

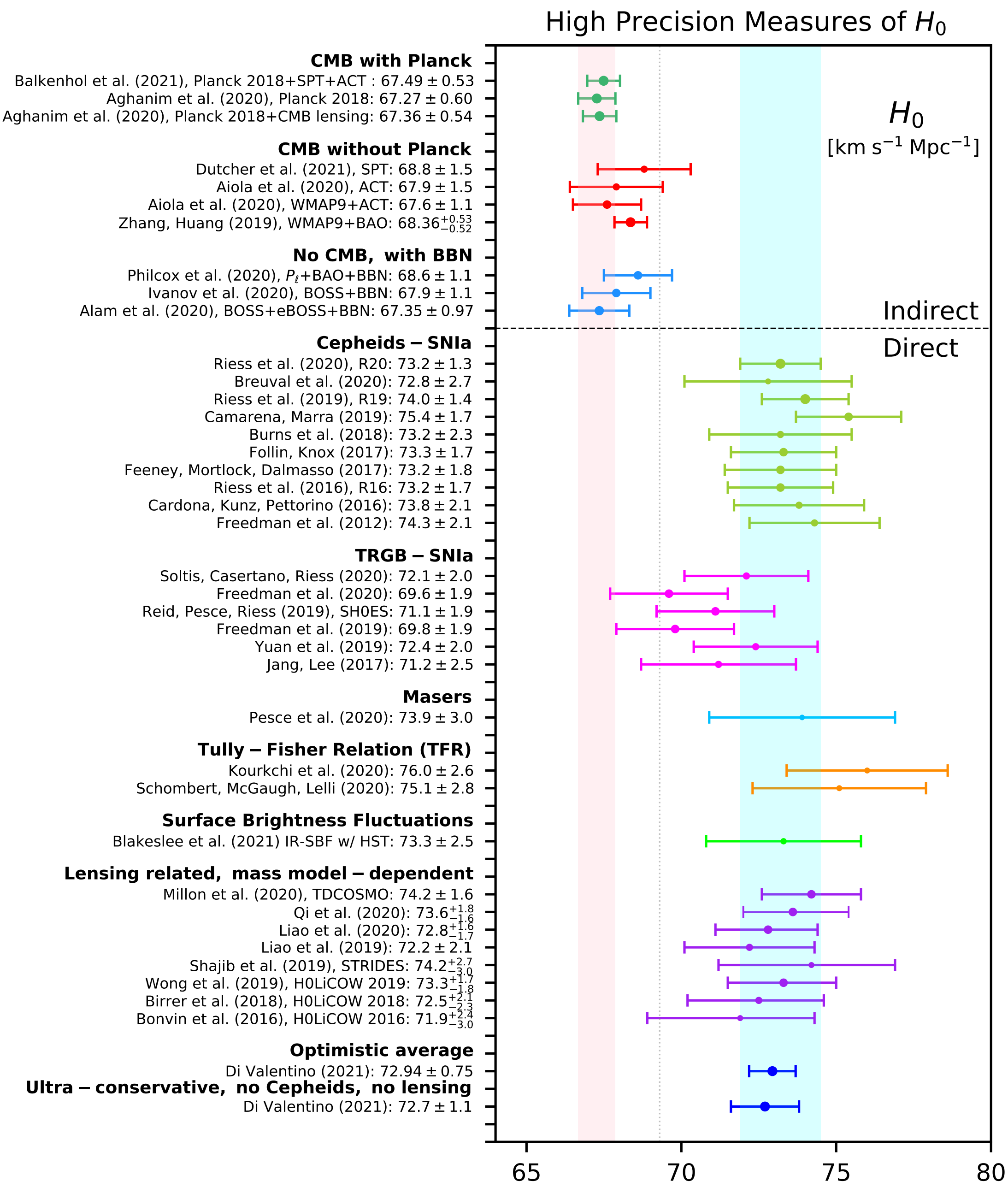

Figure 3.3.: Constraints at 68% confidence level of the Hubble constant according to different data sets, both at low and high redshifts. It is easy to note the discrepancy between early and late times determinations of the Hubble constant. Note that, the cyan vertical band corresponds to the value of H_0 as constrained by the cosmic distance ladder technique, while the light pink vertical band corresponds to the H_0 constraint as inferred by the CMB data by the Planck 2018 collaboration. Figure from Di Valentino et al. [117].

presented in [H0 Paper I] provides the higher value, constraining $H_0 = 75.4 \pm 1.7$ km s^{-1} Mpc^{-1}. This particular measurement will be discussed in detail in Section 3.5.1.

Undiscovered systematic errors could be the principal source of the Hubble tension. Nevertheless, in the absence of such, the 5σ discrepancy would indicate the existence of new physics. Commonly, models proposed to explain or alleviate the H_0 tension modify the standard model either at late or early times. In general, these proposals aim to accommodate the CMB constraints with a larger value of H_0 while keeping a good fit for the whole power spectrum. Strictly speaking, to provide a theoretical prediction of the CMB power spectrum one should solve the Boltzmann-Einstein equations. Hence, fully understanding how the non–standard cosmological models allow for a faster expansion of the Universe and explain the CMB data at the same time is not a trivial task. However, by considering the angular scale parameter, θ_*, we can gain an insight into how the modifications to the ΛCDM model change the H_0 constraint provided by the CMB.

The angular scale is defined through the angular diameter distance and the comoving sound horizon at the recombination, $r_s^* \equiv r_s(z_*)$ and $D_A^* \equiv D_A(z_*)$, respectively, such that

$$\theta_* = \frac{r_s^*}{(1+z_*)D_A^*}\,, \tag{3.1}$$

with z_* being the redshift of the recombination. By considering a flat Universe and using the definition of the angular diameter distance, Equation (2.29), we can explicitly isolate the contribution of the Hubble constant in the equation above. Thus, we can recast Equation (3.1) as

$$\theta_* = \frac{r_s^* h}{(1+z^*)d_A^*}\,, \tag{3.2}$$

where we used the normalized angular distance d_A, which is defined according to

$$d_A = 10^{-2}\int_0^z \frac{\mathrm{d}\bar{z}}{E(\bar{z})}\,\mathrm{Mpc}\,.$$

We can deduce, from Equation (3.2), how a change in the value of the Hubble constant would affect the constraint on the CMB. Particularly, one can note that in order to keep θ_* fixed, and therefore a good agreement with CMB constraints, any change on h should be accompanied by a change either on d_A^* or r_s^*. Note that, the CMB temperature and polarization power spectrum constrains, with an astonishing 0.03% precision, the acoustic angular scale to the value $\theta_* = 1.04109 \pm 0.00030$.

Proposed cosmological models with non-standard physics at early times typically introduce new degrees of freedom around the recombination time. This modifies the comoving sound horizon scale, r_s^* [see 119, and references therein]. For instance, if we assume a ΛCDM model with $N_{\rm eff} = 3.75$, the presence of radiation at early times will be boosted, see Equation (2.17), and, consequently, we will have a significant increase in the Hubble rate at $z \gtrsim 100$. Given that $r_s \propto 1/H(z)$, a decrease in the sound horizon scale will be obtained, explaining, therefore, the rise in the value of the Hubble constant needed to constrain θ_*. In opposition, new physics at late times aims to resolve the Hubble tension by increasing the angular distance to the recombination [see 117, for an extensive review of this class of solutions]. This is often addressed by modifying the dark sector of the Universe. For example, the inclusion of dark energy fluid with $w_{\rm de} = -1.25$ in the ΛCDM model will modify the Hubble diagram by enhancing the dark energy contribution to the expansion of the Universe. As a consequence, the distance to the recombination epoch will increase along with the value of the Hubble constant. We illustrate the aforementioned in

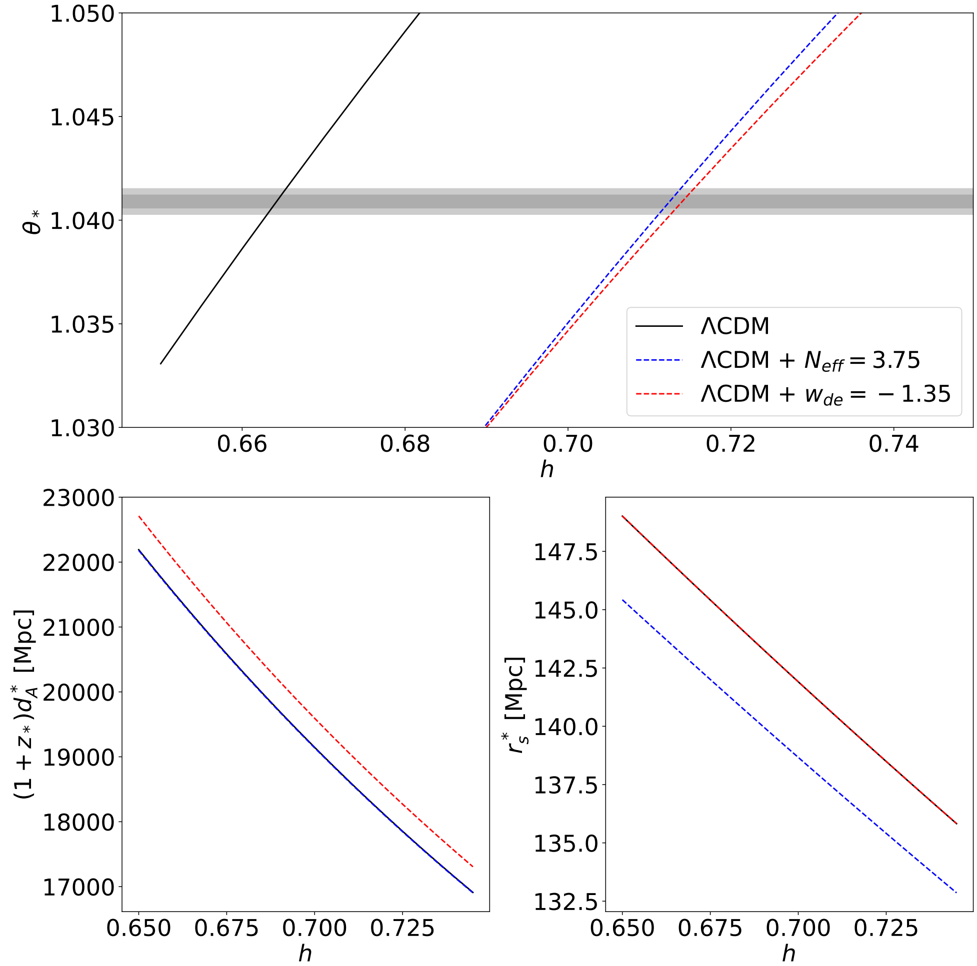

Figure 3.4.: θ_* (top panel), r_s^* (bottom left panel), and d_A^* (bottom right panel) as a function of h for the ΛCDM (black lines), ΛCDM + $N_{\rm eff}$ (blue dashed lines), and ΛCDM + $w_{\rm de}$ (red dashed lines) models. The increase in the effective number of neutrino species, which is assumed to be $N_{\rm eff} = 3.75$, leads to higher value of h consistently with the Planck constraints (grey bands) by reducing the sound horizon scale (bottom right panel) and leaving the normalized angular scale unalterable (bottom right panel). The opposite is observed when the dark energy component is assumed to have a EoS different to -1, ΛCDM + $w_{\rm de}$.

Figure 3.4, where θ_*, r_s^*, and d_A^* as a function of h for the ΛCDM, ΛCDM + $N_{\rm eff}$, and ΛCDM + $w_{\rm de}$ models are shown. The grey bands correspond to the value of the constraint on θ_* provided by Planck 2018 [16].

Although several proposals have shown noticeable success in easing the tension on H_0, data analysis has not confirmed the existence of new physics [120]. In addition, the hitherto proposed models seem to follow a trend of aggravating other problems. Adjustments around recombination increase the value of the Hubble constant by modifying the sound horizon scale. However, such modifications typically lead to tensions with BAO and galaxy clustering/lensing data [119]. For instance, the inclusion of an early dark energy component can fit a local value of the Hubble constant at the cost the of exacerbating the galaxy clustering S8 tension [121]. On the other hand, given that BAO and SNe constrain the Hubble diagram to be consistent with the cosmological constant, late time extensions of the ΛCDM could be not allowed by this kind of data [8]. Finally, models with transitions at very low redshift can fit very well BAO, SNe, and CMB data, but, they will be inconsistent with the SNe calibration provided by Cepheids [H0 Paper III,Benevento et al.], see Section 3.5.3.

One of the goals of this thesis is to determine if a violation of the Copernican principle can explain away the Hubble tension, see Section 5.4. In this context, it will be fruitful, for our future discussion, to review some of our previous analyses of the Hubble problem.

3.5.1. Revising the local determination of H_0

Because of the Equation (2.2), Hubble-Lemaître law, the issue of determining the expansion rate of the Universe reduces to measuring velocities and distances. At small scales, the former can be easily determined from the redshift, this given that $v \approx z$. However, measuring distances is rather challenging. In this context, the cosmic distance ladder, an observational technique that allows us to directly determine the value of the Hubble constant in a model-independent way, was established.

Strictly speaking, the cosmic distance ladder employed by the SH0ES collaboration is a three-step procedure that simultaneous fit geometric distances, Cepheids, SNe in nearby galaxies, and SNe in the Hubble flow, to provide an accurate constraint on the Hubble constant value [17]. Nevertheless, pragmatically speaking, the cosmic distance ladder can be assembled in two steps. First, Cepheid and geometrical distances are combined to provide a calibration of SNe in nearby galaxies. Secondly, such calibration is propagated on SNe in the Hubble flow to determine H_0. As discussed later, the calibration of SNe will be carried out by the absolute magnitude parameter, M_B. Figure 3.5 shows a schematic representation of the SH0ES cosmic distance ladder. Note that the data employed by SH0ES collaboration is also displayed.

3.5.1.1. The effect of peculiar velocities — cosmic variance intrusion

Since the cosmic distance ladder measures the Hubble constant at low redshifts, local effects could influence or bias the determination of H_0. In particular, the presence of peculiar velocities could lead to over/underestimating the value of the expansion rate. In effect, the linear perturbation theory predicts a *local* Hubble constant, $H_0^{\rm loc}$, that deviates from the *global* Hubble constant, H_0, by [123, 124, 125]

$$\delta_H = \frac{H_0^{\rm loc} - H_0}{H_0} = \frac{f(z)}{(2\pi^3)} \int {\rm d}k^3 \delta_m \mathcal{L}(kR) e^{i\vec{k}\cdot\vec{x}} \,, \tag{3.3}$$

where δ_m is the density contrast, $f(z)$ is the growth rate, and R is the scale where the peculiar velocities act. Additionally, $\mathcal{L}$ is a negative function defined as

$$\mathcal{L}(x) \equiv \frac{3}{x^3}\left(\sin x - \int_0^x {\rm d}y \frac{\sin y}{y}\right) .$$

From Equation (3.3), one can note that in an overdense region, $\delta_m > 0$, the Hubble constant is under-estimated, $\delta_H < 0$; while in underdense regions, $\delta_m < 0$, the Hubble constant will be locally over-estimated, $\delta_H > 0$. Statistically, the effect of peculiar velocities is accounted via the variance

$$\langle \delta_H^2 \rangle = \frac{f^2(z)}{2\pi^2 R^2} \int_0^{+\infty} {\rm d}k P_m(k,z) \left[(kr)\mathcal{L}(kr)\right]^2 \,, \tag{3.4}$$

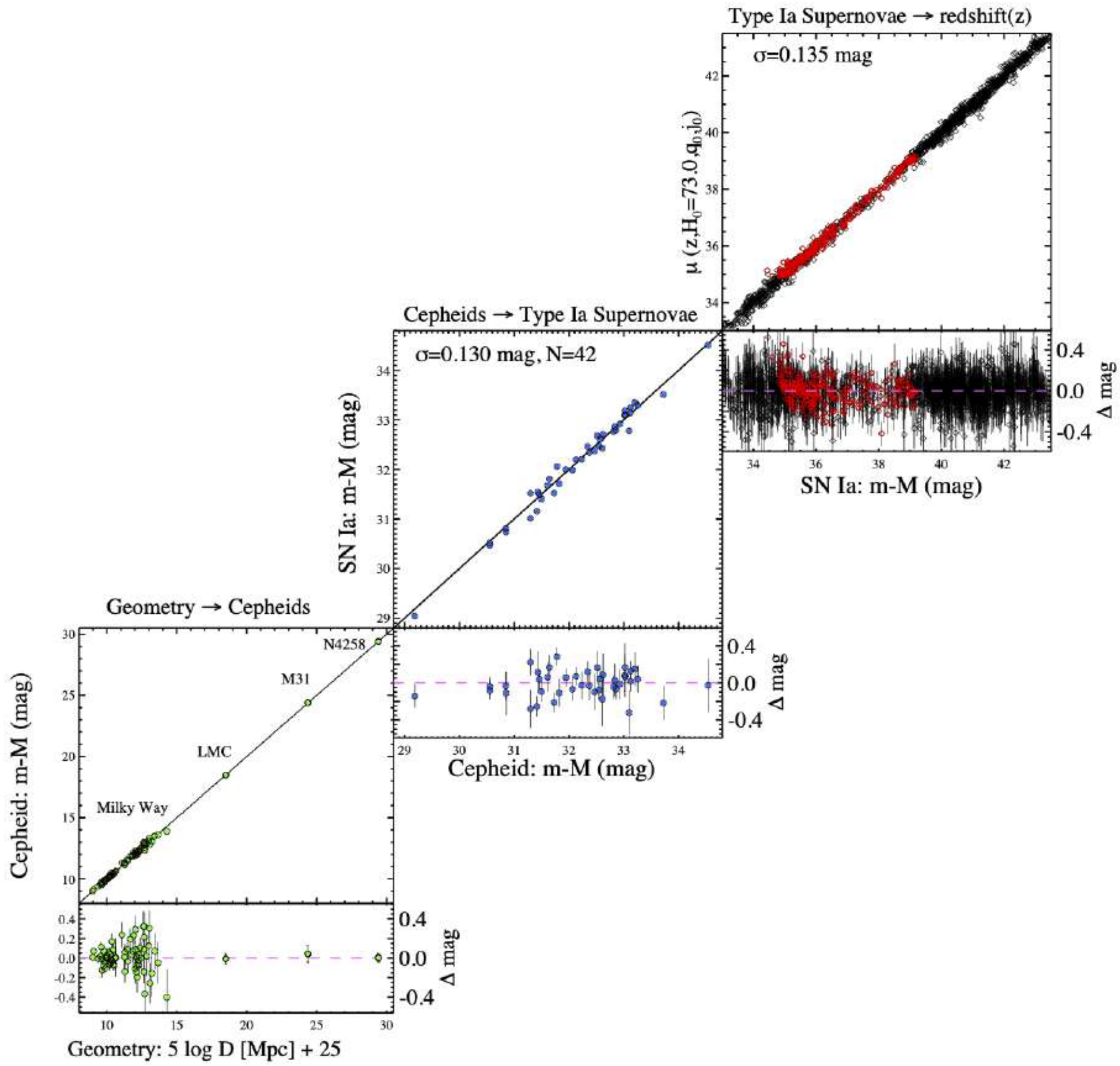

Figure 3.5.: A schematic view of the cosmic distance ladder. Geometrical distances and Cepheids (lower left panel) are used to calibrate nearby SNe (middle panel). This calibration on M_B is then propagete into the SNe in the Hubble flow (upper right panel). Note even though SNe data spams over a wide redshift range (black data points), only those at $0.023 < z < 0.15$ (red data points) will be used to measure the Hubble constant. Figure from Riess et al. [17]

where P_m is the matter power spectrum and the operator $\langle \, \rangle$ denotes the ensemble (or position) average over the perturbation fields, see Section 2.4.3. This variance is the so-called cosmic variance on the Hubble constant. Figure 3.6 shows the root mean square associated with the cosmic variance. As expected, contributions of the peculiar velocities are conspicuous around $z \sim 0.01$ but negligible at $z \sim 0.1$.

The cosmic variance will source a systematic error that could affect the local determination provided by SH0ES and, consequently, produce the discrepancy between early and late times determinations. Such a systematic error can not be assessed by Equation (3.3), given that this latter assumes that SNe are uniformly distributed over the redshift. Instead, to accurately

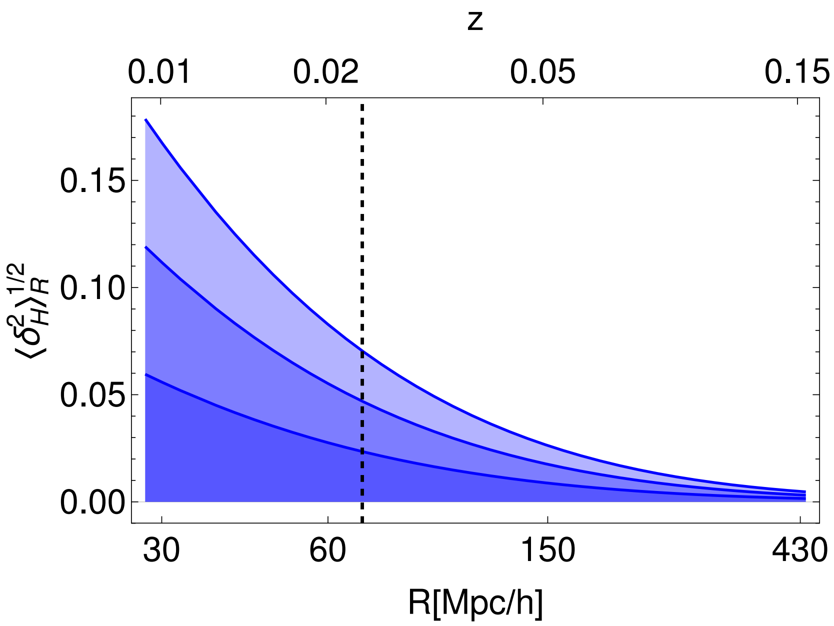

Figure 3.6.: 1, 2, and 3 times the root mean square of the local deviations on the Hubble constant, $\langle\delta_H^2\rangle$, as a function of the scale, R, and redshift, z. As expcted, larger fluctuations are found in small scales (small redshift). The dashed vertical line denotes the redshift $z = 0.0233$. Figure from Camarena and Marra [126]

compute the budget error produced by peculiar velocities it is necessary to include the redshift distribution of the SNe used in the cosmic distance ladder. Thus, the systematic generated by the cosmic variance follows

$$\sigma_{\delta H} = \left[\int_{z_{min}}^{z_{max}} dz W_{\rm SNe}(z) \left\langle \delta H^2 \right\rangle \right]^{\frac{1}{2}} , \tag{3.5}$$

where $W_{\rm SNe}$ is the redshift distribution of the SNe and z_{min} and z_{max} are the limits established by the redshift range of the SNe data set adopted in the cosmic distance ladder

In a manuscript published in 2018, we analyzed if the Hubble tension could be eased by the cosmic variance [126]. By using Equation (3.5), we found that cosmological data constraints $\sigma_{\delta H} = 2.1\%$ for SNe with redshift $0.01 < z < 0.15$ and $\sigma_{\delta H} = 1.2\%$ for SNe with redshift $0.023 < z < 0.15$. Thus, we concluded that this systematic, although it could bias the conclusion of model comparison analysis, can not resolve the Hubble tension. Other approximations have been used to compute the systematic error produced by the cosmic variance. A Hubble bubble model leads to estimating $\sigma_{\delta H} = 1.2\%$ for SNe $0.023 < z < 0.15$ and $\sigma_{\delta H} = 2.1\%$ [127] for SNe $0.01 < z < 0.15$. In agreement with the latter, N-body simulation analyses constrain $\sigma_{\delta H} \approx 1\%$ [128, 129]. On the other hand, Macpherson et al. [130] showed that inhomogeneous and anisotropic cosmological simulation predicts $\sigma_{\delta H} < 1$. Finally, using the called sample variance, Wu and Huterer [131] estimated $\sigma_{\delta H} = 0.4\%$.

Although all the estimates mentioned above do not agree precisely on the estimated cosmic variance error budget, it is easy to conclude from Figure 3.7 that systematic error caused by peculiar velocities can alleviate but not fully explain the tension. Such a conclusion is expected to hold cosmologies beyond the standard model — in contrast to the other results, our estimates are valid not only for the ΛCDM model but also for some phenomenological extensions of it;

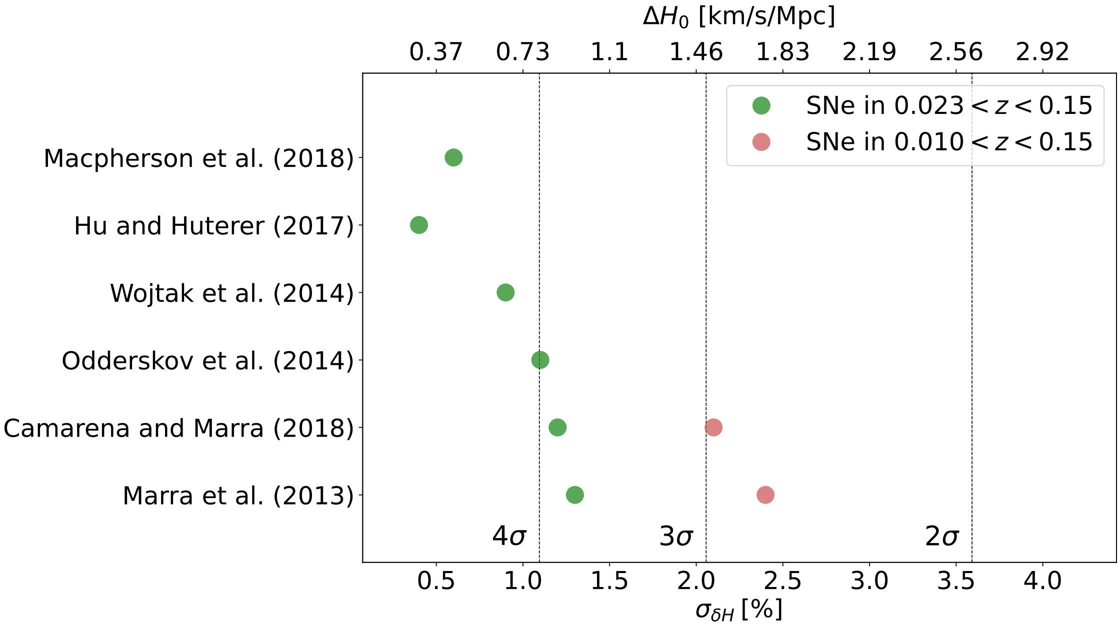

Figure 3.7.: Several estimates of the systematic error produced by peculiar velocities [127, 128, 129, 131, 130]. In SNe with redshift $0.023 < z < 0.15$ are include in the cosmic distance ladder, the cosmic variance can provide at most a deviation of about ~ 1.1 km s^{-1} Mpc^{-1}. Therefore, it is unable to cure the Hubble tension. The inclusion of SNe with arbitrary lower redshift that $z = 0.023$ will boost the effect of peculiar velocities.

extensions that aim to enhance the effect of peculiar velocities. Finally, results presented by Camarena and Marra [126], Marra et al. [127] denote why the current analysis of the SH0ES collaboration adopts $z_{\rm min} = 0.023$ as the minimum redshift for SNe in the Hubble flow, instead of assuming an arbitrary $z_{\rm min} < 0.023$.[5]

3.5.1.2. The role of the deceleration parameter

As discussed above, one of the requirements to provide a precise constraint of H_0 free from cosmic variance systematic is to set a minimum threshold for the redshift of SNe in the Hubble flow. Similarly, in order to keep a model-independent and narrow determination of H_0 it is necessary to limit the maximum redshift of the SNe present in the last step of the cosmic distance ladder.

Recalling the mentioned at the beginning of this section, the problem of determining the Hubble constant is the problem of determining distances. Although standard candles can be used to obtain an observational relation between the redshift and cosmological distances, in order to constraint H_0, a theoretical estimation of distances is necessary. Such theoretical predictions are, in principle, only available under the assumption of a cosmological model, see Section 2.4.2. This complicates the task of providing a model-independent determination of the Hubble constant. However, this problem can be overcome if standard candles are limited to $z \ll 1$.

In order to provide a model-independent determination of H_0, the SNe data in the Hubble flow can be fitted via the so-called cosmographic expansion. This expansion, a Taylor expansion of

[5]Historically, the particular choice of $z_{\rm min} = 0.023$ is justified by the possible existence of a Hubble bubble ending at the same redshift [see 132, and reference therein].

$H(z)$ about $z = 0$, will provide a purely kinematic approximation to the luminosity distance of SNe. Within the cosmographic approximation, the luminosity distance is defined by [133]

$$d_L(z) = \frac{z}{H_0}\left[1 + \frac{1-q_0}{2}z - \frac{1-q_0-3q_0^2+j_0}{6}z^2 + \mathcal{O}(z^3)\right] , \tag{3.6}$$

where j_0, the current value of the jerk parameter, follows

$$j_0 = \left.\frac{\dddot{a}(t)}{H^3(t)a(t)}\right|_{t_0} .$$

Thus, for a SNe at redshift z, the apparent magnitude m_B is given by:

$$\begin{aligned} m_B(z) = {} & 5\log_{10}\frac{zH_0^{-1}}{1\ \mathrm{Mpc}} + 25 + M_B \\ & + 5\log_{10}\left[1 + \frac{1-q_0}{2}z - \frac{1-q_0-3q_0^2+j_0}{6}z^2 + \mathcal{O}(z^3)\right] , \end{aligned} \tag{3.7}$$

where M_B is the absolute magnitude of the given SNe.

Since the apparent magnitude, m_B, is defined to tell us how bright an object appears when viewed from our position, by solely observing SNe we will not be able to determine the distance itself but rather the ratio between the intrinsic luminosity and distance. Therefore, if we aim to determine the distances of SNe, we will also need to measure the absolute magnitude M_B. Defined as the apparent magnitude observed from a distance of 10 pc, M_B effectively calibrates the SNe. Since we can not move from our position to determine the apparent magnitude from a distance of 10 pc, in practice, the absolute magnitude is determined by observing SNe and other standard candles at the same redshift. Within the cosmic distance ladder, such "other" standard candles are the Cepheids.

By definition, the cosmographic expansion holds only at $z \ll 1$, so the SNe data set to be fitted by the cosmographic approximation should be carefully limited if one aims for robust and self-consistent results. Additionally to this, an increase in the redshift maximum adopted for Equation (3.6) could call for an increase in the order of expansion leading to introducing more parameters and virtually introducing more uncertainties in our constraints. Due to this, the SH0ES adopts as the upper limit for the SNe in the Hubble flow $z_{\mathrm{max}} = 0.15$.

The cosmic distance ladder implemented by SH0ES uses the cosmographic expansion up to second-order, Equation (3.7), to fit the SNe data corresponding to the last rung. This technique does not require, in principle, any other further assumption to provide a model-independent measurement of H_0 and the cosmographic parameters. However, the SH0ES baseline analysis fits the Hubble flow SNe by assuming ΛCDM base values for the deceleration and jerk parameters, i.e., it imposes $q_0 = -0.55$ and $j_0 = 1$ on Equation (3.7). Given that such values correspond to the value obtained under the assumption of the ΛCDM model, this is $w_{\mathrm{de}} = -1$ and $\Omega_\Lambda = 0.7$, the main SH0ES determination is not truly model-independent.

In H0 Paper I we perform a reanalysis of the cosmic distance ladder free of the assumption of $q_0 = -0.55$. We first develop a novel statistical method to determine the underlying calibration of the absolute magnitude of SNe, M_B, as given by the Cepheids and geometrical distances, see Appendix A. This method dubbed the demarginalization technique, translates the final constraint provided by Reid et al. [134] into an astrophysical prior of the absolute magnitude of SNe given by $M_B = -19.2334 \pm 0.0404$ (hereafter, astro-prior). Immediately, we use the astro-prior to fit Pantheon SNe at the $0.023 \le z \le 0.15$ using the first-order cosmographic expansion such that

$$d_L(z) = \frac{z}{H_0}\left[1 + \frac{1-q_0}{2}z + \mathcal{O}(z^2)\right] . \tag{3.8}$$

It is possible to demonstrate that neglecting second-order corrections leads to a negligible weighted error of 0.2%. Moreover, tince j_0 is not included in our analysis, our measurements are valid also for a spatially curved Universe.

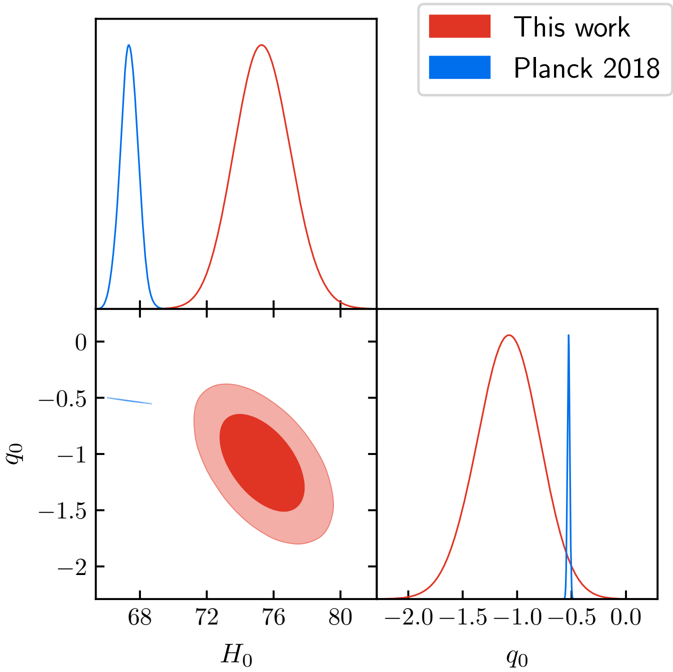

Figure 3.8.: Local determination of the Hubble constant H_0 and the deceleration parameter q_0 from Pantheon SNe and the astro-prior (red contours) [H0 Paper I] compared with the constraints inferred from the CMB data (blue contours) [98]. Figure from H0 Paper I.

Our results show that the assumption of $q_0 = -0.55$ and $j_0 = 1$ leads to underestimate the rate of the expansion of the Universe by ~ 1.9 km s^{-1} Mpc^{-1}, i.e., our analysis constrains the Hubble constant to be $H_0 = 75.35 \pm 1.68$ km s^{-1} Mpc^{-1}. Furthermore, the deceleration parameter is bound to $q_0 = -1.08 \pm 0.29$, which disagrees with the Planck Collaboration at the 2σ level. Although the usage of q_0 as a free parameter leads to an increase in the rate of expansion of the Universe, this does not exacerbate the problem of the tension, because the uncertainties are also raised. Figure 3.8 shows the final results of our analysis presented in H0 Paper I.

Finally, it is important to stress that the latest implementation of the cosmic distance ladder provides an analysis free of the assumption $q_0 = -0.55$. For this analysis, SH0ES reported $q_0 = -0.55 \pm 0.024$ and $H_0 = 73.30 \pm 1.04$ km s^{-1} Mpc^{-1} [17]. While this finding seems to contradict our results, one should note that this complementary analysis provided by SH0ES takes into account SNe with redshift $0.023 \leq z \leq 0.8$ instead of the same used in the main analysis $0.023 \leq z \leq 0.15$. The choice of a broader redshift range is argued by calling upon the necessity of obtaining a $\sim 1.5\%$ estimation of the Hubble constant. We argue that to determine the impact of the deceleration parameter on the local determination of the Hubble constant, an analysis considering $0.023 \leq z \leq 0.15$ is necessary. Note that our finding is consistent with our analysis of the inverse distance ladder and the ΛLTB scenario H0 Paper II and CP Paper II, respectively. In particular, the call for $q_0 < -1$ at local scales could be a hint of fluctuations in the density of matter [135].

3.5.2. The inverse distance ladder

Since the cosmic distance ladder relies on a set of empirical relations used to fit astrophysical data, the presence of systematic errors in such data has been considered as a plausible explanation for the Hubble discrepancy. For instance, Efstathiou [136] claimed that a systematic bias of ~ 0.1 – 0.15 mag in the intercept of the Cepheid period-luminosity relations of SH0ES galaxies would solve the tension. On the other hand, the underlying physics related to cosmological observables such as CMB and BAO is well-defined. This has led cosmologists to propose the so-called inverse distance ladder [137]; a version of the cosmic distance ladder that uses cosmological data instead of astrophysical data.

Besides providing a determination free of astrophysical systematics, the inverse distance ladder also presents an interesting point of view since it directly relates measurements in early times to measurements in late times; in this approach SNe will be calibrated by the CMB and BAO data (or other background probes). However, the main drawback of this method is that, in general, it does not provide a model-independent determination of H_0. The need to convert redshift into distance calls for a fiducial model, [see 137, 138, 139, 140, 141, for instance]. Although some analyses have used the cosmographic expansion [142, 143], one should bear in mind that such approximation only holds at $z \ll 1$; background probes are typically observed around $z \sim 1$. In addition, since SNe at $0.15 < z$ are included in the analysis, the inverse distance ladder does not provide a local determination of the Hubble constant.

To overcome these issues, we presented in H0 Paper II a new method to build the inverse distance ladder.[6] By exploiting Etherington's distance-duality $d_L = (1+z)^2 d_A$ — valid if photon number is conserved and gravity is described by a metric theory — and using binned SNe data, we built up a distance ladder that does not rely on the parameterization of the luminosity-distance relation at $z > 0.15$. This allows us to analyze the typical Hubble flow SNe with redshift $0.023 \leq z \leq 0.15$ to provide local measurements of the Hubble constant and deceleration parameter. Figure 3.9 shows, in a schematic way, how our distance ladder works. SNe data set is splitted in two subset SNe-1 (with redshift $0.023 \leq z \leq 0.15$) and SNe-2 (with redshift $z > 0.15$). The latter will be binned to match the redshift BAO measurements, while the former will be used to constrain H_0 and q_0 by fitting Equation (3.8). Note that we have used two different data sets for BAO measurements coming from anisotropic [144] and angular [145, 146, 147] BAO analyses. Our distance ladder can be anchored by local probes, i.e., the astro-prior on M_B, or early time cosmology, effectively a prior on $r_d \equiv r_s(z_d)$ coming from CMB, where z_d is the redshift of the drag epoch.

Our main results can be inferred from Figure 3.10. First, one can note that the combination $r_d h$ obtained from angular BAO measurements is in tension with the Planck determination at the 4.5σ level. Differently, analysis with anisotropic BAO measurements leads to a value of $r_d h$ that deviates by 1.7σ from the Planck constraints. If a r_d prior from Planck 2018 is assumed, the analysis with angular BAO data will provide constraints on H_0 in perfect agreement with the local determination and strong 4.6σ tension with Planck. Opposite of this, if anisotropic BAO is assumed the final results on H_0 will be consistent both with local and CMB determinations of rate of expansion. Additionally, angular BAO provides a calibration for SNe that is consistent with the astro-prior M_B, but anisotropic BAO raises itself in 3.4σ tension with the latter. On the other hand, analysis adopting the astro-prior on M_B shows that angular BAO provides a constraint on r_d in agreement with CMB and the one from anisotropic BAO is in tension with the latter at the 3.6σ. Finally, all the analyses presented in H0 Paper II constrain the deceleration parameter to

[6] Our approximation also works as a cosmic distance ladder, since it can be used to fit H_0 using the local probes, i.e., the astro-prior.

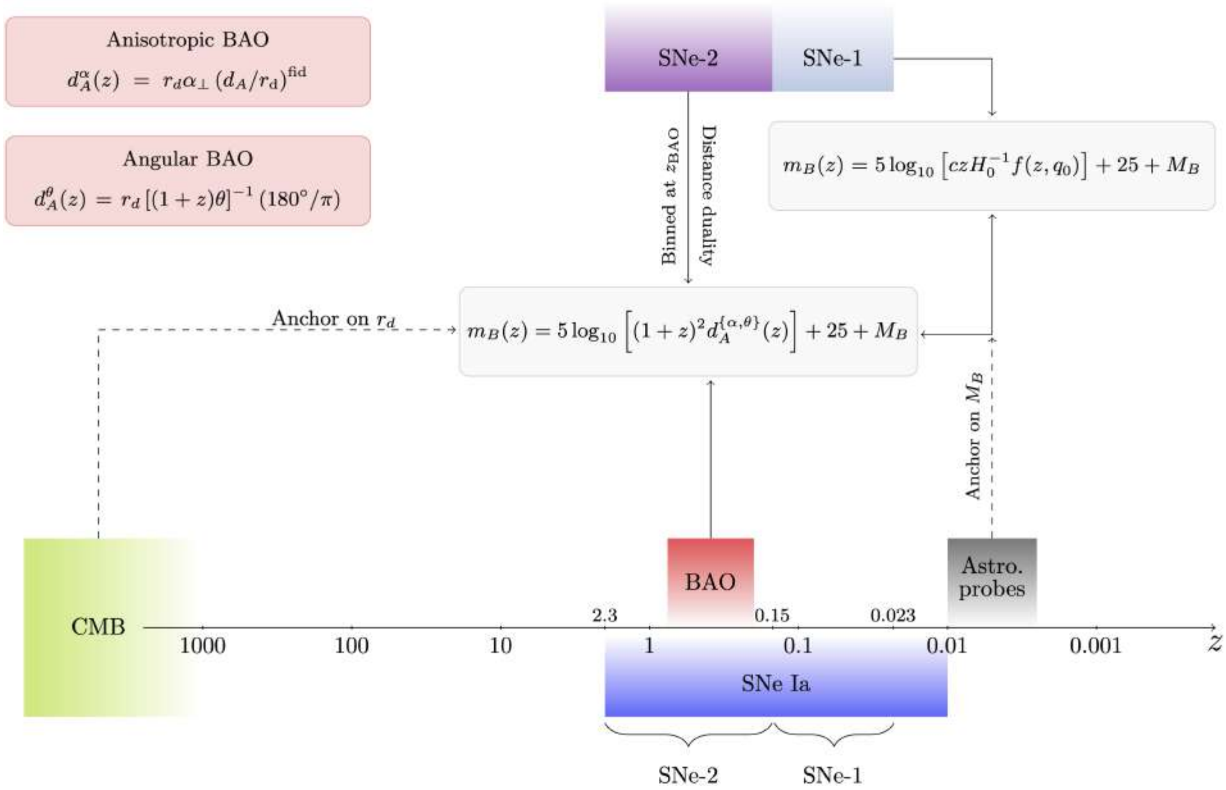

Figure 3.9.: Schematic representation of our approximation to the (inverse) cosmic distance ladder [H0 Paper II]. This novel approximation does not require neither any fiducial model nor parameterization of the luminosity-distance relation at $z > 0.15$. The Hubble constant and deceleration parameter are constrained at $0.023 \leq z \leq 0.15$ by the subset of SNe-1. Figure from H0 Paper II.

$q_0 \approx -1.10 \pm 0.29$ in agreement with our reanalysis of the cosmic distance ladder [H0 Paper I], see Section 3.5.1.

In summary, our analyses consistently bound a deceleration parameter in a 2σ discordance with the CMB constraints; we obtain $q_0 \lesssim -1$. Given that this finding strongly agrees with the results presented in the reanalysis of the cosmic distance ladder [H0 Paper I], see Section 3.5.1, the 2σ discrepancy could be a hint of particular deviations from the ΛCDM model or the presence of systematic in SNe in the Hubble flow. On the other hand, we have found a $\sim 3.5\sigma$ tension between the calibration to M_B provided by the Cepheid, i.e., the astro-prior, and the calibration as inferred from the analysis of CMB and anisotropic BAO data. We will thoroughly discuss this M_B tension on the following Section. Finally, we have to mention that although our results unveil a strong inconsistency between angular and anisotropic BAO measurements, a more recent determination of the angular BAO distances restores the agreement with the main analysis of the BOSS collaboration. Indeed, Menote and Marra [148] demonstrated that the angular BAO distances obtained by analyzing BOSS DR12 and eBOSS DR16 galaxies are in agreement both with the Planck and anisotropic BAO data.

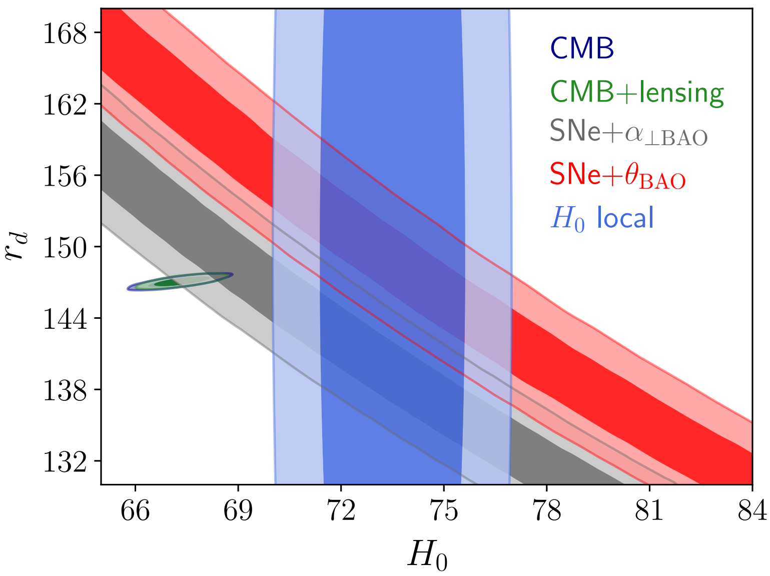

Figure 3.10.: 68% and 95% confidence levels constraints on r_d and H_0 using SNe and BAO data, under our implementation of the (inverse) cosmic distance ladder. It is straightforward to note that there exists a tension between anisotropic (gray contours, $\alpha_{\perp\mathrm{BAO}}$) and angular (red contours, θ_{BAO}) BAO measurements. Depending on which prior is assumed the $\alpha_{\perp\mathrm{BAO}}$ and θ_{BAO} measurements could or not agree with CMB or the local determination of SH0ES. See the text for further information. Figure from H0 Paper II.

3.5.3. The Hubble tension from a Supernovae perspective

Thanks to the demarginalization technique, see Appendix A, we have been able to obtain the calibration of SNe as given by the Cepheids. Further, our novel approach to the inverse distance ladder has shown that the latter is in tension with the effective calibration provided by the combination of CMB and anisotropic BAO. This mean that, from an SNe perspective, the tension between early and late times determinations of H_0 is sourced by the tension on the absolute magnitude, M_B. Being this the case, the role of the absolute magnitude of SNe in the cosmological analysis should be reevaluated — within the cosmological analysis framework, M_B is typically treated as a nuisance parameter. In H0 Paper III we have examined the role of M_B in cosmological inference. Using a toy model whose EoS parameter rapidly crosses to the phantom region at very low redshifts, dubbed the hockey stick model (hereafter, hsCDM model), we performed a cosmological inference analysis considering both the astro-prior and a local prior on H_0. The main results of this analysis are shown in Table 3.1, Figures 3.11 and 3.12.

As shown in Table 3.1, under the usage the prior on H_0 the hsCDM model features an extremely phantom EoS parameter, $w_x \simeq -14$, and provides a significantly lower minimum χ^2 as compared to the wCDM model (top row). Remarkably, the agreement with the SH0ES determination is recovered. The hsCDM, through its rapid transition to the phantom regions, seems then a solution to the Hubble crisis. Nevertheless, the underlying SNe calibration disagrees with the Cepheid calibration — the analysis provides a best-fit on M_B 5σ away from the astro-prior M_B. Given that this particular tension is not introduced in the analysis, i.e., not included in the total χ^2, our results and conclusion will be biased. This fact can be also seen in Figure 3.11, where the

Analysis with prior on H_0	$\hat{\chi}^2_{\rm cmb}$	$\hat{\chi}^2_{\rm bao}$	$\hat{\chi}^2_{\rm sne}$	$\hat{\chi}^2_{H_0}$	$\hat{\chi}^2_{\rm tot}$	$\Delta\hat{\chi}^2$	best-fit vector $\{H_0, \Omega_{M0}, w_x, z_t, M_B, \Omega_{B0}, n_s\}$	distance from $H_0^{\rm R21}$	distance from $M_B^{\rm R21}$
wCDM	2.9	5.1	1030.0	7.8	1045.8	0	{69.6, 0.29, -1.08, ——, -19.39, 0.046, 0.97}	2.8	3.8
hsCDM	1.3	5.9	1027.7	0.3	1035.1	-10.7	{72.5, 0.26, -14.4, 0.010, -19.42, 0.043, 0.97}	0.5	4.9
Analysis with prior on M_B	$\hat{\chi}^2_{\rm cmb}$	$\hat{\chi}^2_{\rm bao}$	$\hat{\chi}^2_{\rm sne}$	$\hat{\chi}^2_{M_B}$	$\hat{\chi}^2_{\rm tot}$	$\Delta\hat{\chi}^2$	best-fit vector $\{H_0, \Omega_{M0}, w_x, z_t, M_B, \Omega_{B0}, n_s\}$	distance from $H_0^{\rm R21}$	distance from $M_B^{\rm R21}$
wCDM	2.8	5.2	1029.3	14.6	1051.9	0	{69.4, 0.29, -1.07, ——, -19.39, 0.047, 0.97}	2.9	3.8
hsCDM	1.8	7.1	1027.1	19.4	1055.4	3.5	{69.3, 0.29, -1.73, 0.055, -19.41, 0.047, 0.97}	3.0	4.4

Table 3.1.: Comparison between the best fits relative to the analyses when the local H_0 prior (top) and the astro-prior on M_B (bottom) are considered. The hat to denotes the minimum χ^2, while the $\Delta\hat{\chi}^2$ values are computed with respect to the best-fit of the wCDM model. The last two columns show the σ-distance $(H_0^{\rm R21} - H_0^{\rm bf})/\sigma_{H_0^{\rm R21}}$ and $(M_B^{\rm R21} - M_B^{\rm bf})/\sigma_{M_B^{\rm R21}}$ from the values of the H_0 and M_B priors, respectively. Table from H0 Paper III.

inferred absolute magnitudes, $M_{B,i} = m_{B,i} - \mu(z_i)$, and Hubble rate according to the best-fit of the hsCDM model are shown. The value found for the Hubble constant is in concordance with the H_0 local prior (left panel), yet, the underlying calibration $M_{B,i}$ shows strong disagreement with the astro-prior (right panel).

On the other hand, the implementation of the astro-prior in the total χ^2 shows that analyses of the hsCDM and wCDM models feature qualitatively similar results. In particular, the hsCDM model effectively yields the same best-fit H_0 as the wCDM model. In both cases the best-fit H_0 is 3σ away from the SH0ES prior. Besides that the hsCDM loses its solving tension appeal, given that the wCDMmodel features a better overall fit to the data. Figure 3.12 explicitly shows how the cosmological inference changes when a prior on M_B is assumed instead of a prior on H_0.

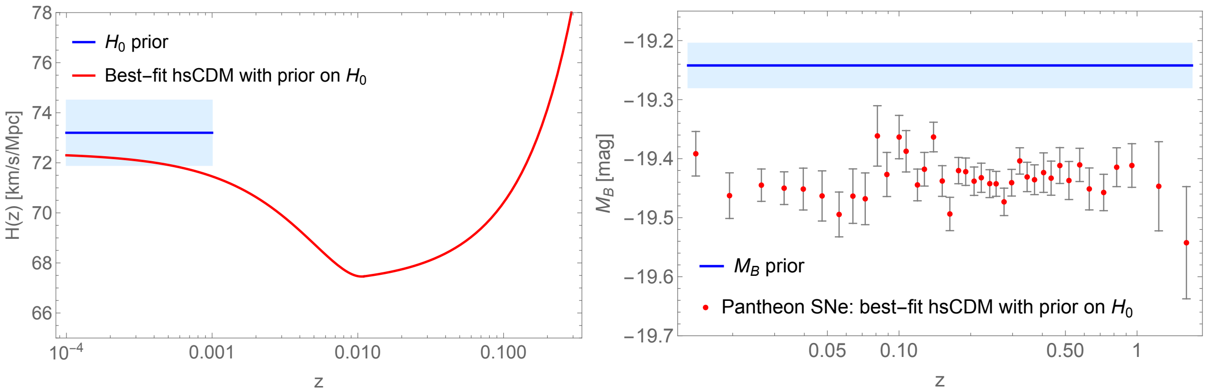

Figure 3.11.: Hubble rate and the inferred absolute magnitudes $M_{B,i} = m_{B,i} - \mu(z_i)$ for the best-fit hsCDM model when using the prior on H_0 (Table 3.1, top). For sake of simplicity, we only show the binned version of the Pantheon catalog. Although the best-fit H_0 agrees well with the H_0 prior (right panel), the inferred $M_{B,i}$ do not agree with the local prior on M_B (left panel).

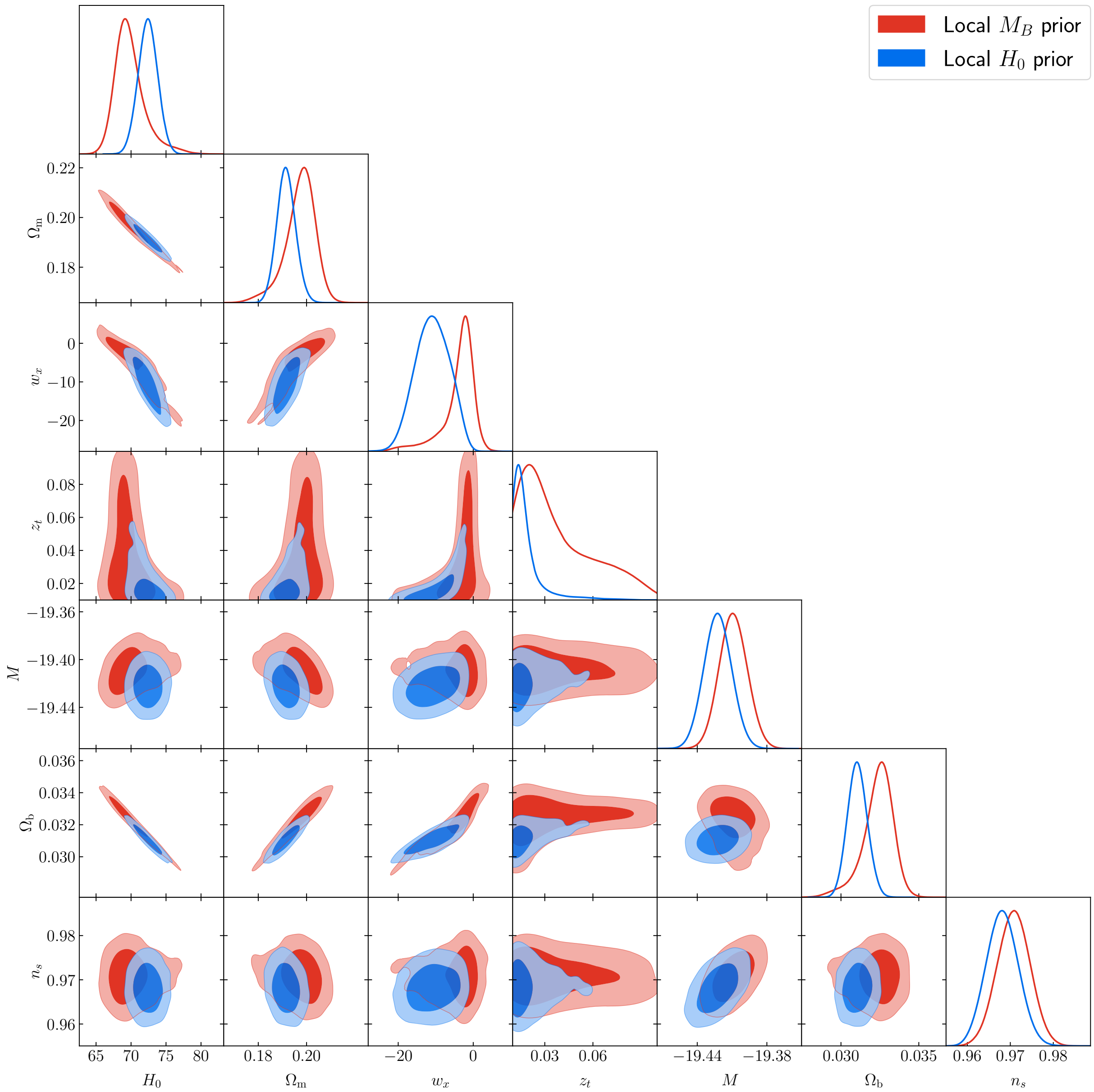

Figure 3.12.: Marginalized constraints for *hs*CDM model from the analysis of CMB, BAO, SNe, and local observations. The two sets of contours show how the cosmological inferences changes when one adopts the prior on MB and the prior on H0. As discussed in the text, the latter analysis leads to biased conclusions by both biasing model selection and distorting the posterior. Figure from H0 Paper III.

From this analysis, we concluded that from an SNe perspective the Hubble crisis is sourced by the mismatch between the calibration on M_B produced by CMB and BAO and the local astro-prior calibration obtained via Cepheids. This result is supported by other analyses [see 140, 122, 96, for instance]. In particular, the present results are in agreement with the conclusions derived from our implementation of the inverse distance ladder [H0 Paper II]. Figure 3.13 shows the calibration to SNe, MB, as obtained from the present analysis and the analysis of the inverse distance ladder. In light of this, we also concluded that when comes to the analysis of late time modifications of the standard model, the astro-prior on M_B should be used instead of a prior on H_0.

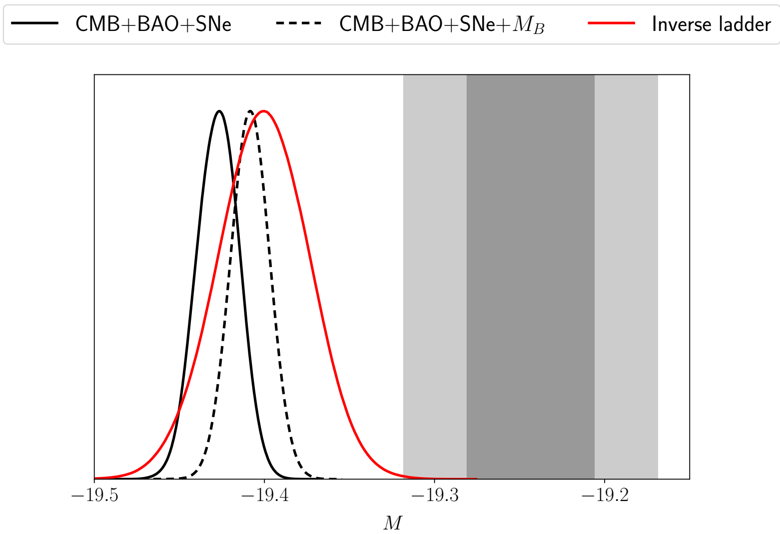

Figure 3.13.: M_B posteriors from the inverse-distance ladder (red line) and the analyses of the hsCDM model (black line) are in strong disagreement with the astro-prior (grey contour). This robustly shows that CMB and BAO measurements produce a SNe calibration in tension with the local astrophysical Cepheid calibration. This remains true even i the astro-prior is used in the analysis of the hsCDM model (black dashed line). We conclude that the difficulty in matching the M_B calibration is the source of the H_0 crisis. Figure from H0 Paper III.

Finally, we would like to highlight that the results and conclusions presented in H0 Paper III have had a remarkable impact on other research; the astro-prior has already been implemented in several cosmological analyses [see 149, 150, 151, 152, for instance]. Additionally, thanks to the discussion raised by H0 Paper III, the last paper presented by the SH0ES collaboration does not only stress the role of the absolute magnitude of SNe M_B in the local determination of the Hubble constant but also explicitly furnishes the underlying calibration used to determinate $H_0 = 73.04 \pm 1.04$ km s^{-1} Mpc^{-1}.

3.5.4. Late M_B transitions models

Although we have robustly demonstrated that late-time modifications of the standard paradigm do not solve tension, there is a class of models that circumvents the problem of the absolute magnitude M_B. We refer to the so-called late M_B transitions models (hereafter, LMT models). By postulating a late time transition on the absolute magnitude of SNe, around $z \sim 1$, the LMT provides a natural explanation for the mismatch between the calibration given by the Cepheids and the effective calibration inferred from the BAO and CMB data.

In collaboration with other researchers, in Alestas et al. [8], we have performed a cosmological analysis considering the LMT model with other dynamical dark energy models. We demonstrated that, while typical models with dynamical dark energy fail on the task of explaining the MB tension, the data allows the transition proposed by the LMT model. It is crucial to mention that, even though, the LMT model is a purely phenomenological approach, a varying gravitational constant could source the late time transition on M_B [153]. On the other hand, analyses of cosmological data have not found evidence in favor of a varying absolute magnitude [see 154, 155, for instance].

3.5.5. The importance of model-independent measurements

An issue that has not yet been discussed, but was subtly present in this Section, is the issue of model-independent measurements. Strictly speaking, there is no such thing as a fully model-independent measurement. In a sense, our measurements, like our cosmological models, are based on fundamental assumptions that provide a suitable framework for interpreting cosmological data. For instance, the dimming of the luminosity of SNe does not directly prove the accelerated expansion of the Universe if the FLRW space-time is not assumed, see Section 2.1.5. Therefore, it is crucial to distinguish that when we describe model-independent measurements we mainly refer to determinations that result agnostic to cosmological dynamics and do not rely on the theoretical framework of the standard ΛCDM model. Yet the cosmological principle is generally assumed. In this context, it is clear why we argue that the main SH0ES analysis, which relies on $q_0 = -0.55$ and $j_0 = 1$, does break the model-independent framework. This also clarifies why we did not refer to our inverse distance ladder determination as a model-independent determination: even though our novel approach to the inverse distance ladder does not assume a fiducial model, it relies on the r_d Planck prior, which is a byproduct of the ΛCDM model and CMB data.

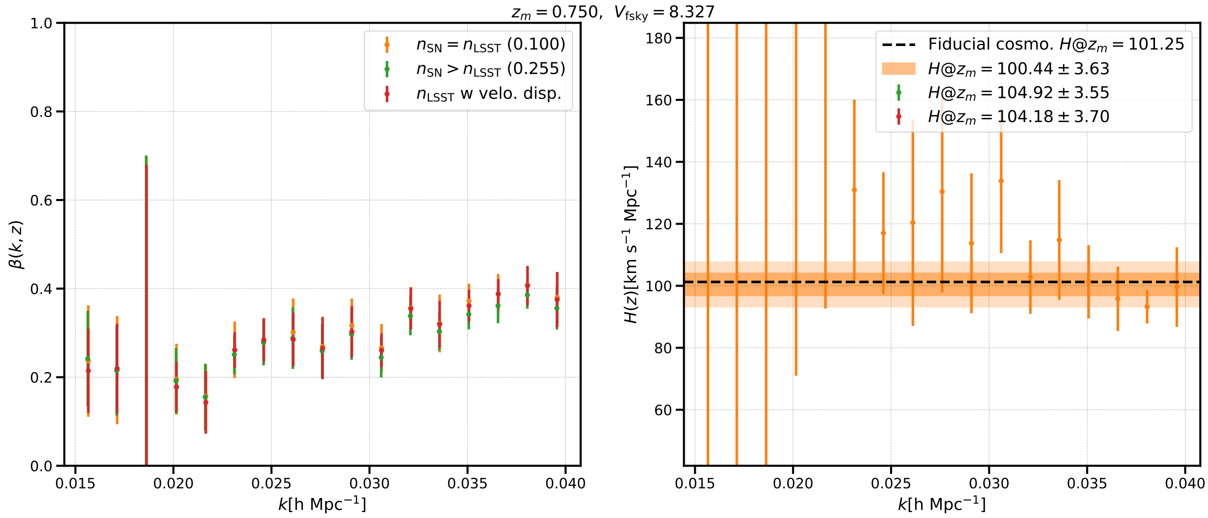

Figure 3.14.: Preliminary results of the CSC project. Cosmological simulations have been obtained through `Pinocchio` [156], while the power spectrums have been reconstructed by using a modified version of the `NBODYKIT` code [157].

Finally, it is worth noting the growing interest in proposing observational methods that increasingly depend on fewer and fewer assumptions [see 158, for instance]. Among these proposed techniques, we emphasize the Cluster of Standard Candles (hereafter, CSC) technique. Presented in 2019 by Amendola and Quartin [159], the CSC method proposes simultaneously measuring the power spectrums of the density matter and peculiar velocities of SNe to provide a model-independent determination of the Hubble rate, $H(z)$, and the $\beta(z) \equiv f(z)/b$. Although this technique will not stand out by its accuracy, the implementation of the CSC method in the cosmological program will be useful to test the fundamental principles of modern cosmology.

In collaboration with my co-supervisor, Prof. Luca Amendola, we are currently working on a more precise forecast analysis of this technique.[7] By using LSST forecast data and cosmological simulations, we aim to forecast the accuracy that this method will provide in the determination of $H(z)$. In July 2021, this ongoing project was accepted as a standard project of the Time Domain Analysis Working Group of the LSST-DESC collaboration. Figure 3.14 shows a preliminary results of the ongoing CSC project. This kind of analyses will allow us to reconstruct, in a model-independent way, the rate of expansion of the Universe.

[7] As part of my PhD training, and in compliance with the PPGCosmo program rules, during 2019-2020 I visited my co-supervisor, Prof. Luca Amendola, at the Institute for Theoretical Physics of Heidelberg University.

Cosmology beyond the Copernican principle: Inhomogeneous space-time solutions

The fundamental assumptions used to build the scientific theory of the Universe represent the frontiers of the standard paradigm of modern cosmology. Thus, expanding such bounds entails extending or rejecting some of the crucial hypotheses of the standard paradigm. From this perspective, it is correct to point out that cosmologists have already embarked on the mission of extending the boundaries of modern cosmology. The accomplishments of such a mission are then remarkable if we talk about the theory of gravity and the matter component of the Universe — cosmologists challenge the general relativity theory and the cosmological constant on a daily basis. However, there are other less explored domains, such as the case of the Copernican principle.

Although we have not yet observationally confirmed the Copernican principle, cosmologists seem to have settled down on the assumption that we do not occupy a special place in the Universe.[1] Compared with the tests of the theory of gravity or the nature of dark energy, the Copernican assumption has lately received less interest. While this could be a bias produced by the historical rejection of the void models as an alternative to dark energy [160, 161] — or the establishment of the concordance cosmology, it could also be related to the underlying complexity of studying non-Copernican models. However, a comprehensive program for cosmology should also include the study of inhomogeneous solutions of the EFE. After all, inhomogeneous models are not alternatives but natural extensions to the FLRW paradigm; and our Universe is not completely homogeneous but rather lumpy.

In this Chapter, we aim to discuss cosmology beyond the Copernican principle by exploring solutions to the EFE that do not rely on the assumption of homogeneity. We open our discussion by briefly reviewing the Szekeres-Szafron, Stephani-Barnes, and Lemaître-Tolman-Bondi solutions. Among the above-mentioned solutions, we shall emphasize the Lemaître-Tolman-Bondi metric by describing both its definition and application in cosmology. By adopting a historical point of view, we reviewed the so-called void models and the observational evidence that led to rule out such models. After this, we shall qualitatively discuss the back-reaction effect. Finally, we present an inhomogeneous generalization to the ΛCDM model: a spherically symmetric inhomogeneous model with a cosmological constant, i.e., the ΛLTB model. Before thoroughly discussing the latter, we advocate the perspective that will define this thesis: although the ΛLTB model does not correspond to a realistic representation of the Universe, it can be used to study the effect of inhomogeneous cosmology.

[1] In the next Chapter, we will discuss on whether or not it is possible to confirm the Copernican principle observationally.

4.1. Inhomogeneous space-times

In a compilation presented in 1997, Krasinski [162] revised and discussed more than 750 papers where inhomogeneous and exact solutions to the EFE were derived. More than a decade later, Bolejko et al. [163] would present an updated discussion of such solutions, including also relevant cosmological analyses presented at the time. Both Krasinski [162] and Bolejko et al. [163] classify the inhomogeneous solutions due to their properties in different families. These families are the Szekeres-Szafron, the Lemaître-Tolman, the Stephani-Barnes families, and other models, including those with null radiation and stiff-fluids. Here, we will succinctly review some of those families.

It is important to note that GR also admits more solutions that do not rely on the Cosmological principle, such as, for instance, the Bianchi solutions. Although these kinds of solutions might be relevant in cosmology, either for historical or pedagogical reasons, we do not review them here as they represent a set of spatially anisotropic but homogeneous solutions of the EFE. The same applies to other types of generalizations to the FLRW that depend on the assumption of homogeneity.

4.1.1. The Szekeres-Szafron family

The solutions belonging to the Szekeres-Szafron family follow the metric [164, 165]

$$ds^2 = -\mathrm{d}t^2 + e^{2\alpha}\mathrm{d}r^2 + e^{2\alpha}\left(\mathrm{d}x^2 + \mathrm{d}y^2\right) , \tag{4.1}$$

with $\alpha \equiv \alpha(t, r, x, y)$ and $\beta \equiv \beta(t, r, x, y)$ being functions to be determined from the EFE with a perfect fluid as the source. This class of solutions possesses two subclasses: when $\partial\beta/\partial r \neq 0$ and when $\partial\beta/\partial r = 0$. While the latter, $\partial\beta/\partial r = 0$, corresponds to a simultaneous generalization of the Friedmann and Kantowski–Sachs models [166] and has no cosmological applications, the former has been applied in different fields of astrophysics and cosmology. For instance, it has been applied to the study of inflationary models [167, 168], the apparent dimming of the supernovae [169], the evolution of cosmological perturbations and cosmic structures [170, 171, 172, 173, 174], CMB [175], the light propagation and ray tracing [176, 177], and anisotropies in the Hubble expansion [178].

4.1.2. The Stephani-Barnes family

The invariant definition of the Stephani-Barnes family of solutions states that this family are all perfect fluid solutions with zero shear, zero rotation, and non-zero expansion. Explicitly, in comoving coordinates, solutions belonging to the Stephani-Barnes family are defined by [179, 180]

$$ds^2 = -D^2\mathrm{d}t^2 + V^{-2}\left(\mathrm{d}x^2 + \mathrm{d}y^2 + \mathrm{d}z^2\right) , \tag{4.2}$$

where $D \equiv D(t)$ has been defined as

$$D = \frac{F(t)}{V}\frac{\partial V}{\partial t} ,$$

with $F(t)$ being an arbitrary function, and $V \equiv V(t, x, y, z)$ a function to determined by the equation

$$w^{-2}\frac{\partial^2 w}{\partial u^2} = f(u) ,$$

where $f(u)$ is another arbitrary function. Although we do not explicitly show this here, the variable u is related in simple ways to the coordinates x, y, z, while the functions $w(t, x, y, z)$ are related in simple ways to the function V.

Similar to the Szekeres-Szafron family, two subsets of solutions compose the Szekeres-Szafron family: the conformally flat solutions and the Petrov type-D solutions. One of the most interesting solutions of this family is the McVittie solution [181], a spherically symmetric solution that asymptotically tends to the FLRW metric. Piattella [182] used this metric to investigate the effect of the cosmological expansion on the bending of light due to an isolated point-like mass.

4.1.3. The Lemaître-Tolman-Bondi metric — a tale about void models

Defined as a spherically symmetric and radial inhomogeneous solution, the Lemaître-Tolman-Bondi (hereafter, LTB) metric follows [183, 184, 185]

$$\mathrm{d}s^2 = -\mathrm{d}t^2 + \frac{R'^2(r,t)}{1-k(r)r^2}\mathrm{d}r^2 + R^2(r,t)\mathrm{d}\Omega\,, \tag{4.3}$$

where $\mathrm{d}\Omega = \mathrm{d}\theta^2 + \sin^2\theta\mathrm{d}\phi^2$ and $k(r)$ is an arbitrary function related to the curvature. The homogeneous case is recovered in the limit $k(r) \to$ constant and $R(r,t) \to a(t)r$, with $a(t)$ being the scale factor as defined in the FLRW metric. Hereafter, we use a prime to denote the partial with respect to the radial coordinate r and a dot to denote the partial derivative with respect to the time t.

4.1.3.1. The light propagation and apparent acceleration

LTB solutions have been widely applied in cosmology, primarily as an alternative explanation for dark energy. The main reason behind this is that the radial dependence introduced by the LTB model can generate an apparent acceleration capable of explaining the dimming of SNe. Generally speaking, any temporal change within our lightcone can be trade for a spatial change; the dimming of the luminosity of SNe could be explained by "faster expansion here than there" rather than "faster expansion now than before". This ambiguity between temporal and spatial change can be demonstrated explicitly using the light propagation equation.

Radiation, as measured by our observations, follows radial null-geodesic paths along our past lightcone, i.e., $\mathrm{d}s = \mathrm{d}\Omega = 0$. Thus, from the LTB line element, we obtain

$$\frac{\mathrm{d}t}{\mathrm{d}u} = -\frac{\mathrm{d}r}{\mathrm{d}u}\frac{R'(r,t)}{\sqrt{1-k(r)r^2}}\,, \tag{4.4}$$

where u is a curve parameter and the minus sign denotes that we are dealing with incoming radiation, $\mathrm{d}r < 0$. This means that the directional derivative along the past lightcone will follow [186]

$$\begin{aligned}\frac{\mathrm{d}}{\mathrm{d}t} &= \frac{\partial}{\partial t} + \frac{\mathrm{d}t}{\mathrm{d}r}\frac{\partial}{\partial r} \\ &= \frac{\partial}{\partial t} - \frac{R'(r,t)}{\sqrt{1-k(r)r^2}}\frac{\partial}{\partial r} \approx \frac{\partial}{\partial t} - \frac{\partial}{\partial r}\,.\end{aligned} \tag{4.5}$$

In the case of the FLRW metric, where the background quantities are r-independent, the last term does not contribute to the total change along the past lightcone. In contrast, in the case of an inhomogeneous metric, the background quantities will be spatially dependent and will provide a not trivial contribution through $\partial/\partial r$. By using the definition of the Hubble rate, we can rewrite the FLRW accelerating condition $\ddot{a} > 0$ as:

$$\frac{\mathrm{d}}{\mathrm{d}t}(aH) = \frac{\mathrm{d}a}{\mathrm{d}t}H + a\frac{\mathrm{d}H}{\mathrm{d}t} > 0\,,$$

given that $\mathrm{d}a/\mathrm{d}t$, a, and H are always positive, we obtain

$$\frac{\mathrm{d}H}{\mathrm{d}t} = \frac{\partial H}{\partial t} - \frac{\partial H}{\partial r} > 0.$$

This is, the typical FLRW acceleration, $\ddot{a} > 0$, can be mimic by an inhomogeneous LTB model through a r-dependent Hubble parameter that satisfies $H'(r) < 0$.[2]

As it will show later, when applied to the EFE, the LTB solution will introduce a non-constant Big Bang time, $t_{\mathrm{BB}}(r)$. This time can be also used to illustrate the apparent acceleration, $H'(r) < 0$. Figure 4.1 shows that $t_{\mathrm{BB}}(r)$ will create an age difference of Δt between a Big Bang FLRW shell and a Big Bang LTB shell that intersect at the same point in our past lightcone. The difference between those shells will observationally translate into a relative velocity and, finally, an apparent acceleration.

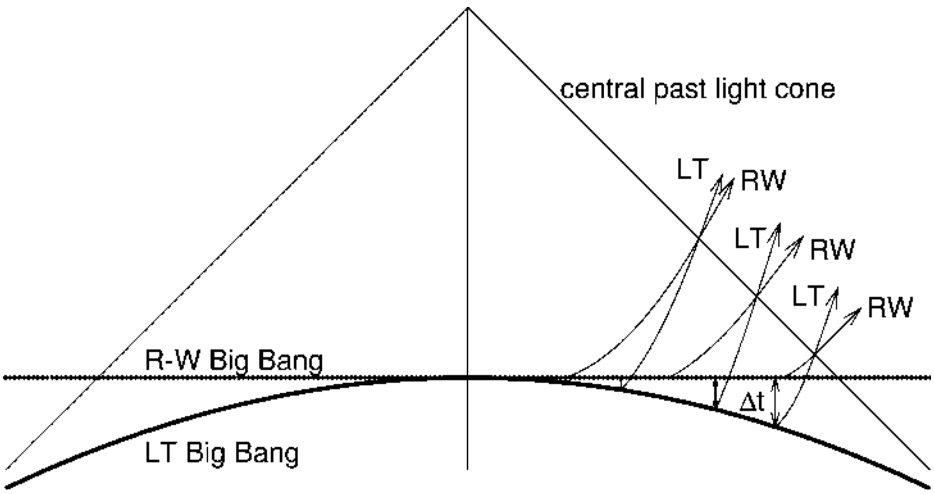

Figure 4.1.: Δt between the FLRW and LTB Big Bang shells generated by $t_{BB}(r)$, the inhomogenous Big Bang time. The age difference between the FLRW and LTB shells will observationally translate into an apparent acceleration. Figure from Krasinski [188]

4.1.3.2. Void models as an alternative to dark energy

Since this family of solutions can feature apparent acceleration, the LTB models have been extensively considered as an alternative to the dark energy component. Substituting to cosmological constant, LTB voids of gigaparsec-scale, with an observer sitting near the center, were shown capable of explaining the dimming of SNe [see 186, 189, 187, 190, 191, 192, 193, for instance]. Although these models exhibited a fine-tuning in the observer's position [194, 163, 38], for more than a decade, the LTB voids were considered a conceivable explanation for the SNe observation and possible indication of a violation of the Copernican principle.

[2]The dimming on the SNe in a LTB model can be also demosntrated through analytical derivation of the luminosity distance, see for instance [187].

Nevertheless, despite its ability to successfully fit the SNe data, the LTB void models were shown to be inconsistent with other observations. In particular, CMB analysis indicated that gigaparsec-scales void would require a low expansion rate of $h \sim 0.65$ to fit the first peak of the CMB [195, 196, 197, 111], raising a substantial disagreement with the local value of the expansion rate measured at the time, $H_0 = 72 \pm 8$ km s^{-1} Mpc^{-1} from [198] and $H_0 = 73.8 \pm 2.4$ km s^{-1} Mpc^{-1} from [199]. Against this, Celerier et al. [200] argued that such conclusions were a consequence of assuming a simultaneous Big Bang time, $t_{\rm BB} = 0$, and that, overall, more general LTB models could easily overcome this issue. Similarly, Clifton et al. [201] explicitly demonstrated that the introduction of an inhomogenous Big Bang time would yield higher values of H_0, and, consequently, lead to an agreement with local measurements.

In spite of all, the LTB void models were ruled out by the analysis of the kinetic Sunyaev–Zeldovich (hereafter, kSZ) effect. Indeed, Zhang and Stebbins [160] proved that LTB inhomogeneities with amplitude large enough to resolve the SNe data would produce a sizable kSZ signal, $\Delta T^2 > 10^3\, \mu K^2$, in strong disagreement with the observationally upper limit established by the South Pole telescope collaboration, $\Delta T^2 < 6.5 \mu K^2$ [202], see left panel of Figure 4.2. Given that the analysis presented by Zhang and Stebbins [160] employed a simplified non-relativistic void model and disregard the dependence of the kSZ amplitude with other cosmological parameters, Zibin and Moss [161] re-examine the evidence against a violation of the Copernican principle found by the previous authors. Overall, Zhang and Stebbins [160] arrived at the same conclusions: void models capable of explaining the dimming of SNe will produce a large amplitude of the kSZ effect, see the right panel of Figure 4.2. Similar analyses relying upon the assumption of a varying Big Bang time led to the same conclusions [203, 204].

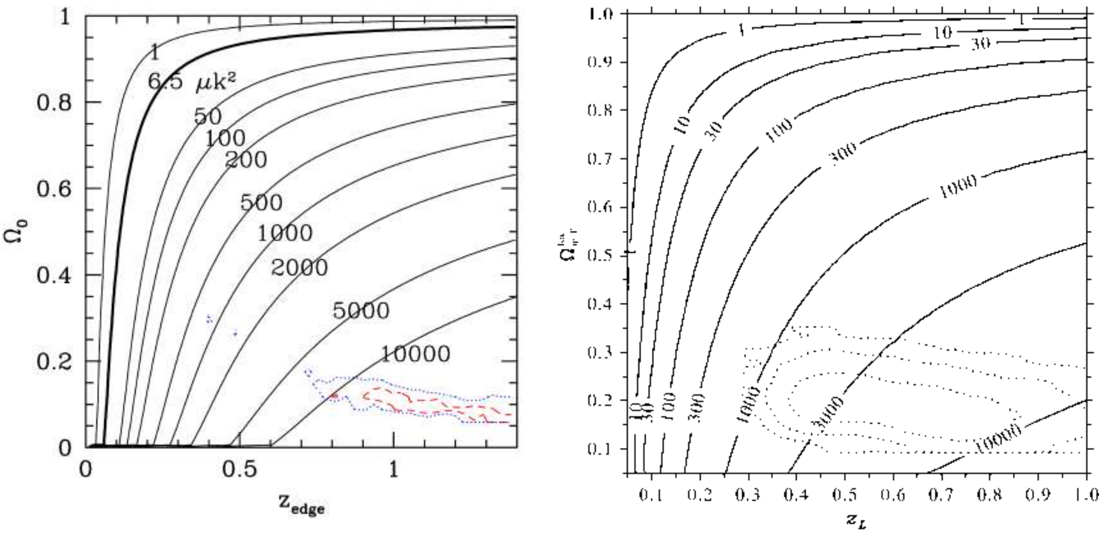

Figure 4.2.: Left panel: Main results of the analyses presented by Zhang and Stebbins [160]. The void model as constrained by the SNe data (blue dotted and red dashed lines) leads to a very large kSZ amplitude in disagreement with the upper limit established by observations, $\Delta T^2 < 6.5\, \mu K^2$ [202]. This constitutes conclusive evidence against the void models. Figure from Zhang and Stebbins [160]. Right panel: Main results of the analyses presented by Zibin and Moss [161]. The LTB region constrained by the cosmological data (black dotted lines) shows an irreconcilable tension with observations. A violation of the Copernican principle as a possible explanation for dark energy is then ruled out. Figure from Zibin and Moss [161].

4.2. Back-reaction effects

The above-mentioned inhomogeneous solutions feature position-dependent background dynamics at large scales, exhibiting a substantial deviation from the standard paradigm. However, fluctuations around the FLRW metric at small scales could also affect the global background dynamics. We refer to the back-reaction effect.

Although we observe extremely non-linear structures at small scales, the standard paradigm assumes that the lumpy Universe is well-described by the FLRW metric and its perturbations. This hypothesis implies that when all inhomogeneities, at small scales, are smoothed out the Universe looks like an FLRW solution — mathematically, an average of the observed Universe will yield the homogeneous and isotropic solution. Following this argument, it is natural to question whether the mentioned assumption does or does not hold in our Universe.

This simplistic explanation could lead one to think that smoothing out the real Universe is a simple process that does not imply any complexity. However, averaging processes are far from trivial in GR. This is evident once we note that because of the non-linearity of the EFE, in general, the smoothing process does not commute. This means that the smooth Einstein tensor and the FLRW Einstein tensor are not the same, i.e.,

$$G_{\mu\nu}^{(\text{smooth})} \neq G_{\mu\nu}^{(\text{FLRW})} \,. \tag{4.6}$$

The difference between those will source the so-called back-reaction effect: the change that small-scale inhomogeneities produce on the global dynamics of the cosmos. To better explain this, we use Figures 4.3 and 4.4.

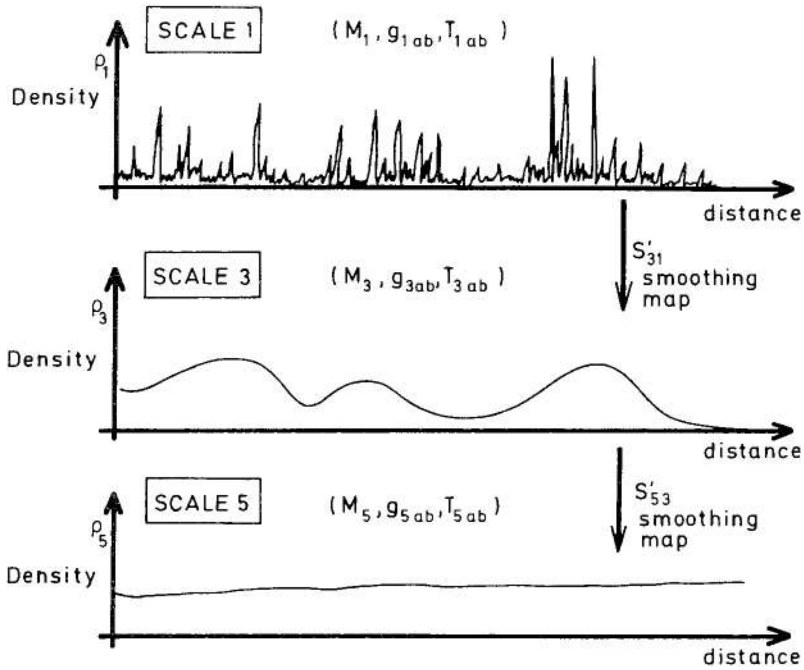

Figure 4.3.: The homogeneous Universe (scale 5) is obtained by smoothing the real lumpy Universe (scales 1 and 3). Each scale will be described by a different metric and energy-momentum tensor, g_{iab} and T_{iab}, which are defined in different manifolds M_i, with $i = 1, 2, 3$. Figure from Ellis [205]

Observations at small scales, where, for instance, stars are relevant structures, will lead to concluding that the distribution of the matter around the cosmos is highly inhomogeneous (scale 1 in Figure 4.3). In contrast, observing the Universe on larger scales will detail the existence of galaxy-like structures and point out a moderately homogeneous energy density (scale 2 in Figure 4.3). Eventually, at sufficiently large scales, observations will display a homogeneous Universe well-described by the FLRW solution (scale 3 in Figure 4.3). Each of those pictures will be mathematically described by their metric, g_{iab}, and energy-momentum tensor, T_{iab}, with $i = 1, 2, 3$, where each pair (g_{iab}, T_{iab}) will correspond to a different manifold, M_i. This denotes that, even if we assume that scale 3 is the resulting picture of smoothing scale 1, mathematically, we are relating quantities that live in different manifolds. Then, it is clear that the smoothing process will carry out by a map that smooths the metric and take us from one scale (manifold) to another scale (manifold).

Figure 4.4 illustrates how the averaging/smoothing process works in the GR framework. The S_{31} map smooths the inhomogeneities present in g_{1ab} to yield g_{3ab}, the metric of the following scale. A different map, S'_{31}, smooths the small-scale fluctuations featured by the energy-momentum tensor T_{1ab} resulting in a moderately homogeneous distribution of matter described by T_{3ab}. Moreover, a third map S''_{31} features the average from scale 1 to scale 3 on the Einstein tensor. Therefore $S' \neq S''$ and, in consequence, $\langle G_{ab}(g_{1ab})\rangle \neq G_{ab}(\langle g_{1ab}\rangle)$. The latter is equivalent to the stated in Equation (4.6). Lastly, the back-reaction of small scale will introduce an extra term, $P_{\mu\nu}$, on the EFE such that [205]

$$G^{(\mathrm{smooth})}_{\mu\nu} = 8\pi G T^{(\mathrm{smooth})}_{\mu\nu} + P_{\mu\nu}\,, \tag{4.7}$$

where $P_{\mu\nu} = G^{(\mathrm{FLRW})}_{\mu\nu} - G^{(\mathrm{smooth})}_{\mu\nu}$.

Because of its relationship with the non-linear structures, cosmologists have conjectured that the back-reaction effect may be responsible for the dark energy phenomena [see for instance 206, and references therein]. Back-reaction avoids the fine-tuning problem and naturally predicts an acceleration phase: the arising of non-linear structures around $z \sim 1$ will affect the dynamics of the Universe through $P_{\mu\nu}$, then leading to an accelerated expansion at late times. Although this scheme has been largely studied, there is no established consensus on the magnitude of the back-reaction effect [207, 208, 209], nonetheless, this is commonly assumed to be negligible. On the other hand, numerical relativity simulations seem to support the hypothesis of a negligible back-reaction contribution [210].

Complementary, within the LTB framework, the question if back-reaction will impact or not the dynamics of the Universe can be analytically assessed [211]. In particular, the kind of ΛLTB models to be considered here are expected to provide a back-reaction effect proportional to $(L/D_H)^2$, with L being the size of the inhomogeneity and $D_H = 1/H_0$ [4]. Given that all the relevant cases here studied will satisfy $(L/D_H)^2 \ll 1$, we disregard the back-reaction effects.

4.3. An inhomogeneous generalization of the standard model: the ΛLTB model

In the previous Chapters, we have described the standard paradigm of modern cosmology as well as the problems facing the standard model. In particular, we have emphasized the fundamental assumptions that ground a scientific theory of the Universe. On the other hand, in the earlier sections of the present Chapter, we have reviewed some of the exact inhomogeneous solutions of the EFE and described the back-reaction effect. Among the revised solutions, we highlighted the historical importance of the so-called void models — Einstein-de Sitter LTB solutions capables

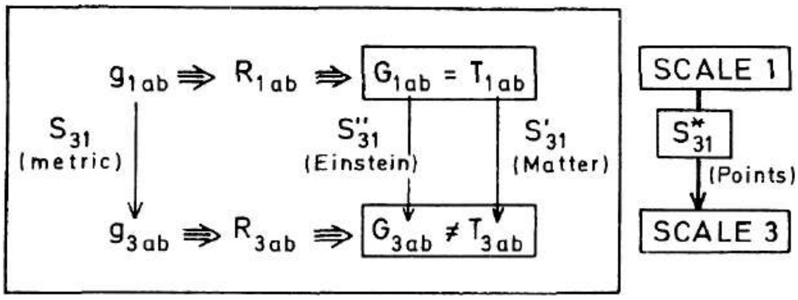

Figure 4.4.: Schematic illustration of the smoothing/averaging procedure within the GR framework. Since $S' \neq S''$, the smoothing operator does not commute resulting in $\langle\, G_{ab}(g_{1ab})\rangle \neq G_{ab}(\langle\, g_{1ab}\rangle)$. Figure from Ellis [205]

of explaining the cosmic acceleration. In this Section, relying on all the hitherto discussed, we shall present the ΛLTB model, a generalization of the standard model that does not rely on the assumption of the Copernican principle. As explained in the following, this model shall portrait the perspective adopted in this thesis to study the physics beyond the Copernican principle.

4.3.1. The ΛLTB model as a non-Copernican cosmological model

Inhomogeneous models are not alternative models to the standard paradigm but generalizations of the same. Indeed, by dropping or easing the hypothesis of homogeneity, we add new degrees of freedom to the paradigm established by the FLRW solution. These will not lead to a completely different and unrelated framework to the one proposed by the FLRW scheme but rather an extension of it. In this context, we propose the study of cosmology beyond the assumption of the Copernican principle through the ΛLTB model: a ΛCDM model endowed with a spherical inhomogeneity. Although we do not use the ΛLTB model as an alternative way to model dark energy phenomena, within the line of thought of this thesis, the inhomogeneous ΛLTB model is interpreted as a violation of the Copernican principle. Assuming that we are placed within an inhomogeneous spherical structure, we aim to test if the cosmological data can constrain such a structure to the Copernican regime. Furthermore, we also intent to determine if the Hubble tension is a hint for a violation of the Copernican principle.

Note that the ΛLTB model is undeniably limited, and the assumption of an inhomogeneous but spherically symmetry metric emerges as an ansatz that simplifies a more complex configuration of the Universe. The framework adopted here does not correspond to realistic modeling of the Universe but is a simplification of it. At the same time, this inhomogeneous model derives from a generalization of the standard model and its idealistic approximation of cosmic homogeneity. We argue that this ΛLTB landscape is suitable for assessing the problems treated here: the local-void scenario as a solution to the Hubble constant and the observational test of the Copernican principle. We believe that the aims of this thesis can be accomplished by considering that more general inhomogeneous degrees of freedom can be condensed into radial deviations from the FLRW metric.

Additionally, we neglect possible anisotropic degrees of freedom by placing the observer at the center of the spherical inhomogeneity. Although the imposition of a center observer lead to a fine-tuning in our model, this choice is empirically justified. In effect, in the case of the test of the Copernican hypothesis, the CMB dipole, see Section 3.3, shall constrain $d_{\rm obs} \lesssim 300$ Mpc yielding to a slight fine-tuning of around $1/40$, where $d_{\rm obs}$ is the distance between the observer and the center. On the other hand, in order to be consistent with the observed CMB dipole, the local void scenario will call for $d_{\rm obs} \lesssim 60$ Mpc consequently leading to a bigger fine-tuning of $\sim 1/1000$. In this case, the high value of fine-tuning is justified since, if successful, one trades a one-in-a-million (5σ) inconsistency in data with a one-in-a-thousand fine-tuning. For a thoroughly discussion of this issue see Sections 5.3.3.5 and 5.4.2.4.

As an alternative point of view, another way of approaching the ΛLTB models is assume that this class of models does not constitute a violation of the Copernican principle but it does imply that the assumption of homogeneity could be valid at larger scales. This approach has been used, for instance, by Marra et al. [4] to develop a program for studying perturbations in an inhomogeneous space-time and provide for the first time a suite of simulations for the ΛLTB models. Although this interpretation is adequate to promote the study of the large-scale structure evolution beyond the assumption of homogeneity, it dissents from the objectives of this thesis. We aim to determine if cosmological data can constrain the LLTB inhomogeneity to be Copernican level, with the scale of homogeneity being tacitly set by the latter.

Finally, in agreement with our interpretation of ΛLTB models, we adopt a particular class of spherical inhomogeneous models: the early-FLRW cosmological models. Given that, our test of the Copernican principle and the Hubble tension problem relates to the late time cosmology, we require that, at early times, a near-FLRW metric is recovered. We maintain the concordance with the standard inflationary paradigm and leave unchanged (pre-)recombination physics.

4.3.2. Background dynamics

4.3.2.1. The inhomogeneous Friedmann-like equations

By using the EFE, see Equation (2.22), and an energy-momentum tensor with a dust component, $T_{\mu\nu} = \rho_m(r,t)U_\mu U_\nu$, we obtain the set of equations that will reign the global dynamics of the ΛLTB model. Such equations are defined through [186]:

$$\frac{\dot{R}^2}{R^2} + \frac{k(r)r^2}{R^2} + \frac{2\dot{R}\dot{R}'}{RR'} + \frac{\left[k(r)r^2\right]'}{RR'} = 8\pi G\left(\rho_m + \rho_\Lambda\right)\,, \tag{4.8}$$

$$\dot{R}^2 + 2R\ddot{R} + k(r)r^2 = 8\pi G\rho_\Lambda R^2\,, \tag{4.9}$$

where we have used $\rho_\Lambda = \Lambda/8\pi G$, see Section 2.4.1. Note that, for the sake of simplicity, we have dropped the argument (r,t) in the functions ρ_m, R, and the different derivatives of the latter.

At first glance, Equations (4.8) and (4.9) remind us of the Friedmann equations, Equations (2.7) and (2.8), mainly because terms likes $\dot{R}/R$, $8\pi G\rho_m$, or kr^2/R^2 appear. However, these last equations also include terms that do not seem to have an FLRW counterpart. In pro of developing an analog picture between the FLRW and LTB models, we rewrite the above-mentioned equations to obtain the "inhomogeneous Friedmann" equations.

Integrating Equation (4.9) over R

$$\int\left(\dot{R}^2 + 2R\ddot{R}\right)\mathrm{d}R = \int\frac{\mathrm{d}}{\mathrm{d}R}\left(R\dot{R}^2\right)\mathrm{d}R = \int\left[8\pi G\rho_\Lambda R^2 - k(r)r^2\right]\mathrm{d}R\,,$$

we can obtain the equation analogue to the first Friedmann equation

$$\frac{\dot{R}^2(r,t)}{R^2(r,t)} = \frac{8\pi G}{3}\rho_\Lambda + \frac{2m(r)}{R^3(r,t)} - \frac{k(r)r^2}{R^2(r,t)}\,, \tag{4.10}$$

where $m(r)$, defined as an arbitrary and positive function, arose as a constant of integration.[3] Additionally, if we derive Equation (4.10) with respect to the radial coordinate and substitute

[3] Note that a factor of 2 has been artificiality placed in front of the function $m(r)$. This is just a convention with no physical repercussions. In general, such a factor can be absorbed by the arbitrary function m.

the results in Equation (4.8), we get the

$$\rho_m(r,t) = \frac{m'(r)}{4\pi G\, R'(r,t) R^2(r,t)}\,. \tag{4.11}$$

Due to the above equation, $m(r)$ is called the mass function. As expected, in the FLRW limit, this is, when $R = a(t)r$, $\rho_m(r,t) = \rho_m(t)$, and $k(r) = \text{const.}$, Equation (4.10) trivially reduces to Equation (2.7), the first Friedmann equation. On the other hand, the equation analog to the acceleration equation can be obtained by combining Equations (4.8) and (4.9), such that

$$\frac{2}{3}\frac{\ddot{R}(r,t)}{R(r,t)} + \frac{1}{3}\frac{\ddot{R}'(r,t)}{R'(r,t)} = -\frac{4\pi G}{3}\left[\rho_m(r,t) + \rho_\Lambda\right]\,. \tag{4.12}$$

The last equation illustrates, once again, why the inhomogeneous LTB models were considered as an alternative to dark energy phenomena: the cosmic acceleration can be attained even if $2\rho_\Lambda < \rho_m$ at the cost of $\ddot{R}'(r,t) < 0$.

In addition, one should note that the line element Equation (4.3) states an inhomogeneous and anisotropic expansion — instead of a unique scalar factor, there are two scale factors: a transverse scale factor, $a_\perp(r,t) = R(r,t)/r$, and a longitudinal one, $a_\parallel(r,t) = R'(r,t)$. Using these, we defined the corresponding expansion rates

$$H_\perp(r,t) = \frac{\dot{a}_\perp(r,t)}{a_\perp(r,t)}\,, \tag{4.13}$$

$$H_\parallel(r,t) = \frac{\dot{a}_\parallel(r,t)}{a_\parallel(r,t)}\,. \tag{4.14}$$

The transverse Hubble rate can be used to recast Equation (4.10), such that

$$\left[\frac{H_\perp(r,t)}{H_\perp(r,t_0)}\right]^2 = \Omega_{m0}(r)\left[\frac{a_\perp(r,t_0)}{a_\perp(r,t)}\right]^3 + \Omega_{k0}(r)\left[\frac{a_\perp(r,t_0)}{a_\perp(r,t)}\right]^2 + \Omega_{\Lambda 0}(r)\,, \tag{4.15}$$

where the present-day density parameters are now functions of r,

$$\Omega_{\Lambda 0}(r) = \frac{\Lambda}{3H_\perp^2(r,t_0)}\,, \tag{4.16}$$

$$\Omega_{k0}(r) = -\frac{k(r)}{H_\perp^2(r,t_0)\, a_\perp^2(r,t_0)}\,, \tag{4.17}$$

$$\Omega_{m0}(r) = \frac{2\, m(r)}{H_\perp^2(r,t_0)\, a_\perp^3(r,t_0)\, r^3}\,, \tag{4.18}$$

which, akin to the FLRW case, fulfill $\Omega_{m0}(r) + \Omega_{k0}(r) + \Omega_{\Lambda 0}(r) = 1$.

In analogy to the ΛCDM model, we can use the inhomogeneous first Friedmann equation to compute the age of the Universe, t_0. Integrating Equation (4.15), we obtain

$$t_0 - t_{\rm BB}(r) = \frac{1}{H_\perp(r,t_0)}\int_0^1 \frac{\mathrm{d}x}{\sqrt{\Omega_{m0}(r)x^{-1} + \Omega_{k0}(r) + \Omega_{\Lambda 0}(r)x^2}}\,, \tag{4.19}$$

where $t_{\rm BB}(r)$, the so-called Big Bang time, is another arbitrary function of the ΛLTB model. The Big Bang time function can be interpreted as the time corresponding to the Big Bang singularity surface.

4.3.2.2. The geodesic equations and cosmological distances

The equations above define quantities as a function of the time t and radius r in our past lightcone. Since, eventually, most of such quantities will be related to the observational phenomena, it is necessary to rewrite such function as a function of the redshift z in the past lightcone. The geodesic equations are needed in order to do so.

Assume that a standard candle emits two photons, one at t_1 and the other at $t_2 = t_1 + \lambda$. Since these photons follow radial null, from the LTB line element, or Equation (4.4), it is clear that

$$\frac{\mathrm{d}t_1}{\mathrm{d}u} = -\frac{\mathrm{d}r}{\mathrm{d}u}\frac{R'(r,t_1)}{\sqrt{1+2r^2k(r)\tilde{M}^2}}\,, \tag{4.20}$$

$$\frac{\mathrm{d}t_2}{\mathrm{d}u} = \frac{\mathrm{d}\,(t_1+\lambda)}{\mathrm{d}u} = -\frac{\mathrm{d}r}{\mathrm{d}u}\frac{R'(r,t_1)}{\sqrt{1+2r^2k(r)\tilde{M}^2}} + \frac{\mathrm{d}\lambda}{\mathrm{d}u}\,. \tag{4.21}$$

On the other hand, from Equation (4.4) is also true

$$\begin{aligned}\frac{\mathrm{d}t_2}{\mathrm{d}u} &= -\frac{\mathrm{d}r}{\mathrm{d}u}\frac{R'(r,t_1+\lambda)}{\sqrt{1+2r^2k(r)\tilde{M}^2}}\,,\\ &= -\frac{\mathrm{d}r}{\mathrm{d}u}\left[\frac{R'(r,t_1)+\dot{R}'(r,t_1)\lambda}{\sqrt{1+2r^2k(r)\tilde{M}^2}}\right]\end{aligned} \tag{4.22}$$

where we have used the Taylor expansion in the last line. Using the definition of the redshift, $z \equiv \lambda(0)/\lambda(u) - 1$, and Equations (4.21) and (4.22), we obtain

$$\frac{\mathrm{d}z}{\mathrm{d}u} = \frac{\mathrm{d}r}{\mathrm{d}u}\frac{(1+z)\dot{R}'(r,t)}{\sqrt{1+2r^2k(r)\tilde{M}^2}}\,. \tag{4.23}$$

Subsequently, the radial and temporal evolution of the redshift will be determined by set the of differential equations [186]:

$$\frac{dz}{dt} = -\frac{(1+z)\dot{R}'(r,t)}{R'(r,t)}\,, \tag{4.24}$$

$$\frac{dz}{dr} = \frac{(1+z)\dot{R}'(r,t)}{\sqrt{1+2r^2k(r)\tilde{M}^2}}\,. \tag{4.25}$$

Since we assume an observer placed at the center of the spherical structure, the equations above will be solved by using as initial condition: $z(t=t_0) = 0$ and $z(r=0) = 0$.

Finally, from the LTB metric, Equation (4.3), one can note that the angular and luminosity distances, respectively, are

$$D_A(z) = R(r(z),t(z))\,, \tag{4.26}$$

$$D_L(z) = (1+z)^2R(r(z),t(z))\,, \tag{4.27}$$

with $t(z)$ and $r(z)$ being the solutions to the geodesic equations.

4.3.3. Arbitrary degrees of freedom — free functions: $m(r)$, $t_{\rm BB}(r)$, and $k(r)$

As already mentioned, the assumption of the Copernican principle reduces the number of degrees of freedom needed to develop a mathematical description of the Universe. Thus, it is not a surprise that if such a principle is dropped new degrees of freedom arise. In the case of the ΛLTB model, such new degrees of freedom will be characterized by the three arbitrary functions introduced in the previous Section: the mass function $m(r)$, the curvature profile $k(r)$, and the Big Bang function $t_{\rm BB}(r)$.

Here, we describe and argue our particular choice for such arbitrary functions. We carefully set these degrees of freedom in concordance with our aims.

4.3.3.1. $m(r)$ as a gauge of freedom

Due to the spherical symmetry established by Equation (4.3), the free functions introduced by the ΛLTB model are all invariant under a coordinate transformation of the form $\hat{r} = f(r)$, with f being a monotonic function. This means that it is possible to define the radial coordinate such that one of the three arbitrary functions is fixed [212]. Here, we fix this extra gauge of freedom by choosing a radial coordinate such that the mass function can be defined by $m(r) = m_0 r^3$, where m_0 is a proportionality constant to be defined.

Although fixing $m(r)$ is allowed by the extra gauge of freedom, this particular choice exhibits a drawback: vacuum regions are only available at $r = 0$. Indeed, our particular choice defines a derivative $m'(r) = 3m_0 r^2 > 0$ and therefore $m'(r) \propto \rho_m \neq 0$ for any $r > 0$. This is, vacuum solutions do not exist for $r \neq 0$. This limitation will not impact our future analyses since it will only prevent us from modeling extreme void regions, i.e., with a density contrast with $\delta = -1$.

4.3.3.2. $t_{\rm BB}(r)$ and the (presence of) decaying modes

While $m(r)$ can be set through an extra degree of freedom, the other two functions, $t_{\rm BB}(\rm r)$ and $k(r)$, will define the physical nature of our model. For instance, since our analysis of the Copernican principle will be presented in the context of early-FLRW cosmologies, we can impose $t_{\rm BB}(\rm r)$ and $k(r)$ in agreement with near-FLRW metrics at early times. This condition is particularly constraining for the Big Bang time, which is expected to introduce decaying modes [213] leading to a disagreement with the standard paradigm of inflation and an inhomogeneous space-time at early times [214].

Intuitively, this occurs because different Big Bang shells will occur at various points in time, leading to a non-negligible inhomogeneity at early times. Mathematically, this can be illustrated by the derivative of Equation (4.19)

$$\frac{{\rm d}t}{{\rm d}a_\perp} = \frac{t'(r)}{a'_\perp(r,t)} = \frac{1}{H_\perp(r,t_0)}\left[\Omega_{m0}(r)x^{-1} + \Omega_{k0}(r) + \Omega_{\Lambda 0}(r)x^2\right]^{-1/2} ,$$

$$t'(r) = \frac{(a_\parallel - a_\perp)}{H_\perp(r,t_0)r}\left[\Omega_{m0}(r)x^{-1} + \Omega_{k0}(r) + \Omega_{\Lambda 0}(r)x^2\right]^{-1/2} ,$$

where we have used $a'_\perp(r) = (a_\parallel - a_\perp)/r$ and defined $x = a_\perp(r,t)/a_\perp(r,t_0)$. Clearly, a non-simultaneous Big Bang $t'_{\rm BB} \neq 0$, would mean an inhomogeneous Universe at early times, this is $a_\parallel^{\rm BB} \neq a_\perp^{\rm BB}$. Finally, we neglect the presence of decaying modes by imposing $t_{\rm BB}(r) = 0$.

Note that in contradiction to the discussion presented here, Krasinski [188] argued that a non-simultaneous Big Bang time corresponds to an arbitrary choice that could oversimply the LTB models. The author states that the LTB models should not be taken at the face value, especially, at times close to the Big Bang. Although this argument could be valid for LTB models, without cosmological constant, that aim to reproduce cosmological observations, the same should not be applied to our framework, see Section 4.3.1.

4.3.3.3. The curvature profile $k(r)$

Once the mass function, $m(r)$, and the Big Bang time, $t_{\rm BB}(r)$, are fixed, we end up with just one arbitrary degree of freedom: the curvature profile $k(r)$. Since $m(r)$ and $t_{\rm BB}(r)$ are uninformative about late times, the dynamics of the model will be carried out by $k(r)$.

We model the curvature profile through the function

$$k(r) = k_B + (k_C - k_B)\, P_3(r/r_B)\,, \tag{4.28}$$

where r_B is the comoving radius of the spherical inhomogeneity, $k_B \equiv k(r = r_B)$ is the background curvature, $k_C \equiv k(r = 0)$ is the central curvature, and the function P_n follows

$$P_n(x) = \begin{cases} 1 - \exp\big[-(1-x)^n/x\big] & \text{for } 0 \le x < 1 \\ 0 & \text{for } 1 \le x \end{cases}\,. \tag{4.29}$$

This curvature profile describes a compensated spherical structure of comoving radius r_B embedded in a ΛCDM background. Given its compensating properties, it ensures that at the finite radius $r = r_B$, the ΛLTB model trivially becomes a ΛCDM model. In addition, this compensated profile establishes the existence of the compensating scale, here denoted by r_L, at which the central over/underdense region makes a transition to the surrounding mass-compensating under/overdense region.

It is straightforward to note that this compensated profile is consistent with the program proposed to test and observationally study the Copernican principle, se Section 4.3.1, and, unequivocally, corresponds to an early-FLRW model. Those features will be fundamental to keep a robust treatment of cosmological data, especially, CMB data. Lastly, we would like to highlight that compensated structures are not artificial but are common in nature: for instance, superclusters are typically surrounded by voids, and voids by sheets and filaments.

Once the three arbitrary functions are fixed, we can compute the matter density contrast using

$$\delta(r,t) \equiv \frac{\rho_m(r,t)}{\rho_m(r_B,t)} - 1\,, \tag{4.30}$$

and we can also compute the mass (integrated) density contrast via

$$\begin{aligned}\Delta(r,t_0) &= \frac{4\pi \int_0^r \mathrm{d}\bar r\, \delta(\bar r,t_0)\, a_\perp^2(\bar r,t_0) a_\parallel(\bar r,t_0) r^2}{4\pi\, a_\perp^3(r,t_0)\, r^3/3} \\ &= \frac{m(r)}{4\pi G\, R^3(r,t_0)/3\, \rho_m^{\rm out}(t_0)} - 1 = \frac{\Omega_{m0}(r)}{\Omega_{m0}^{\rm out}} \left[\frac{H_\perp(r,t_0)}{H_\perp^{\rm out}(t_0)}\right]^2 - 1\,.\end{aligned} \tag{4.31}$$

Hereafter, we will use the superscript "out" to denote the FLRW background quantities outside the inhomogeneity, e.g. $\rho_m(r \ge r_B, t_0) = \rho_m^{\rm out}(t_0)$. Note that the compensated profile features, by construction, $\Delta(r = r_B, t_0) = \delta(r = r_B, t_0) = 0$ and $\delta(r = r_L, t_0) = 0$. Additionally, Equation (4.31) implies $\Delta(r = 0, t_0) = \delta(r = 0, t_0)$. Finally, we define the FLRW comoving coordinate at the present time, $r^{\rm out}$, such that

$$r^{\rm out} \equiv R(r,t_0)/a^{\rm out}(t_0)\,. \tag{4.32}$$

Given that we used the standard normalization $a_0^{\rm out} \equiv a_\perp(r_B, t_0) = 1$, the size of the inhomogeneity satisfies $r_B^{\rm out} = r_B$.

4.3.4. Scale invariance

Due to the absence of spatial gradients in the dynamical equations, see Equation (4.10), the dynamics of the LTB model is scale invariant. In turn, this is a consequence of the spherical symmetry and the fact that the energy-momentum tensor is solely sourced by dust. While the former ascribes a null magnetic Weyl tensor and, therefore, no gravitational waves, the latter suggests no pressure and, hence, no sound waves. Explicitly, this kind of spacetimes are dubbed 'silent' because it can not exist direct communication between neighboring worldlines [215, 216]. In particular, the appearance of pressure gradients would induce to the transfer of energy between shells and make the energy function $E \equiv -k(r)r^2/2$ and the mass function $m(r)$ time dependent [see 217].

Strickly speaking, starting from the solution of Equation (4.10) for a given r_B, it is possible to obtain a new scaled inhomogeneity with radial coordinate $\hat{r} = \lambda r$ and size $\hat{r}_B = \lambda r_B$. Thus, the Friedmann-like equation can be recast as

$$\frac{\dot{\hat{a}}_\perp(\hat{r},t)}{\hat{a}_\perp(\hat{r},t)} = \frac{8\pi G}{3}\rho_\Lambda + \frac{2m_0}{\hat{a}^3_\perp(\hat{r},t)} - \frac{\hat{k}(\hat{r})}{\hat{a}^2_\perp(\hat{r},t)}\,, \tag{4.33}$$

where we used the definition of the mass function the $m(r) = m_0 r^3$. The functions relative to the scaled inhomogeneity are then defined according to:

$$\hat{a}_{\{\perp,\|\}}(\hat{r},t) = a_{\{\perp,\|\}}(r,t)\,, \tag{4.34}$$
$$\hat{H}_{\{\perp,\|\}}(\hat{r},t) = H_{\{\perp,\|\}}(r,t)\,, \tag{4.35}$$
$$\hat{k}(\hat{r},t) = k(r,t)\,, \tag{4.36}$$
$$\hat{\rho}_m(\hat{r},t) = \rho_m(r,t)\,, \tag{4.37}$$
$$\hat{R}(\hat{r},t) = \lambda\, R(r,t)\,, \tag{4.38}$$
$$\hat{m}(\hat{r},t) = \lambda^3 m(r,t)\,. \tag{4.39}$$

Starting from one numerical solution, one can then obtain a family of solutions by varying λ.

4.3.5. Configuration of the parameter space and the ΛLTB solutions

4.3.5.1. Free parameters of the ΛLTB model

We have presented the free functions assumed in the presented thesis. Now, we discuss which are free parameters of the ΛLTB model and, more important, which are the parameters that will lead to the generalization of the ΛCDM model.

The background parameters can be trivially identified. Since the LTB metric matches the FLRW case at the finite radius at $r = r_B$, the background expansion of our model will be specified by the six parameters of the standard model: the normalized Hubble constant h, the baryon density Ω_{b0}, the cold dark matter density Ω_{c0}, the optical depth τ, the amplitude of the power spectrum A_s and its tilt n_s.

The case of the inhomogeneous parameters is, in contrast, a bit subtle. The free functions, here adopted, explicitly introduce new four parameters: the normalization of the mass function m_0, the background curvature k_B, the central curvature k_c, and the comoving boundary radius r_B. While the two last parameters, k_c and r_B, will be the free parameters of the ΛLTB model, m_0 and k_B will be related to the background ΛCDM parameters. Indeed, in the FLRW limit, the matter and curvature density parameters, Equations (4.16) and (4.18), imply

$$m_0 = \frac{\Omega_{m0}^{\rm out}\left(H_0^{\rm out}\right)^2}{2}\,, \tag{4.40}$$

$$k_B = -\Omega_{k0}^{\rm out}\left(H_0^{\rm out}\right)^2\,, \tag{4.41}$$

where we have used the standard FLRW normalization $a_0^{\rm out} \equiv a_\perp(r_B, t_0) = 1$.

It is important to highlight that although the central curvature, k_c, and comoving radius of the spherical inhomogeneity, r_B, are the free parameters of our model, we will use the boundary redshift, z_B, and central density contrast, $\delta_0 \equiv \delta(r=0,t_0)$, to sample the parameter space. This change is motivated by the fact that z_B and δ_0 are easier to interpret in the context of a late time, low-redshift, violation of the Copernican principle. Furthermore, a flat prior on k_c will not ensure a homogeneous exploration of under and overdense regions. Finally, because the central density contrast is unbound, $-1 \leq \delta_0 < \infty$, in order to avoid numerical issues in the cosmological analysis, we normalize δ_0 such that

$$\tilde{\delta}_0 = \begin{cases} \delta_0 & \delta_0 \leq 0 \\ \delta_0/(1+\delta_0) & \delta_0 > 0 \end{cases}\,, \tag{4.42}$$

which satisfies $-1 \leq \tilde{\delta}_0 < 1$. We will apply the same normalization to $\Delta_L \equiv \Delta(r_L, t_0)$. For the sake of simplicity, hereafter we drop the tilde.

4.3.5.2. Semi-analytical solutions: the `vd2020` and `monteLLTB` codes

In the absence of the cosmological constant, LTB models with dust and curvature feature analytical solutions for the cosmic time, $t(a_\perp, r)$, as a function of the transverse scale factor, $a_\perp$, and the radial coordinate, r, such that [218]:

$$t(a_\perp, r) \propto k(r)^{-\frac{3}{2}}\left\{\sqrt{a_\perp k(r)\left[\frac{a_\perp k(r)}{2} + \frac{2\pi}{3}\right]} - \frac{2^{\frac{3}{2}}\pi}{3}\sinh^{-1}\left[\sqrt{\frac{3a_\perp k(r)}{4\pi}}\right]\right\}$$

for the case of a positive curvature $k(r) > 0$.[4] On the other hand, the introduction of a cosmological constant leads to more complex solutions. Indeed, in a ΛLTB model, the cosmic time follows Equation (4.19).

In 2012, Valkenburg [218] demonstrated that Equation (4.19) can be recast using Carlson's symmetric form of elliptic integrals.[5] This will allow us to obtain an exact solution for the cosmic time, $t(a_\perp, r)$, that can be later used to compute the angular scale factor, $a_\perp(r,t)$, through numerical inversion. Additionally, according to the author, Carlson's symmetric form of elliptic integrals will also allow us to provide exact expressions for diverse metric functions as $H_\perp(r,t)$, $a_\parallel(r,t)$, or its derivative. Given that this method does not employ numerical integration, the author argued that solutions provided by Carlson's integral are accurate and fast-evaluable semi-analytical functions. Furthermore, the authors presented an early version of a `Fortran` module capable of computing the ΛLTB dynamics. About a decade later, Valkenburg provide an update of this `Fortran` module and provide the ΛLTB solver: `vd2020`.[6]

[4] In the case of a negative curvature profile $k(r) < 0$, the solution holds by imposing $\sinh \to \sin$.
[5] See https://dlmf.nist.gov/19.16.
[6] Available at https://github.com/valkenburg/vd2020.

Label	$\Omega_{m0}^{\rm out}$	$\Omega_{b0}^{\rm out}$	$H_0^{\rm out}$	δ_0	z_B
Model 1: Extreme void	0.3	0.048	68	−0.8	0.5
Model 2: Shallow but big void	0.3	0.048	68	−0.15	0.5
Model 3: Deep but small void	0.3	0.048	68	−0.8	0.15

Table 4.1.: Three different sets of parameters used to illustrate the ΛLTB model. $H_0^{\rm out}$ is shown in units of km s^{-1} Mpc^{-1}.

Combining `vd2020` and `montepython`[7] codes, we have created `monteLLTB`: a cosmological solver and sampler for the ΛLTB model. By adapting the likelihood computation scheme, we have embedded `vd2020` into `montepython`. First, we modify the file `sampler.py`, to include `ini_LLTB`, the method that will execute the `vd2020` solver using the current sampled point of parameter space. Then, to pass the ΛLTB solution to the corresponding likelihood, we modify the `compute_lkl` method to include a call for `ini_LLTB` on it. The ΛLTB cosmology will be passed to the method of the likelihood, `loglkl`, through a new argument `LLTBin`. The likelihoods have been also modified to account for the observables according to the ΛLTB predictions. Complementary, we have created the file `LLTB_functions.py`. This file contains the fundamental definitions of the ΛLTB model that will be used to compute the cosmological observables. Additionally, this file will be also in charge of managing the output of `vd2020`. Finally, it is important to mention that we have also modified the `vd2020` code. While keeping unalterable the main results of the ΛLTB solver — the implementation to compute $t(a_\perp, t_0)$ — we customize the management of error, output precision, and outputted functions of `vd2020` and build a new version of ΛLTB solver suitable to be implemented in `montepython`. The `monteLLTB` code is available at github.com/davidcato/monteLLTB.

Using three different sets of parameters, see Table 4.1, we illustrate our model in Figures 4.5 and 4.6. The top row of Figure 4.5 shows the density parameter for the matter, curvature, and cosmological constant as a function of the FLRW comoving radial coordinate, $r^{\rm out}$, for the different models displayed in Table 4.1. The density contrast and the integrated mass density contrast as a function of $r^{\rm out}$ are displayed in the middle row of Figure 4.5. Furthermore, the bottom row shows the transverse and longitudinal Hubble expansion rates, of the three cases considered, as a function of the FLRW comoving radial coordinate.

From Figure 4.5, it is easy to note, that Model 1 — the extreme void — features the largest and longest deviation from the ΛCDM background. It leads to an inner region with almost non-matter, $\Omega_{m0} \approx 0$, and therefore increases the local value Hubble constant by more than 10 km s^{-1} Mpc^{-1} with respect $H_0^{\rm out}$. On the other hand, as expected, Model 2 — the shallow but large void — exhibits an almost negligible deviation from the ΛCDM background. In contrast, due to its small size, Model 3 — the deep but small void — shows a large and sharp deviation from the homogeneous ΛCDM case.

One should bear in mind that, in real life, cosmological observables are measured inside our past lightcone rather than in a particular time. This is, cosmological observations, e.g., cosmic chronometers, will bound $H_\parallel(z) \equiv H_\parallel(r(z), t(z))$ and not $H_\parallel(r, t_0)$. To illustrate the typical behavior of observables along the past lightcone, we plot in Figure 4.6 the transversal and longitudinal scales factors (top row), the transversal and longitudinal expansion rates (middle row),

[7]Available at `https://github.com/brinckmann/montepython_public`.

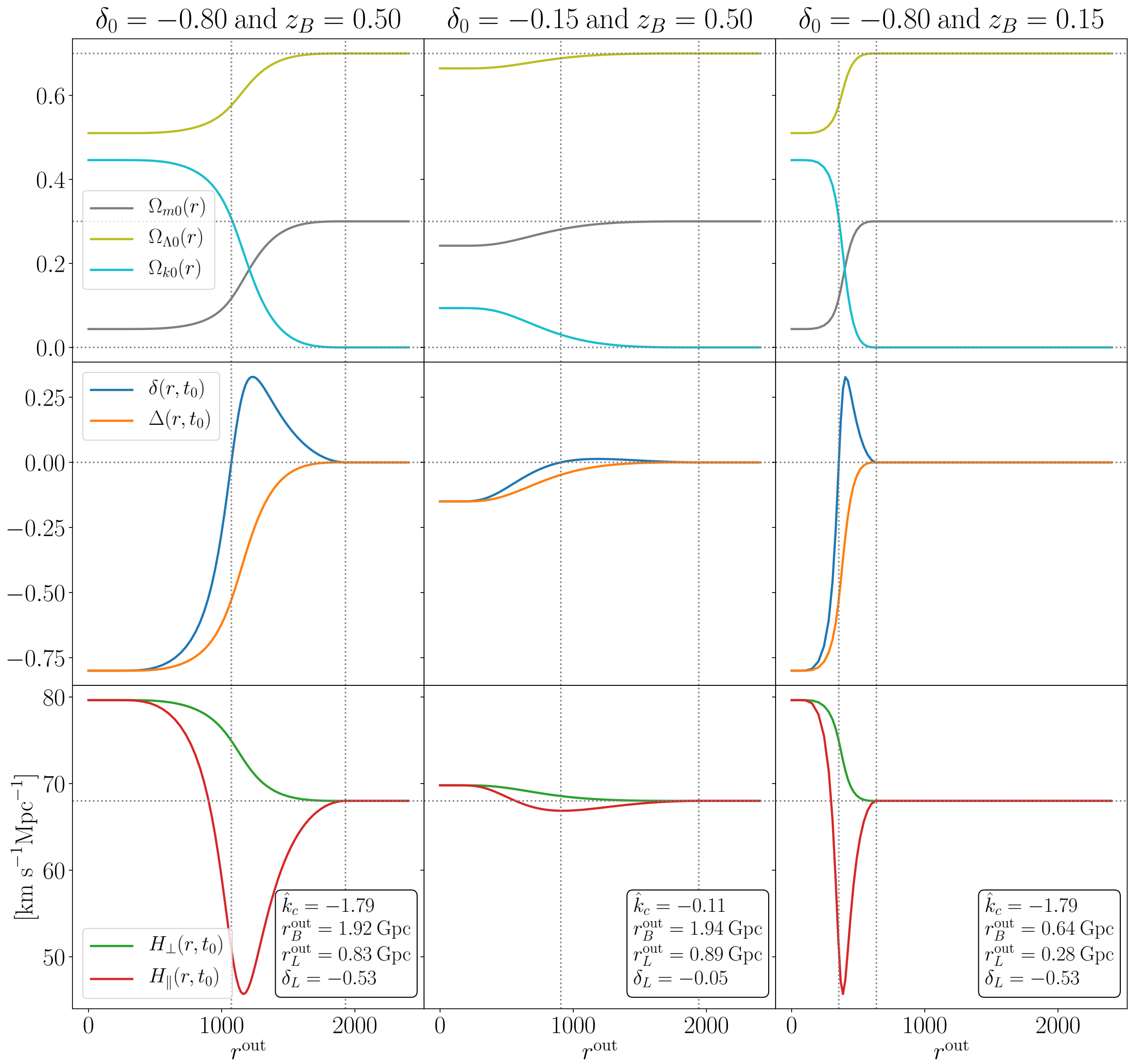

Figure 4.5.: Several metric functions as a function of the FLRW comoving radial coordinate, $r^{\rm out}$ for the three different configurations of ΛLTB model showed in Table 4.1. The vertical dotted black lines denote the compensating, $r_L^{\rm out}$, and boundary, $r_B^{\rm out}$, scales. Additionally, the horizontal dotted black lines mark down the ΛCDM limit of the corresponding quantity, for instance, $\Omega_{m0}^{\rm out}$ for $\Omega_{m0}(r_B)$. In the last row, we also show some of the parameters that can be derived in the ΛLTB framework. For sake of the simplicity, we have defined the dimensionless central curvature as $\hat{k} \equiv k/(H_0^{\rm out})^2$.

and the luminosity and diameter angular distances (bottom row) as a function of the redshift for the three different configurations of the ΛLTB model showed in Table 4.1. As in the case of the previous Figure, it is straightforward to note that Model 1 does provide the largest deviation from the ΛCDM model, while models like Model 2 and Model 3 will feature less considerable modification to the ΛCDM background. Such kinds of models will be highly degenerated with the plain ΛCDM model, especially if we consider cosmological distances.

Before enclosing this Chapter, it is essential to highlight that, as anticipated by Equation (4.28),

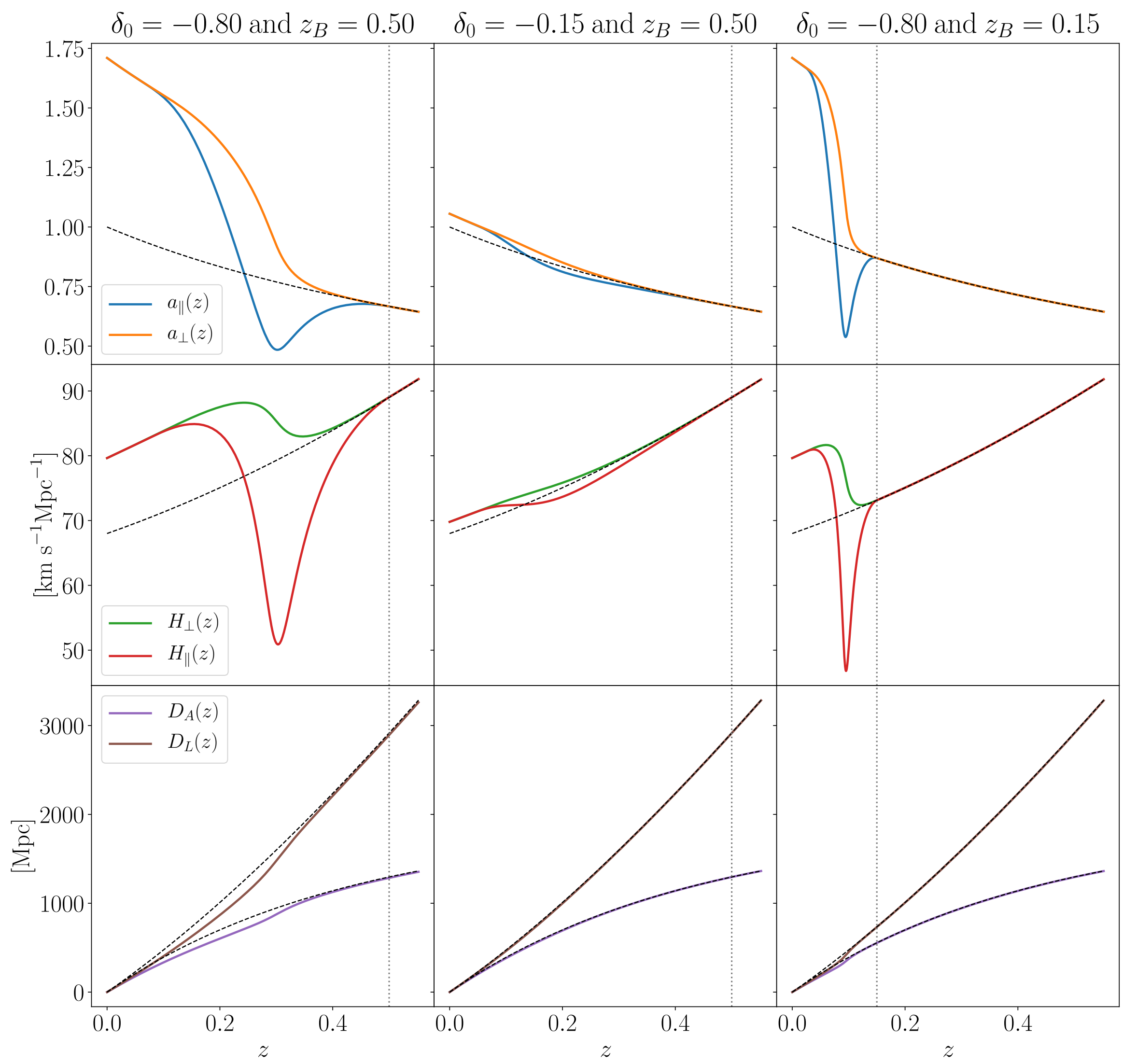

Figure 4.6.: Some metric functions related to cosmological observables as a function of redshift, z, for the three different configurations of the ΛLTB model showed Table 4.1. While the vertical dotted black lines denote the redshift corresponding to the boundary scale, z_B, the ticker dashed black lines represent the corresponding quantities for the ΛCDM model.

Figures 4.5 and 4.6 exhibit a smooth and exact transition between the LTB and FLRW metric at the finite scale r_B (or z_B); the ΛCDM model is recovered at scales $r \geq r_B$ (or $z \geq z_B$). Furthermore, the cases exposed in Table 4.1 were *ad hoc* chosen to illustrate how the ΛLTB model will relate to the problems treated in this thesis. On the one hand, Model 1 exemplifies how a ΛLTB underdense inhomogeneity could explain the Hubble tension, see left bottom panel of Figure 4.5. On the other hand, Model 2 and Model 3 represent regions of the parameter space that will be difficult to constrain, mainly because these models provide small deviations from the ΛCDM cosmological distances, see the middle bottom and right bottom panels of Figure 4.6.

Cosmology beyond the Copernican principle: the role of the cosmological probes

In the previous Chapters, we have introduced the theoretical and observational groundwork necessary to investigate physics beyond the Copernican principle. Here, we propose and apply a suitable program for studying, analyzing, and interpreting cosmological data in inhomogeneous spacetimes. We also apply this program to observationally test the Copernican principle and assess the problem of the Hubble tension. The results presented here are nothing more than the first steps toward an extension of the boundaries of the standard paradigm of modern cosmology. The discussion is based on three manuscripts that I have published during my PhD, these are CP Paper I, CP Paper II, CP Paper III. It is important to highlight that I have led these works.

We begin this Chapter by discussing the observables that will be used in our analyses. The first Section intends to set up the framework needed to confront the theoretical predictions of the ΛLTB model with the data coming from CMB, SNe, BAO, the y-distortion, the kSZ effect, and a local prior either on M_B or H_0. Later, we use the latest cosmological data to place constraints on the ΛLTB model. We compare the results of this analysis with the constraints coming from the Copernican prior — the statistical counterpart of the Copernican principle. This comparison corresponds to a test of the Copernican principle [CP Paper I], which is then presented. After this, by considering future data coming from DESI, Euclid, and LSST, we forecast constraints on the ΛLTB model. Such analysis aims to determine the precision with which forth-coming surveys will be able to test the Copernican principle and to test their ability to detect any possible violations of it. Finally, we carefully compute the Hubble constant in the ΛLTB framework in order to investigate if a local void can explain away the 5σ Hubble crisis [CP Paper II].

5.1. Cosmological observations in a ΛLTB Universe

Results discussed in this Chapter could be, at some level, biased by the cosmological data and its underlying fiducial model. We refer to the fact that most cosmological observations are not model-independent. Indeed, the standard pipelines employed to convert raw data into cosmological observations usually call upon a fiducial model. Such fiducial models are either used to accurately model the uncertainties or directly apply a standard template to interpret observational phenomena. For instance, the standard BAO analyses make use of a fiducial cosmological model to analyze the observed redshifts and angles and consequently measure the transverse and longitudinal BAO peak positions. Although in this particular case, analyses under the presumptions of a wide range of wCDM cosmologies found no evidence for systematic errors in the measured BAO signal Carter et al. [219], this could not be the case for other observations. This remarks again, on the need for model-independent techniques in cosmology, see Section 3.5.5. We argue that this caveat is intrinsic to most of the cosmological analyses and do not have a large impact on our results.

5.1.1. Cosmic microwave background

As discussed in the previous Chapter, this thesis relies on the assumption that at early times our model matches the standard paradigm, and the physics at decoupling (or pre-decoupling) is as in the standard ΛCDM model. In other words, the compensated profile defined by Equation (4.28) is consistent with an early-FLRW Universe. If, in addition to that, we also assume the standard adiabatic power spectrum, changes on the CMB power spectrum produced by our model will be only sourced by line-of-sight effects. Specifically, in contrast to a ΛCDM model, the spherical inhomogeneity only modifies the primary CMB spectrum via the late-time Integrated Sachs-Wolfe effect (hereafter, ISW) and the angular distance to the last scattering surface, D_A^*. The assumption of a standard power spectrum will be *a posteriori* justified since observations will only permit radial inhomogeneities whose density contrast can be understood as a linear perturbation of ΛCDM paradigm [220]. The same argument implies that the local ΛLTB structure will not change the late-time ISW effect as compared with the ΛCDM framework.

Thus, in this picture, in what it concerns to the CMB data, the ΛLTB model is reduced to a simply late time modification of the ΛCDM model, which aims to change the constraints on the different cosmological parameters through D_A^*, see Section 3.5. Since our ΛLTB model does not include radiation, the angular diameter distance to the last scattering can not be directly computed from our framework. However, one can re-scale the background cosmology to create an effective FLRW model that accounts for the changes produced in the CMB [221, 222, 111, 197]. Here, in order to obtain the effective FLRW model, we follow the procedure proposed by Marra and Paakkonen [222].

First, we solve the geodesic equations of the effective ΛCDM cosmology by using as initial conditions the matching shell, i.e., $\left\{t^{\mathrm{FLRW}}, r^{\mathrm{FLRW}}\right\} = \{t_B, r_B\}$ and $D_A^{\mathrm{FLRW}} = R(r_B, t_B)$, where $t_B = t(r_B)$. These solutions will allowed us to compute the age of the effective FLRW cosmology, $t^{\mathrm{FLRW}}(r=0) = t_0^{\mathrm{eff}}$, and the new boundary redshify, such that $z_B^{\mathrm{eff}} = a^{\mathrm{FLRW}}(t_0^{\mathrm{eff}})/a^{\mathrm{FLRW}}(t_B) - 1$. Using both quantities, t_0^{eff} and z_B^{eff}, we will re-scale the background parameters such that [222]

$$H_0^{\mathrm{eff}} = H_\perp^{\mathrm{out}}(t_0^{\mathrm{eff}})\,, \tag{5.1}$$

$$T_0^{\mathrm{eff}} = \left(\frac{1+z_B}{1+z_B^{\mathrm{eff}}}\right) T_{\mathrm{CMB}}\,, \tag{5.2}$$

$$\Omega_{\gamma 0}^{\mathrm{eff}} = 2.469 \times 10^{-5} h_{\mathrm{eff}}^{-2} \left(\frac{T_0^{\mathrm{eff}}}{T_{\mathrm{CMB}}}\right)^4\,, \tag{5.3}$$

$$\Omega_{r0}^{\mathrm{eff}} = \left[1 + \frac{7}{8}\frac{N_{\mathrm{eff}}}{2}\left(\frac{4}{11}\right)^{4/3}\right]\Omega_{\gamma 0}^{\mathrm{eff}}\,, \tag{5.4}$$

$$\Omega_{\Lambda 0}^{\mathrm{eff}} = \Omega_{\Lambda 0}^{\mathrm{out}}\left[\frac{H_\perp^{\mathrm{out}}(t_0)}{H_0^{\mathrm{eff}}}\right]^2\,, \tag{5.5}$$

$$\Omega_{k0}^{\mathrm{eff}} = \Omega_{k0}^{\mathrm{out}}\left[\frac{a^{\mathrm{FLRW}}(t_0) H_\perp^{\mathrm{out}}(t_0)}{a^{\mathrm{FLRW}}(t_0^{\mathrm{eff}}) H_0^{\mathrm{eff}}}\right]^2\,, \tag{5.6}$$

$$\Omega_{m0}^{\mathrm{eff}} = 1 - \Omega_{\Lambda 0}^{\mathrm{eff}} - \Omega_{k0}^{\mathrm{eff}} - \Omega_{r0}^{\mathrm{eff}}\,, \tag{5.7}$$

$$\Omega_{b0}^{\mathrm{eff}} = \omega_{b0}^{\mathrm{out}} h_{\mathrm{eff}}^{-2}\left(\frac{T_0^{\mathrm{eff}}}{T_{\mathrm{CMB}}}\right)^3\,. \tag{5.8}$$

with the effective number families of neutrinos fixed to $N_{\rm eff} = 3.046$ and the amount of baryons ω_{b0} defined as $\omega_{b0} = \Omega_{b0} h^2$. Note that the non-background parameters, A_s, n_s and $\tau_{\rm reio}$ will remain unchanged. Finally, it is important to mention that the CMB power spectrum of the effective FLRW model shall be computed through the `CLASS` code [223].[1]

5.1.2. Type Ia Supernovae

Largely used in cosmology, SNe are standardizable candles whose apparent magnitudes, m_B, can be used to constrain cosmological models through the relation

$$m_B(z) = 5 \log_{10} \frac{D_L(z)}{1\text{Mpc}} + 25 + M_B \,, \tag{5.9}$$

with D_L being the luminosity distances and M_B the absolute magnitude. Note that this fundamental relation does keep unalterable if we compare with its FLRW version.

Some authors have argued that inhomogeneous models would lead to a redshift-dependent absolute magnitude, such that $M_B(z) \neq \text{const}$ [224]. We believe that such an assumption is an extra assumption that goes beyond the ΛLTB paradigm and corresponds to assuming that SNe are not standard candles. Here, we consistently assume that M_B is constant over the redshift.

5.1.3. The local Hubble constant

In contrast to the FLRW case, and due to the radial degree of freedom, the ΛLTB model does not possess a unique definition of the Hubble constant, i.e., $H_\perp(r, t_0) \neq$ constant. Since, *a priori*, there does not exist any particular scale, r_x, at which one can robustly define $H_0 = H_0(r_x)$, the definition of the Hubble constant remains arbitrary.

In this Section, we propose three different ways of computing the local Hubble rate in an inhomogeneous model. These proposals will be obtained by extending some of the FLRW concepts and using observational reasoning. The approaches presented here will use a mock catalog of SNe in the Hubble flow, this is, in the redshift range $0.023 < z < 0.15$. Such mock will be generated considering ΛLTB luminosity distances as the observed quantity, and the redshift distribution and covariance matrix of the Pantheon compilation [225]. Given that these approaches will be applied in the cosmological analysis, it is important to highlight that the mock SNe data set will be generated at each sampled point of the parameter space. Finally, in this Section, we also discuss the usage of the absolute magnitude of SNe, M_B.

5.1.3.1. Mean Hubble constant $H_0^{\rm M}$

We first propose the mean Hubble constant, $H_0^{\rm M}$, an extension of the approach presented by Valkenburg et al. [220]. Through a weighted comparison between a radial dependent cosmographic expansion and the luminosity distance over the range $0.023 < z < 0.15$, we define the mean Hubble constant to be:

$$H_0^M = \left\{ \int_{0.023}^{0.15} W(z) \frac{d_L(z)}{z + \frac{1}{2}\left[1 - q_0(r)\right] z^2} \mathrm{d}z \right\}^{-1} , \tag{5.10}$$

with $W(z)$ being the normalized redshift distribution of the mock SNe and the r-dependent deceleration parameter following

$$q_0(r) = \Omega_{m0}(r)/2 - \Omega_{\Lambda 0}(r) \,. \tag{5.11}$$

[1] Available at https://github.com/lesgourg/class_public.

5.1.3.2. SH0ES Hubble constant $H_0^{\rm R}$

Our second approach relies on the procedure proposed by Redlich et al. [226], and lately revised by Efstathiou [227]. In this approach the Hubble constant is obtained by mimicking the typical cosmic distance ladder procedure, see Section 3.5.1, this is, by fitting the mock catalog through the FLRW cosmographic expansion and assuming a constant value for H_0 along with fixed deceleration and jerk parameters to $q_0 = -0.55$ and $j_0 = -1$, respectively.

Although the procedure defined for this determination, dubbed $H_0^{\rm R}$, neglects the spatial degrees of freedom introduced by the LTB metric, it could be useful to identify if deviations of statistical homogeneity could substantially bias the cosmic distance ladder determinations. It is important to stress that, while Redlich et al. [226] first presented this method in the context of inhomogeneous models, Efstathiou [227] proposed this approach to point out that the cosmic distance ladder technique does not truly determine $H_0 = H(z = 0)$ but rather a low redshift approximation of it.

5.1.3.3. Local Hubble constant $H_0^{\rm L}$

Our last approach to determine the local Hubble constant in a homogeneous Universe, $H_0^{\rm L}$, raises as an intermediate alternative to $H_0^{\rm M}$ and $H_0^{\rm R}$. This proposal will be determined as $H_0^{\rm R}$ but with a radial-dependent deceleration parameter:

$$\tilde{q}_0(r, H_0^L) = q_0(r) \left[\frac{H_0(r)}{H_0^L}\right]^2 , \tag{5.12}$$

where the last factor enforces the constant $H_0^{\rm L}$ as the local Hubble rate in the definition the density parameters, Equations (4.16) and (4.18).

Figure 5.1 shows $H_0^{\rm M}$, $H_0^{\rm R}$, and $H_0^{\rm L}$ as a function of δ_0 for two particular cases of the boundary redshift: $z_B = 0.4$ (solid lines) and $z_B = 0.2$ (dashed lines). Notably, $H_0^{\rm R}$ (blue lines) and $H_0^{\rm L}$ (red lines) provide very similar values for all pairs of δ_0 and z_B here considered. At the same time, $H_0^{\rm M}$ (green lines) amplifies the deviations from $H_0^{\rm out}$, especially at $|\delta_0| \gtrsim 0.1$ for $z_B = 0.2$. A ΛLTB inhomogeneity with a density contrast $\delta_0 \approx -0.5$ and a redshift size $z_B = 0.2$ — or $\delta_0 \approx -0.3$ and $z_B = 0.4$ — with a background Hubble rate of $H_0^{\rm out} = H_0^{\rm Planck}$ can possibly explain the mismatch between the CMB and cosmic distance ladder observations.

5.1.3.4. The absolute magnitude M_B

As already discussed in Section 3.5.3, the M_B parameter is often considered a nuisance parameter in the cosmological analysis. This biases the results of the cosmological inference, the evidence for late time modifications to the ΛCDM model spuriously increases. Thus, in light of the M_B tension [7], our main analyses will be performed considering a prior on M_B instead of H_0. s

5.1.4. Cosmic chronometers

The relative age between a pair of passively-evolving galaxies at different redshifts can be determined through spectroscopic techniques. That differential age can be combined with the redshift to measure the rate $\mathrm{d}z/\mathrm{d}t$, without any underlying assumption about cosmology [228]. This technique is the denominated cosmic chronometers.

From the definition of the Hubble parameter, $H(z) = \dot{a}/a$, it is straightforward to note that, in the FLRW case, the cosmic chronometers will constrain $\mathrm{d}z/\mathrm{d}t = -(1 + z)H(z)$. Instead, in

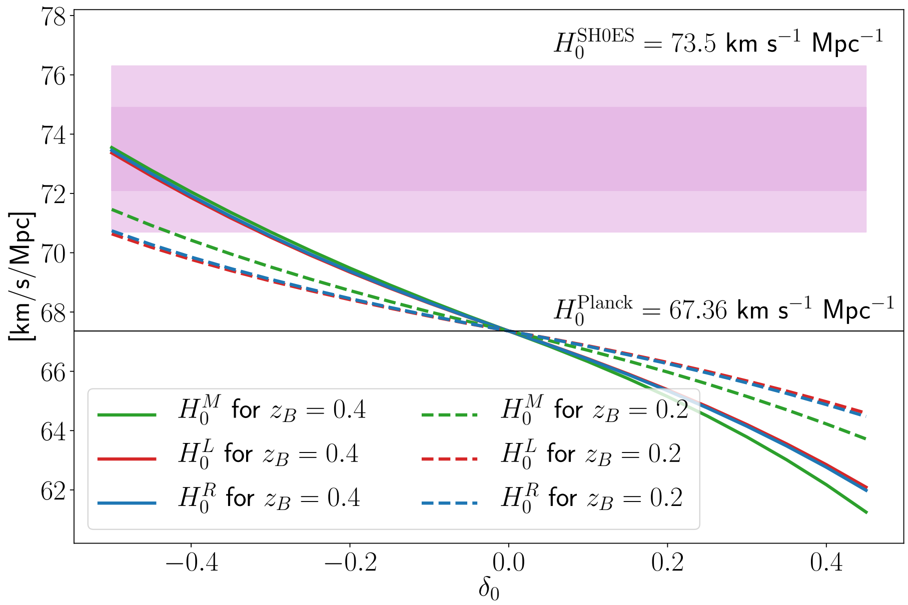

Figure 5.1.: $H_0^{\rm M}$, $H_0^{\rm R}$, and $H_0^{\rm L}$ as a function of the density contrast at the center, δ_0, and for two cases of the boundary redshift: $z_B = 0.2$ and $z_B = 0.4$. A local underdensity with $\delta_0 \approx -0.5$ and $z_B = 0.2$ — or $\delta_0 \approx -0.3$ and $z_B = 0.4$ — with a background expansion rate of $H_0^{\rm out} = H_0^{\rm Planck}$ (horizontal black line) could potentially solve the Hubble crisis by providing a local rate that agrees with $H_0^{\rm SH0ES}$ (pink region).

the case of a LTB space-time, such observations will provide information about the longitudinal expansion rate. This can be demonstrated if we use Equations (4.14) and (4.24), such that

$$\frac{{\rm d}z}{{\rm d}t} = -(1+z)H_{\parallel}(z)\,. \tag{5.13}$$

5.1.5. Baryonic Acoustic Oscillations

The so-called Baryonic Acoustic Oscillations imprint, at the drag epoch t_d, the comoving sound horizon scale $r_s(t_d) \equiv r_d$ in the matter power spectrum. This scale constitutes a standard rule that can be used to constrain cosmological models through the combination of the comoving sound horizon, r_d, the Hubble rate, $H(z)$, and the diameter angular distance, $D_A(z)$.

More specific, within the standard paradigm, the BAO establishes the longitudinal and transverse scales denoted by $\Delta z = l_d(1+z)H(z)$ and $\Delta\theta = l_d/D_A(z)$, respectively, as standard rulers. Note, that we have conveniently defined the proper sound horizon scale $l_d = r_d/(1+z)$. In the case of spherically inhomogeneous space-time, this scales will be modified by the anistropic expansion rate. Precisely, in the ΛLTB model the BAO scales follow [229, 221, 111]:

$$\Delta z(z) = l_{\parallel}(1+z)H_{\parallel}\,, \tag{5.14}$$

$$\Delta\theta(z) = \frac{l_{\perp}}{D_A(z)}\,, \tag{5.15}$$

where a transverse and longitudinal proper sound horizon scales have been defined through

$$l_\perp = \frac{a_\perp(r(z),t(z))}{a_\perp(r(z),t_d)}\frac{r_d}{(1+z_d)}\,, \tag{5.16}$$

$$l_\parallel = \frac{a_\parallel(r(z),t(z))}{a_\parallel(r(z),t_d)}\frac{r_d}{(1+z_d)}\,. \tag{5.17}$$

Although the most recent measurements separately determine the radial, Δz, and angular, $\Delta\theta$, BAO scales, old surveys used to detect a combination of them. This combination is called the isotropic BAO and its defined by

$$d_V = r_d\left(\frac{z}{\Delta\theta^2\Delta z}\right)^{1/3}\,. \tag{5.18}$$

5.1.6. Compton y-distortion

Relying on the assumption that we are placed at the center of the spherically inhomogeneity, see Section 4.3.1, secondary anisotropies of the CMB can be used to constrain the ΛLTB model.

Effectively acting as mirrors, reionized off-center structures scatter CMB photons inside our past lightcone along our line-of-sight. Since photons with different temperature will be injected by this scattering, a spectral distortion on the CMB thermal black body spectrum will be produced. Such distortion is the well-known Compton y-distortion. In the linear single-scattering approximation, and neglecting the contribution of multipoles higher than $\ell > 2$, the y-distortion produced by an off-center structure is given by [197, 230, 204]:

$$y = \frac{7}{10}\int_0^{z_{re}} dz\frac{d\tau}{dz}\beta^2(z)\,, \tag{5.19}$$

where z_{re} is the redshift of the reionization epoch, $\beta(z)$ is the dipole of the off-center structure and the derivative of the optical depth τ with respect to the cosmic time is

$$\frac{d\tau}{dt} = \sigma_T f_b\left(1-\frac{Y_{He}}{2}\right)\frac{\rho_m(t)}{m_p}\,, \tag{5.20}$$

with σ_T being the Thompson cross section, f_b the baryon fraction, Y_{He} the helium mas fraction and m_p the proton mass.

While, in the ΛCDM framework, the y-Compton effect is sourced by the cosmological perturbations, in a ΛLTB model such distortion is instead a background effect. Indeed, in a ΛLTB model, the dipole of an off-center structure can be roughly approximate to $\beta(z) \simeq D\left[H_0(z) - H_0^{\rm out}\right]$, where D is some proper distance [108]. Here, we compute the dipole $\beta(z)$ by following the procedure discussed in [231]. We first identify the redshift of the reionized off-center structure, $z_{\rm off}$. Next, by adopting as the starting point $\{t(z_{\rm off}), r(z_{\rm off})\}$, we solve the outgoing and ingoing geodesic equations to the surface of last scattering obtain z_- and z_+, respectively. Finally, by taking into account that the temperature of CMB scales according to $T \propto 1/z$, the dipole in the light-cone is given by $\beta(z) = (z_+ - z_-)/(2 + z_+ + z_-)$ [see Figure 1 in 231].

5.1.7. The kinetic Sunyaev–Zeldovich effect

The dipole featured by the off-center structures will also produce anisotropies in the CMB spectrum through the kinetic Sunyaev–Zeldovich effect (hereafter, kSZ efect). Generated by the inverse Compton scattering of low-energy photons with high energy electrons, the kSZ provide an interesting window to test the the radial degrees of freedom introduced by a spherically inhomogeneity. Indeed, as mentioned in the review of void models, see Section 4.1.3, the kSZ effect is a powerful observable that can be used to test the Copernican principle [231, 160, 232, 203].

Here, by considering Limber approximation and the effect due to all free electrons in the reionized universe, we compute the linear kSZ effect [160, 232]:

$$C_\ell^{\rm kSZ} \simeq \frac{16\pi^2}{(2\ell+1)^3}\int_0^{r_{\rm re}} dr\, r\left[\beta(r)\frac{d\tau}{dr}\right]^2 \Delta_m^2\,, \tag{5.21}$$

where $r_{\rm re}$ is the radial coordinate at $z_{\rm re}$ and Δ_m is the nonlinear dimensionless matter power spectrum, whose definition depends on r according to:

$$\Delta_m^2 = \Delta_m^2\Big(\big(\bar{k} = \frac{2\ell+1}{2r}\big)\times\Xi,\; z(r)\Big)\,. \tag{5.22}$$

Note that Ξ was introduced in order to correct for the anisotropic expansion of our inhomogeneous model. This correction is defined by

$$\Xi = \left(\frac{1+\bar{z}}{1+z}\right)\left[\frac{a^2(\bar{t}, r(z))}{a^2(t(z), r(z))}\frac{a_\parallel(\bar{t}, r(z))}{a_\parallel(t(z), r(z))}\right]^{1/3}\,. \tag{5.23}$$

Let us consider $\bar{k}$ as the comoving FLRW wavenumber. Since our model is an early-FLRW model, the comoving ΛLTB wave number will coincidence, at an early-enough time $\bar{t}$, with the FLRW definition $\bar{k}$. However, because of the subsequent anisotropic expansion, in ΛLTB model, the proper mode $\bar{k}/\bar{a}$ will be stretched differently along the longitudinal and transverse direction. This means, that today, the comoving ΛLTB wave number will follow

$$\frac{k_{\{\parallel,\perp\}}}{a} = \frac{\bar{k}}{\bar{a}}\frac{a_{\{\parallel,\perp\}}(\bar{t}, r)}{a_{\{\parallel,\perp\}}(t, r)}\,. \tag{5.24}$$

Additionally, since the standard power spectrum does only consider a single wavenumber, in analogy to the BAO scales, one can define the isotropic comoving wavenumber to be $\Xi \propto \left[k_\perp^2(z)k_\parallel(z)\right]^{1/3}$, justifying then Equations (5.21) and (5.23).

5.2. The Copernican principle in light of the latest cosmological data

In CP Paper I, we tested the Copernican principle by placing constraints in a ΛCDM model endowed with a spherical inhomogeneity around us, i.e., the ΛLTB model. We confront the constraints coming from the analyses of the latest cosmological data, with the constraints coming from the Copernican prior — the statistical counterpart of the Copernican principle. Here, we discuss the results of this test.

We start our discussion by presenting the cosmological data that will be considered during this Section. We will later introduce the Copernican prior and its relation to the ΛLTB parameter space. After that, we present the results of our analyses and promote the discussion of those. Finally, we shall enclose this Section discussing the conclusions and final remarks of CP Paper I.

5.2.1. Data sets used in the analysis

We adopt the latest cosmological data available to constrain the ΛLTB model. Specifically, we use: Planck 2018 data coming from the high-ℓ and low-ℓ TT+TE+EE power spectrum [233]; Pantheon compilation with 1048 SNe data in the range $0.01 < z < 2.3$ [225]; BAO measurements from 6dFGS [234], SDSS-MGS [235] and BOSS-DR12 [144]; 30 cosmic chronometer points spanning the redshift range $0 < z < 2$ measurements from [236, 237, 238, 239, 240, 241]; a 2σ upper bound on the Compton y-distortion coming from the COBE-FIRAS satellite [242]; a Gaussian prior on the amplitude of the kSZ at $\ell = 3000$, i.e., $D_{3000}^{\rm obs}$, from the SPT-SZ + SPTpol surveys [243]; and the astro-prior on M_B from H0 Paper I.

It is important to highlight that the assumption that the late-time ISW does not change in the presence of inhomogeneity is not only *a posterior* assured by the constraints but also justified by the fact that fully computing the contribution of the late-time ISW effect in an inhomogeneous ΛLTB model is a non-trivial task [244, 245, 163]. Indeed, accurate computation of this effect — and, in general, of all contributions of large-scale inhomogeneities in low-ℓ multipoles — involves the use of a not yet fully developed cosmological perturbations theory in an inhomogeneous space-time. In order to assess the impact of the low-ℓ data in our main results, and also to test our assumption about the late-time ISW effect, we have performed an extra analysis without the low-ℓ data. The results of this are discussed in Appendix B.

As mentioned above, we will impose a Gaussian prior on the amplitude of the kSZ effect. More specific, we will constrain the spherically inhomogeneities around us using the first kSZ measurement at more than 3σ, $D_{3000}^{\rm obs} = 3.0 \pm 1.0\,\mu$K, provided by SPT-SZ + SPTpol surveys [243], where $2\pi D_\ell = \ell(\ell+1)C_\ell$. In order to provide a consistent confrontation between observations and theory, it is crucial to note that the kSZ effect would not disappear in the limit $\delta_0 \to 0$ and $z_B \to 0$, given that the linear perturbations of the ΛCDM are also expected to provide a contribution. Here, we use the patchy and homogeneous parameterizations to compute the ΛCDM perturbation contribution [246]:

$$\text{h-A}_{\rm kSZ} = 1.65 \left(\frac{\sigma_8}{0.8}\right)^{4.46}, \tag{5.25}$$

$$\text{p-A}_{\rm kSZ} = 2.03 \left[\frac{(1+z_{re})}{11} - 0.22\right] \left(\frac{\Delta z_{re}}{1.05}\right)^{0.51}, \tag{5.26}$$

where $\Delta z_{re} = z(x_i = 25\%) - z(x_i = 75\%)$ is the duration of reionization and x_i is the ionization fraction of hydrogen. We compute x_i using the tanh model [247]. Finally, one should note, that as in the case of the low-ℓ scales, fully consistent treatment of kSZ requires the not-yet available understanding of the growth of matter perturbations in an inhomogeneous background.

5.2.2. Copernican prior

The large-scale structure of the Universe might feature arbitrary radial inhomogeneities in the absence of the Copernican principle. As opposed to this, within the standard paradigm, those structures are constrained by the Copernican principle. Indeed, the assumption that we do not occupy a special location in the Universe assigns a likelihood to the large-scale structures. Through linear perturbation theory, one can demonstrate that such probability follows [CP Paper I]:

$$\mathcal{P}(\delta_0, z_B) \propto \exp\left[-\frac{1}{2}\frac{\Delta^2(r_L, t_0)}{\sigma^2(r_L^{\rm out})}\right], \tag{5.27}$$

where the effective density contrast, $\Delta(r_L, t_0)$, has been assumed to be a Gaussian field whose root-mean-square is defined by

$$\sigma^2(r) = \int_0^\infty \frac{{\rm d}k}{k} \left[\frac{k^3 P_{m0}(k)}{2\pi} \frac{3 j_1(rk)}{rk}\right]^2, \tag{5.28}$$

with $P_{m0}(k)$ being the standard power spectrum today and j_1 the spherical Bessel function of the first kind. Equation (5.27) is the so-called Copernican prior. Note that, since $r_L^{\rm out}$ defines the radius of the center under/overdensity, it is the scale of interest of our model. This is confirmed by the Copernican prior, which value acquires a physical meaning if evaluated $r_L^{\rm out}$; by definition Equation (5.27) would be trivial is one considers r_B instead of r_L, this because the matter and mass fluctuations disappear at the boundary scale, $\delta(r_B, t_0) = \Delta(r_B, t_0) = 0$.

Although Equation (5.27) does constrain the radial degree of freedom introduced by the ΛLTB model — by effectively constraining δ_0 and z_B — the Copernican prior does not bound the power matter spectrum, P_{m0}, or the cosmological parameters needed to asses to it. On the other hand, under the assumption of the Copernican prior, the cosmological perturbations inferred from CMB data should describe the early universe at any point and, in particular, also at our observing position. That means, CMB summary statistics, such as the power spectrum, do constrain both the background and ΛLTB parameters.

Thus, constraints coming from the assumption of the Copernican principle will be actually obtained by the convolution of the Copernican prior with the CMB likelihood. Explicitly, if the Copernican principle is valid, the probability distribution of δ_0 and z_B, given the initial conditions obtained from the CMB and their uncertainty, will defined by:

$$P(\delta_0, z_B) = \int \mathrm{d}p_i \, \mathcal{P}(\delta_0, z_B) \, \mathcal{L}_{\rm CMB}(p_i, \Delta_0, z_B) \,, \tag{5.29}$$

where p_i denotes the standard ΛCDM parameters and $\mathcal{L}_{\rm CMB}$ is the CMB likelihood adopted here, see Section 5.2.1.

Finally, it is important to mention that despite our approach to the statistical counterpart of the Copernican principle follows on the idea presented by Valkenburg et al. [220], the Copernican prior presented here differs in three aspects from the one adopted by Valkenburg et al. [220]. First, since the latter spuriously reduce the likelihood of inhomogeneities with $z_B \sim 0$, we have removed the normalization factor $(\sigma_L \sqrt{2\pi})^{-1}$ on Equation (5.27). Second, while Valkenburg et al. [220] adopt the relativistic mass to compute $\Delta(r, t_0)$, we have used the Euclidean mass. By internal analyses, we have confirmed that this change does not have a large impact on our results. Finally, we have corrected the LTB gauge by using $r^{\rm out}$ instead of r.

5.2.3. Results and discussion

We perform the cosmological analysis using the ΛLTB solver and sampler: `monteLLTB`, see Section 4.3.5.2. Since the parameter space will be sampled using the Markov-chain Monte Carlo (hereafter, MCMC) technique, we evaluate the convergence of the MCMC chains by using the Gelman-Rubin diagnostic $\mathcal{R}$ [248]. Given the complexity of the ΛLTB parameter space, we establish the threshold $(\mathcal{R} - 1) \lesssim 0.05$ for the inhomogeneity parameters δ_0 and z_B and $(\mathcal{R} - 1) \sim \mathcal{O}(10^{-3})$ for the background ΛCDM parameters as the criterion of convergence. Most of the plots shown here have been produced using `getdist` [249].

5.2.3.1. Constraints on the inhomogeneity

We show in Figure 5.2 the marginalized constraints on the comoving compensating scale $r_L^{\rm out}$ and integrated mass contrast $\Delta_L = \Delta(r_L, t_0)$ of the spherical inhomogeneity for various combinations of the cosmological data. Figure 5.2 also shows the constraints coming from the Copernican prior convolved with the CMB likelihood of Equation (5.29), i.e., the radial fluctuations as allowed by the standard paradigm. When all observables are taken into account, it becomes evident that

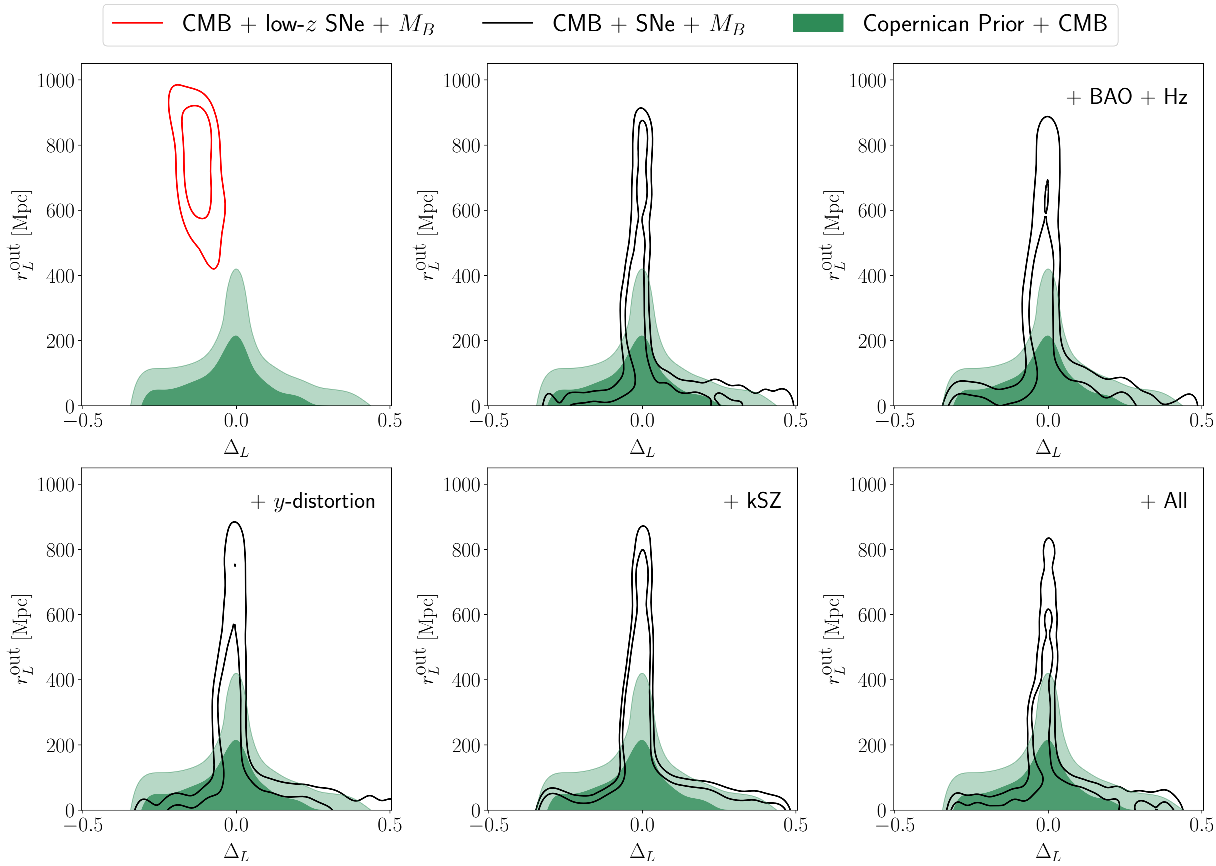

Figure 5.2.: Marginalized constraints on the effective density contrast Δ_L and compensating scale r_L^{out} of the ΛLTB inhomogeneity at 68% and 95% confidence level. The empty contours denote the constraints from the analyses of the corresponding cosmological data. The green area, instead, shows the region of the ΛLTB parameter space that is allowed by the standard paradigm and the Copernican principle, here represented via the Copernican prior convolved with the CMB likelihood, $P(\delta_0, z_B)$.

only linear non-Copernican structures are permitted at greater radii, however for smaller scales, the Copernican principle (CP) is confirmed and observations begin to map the local structure.

To better explain this, we define the effective non-Copernican density contrast as

$$\Delta_L^{\text{non.}} = \sqrt{\sigma_{\text{obs}}^2 - \sigma_{\text{CP}}^2}$$

where σ_{obs}^2 and σ_{CP}^2 are the variances of Δ_L relative to the empty and green contours of Figure 5.2, respectively. We show in Figure 5.3 the effective contrast beyond what is allowed by the Copernican principle, $\Delta_L^{\text{non.}}$, as a function of the FLRW comoving compensating scale r_L^{out}. Note that $\Delta_L^{\text{non.}}$ is computed using r_L^{out} bins. Figure 5.3 shows that non-Copernican structures can features small extra effective contrast of just $\Delta_L^{\text{non.}} \sim 0.01$.[2]

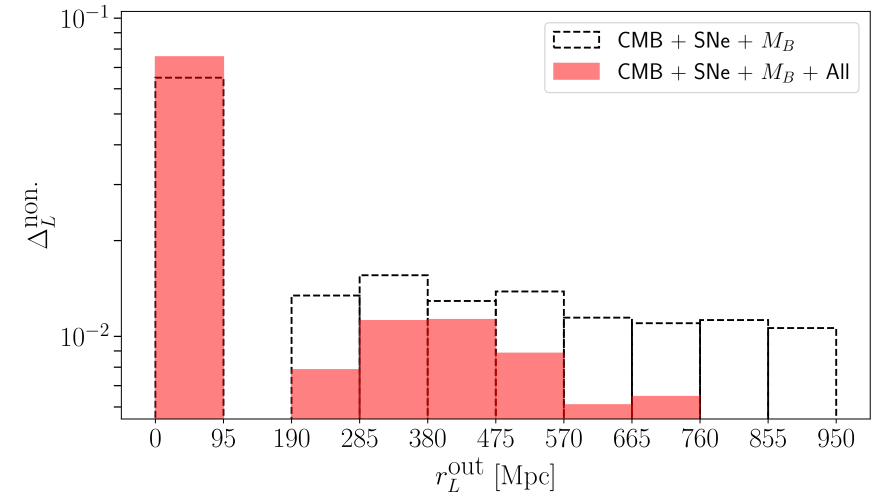

Figure 5.3.: Effective contrast beyond what is allowed by the Copernican principle, $\Delta_L^{\rm non.}$, as a function of the effective size $r_L^{\rm out}$ of the ΛLTB inhomogeneity. Cosmological data allows for non-Copernican structures with a small extra effective contrast of just $\Delta_L^{\rm non.} \sim 0.01$.

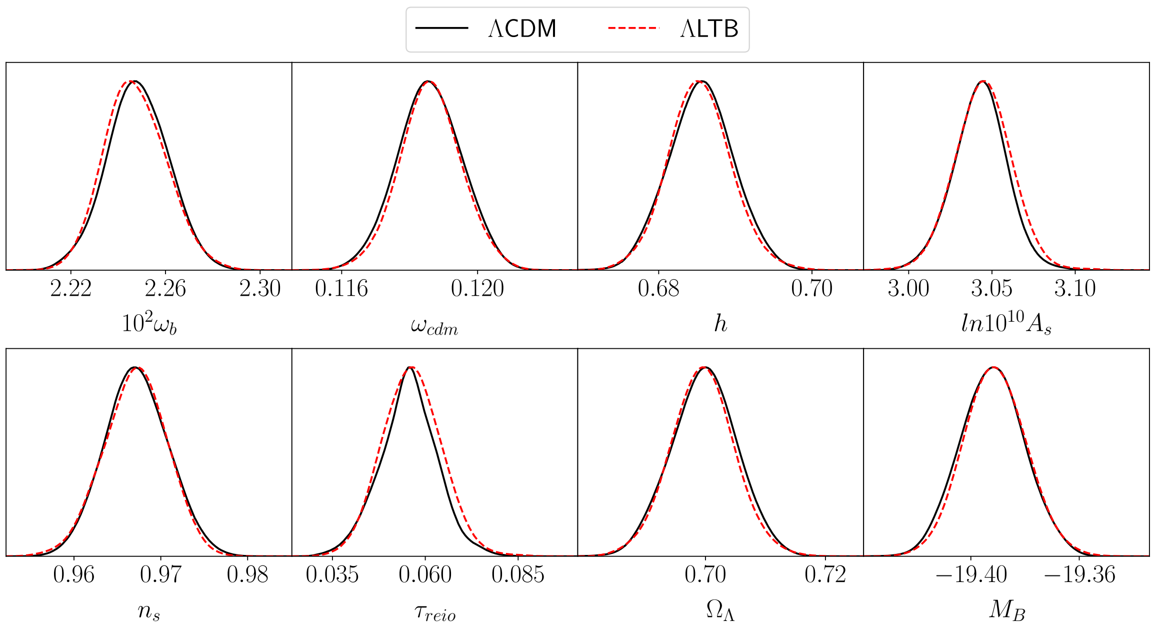

Figure 5.4.: Marginalized constraints on the six ΛCDM parameters and also the density parameter of the cosmological constant Ω_Λ and the SNe absolute magnitude M_B. This plot shows that the standard ΛCDM constraints are robust against the effect of inhomogeneities, whose effect is essentially negligible, see Table 5.1. This point that cosmological inference without the Copernican principle not only is possible but is affected to a very minor extent.

Parameter	ΛCDM	ΛLTB
$10^2\omega_b$	$2.25^{+0.026}_{-0.027}$	$2.25^{+0.027}_{-0.025}$
ω_{cdm}	$0.119^{+0.002}_{-0.002}$	$0.119^{+0.002}_{-0.002}$
H_0	$68.56^{+0.84}_{-0.82}$	$68.53^{+0.82}_{-0.81}$
$ln10^{10}A_s$	$3.04^{+0.03}_{-0.03}$	$3.04^{+0.03}_{-0.03}$
n_s	$0.967^{+0.007}_{-0.007}$	$0.967^{+0.007}_{-0.007}$
τ_{reio}	$0.056^{+0.016}_{-0.016}$	$0.056^{+0.016}_{-0.015}$
Ω_Λ	$0.70^{+0.011}_{-0.011}$	$0.70^{+0.011}_{-0.011}$

Table 5.1.: 68% confidence level intervals for the six ΛCDM parameters and also the derived parameter Ω_Λ, marginalized over the effect of inhomogeneities around us (ΛLTB) and for the standard ΛCDM model that assumes the Copernican principle.

5.2.3.2. Constraints on the the standard model parameters

Besides examining if the cosmological data can prove the Copernican principle, we also investigate if dropping the Copernican hypothesis does affect the cosmological constraints on the parameters of the standard model.

Figure 5.4 and Table 5.1 show the constraints on the six ΛCDM parameters, marginalized over the ΛLTB parameters. We also show, for comparison sake, the constraints relative to the standard ΛCDM model and the assumption of the Copernican principle. Our results show that dropping the Copernican principle has an almost negligible effect on the constraints of the ΛCDM parameters. We also report small correlations between the background parameters and the parameters that model the inhomogeneity around us, δ_0 and z_B. See Figure 5.5, the triangular plot with the eight free parameters of the ΛLTB model.

5.2.3.3. Towards inhomogeneous cosmology

Figure 5.2 shows that the region Δ_L - $r_L^{\rm out}$ of the parameter space allowed by the data is progressively constrained to closely follow the constraints obtained by the Copernican prior. This means that cosmological data allows spherical inhomogeneity around us that are close to the typical FLRW perturbations of the standard paradigm. Further, it is interesting to note that although the combination of CMB+ SNe + M_B data already tightly constrains the ΛLTB model, large-scale inhomogeneities at $r_L^{\rm out} \gtrsim 500$ Mpc are efficiently constrained only if the combinations of all probes is considered. This shows that the synergies between different probes are fundamental to the test deviation from the FLRW metric. The results presented here represent a substantial improvement as compared to the previous analysis of Valkenburg et al. [220].

As proposed by Valkenburg et al. [220], one can globally quantify how much non-Copernican structure is allowed by comparing, in Figure 5.2, the CP area with the one allowed by data. Table 5.2 shows the ratios of the areas of the 2σ contours for the different cases here analyzed. It is straightforward to note that, when areas are compared using the whole parameter space, the ratio is close to 1. These estimations seem to point to an almost confirmation of the Copernican

[2] Note that, because of the non-Gaussian nature of the posterior, it is not straightforward to compare Figure 5.3 with Figure 5.2.

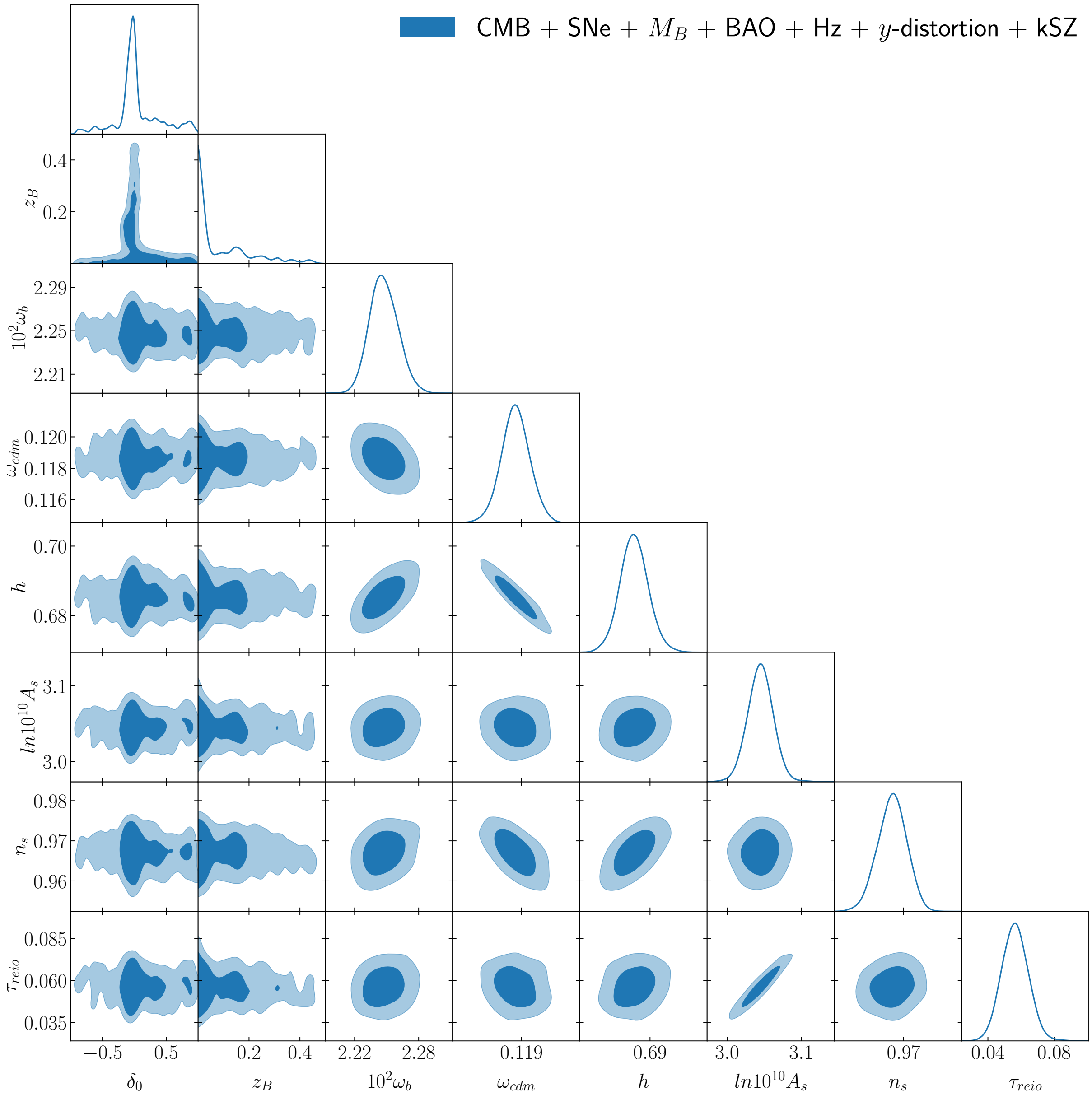

Figure 5.5.: 68% and 95% marginalized constraints on the eight independent parameters of the spherically inhomogeneous extension of the standard model, the ΛLTB model.

Case	$A_{\rm obs}/A_{\rm CP}$ $0 \leq r_L^{\rm out}$	$A_{\rm obs}/A_{\rm CP}$ $190{\rm Mpc} \leq r_L^{\rm out}$
CMB + SNe + M_B	1.16	2.85
CMB + SNe + M_B + BAO + HZ	1.11	2.88
CMB + SNe + M_B + y-dist.	1.12	2.83
CMB + SNe + M_B + kSZ	1.07	2.35
CMB + SNe + M_B + All	1.02	2.15

Table 5.2.: Ratios of the areas of the 2σ constraints from observations and the Copernican principle, see Figure 5.2.

principle. However, as pointed out earlier, large-scale inhomogeneities are more difficult to constrain — noticeably, as can be seen from Figure 5.2, at scales $r_L^{\rm out} \geq 190$ Mpc, cosmological data still allow for a region of parameter space that is rejected by the Copernican prior. Thus, in order to take this into account, we also compute the ratios considering only scales $r_L^{\rm out} \geq 190$ Mpc. Results from such analyses show that the ratio is ~ 3 when CMB+SNe+M_B are considered and decreases to ~ 2 when all data are included.

Further, we have also considered the case of a nonzero background curvature. In the analyses of this case, we found that our results remained unaltered. The reason is that CMB strongly constrains the background value of Ω_k, and this is not affected by the compensated LTB inhomogeneity, which is constrained to small contrasts by the other observables.

All these results imply that, within the present modeling, we are close to observationally establishing the Copernican principle and, even more important, that dropping the Copernican principle assumption does not imply worse constraints on the cosmological parameters.

5.2.3.4. The LTB parametrization

It is crucial to mention that although our choice for the curvature profile is justified in the framework of an early-FLRW model, the presumption of Equation (4.28) is still arbitrary. This is, our results depend, to some extent, on the chosen parametrization for the curvature function given in Equation (4.28). While it is clear that the two physical parameters that best describe a spherical inhomogeneity are its size r_B and contrast δ_0, it is also true that, as constraints get ever-tighter, other aspects of the curvature profile, such as its smoothness, may start to have an important impact. This limitation on the modeling of the curvature — or density profile — could be overcome by considering a more flexible parametrization as proposed by Redlich et al. [226], where an n-node spline is considered. This approach is clearly recommended if one wants to find the best-fit inhomogeneous model for observations.

Since we aim to test the Copernican principle and democratically explore the parameter space of the ΛLTB model, the adoption of a more general profile may lead to problems. Indeed, meaningful analyses should similarly explore the overdensities and underdensities, which, within the LTB framework, is not a trivial task. The main reason behind this is that underdensities may experience shell-crossing singularities which, although unphysical, prevent the analysis and create a spurious asymmetry in the parameter space. Shell crossing will occur when $R' = 0$, and this would happen when the inner faster-expanding underdensity pushes against the compensating shell. In other words, when exploring the parameter space of a more flexible profile, shell crossing could lead to volume effects which would bias the results.

By performing an internal consistency test of the ΛLTB model, we have confirmed that the parametrization of the curvature profile, Equation (4.28), does not penalize underdensities or overdensities. However, it is crucial to bear in mind that the results shown in Figures 5.2 and 5.3 are conditional to the assumed parametrization of the LTB model.

Also corresponding to the parametrization of our model is the assumption of a center observer. Even though, we argued in Section 4.3.1 that considering radial inhomogeneities around us is enough for the treatment of this thesis, the real anisotropy of the Universe could affect observations as much radial inhomogeneities do. Our approach to non-Copernican cosmologies introduced a fine-tuning in the observer position. Given that the test presented in the following Section provides qualitatively similar results as the results presented here, we refer to the reader to Section 5.3.3.5, for a thorough discussion of the fine-tuning position of the observer.

5.2.4. Final considerations

The analysis presented here constitutes but a first step in the direction of analyzing and interpreting cosmological and astrophysical data within the framework of inhomogeneous cosmologies, where the latter are natural extensions of the standard paradigm. Given that data itself could prove the existence of large-scale inhomogeneities and isotropies in the Universe at odds with the standard paradigm of modern cosmology, it is fundamental to pursue a program that confronts observations with arbitrarily inhomogeneous cosmologies.

Here, we adopted a simple approach by embedding a spherical inhomogeneity in a ΛCDM background. Our results show that, within the ΛLTB framework, data can stringently constrain the radial inhomogeneity around us. Also, we found that the typical constraints on the standard ΛCDM parameters are not weakened after marginalizing over the local inhomogeneity parameters. Namely, dropping the Copernican hypothesis does not necessarily imply significantly worse constraints on the background parameters. This positive result demonstrates that the inhomogeneous cosmology framework can be used to meaningfully analyzed future and present data.

A possible route that can be taken to develop the present analysis is to consider inhomogeneities in the radiation field, as proposed by Regis and Clarkson [70]. If the universe features large-scale inhomogeneities in the matter, one may anticipate a similar trend in the baryon fraction or baryon-to-photon ratio or other domains, which can drastically affect parts of the analysis and restrictions. We envision that present and future cosmological data will nevertheless be able to constrain the free functions of these models.

Finally, mapping the local structure may have important implications; a notable one is its effect on the H_0 crisis, see Figure 4.5. This topic will be discussed in Section 5.4.

5.3. Testing the Copernican principle with next-generation surveys

Given the common scientific interests, in 2018, I joined, as an external collaborator, the Work Package 5 “Deviations from homogeneity and Isotropy” of the Theory Science Working Group of Euclid Consortium. To date, I have actively participated in the activities of this group, not only collaborating on a project [14] but also leading the most recent project of this group: the “Testing the Copernican principle with next-generation survey” project [CP Paper III], where, using mock data coming from DESI, Euclid, LSST, SH0ES, and current surveys, we forecast constraints on the ΛCDM model. We aim to determine the precision with which forthcoming surveys will be

Label	M_B	Ω_{m0}	ω_{b0}	H_0	δ_0	z_B
ΛCDM: standard model	-19.3	0.32	0.02225	67	-	-
ΛLTB 1: Copernican structure	-19.3	0.32	0.02225	67	-0.5	0.05
ΛLTB 2: Shallow but large void	-19.3	0.32	0.02225	67	-0.1	0.4
ΛLTB 3: Shallow but huge void	-19.3	0.32	0.02225	67	-0.1	0.8

Table 5.3.: The configurations of the fiducial models that were adopted to create the forecast data. The parameters value assumed here for the ΛCDM model follows the fiducial of Euclid Collaboration: Blanchard et al. [250], where a flat background is assumed. H_0 is shown in units of km s^{-1} Mpc^{-1} and M_B is shown in units of mag.

able to test the Copernican principle and their ability to detect any possible violations of it. In this Section, we discuss the results of this project.

In the first part of this Section, we present both the forecast and current data used to constrain the ΛLTB model. Despite we aim to forecast constraints on the Copernican principle considering data from future surveys, it is crucial to point out that the inclusion of current data is still needed to tightly constrain the ΛLTB model, especially, at small scales where the model highly degenerates with ΛCDM model, see Figure 4.6, for instance. Later, we show the results and discuss several aspects of our analysis. We end the discussion of this project by mentioning the conclusions and final remarks of CP Paper III.

Before presenting the data that is used in this analysis, it is crucial to mention that forecast data sets are generated considering four fiducial models, see Table 5.3. The analyses of such mock catalogs, which are based on the ΛCDM and ΛLTB models, have different aims. While the analysis of ΛCDM forecast data aims at estimating the accuracy with which next-generation surveys will be able to probe for spherically inhomogeneities around the FLRW metric, the study of the ΛLTB mock data, instead, is used to address the ability of future surveys to detect a violation of the Copernican principle. Furthermore, current, i.e., real, data is rescaled to agree with the fiducial models shown in Table 5.3. For sake of the readability of the text, we discuss the re-scaling procedure in Appendix C. Since this analysis corresponds to a forecast analysis, we idealize cosmological data by assuming that there are no tensions among the different data sets; this includes tensions between early and late determinations.

5.3.1. Data sets used in the analysis: forecast data

In order to forecast the impact of DESI, Euclid, and LSST surveys on constraints of deviations from the Copernican principle, we generate mock SNe and BAO catalogs. As already discussed, within the ΛLTB framework, BAO measurements will effectively constrain the longitudinal Hubble rate and the diameter angular distances by Equations (5.14) and (5.15), while the apparent magnitude of SNe will bound the cosmology through the luminosity distance, see Equation (5.9). Note that, the recipes described in this Section are used to create the ΛCDM forecast data using. In contrast, the ΛCDM catalogs will be obtained by a suitable re-scaling of data as thoroughly explained in Appendix C.

We use four fiducial cosmologies, based on the ΛCDM and the ΛLTB model, to create the forecast catalogs. These are shown in Table 5.3, with being the ΛCDM configuration the one also used in Euclid Collaboration: Blanchard et al. [250]. To produce the ΛCDM catalogs, we computed the redshift evolution of the Hubble parameter, along with the luminosity and angular diameter distances, as described in the following. The forecast recipe will be based on the specifications of the corresponding surveys, i.e., DESI, Euclid, and LSST. In contrast, as remarked earlier, we will obtain the ΛLTB catalogs following the process described in Appendix C. Given that computing correlation matrices for non-ΛCDM cosmologies may be not feasible [251, 252, 253], we first compute the correlation matrix assuming the ΛCDM fiducial to later apply the re-scaling method described in Appendix C to obtain the corresponding ΛLTB matrices.

5.3.1.1. SNe surveys

Our analysis will rely on the usage of two forthcoming SNe experiments: the Euclid DESIRE [254, 255] and LSST surveys [256]. In particular, to create the Euclid DESIRE-based catalog we assume that 1700 SNe will be observed in the redshift range $z \in [0.7, 1.6]$, while in order to create the LSST-based data 8800 SNe in the redshift range $z \in [0.1, 1.0]$ will be assumed. In total, our forecast data catalog will contain 10 500 SNe data point.

In both cases, we assume the redshift distributions of the SNe events as described in Astier et al. [255], where we will also assume that the points are not correlated with each other. The total error on the measurements of SNe will be modeled through

$$\sigma^2_{\text{tot},i} = \delta\mu_i^2 + \sigma^2_{\text{flux}} + \sigma^2_{\text{scat}} + \sigma^2_{\text{intr}}\,, \tag{5.30}$$

where the terms corresponding to the intrinsic contributions, the scatter and the flux are the same for all events: $\sigma_{\text{intr}} = 0.12$, $\sigma_{\text{scat}} = 0.025$, and $\sigma_{\text{flux}} = 0.01$ respectively. Lastly, we consider an error on the modulus distance $\mu = m - M_B$ that with a linear dependence on the redshift such that $\delta\mu = e_{\text{M}}\, z$, where e_{M} follows a Gaussian distribution with zero mean and standard deviation $\sigma(e_{\text{M}}) = 0.01$ [see 257, 255]. This latter also includes the possible redshift evolution of SNe not taken into account by the distance estimator, see Astier et al. [255]. It is important to point out that although $e_{\text{M}} = 0.01$ is required to take into account a possible systematic evolution, this term would be quadratically propagated together with the effective term that arose from the SNe lensing $e_{\text{M}} = 0.055$. Several authors have theoretically computed this error consistently finding $\sigma_{lens} \simeq 0.055\, z$ [258, 259, 260]. Note that observationally determinations agree with the theoretically predicted value of σ_{lens}. For instance, Supernova Legacy Survey found this error to be $\sigma_{\text{lens}} = (0.055 \pm 0.04)\, z$ [261] and $\sigma_{\text{lens}} = (0.054 \pm 0.024)\, z$ [262].

We would like to highlight that, despite that the Euclid SNE survey is not yet assured to take place, we resolve to include it in the analysis in order to broaden the redshift range of the SNe data; the inclusion of Euclid DESIRE-based SNe allows us to reach luminosity distances up to $z_{\text{max}} = 1.6$.

5.3.1.2. Local prior on the Hubble constant

The inclusion of a local prior is essential to effectively calibrate the luminosity distance of SNe. We have earlier argued that in light of the Hubble constant analyses of late time modifications of the ΛCDM model should include a prior on the absolute magnitude of SNe instead of on the local Hubble constant. Here, since the forecast analysis neglect any tension, we impose a constraint on the H_0 instead of M_B. This choice is also justified by the fact that the great goal of the SH0ES collaboration is to provide a 1% local measurement of the Hubble constant. In particular, we forecast

$$H_0 = \begin{cases} 67.00 \pm 0.67\,\mathrm{km\,s^{-1}\,Mpc^{-1}} & \text{for } \Lambda\mathrm{CDM} \\ 67.62 \pm 0.68\,\mathrm{km\,s^{-1}\,Mpc^{-1}} & \text{for } \Lambda\mathrm{LTB}\ 1 \\ 68.22 \pm 0.68\,\mathrm{km\,s^{-1}\,Mpc^{-1}} & \text{for } \Lambda\mathrm{LTB}\ 2 \\ 68.45 \pm 0.68\,\mathrm{km\,s^{-1}\,Mpc^{-1}} & \text{for } \Lambda\mathrm{LTB}\ 3 \end{cases}, \tag{5.31}$$

where the central value correspond the fiducial H_0 value for the ΛCDM fiducial model, meanwhile, for the ΛLTB models, the central value is computed through H_0^{L}, see Section 5.1.3. The corresponding Gaussian prior of Equation (5.31) is imposed on H_0^{L}; our choice of H_0^{L} over H_0^{R} or H_0^{R} will be justified in Section 5.4.

Lastly, we remark that the forecast scenario neglects the tension between early and late determinations of the Hubble constant. By assuming a single consistent fiducial model, we focus on the constraining potential of future surveys to test the Copernican principle, leaving the issue of the Hubble tension to other studies. This particular choice will be also justified by the analysis presented in the next Chapter — or CP Paper I, CP Paper II.

5.3.1.3. Large-scale structure surveys

Here, we will succinctly outline our method for producing mock BAO data based on Euclid specifications using a Fisher matrix approach. Since we are interested in accurately measuring the angular diameter distance $D_A(z)$ and the Hubble parameter $H(z)$, we follow the methodology of Euclid Collaboration: Blanchard et al. [250] for the spectroscopic survey. Future Euclid weak lensing, nor other perturbation level observables such as redshift space distortions, will consider in this analysis. This is because there is not yet a fully developed linear perturbation theory on inhomogeneous backgrounds.

As explained in Euclid Collaboration: Blanchard et al. [250], the main targets of the Euclid survey will be Emission Line Galaxies (ELGs). The latter are bright emitters in specific lines, like H_α and [O III], that can be seen in the redshift range $z \in [0.9, 1.8]$, and are useful to measure the galaxy power spectrum. Euclid will determine, in particular, approximately 30 million spectroscopic redshifts with an uncertainty of $\sigma_z = 0.001(1+z)$ [263], which will provide the galaxy power spectrum with information on the distortions due to the redshift uncertainty, the residual shot noise, the galaxy bias, the Alcock-Paczynski effect, and the redshift space distortions. Where, nonlinear effects, such as nonlinear smearing of the BAO feature or a nonlinear scale-dependent galaxy bias that distort the shape of the power spectrum, have also been taken into account, see Wang et al. [264] and de la Torre and Guzzo [265], respectively.

For this analysis, we will use the same binning scheme as in Martinelli et al. [266, 267]. Particularly, this differs from that of Euclid Collaboration: Blanchard et al. [250] such that instead of four equally spaced redshift bins nine bins of width $\Delta z = 0.1$ are considered. After rebinning the data provided in Euclid Collaboration: Blanchard et al. [250], we obtain the following specifications for the galaxy number density $n(z)$, given in units of Mpc^{-3}, and that of the galaxy bias $b(z)$:

$$n(z)=\{2.04, 2.08, 1.78, 1.58, 1.39, 1.15, 0.97, 0.7, 0.6\} \times 10^{-4}; \tag{5.32}$$

$$b(z)=\{1.42, 1.5, 1.57, 1.64, 1.71, 1.78, 1.84, 1.90, 1.96\}. \tag{5.33}$$

Under the assumption of the ΛCDM fiducial, we can use the methodology described in Euclid Collaboration: Blanchard et al. [250] to derive the Fisher — and covariance — matrix for the cosmological parameters. Thus, in order to create the ΛLTB mock, we specifically consider the background quantities $\{\omega_m,\, h,\, \omega_b,\, n_s\}$, two non-linear parameters $\{\sigma_\mathrm{p},\, \sigma_\mathrm{v}\}$ and the five redshift dependent parameters$\{\ln D_A,\, \ln H,\, \ln f\sigma_8,\, \ln b\sigma_8,\, P_s\}$, which are estimated in every redshift bin. Note that, we have defined $f\sigma_8 \equiv f(z)\sigma_8(z)$ as the linear growth rate multiplied by σ_8, and $b\sigma_8 \equiv b(z)\sigma_8(z)$ and P_s as the galaxy bias and the shot noise, respectively. Thus, using this approach we can determine the expected uncertainty of the measurements of the Euclid survey for both the angular diameter distance $D_A(z)$ and the Hubble parameter $H(z)$, in every redshift bin. The approach presented in Appendix C is, on the other hand, applied to generate the corresponding ΛLTB data.

Although Euclid will provide accurate measurements at redshift $z \sim 1$, its spectroscopic survey will be rather limited in the redshift range $z \in [0.9, 1.8]$. Therefore, in order to complement Euclid, we will also use data products from the DESI survey covering then smaller redshifts. DESI — operating since 2021 — is expected to eventually provide spectra for tens of millions of galaxies and quasars up to $z \sim 4$. Here, to produce both the angular diameter distance $D_A(z)$ and the Hubble parameter $H(z)$ DESI mock for the ΛCDM fiducial, we adopt the technique discussed in Aghamousa et al. [268]. These Fisher matrix forecasts were also derived using the full anisotropic galaxy power spectrum, i.e. measurements of the matter power spectrum as a function of the angle with respect to the line of sight, as described in Font-Ribera et al. [269]. This approach is similar to that of the Euclid forecasts and it also includes all information from the two-point correlation function. In particular, the baseline DESI survey will cover approximately $14\,000\,\mathrm{deg}^2$ and will target emission line galaxies (ELGs), luminous red galaxies (LRGs), bright galaxies (BGs) and quasars, all in the redshift range $z \in [0.05, 3.55]$, albeit the precision of the measurements will depend on the target population. Regarding the specific populations, the BGs will be in the range $z \in [0.05, 0.45]$ in five equally spaced redshift bins, while the ELGs and the LRGs will be in the range $z \in [0.65, 1.85]$ in 13 equally spaced bins. Finally, the Ly-α forest quasars will be in the range $z \in [1.96, 3.55]$ in 11 equally spaced bins and we will assume that the points are uncorrelated with each other. In order to avoid overlap between the DESI and Euclid and the introduction of undesired correlations, when these two surveys are used in combination, we will only consider the DESI points that do not overlap with those of Euclid.

5.3.2. Data sets used in the analysis: Current data

As discussed in Section 5.2.3.3, the combination of CMB + SNe is needed to tightly constrain the ΛLTB model, particularly, at small scales. In the context of the forecast analysis, this signal that the presence of real data, i.e., Planck 2018 and Pantheon SNe, is essential even if we aim to forecast the contribution of future surveys. The usage of CMB data is necessary to constrain the background parameters, while the introduction of low-z SNe is needed to break the degeneracy of the ΛLTB parameters model at small scales. Here, we present the complementary current data that will be considered in the forecast analysis. As mentioned earlier, in order to use a consistent fiducial model, this data will be rescale considering the predictions of the fiducial models shown in Table 5.3 and according to the procedure described in Appendix C.

5.3.2.1. Cosmic Microwave background

The latest Planck CMB data [16] will be included in the analysis of the ΛCDM forecast. In particular, we will use the high-ℓ TT+TE+EE, low-ℓ TT, and low-ℓ EE likelihood, where data for high-ℓ will be considered in its compressed version, i.e., the likelihood normalized over all nuisance parameters except A_planck. Note that these likelihoods for Planck will not be rescaled since its typical constraints from ΛCDM model will agree with the fiducial values adopted for the forecast data (Table 5.3) within 68% confidence level.

In contrast, the ΛLTB model presented in Table 5.3 could lead to a significant change in the power spectrum of CMB and it is not ensured that they could agree with the constraints of the aforementioned likelihoods. Therefore, a rescaling of the CMB data according to the ΛLTB fiducial cosmologies is necessary. However, given the complex structure of the CMB likelihoods and our limited understanding of perturbations on the inhomogeneous models, rescaling Planck data may not be a trivial task. To overcome this issue, for the analyses of the ΛLTB mock catalogs we adopt the CMB distance priors on the shift parameter R, the acoustic scale l_A, the amount of baryons ω_b, and the tilt of the power spectrum n_s. We build the mock CMB priors considering the current measurements given by Chen et al. [270] and the effective FLRW model methodology presented in Section 5.1.1.

5.3.2.2. SNe surveys

LSST forecast data span over the redshift range $z = [0.1, 1.0]$, clearly pointing out a lack of SNe at very low redshifts. The lack of such will lead to weakening the constraints on the ΛLTB model by increasing the degeneracy between δ_0 and z_B. Here, to overcome this limitation, our analyses will also include the Pantheon SNe compilation [225]. This data set will be rescaled according to our method presented in Appendix C.

5.3.2.3. Large-scale structure surveys

We also include BAO measurements coming from the 6dFGS [234], SDDS-MGS [235] and BOSS-DR12 [144] surveys. While BOSS data will allow us to test $H_{\|}(z)$ and $D_A(a)$ at the redshifts $z = \{0.38, 0.51, 0.61\}$, isotropic measurements from 6dFGS and SDSS-MGS will conveniently constrain the ΛLTB dynamics at low redshift, specifically $z = \{0.1, 0.15\}$. Despite the current BAO measurements displayed here overlap with the forecast DESI mock, we assume no correlations between these data sets. For sake of simplicity, hereafter, we collectively refer to this set of data as BAO. Furthermore, our analysis does not use the latest eBOSS data [271, 272, 273, 274], mainly, because, eBOSS data set spans all the redshift range of the forecast Euclid data. Finally, in line with earlier mentioned, we rescale the BAO measurements, to agree with the fiducial cosmologies Table 5.3, according to the method discussed in Appendix C.

5.3.2.4. y-Compton distortion and the kSZ effect

In the analysis of forecast data from ΛCDM, we impose priors both on the y-Compton distortion and the kinetic Sunyaev-Zeldovich (kSZ) effect. On the one hand, for the kSZ effect, we adopt the $\sim 47\%$ constraint from SPT-SZ and SPTpol surveys [243] — considering the ΛCDM fiducial model, and a 46% precision, we obtain the Gaussian prior $D_{3000} = 3.49 \pm 1.63\mu\ K$ for the amplitude of the kSZ effect. On the other hand, for the y-Compton distortion, we adopt the upper limit prior at 95.4% uncertainty provided by COBE-FIRAS $y < 1.5 \times 10^{-5}$ [242].

Priors on the y-Compton distortion and the kSZ effect are instead not implemented in our analyses of the ΛLTB forecast data — our complimentary analyses demonstrate that in this case, these priors do not improve upon constraints given by the combinations of the other data sets.

5.3.3. Results and discussion

Similar to the Section 5.2, we constrain the ΛLTB model using several combinations of current and forecast data. We denote as the baseline analysis (hereafter 'Base') the combination of CMB, Pantheon SNe, LSST, and H_0 data, note that possible correlations between LSST and Pantheon are neglected. Further, the baseline analysis relative to current data (hereafter 'Base C') is defined as the combination of CMB, Pantheon, and M_B data. We also neglect any possible correlation between the future DESI and Euclid data set with the current BAO. When DESI and Euclid data are combined, we replace DESI measurements between $z \in [0.95, 1.75]$ with the Euclid data points. Here, we also explore the parameter space using the solver and sampler for the ΛLTB model, the `monteLLTB` code. Most of the plots shown in this section have been produced using `getdist` [249].

For sake of readability, we present separately our results for the cases of the ΛCDM and ΛLTB fiducial models of Table 5.3. As already discussed, we consider the ΛCDM fiducial model to test how well future data can constrain deviations from the Copernican principle, while we use the ΛLTB fiducial models to see if future data can detect a violation of the same.

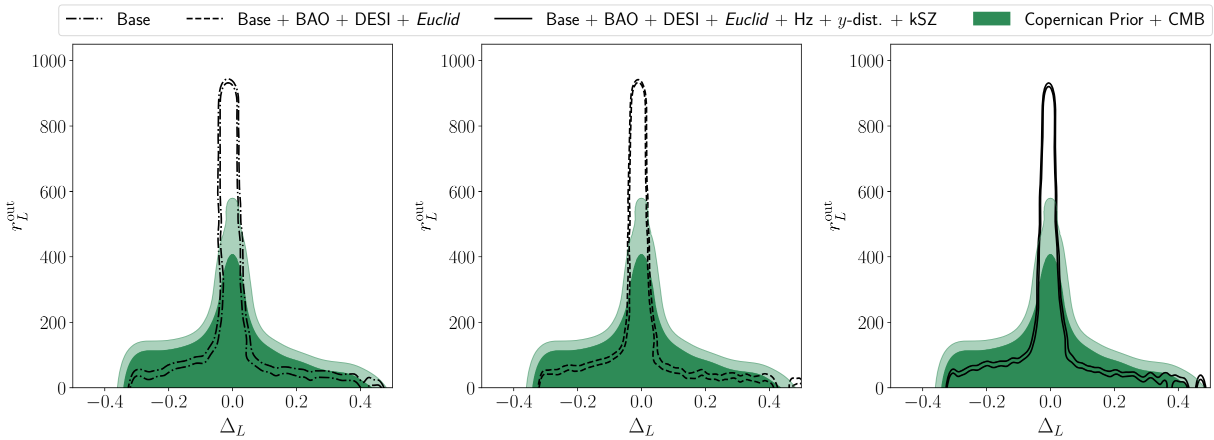

Figure 5.6.: The 95% and 99% confidence level constraints on the integrated mass contrast, Δ_L, and the comoving size, $r_L^{\rm out}$, for three different data combinations as compared to the constraints from the Copernican prior convolved with the CMB likelihoods.

5.3.3.1. ΛCDM mocks: The Copernican principle in light of the forthcoming surveys

In Figure 5.6 we show the marginalized constraints at the 95% and 99% confidence levels on the integrated mass contrast, Δ_L, and the comoving size, $r_L^{\rm out}$, for three different data combinations as compared to the constraints coming from the Copernican prior convolved with the CMB likelihoods.

The constraining power of future surveys on the radial inhomogeneity can be quantitatively compared to the expectation from the Copernican prior and CMB by comparing the ratio of the 95% confidence regions in the parameter space, see Table 5.4. Considering all scales, the ratio is always less than one, showing the capability of future surveys to rule out non-Copernican structures. However, at large scales, constraints provided by data still allow for non-Copernican mass density fluctuations since for $r_L^{\rm out} \geq 190\,$Mpc the ratio is approximately equal to two. Note that, for both cases, the combination Base + DESI + Euclid provides constraints comparable to

Observables	$A_{\text{obs}}/A_{\text{CP}}$	
	$0 \leq r_{\text{L}}^{\text{out}}$	$190\,\text{Mpc} \leq r_{\text{L}}^{\text{out}}$
Flat background FLRW metric		
Base (CMB+Pantheon+LSST+H_0)	0.82	2.1
Base + BAO + Euclid	0.80	2.0
Base + BAO + DESI	0.78	1.9
Base + BAO + Euclid + DESI	0.75	1.9
Data above + y-dist. + kSZ	0.75	1.7
Curved background FLRW metric		
Data above	0.82	1.9

Table 5.4.: Ratios of the areas of the 95% contours from observations and the Copernican principle. We also include (last row) the case with background curvature, $k_B \neq 0$ in Equation (4.28).

those obtained from the combination of all data, pointing out the important role that forthcoming large-scale structure surveys will have to test the Copernican principle.

We also consider the case of nonzero background curvature, i.e. $k_B \neq 0$ in Equation (4.28). The result is shown in the last row of Table 5.4. The inclusion of background curvature degrades the constraints by approximately 10% compared to the flat case, still providing a competitive constraint on the non-Copernican parameters.

5.3.3.2. ΛCDM mocks: Comparison with present-day constraints

In order to quantify the role of future surveys in constraining inhomogeneity around us, we compare our constraints with the ones from current data only, as obtained in CP Paper I. Specifically, we compute the improvement on the observed area A_{obs} considering the data combinations presented in Table 5.5. Our present analyses do not include a Cosmic chronometer data set as contributions of this kind of data are expected to be secondary as compared with SNe and BAO [CP Paper I]. Note that our previous implementation of such data did not include the full covariance matrix presented in [275], revised and discussed in [158].

Our Base analysis shows an improvement upon the current constraints by more than 20%, when all scales are considered, and provides an improvement of 28% when compared to the constraints from Base C and Base C + BAO + HZ at scales $r_L^{\text{out}} \geq 190\,\text{Mpc}$, where HZ denotes the Cosmic chronometers data set used in CP Paper I. It is interesting to note that our forecast Base analysis provides constraints comparable to those obtained with all the latest cosmological data available, Base C + BAO + HZ + y-dist + kSZ case, showing the importance of forthcoming SNe surveys and 1% prior on the Hubble constant.

On the other hand, LSS surveys will play an important role in testing the Copernican principle. As shown in Table 5.5, future measurements from Euclid and DESI will sharpen the current constraints of Base C by approximately 35%, both at $0 \leq r_L^{\text{out}}$ and $190\,\text{Mpc} \leq r_L^{\text{out}}$. The inclusion

Observables used in this analysis	Present-day observables used in Camarena et al. [1]	Percent improvement $0 \leq r_{\mathrm{L}}^{\mathrm{out}}$	Percent improvement $190\,\mathrm{Mpc} \leq r_{\mathrm{L}}^{\mathrm{out}}$
Base	Base C (CMB + Pantheon + M_B)	29%	28%
	Base C + BAO + HZ	26%	28%
	Base C + BAO + HZ + y-dist. + kSZ	20%	0%
Base + BAO + Euclid + DESI	Base C	35%	34%
	Base C + BAO + HZ	32%	34%
	Base C + BAO + HZ + y-dist. + kSZ	26%	10%
Base + BAO + Euclid + DESI + y-dist. + kSZ	Base C	35%	41%
	Base C + BAO + HZ	32%	41%
	Base C + BAO + HZ + y-dist. + kSZ	26%	19%

Table 5.5.: Percent improvement on constraints on radial inhomogeneity from next-generation surveys as compared to present-day constraints.

of Euclid and DESI will also tighten the parameter space by more than 30% compared to the combination Base C + BAO + HZ. When compared to the combination Base C + BAO + HZ + y-dist. + kSZ, our analysis with the forthcoming Euclid and DESI data shows an improvement of 26% for $0 \leq r_L^{\mathrm{out}}$ and 10% for $190\,\mathrm{Mpc} \leq r_L^{\mathrm{out}}$.

Finally, the combination of all data considered here will tighten our current constraints leading to improvements up to 41% for scales at $190\,\mathrm{Mpc} \leq r_L^{\mathrm{out}}$ and 35% for $0 \leq r_L^{\mathrm{out}}$, see Table 5.5.

5.3.3.3. ΛLTB mocks

In Figure 5.7 we show the marginalized constraints at the 95% and 99% confidence levels on δ_0 and z_B, for the three ΛLTB fiducial cosmologies, as compared to the constraints coming from the Copernican prior and CMB observations.

From the analysis relative to ΛLTB 1 (top row), we can see that future data will be able to probe the local structure. This means that the effect of the cosmic variance on the position of the observer will be reduced thanks to the forthcoming surveys.

On the other hand, from the analysis relative to ΛLTB 2 (middle row) and 3 (bottom row), we see that inhomogeneities that are large, but relatively shallow, can be detected with high significance thanks to future data. More precisely, one can note that our analyses exclude the FLRW case ($\delta_0 = 0$ and $z_B = 0$) by $\gtrsim 3\sigma$ (pink contours). This stresses the important roles of the next-generation surveys in testing the Copernican principle.

5.3.3.4. The role of large-scale structure data

We have seen from the results of Sections 5.3.3.1 and 5.3.3.2 on the ΛCDM mocks that future surveys, such as Euclid, will grant a $\approx 30\%$ improvement on inhomogeneity around the observer. In particular, for scales greater than 190 Mpc, the combination of all data will constrain inhomogeneity to only 1.7 times the area of the region allowed by standard cosmology. Given the fact that Euclid probes the redshift range $0.9 < z < 1.8$, one may wonder if the improvement due to Euclid comes directly from better constraints on the shape of the angular diameter distance and Hubble rate or indirectly from better constraints on the cosmological parameters.

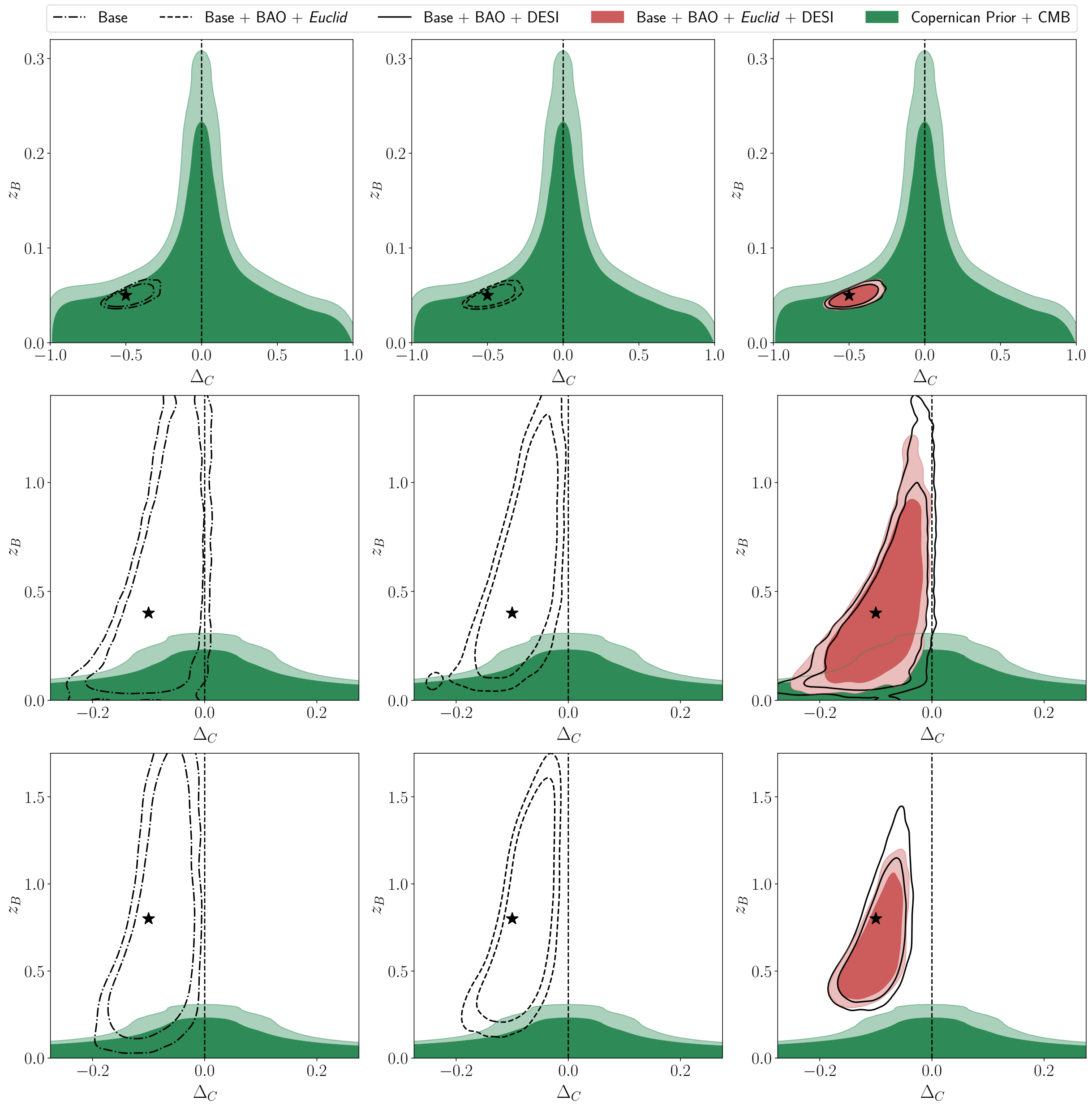

Figure 5.7.: The 95% and 99% confidence level constraints on the density contrast at the center, δ_0, and the redshift of the boundary, z_B, for the ΛLTB mock catalogs of Table 5.3 as compared to the constraints from the Copernican prior convolved with the CMB likelihood. The black star is placed at the fiducial values for the LTB parameters, i.e. $\delta_0 = -0.5$ and $z_B = 0.05$ (top row, ΛLTB 1), $\delta_0 = -0.1$ and $z_B = 0.4$ (middle row, ΛLTB 2), and $\delta_0 = -0.1$ and $z_B = 0.8$ (bottom row, ΛLTB 3). Note that the z_B-axis is not the same for all figures.

In order to answer the previous question, we show in Figure 5.8 the fluctuations in the apparent magnitude, Hubble rate, and angular diameter distance for the ΛLTB model as compared to the fiducial ΛCDM one. The 68% and 95% bands are obtained by evaluating the relevant functions at every point of the chains. We compare three analyses: the Base one, Base with present BAO and Euclid, and Base with present BAO and DESI. From this plot, it appears that the shape of the various functions does not change when adding Euclid or DESI. In other words, these two surveys do not improve the constraints in specific redshift ranges but rather they help at tightening the overall uncertainties. From this, we conclude that the improvement due to Euclid comes mostly from better constraints on the cosmological parameters, although this works in synergy with DESI and the other observables.

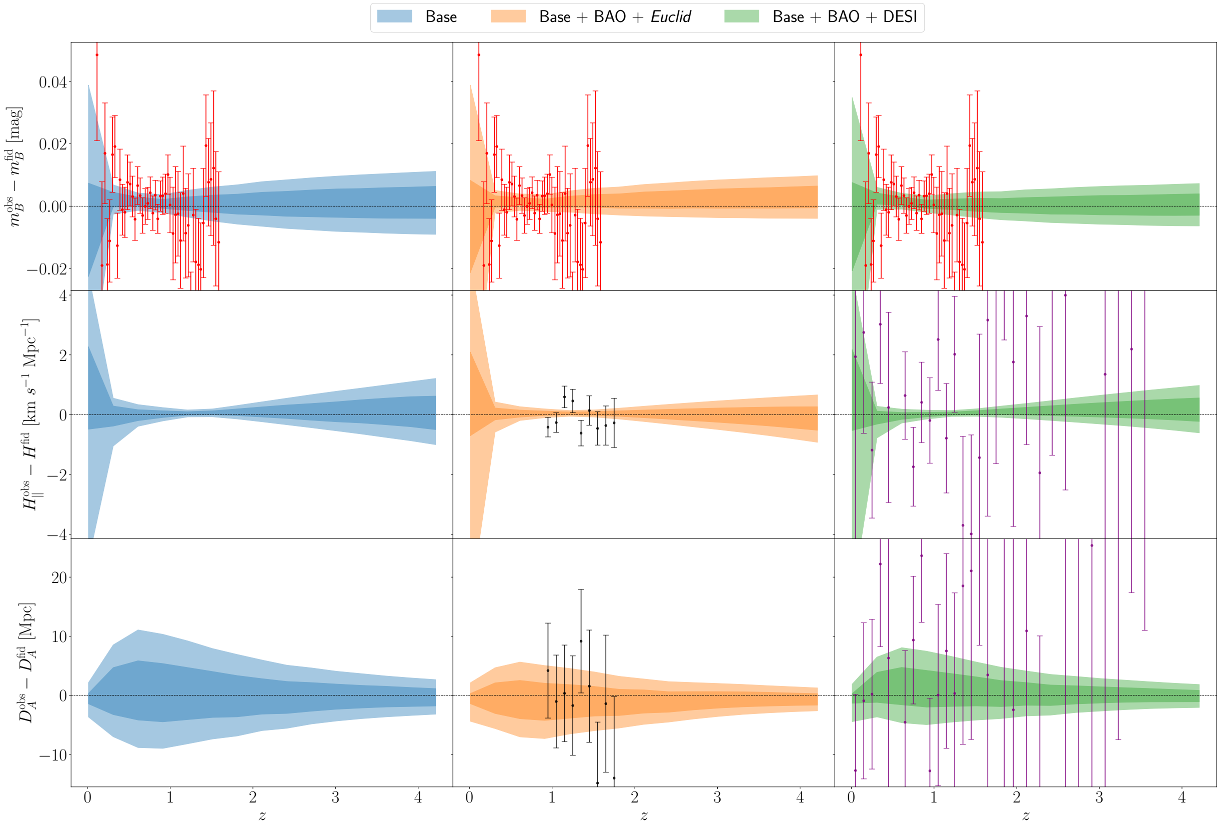

Figure 5.8.: Fluctuations in the apparent magnitude (top row), Hubble rate (middle row) and angular diameter distance (bottom row) for the ΛLTB model as compared to the fiducial ΛCDM one. The 68% and 95% bands are obtained by evaluating the relevant functions at every point of the chains. The red points show LSST and Euclid DESIRE supernovae data, the black ones Euclid data, and the purple ones DESI data. See Section 5.3.3.4.

5.3.3.5. Beyond the central observer

As mentioned earlier, our aim is to test radial homogeneity around us, neglecting anisotropies. We then placed the observer at the centre of the spherical over/underdensity. However, in an inhomogeneous universe beyond FLRW, neglecting anisotropies could not be justified because anisotropies may affect observables as much as radial inhomogeneities. In other words, the modelling adopted in this work implies a spherically symmetric inhomogeneity and a fine tuning of the observer's position.

From the results of Sections 5.3.3.1 and 5.3.3.2 on the ΛCDM mocks we see, *a posteriori*, that large structures with shallow contrasts are allowed by future data. If, for example, we consider a contrast of $\delta = -0.1$, the corresponding change in the Hubble rate is approximately

$$\begin{aligned} \delta H_0/H_0 &= -f(\Omega_m)\delta/3\,, \\ &\simeq 0.017\,, \end{aligned} \tag{5.34}$$

where $f \simeq 0.5$ is the present-day growth rate for the concordance ΛCDM model. The CMB dipole, if the observer were at e.g. a distance $d_{\rm obs} = 300$ Mpc from the centre, using $v = \Delta H\, d_{\rm obs}$, is then:

$$\beta = \frac{v}{c} \simeq 1.2 \times 10^{-3}\,, \tag{5.35}$$

which is basically the observed CMB dipole [98]. As the structures that we consider in this work extend to, at most, 1000 Mpc (see Figure 5.6), the required fine tuning is less than 1 in 40 chances. In other words, the fine tuning required to satisfy the CMB dipole is rather mild and therefore the motivation for considering an off-centre observer is to provide a better description of possibly anisotropic data, rather than to relieve the fine tuning of the observer's position.

It is worth mentioning that the fine-tuning is instead very severe when considering void models as alternatives to dark energy, a possibility that was not explored here and not favoured by data, see BEHOMO Paper I and CP Paper II. Indeed, in this case the underdensity has a radius of ≈ 3 Gpc and $\delta H_0/H_0 \approx 0.2$ so that the observer has to be within ≈ 30 Mpc from the centre, giving rise to a fine tuning of one in a million [194]. Note, however, as pointed out in Garcia-Bellido and Haugboelle [276], that it is possible to alleviate this improbability by displacing the observer and then making them move towards the centre. For distances of a few hundred Mpc and velocities of a few thousand $\mathrm{km\,s^{-1}}$, the effect is indistinguishable from the observed CMB dipole. In a way, one exchanges an improbability in location for an improbability in the direction of motion. The overall effect is to reduce the coincidence to a few parts in a thousand.

5.3.4. Final considerations

Testing fundamental assumptions of cosmology is a crucial step toward improving our understanding of the Universe and firmly establishing the foundations of the standard cosmological paradigm. In CP Paper I, we have tested the Copernican principle by placing constraints on the ΛLTB model using current and forecast data products. Specifically, we focus on the capability of forthcoming surveys, such as SH0ES, DESI, Euclid, and LSST, to test the Copernican principle in conjunction with current data.

In particular, we compare constraints on the ΛLTB model coming from the forecast and current data against constraints drawn from the Copernican prior—the statistical counterpart of the Copernican principle. This comparison allows us to quantify how well we can constrain deviations from the Copernican principle.

We have considered two types of fiducial models: the standard ΛCDM model and the inhomogeneous ΛLTB model. By analyzing the latter we aim to determine if next-generation surveys will be able to detect deviations from the Copernican principle, while our analysis of ΛCDM data aims to investigate if forthcoming data can successfully test the Copernican principle.

We have found that the inclusion of future data, coming from SH0ES, DESI, Euclid, and LSST, will improve the current constraints on the Copernican principle by up to 40%. This improvement will be especially important at scales $r_B \geq 190$ Mpc, where the inclusion of next-generation surveys will reduce the constrained area of the space parameters to a factor of < 2 as compared with the area allowed by the Copernican prior. Furthermore, we found that using the forthcoming SH0ES, DESI, Euclid, and LSST data, we will be able to detect inhomogeneous deviations of the FLRW metric, including Gpc-scale inhomogeneities of contrast -0.1. Our analyses show that given the precision of next-generation of surveys a detection of this kind would allow us to rule out the FLRW space-time ($\delta_0 = 0$ and $z_B = 0$) by $\gtrsim 3\sigma$.

In summary, this work highlights the importance of synergies the forthcoming surveys in testing the Copernican principle, which is one of the fundamental assumptions of the standard paradigm of modern cosmology.

5.4. A void in the Hubble tension? The end of the line for the Hubble bubble

Current data can tightly constraint radial inhomogeneities at almost to the cosmic variance level, see Section 5.2 and [CP Paper I], effectively pointing out to fluctuations with magnitude $\delta \sim 0.01$ on scales $\gtrsim 100$ Mpc. In this Section, we discuss the results of the analyses presented in CP Paper II, where we have investigated if the current inhomogeneous non-Copernican fluctuations allowed by the data could explain the Hubble tension. Besides studying the Hubble tension problem, we also perform a model selection analysis between the standard ΛCDM model and its inhomogeneous extension, the ΛLTB model. Additionally, by considering the best fit to the cosmological data, we reconstruct our local space-time.

Similar to the previous Sections, we start our discussion by presenting the cosmological data that have been considered in the analysis of CP Paper II. Later, we present and discuss the results of the same, mainly focusing on the Hubble tension, the model selection analysis, and the reconstruction of the local structure of the Universe. We end this Section by stating the final remarks and conclusions of our analysis.

5.4.1. Data sets used in the analysis

Given that this analysis is an extension of the test of the Copernican principle, see Section 5.2 and CP Paper I, we will carry out our analyses using several combinations of the data presented in Section 5.2.1. We will also consider combinations of data including not the whole set of Pantheon supernovae but only SNe in the redshift range $0.023 < z < 0.15$ — the so-called Hubble flow supernovae that are used by SH0ES in the determination of H_0. We dub this subset of the Pantheon catalog as low-z supernovae. Additionally, we carried out analyses including a prior on the Hubble constant, instead of a prior on M_B. Specifically, we impose the SH0ES determination $H_0 = 73.5 \pm 1.4$ km s^{-1} Mpc^{-1} [134] on H_0^{L}. These extra analyses aim to demonstrate that both methods, either with a prior on M_B or a prior on H_0, are statistically equivalent when the local H_0 prior is implemented considering that the cosmic distance ladder technique does not measure the Hubble rate at $z = 0$ but rather in a specific redshift range [227].

5.4.2. Results and discussion

We repeat the approach used in Section 5.2: cosmological analysis is performed using `monteLLTB`, we adopt as convergence criteria the threshold $(\mathcal{R} - 1) \lesssim 0.05$ for the inhomogeneity parameters, δ_0 and z_B, and $(\mathcal{R} - 1) \sim \mathcal{O}(10^{-3})$ for the background ΛCDM parameters. Here, we also use `getdist` to produce most of the plots of this Section.

Given that Planck data has shown moderate evidence for a closed Universe [95, 277], the question, of whether our Universe is flat or curved, has been recently investigated, see Section 3.2.3. Additionally, the FLRW curvature has been found to have a strong correlation with a possible change in the CMB temperature, potentially pointing out the existence of a strong correlation with the parameters of an inhomogeneous model, see also Section 3.2.3. Here we will analyze the ΛLTB model considering both a flat and a curved ΛCDM background. Finally, we denote as Base the combination of CMB, SNe, and the local prior (either on H_0 or M_B).

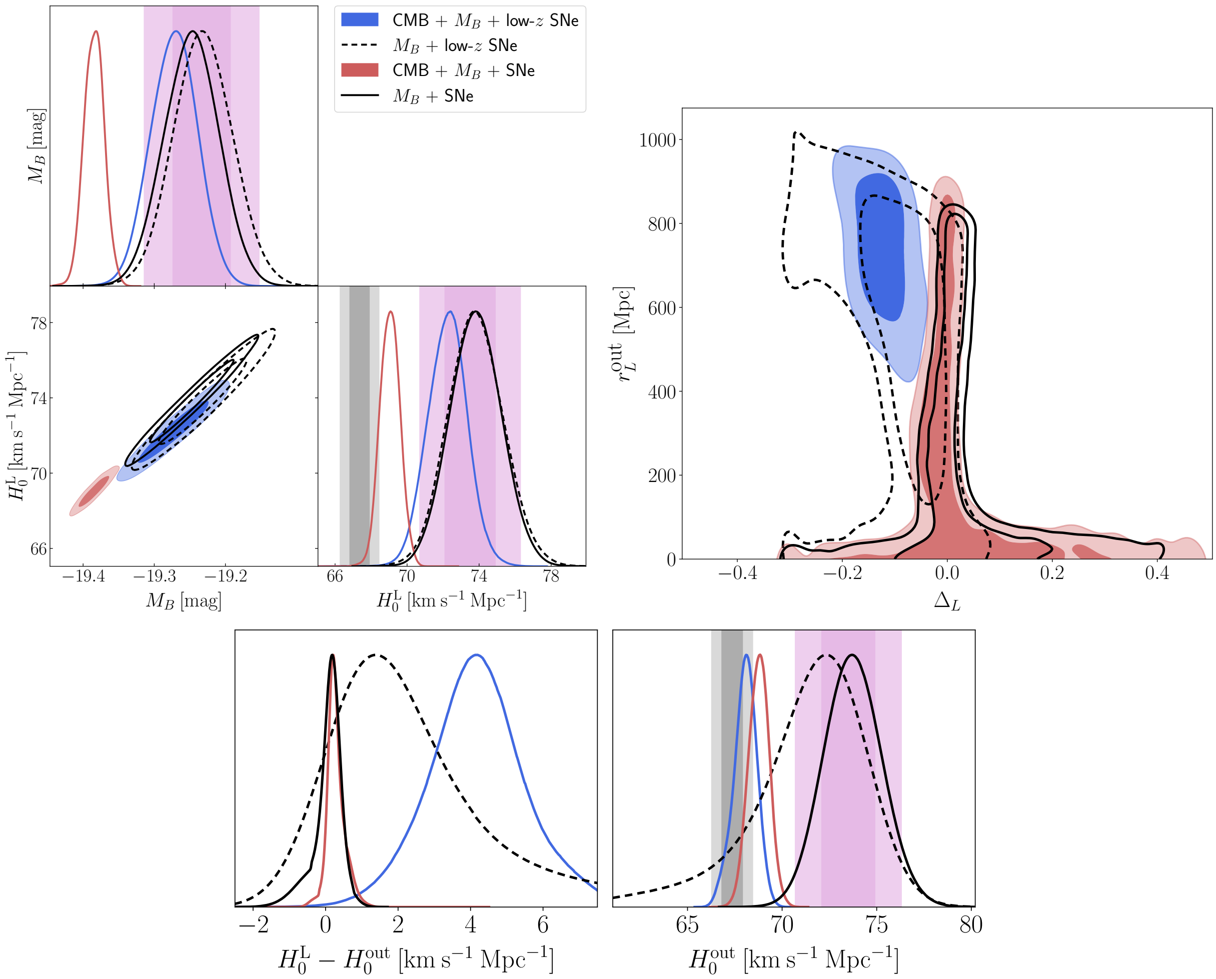

Figure 5.9.: Marginalized constraints, at 68% and 95% confidence level, on several parameters of interest when considering, in a flat background Universe, combinations of CMB and supernova data, together with the local prior on the supernova absolute magnitude M_B. Shown are M_B and the local Hubble rate $H_0^{\rm L}$ (top), the effective mass density contrast Δ_L and compensating scale $r_L^{\rm out}$ of the ΛLTB model (center), and background Hubble constant $H_0^{\rm out}$ and the local increase with respect to the background rate, $\Delta H = H_0^{\rm L} - H_0^{\rm out}$ (bottom). Note that there is tension only when considering all supernovae and the CMB. See Section 5.4.2.1.

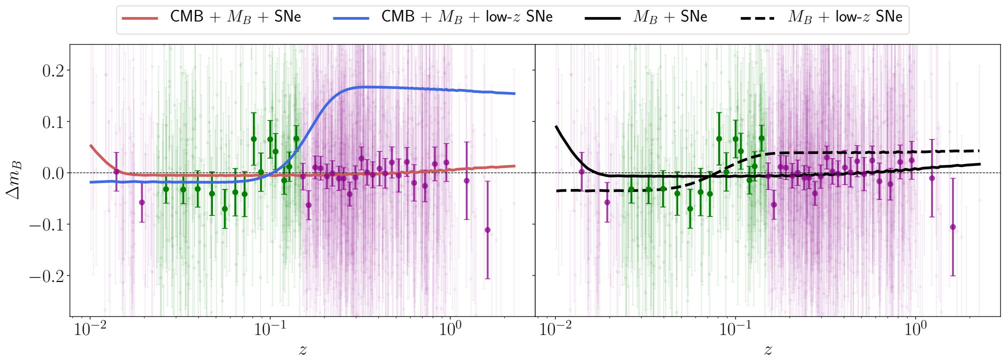

Figure 5.10.: Apparent magnitude residuals of the Pantheon supernovae, as function of the redshift, taking as a reference the best fit of the ΛCDM model to the combination CMB + M_B + SNe + All. One can see, from the left panel, that the best fit of the ΛLTB model to CMB + M_B + low-z SNe (blue line) fits well the supernovae in the range $0.023 < z < 0.15$ (green data points) and provides a solution to the Hubble crisis, see Section 5.4.2.1. However, the other supernovae (purple data points) constrain the ΛLTB luminosity distance (red line) to a shape similar to the ΛCDM one. The result is that the ΛLTB model cannot explain the Hubble tension. The right panel shows the case without CMB data. While the full supernova sample does not prefer an underdensity (solid curve), when only considering low-z supernovae one sees that the profile is compatible with a local void (dashed black line). This is due to a fluctuation in the supernova apparent magnitudes at $0.1 \lesssim z \lesssim 0.15$.

5.4.2.1. Flat background FLRW metric

We start by considering a flat ΛCDM background ($k_B = 0$) and only CMB and SNe observations, together with the local prior on the supernova absolute magnitude M_B. Figure 5.9 shows marginalized constraints on several parameters of interest for four observable combinations. Figure 5.10 shows the corresponding apparent magnitude residuals of the ΛLTB best fits with respect to the ΛCDM best fit.

As it is well known, the freedom in defining the LTB curvature function allows one to fit any luminosity-distance-redshift relation, that is, any supernova sample. If one adds a prior on M_B, then the latter simply constrains the supernova absolute magnitude, and so local H_0, without changing the fit to supernova data. We start by discussing this case for the full Pantheon sample and its low-redshift subset ($0.023 < z < 0.15$). From Figure 5.9 we see that the constraints on Δ_L and $r_L^{\rm out}$ from the full SN sample (solid black lines) are along the $\Delta_L = 0$ axis, not favoring under- or overdensities. In particular, one has $H_0^L \approx H_0^{\rm out} \approx H_0^{\rm SH0ES}$. In other words, there is no local void nor H_0 tension, as expected.

If one considers only low-z supernovae (dashed black lines), the situation is qualitatively the same, albeit with weaker constraints. Note, however, that a local underdensity is somewhat preferred: this is caused by fluctuations in the supernova apparent magnitudes at $0.1 \lesssim z \lesssim 0.15$, as evident from Figure 5.10. Because of this allegedly random fluctuation, there is a small shift between H_0^L and $H_0^{\rm out}$, see Figure 5.9.

Next, we add CMB observations, which are fit by a lower background H_0 as compared with $H_0^{\rm SH0ES}$. If we consider low-z supernovae (blue curves), then one can have all the supernovae inside a local underdensity and is free to fit any $\Delta H = H_0^L - H_0^{\rm out}$, see Figures 5.9 and 5.10. Specifically, the data favors a local underdensity and the local value of the Hubble rate is in agreement with the local prior and the tension between CMB observations and the local prior is solved. Note also that the local calibration of M_B is not affected by CMB observations. Table 5.6 shows the marginalized constraints for the relevant parameters, including H_0^{L}, H_0^{R}, and H_0^{M}. We also show the change in the observed CMB temperature $\Delta T \equiv T_0^{\mathrm{obs}} - T_0^{\mathrm{out}}$, with T_0^{obs} being the CMB temperature measured by the observer and $T_0^{\mathrm{out}} = 2.7255$ K the background temperature.[3] Indeed, analogous to other parameters, the observer at the center of the inhomogeneity is expected to measure a different CMB temperature as compared with the expected FLRW background temperature. This change in the temperature is strongly related to the features of inhomogeneity. Within this scenario, one expects a ≈ 2 mK change in the CMB temperature. It is worth pointing out that the fact that the analysis M_B + low-z SNe also suggests a similar underdensity is a coincidence: even without the fluctuation at $0.1 \lesssim z \lesssim 0.15$ one would have obtained here a similar result.

[3] Note that we have neglected possible dynamical effects of radiation [245].

Parameter	CMB + loc. prior + low-z SNe	Base	Base + BAO + Hz	Base + y-dist.	Base + kSZ	Base + All
			Prior on M_B			
M_B [mag]	$-19.271^{+0.032}_{-0.035}$	$-19.384^{+0.014}_{-0.014}$	$-19.389^{+0.011}_{-0.012}$	$-19.386^{+0.014}_{-0.014}$	$-19.384^{+0.014}_{-0.014}$	$-19.391^{+0.012}_{-0.012}$
H_0^{M} [km/s/Mpc]	$72.47^{+1.09}_{-1.10}$	$69.06^{+0.53}_{-0.60}$	$68.89^{+0.44}_{-0.46}$	$69.01^{+0.58}_{-0.55}$	$69.07^{+0.56}_{-0.54}$	$68.77^{+0.40}_{-0.46}$
H_0^{L} [km/s/Mpc]	$72.29^{+1.11}_{-1.12}$	$69.06^{+0.54}_{-0.57}$	$68.89^{+0.43}_{-0.46}$	$69.00^{+0.57}_{-0.53}$	$69.07^{+0.55}_{-0.54}$	$68.78^{+0.39}_{-0.44}$
H_0^{R} [km/s/Mpc]	$72.38^{+1.12}_{-1.14}$	$69.06^{+0.52}_{-0.54}$	$68.90^{+0.41}_{-0.44}$	$69.00^{+0.54}_{-0.51}$	$69.07^{+0.53}_{-0.50}$	$68.79^{+0.37}_{-0.42}$
ΔT [mK]	$1.861^{+0.639}_{-0.918}$	$-0.017^{+0.042}_{-0.041}$	$-0.007^{+0.027}_{-0.045}$	$-0.009^{+0.025}_{-0.048}$	$-0.023^{+0.023}_{-0.027}$	$-0.022^{+0.022}_{-0.025}$
Tension on H_0	0.7	3.0	3.1	3.0	2.9	3.2
Tension on M_B	0.7	3.5	3.7	3.6	3.5	3.8
χ^2_{min}	2996.1	3808.7	3826.7	3807.3	3808.0	3828.2
			Prior on H_0			
M_B [mag]	$-19.258^{+0.047}_{-0.044}$	$-19.386^{+0.015}_{-0.015}$	$-19.391^{+0.012}_{-0.012}$	$-19.389^{+0.015}_{-0.015}$	$-19.389^{+0.014}_{-0.014}$	$-19.392^{+0.011}_{-0.012}$
H_0^{M} [km/s/Mpc]	$73.01^{+1.49}_{-1.53}$	$69.09^{+0.56}_{-0.58}$	$68.90^{+0.47}_{-0.49}$	$68.98^{+0.59}_{-0.60}$	$68.94^{+0.55}_{-0.51}$	$68.83^{+0.43}_{-0.46}$
H_0^{L} [km/s/Mpc]	$72.83^{+1.53}_{-1.49}$	$69.08^{+0.57}_{-0.56}$	$68.88^{+0.44}_{-0.47}$	$68.97^{+0.55}_{-0.58}$	$68.94^{+0.54}_{-0.51}$	$68.83^{+0.41}_{-0.44}$
H_0^{R} [km/s/Mpc]	$72.94^{+1.56}_{-1.51}$	$69.08^{+0.54}_{-0.53}$	$68.89^{+0.46}_{-0.46}$	$68.98^{+0.54}_{-0.55}$	$68.94^{+0.51}_{-0.48}$	$68.84^{+0.39}_{-0.42}$
ΔT [mK]	$2.145^{+0.869}_{-1.043}$	$0.004^{+0.021}_{-0.065}$	$0.007^{+0.024}_{-0.061}$	$0.001^{+0.056}_{-0.067}$	$-0.017^{+0.026}_{-0.032}$	$-0.015^{+0.020}_{-0.036}$
Tension on H_0	0.3	2.9	3.1	3.0	3.0	3.2
Tension on M_B	0.4	3.6	3.8	3.6	3.6	3.8
χ^2_{min}	2998.3	3803.8	3826.8	3805.0	3803.0	3824.5

Table 5.6.: 68% confidence level intervals for the relevant parameters for the different combinations of data here analyzed, considering both the prior on H_0 and M_B. We also report the χ^2_{min} and the tensions on H_0 and M_B in sigma units.

Then, we consider the full Pantheon sample. In this case, the luminosity-distance-redshift relation mapped by the supernovae does not allow for a sufficiently large and deep underdensity that can solve the H_0 tension: a sudden change in the luminosity distance is not allowed by the supernovae at $z > 0.15$, see Figures 5.9 and 5.10. In particular, CMB data induce a lower value of M_B, at odds with the local prior, the so-called M_B tension [H0 Paper III]. Also, in this case, the change in the CMB temperature is much smaller, approximately ≈ 0.01 mK. Our results are that a local void is not favored by the data and the H_0 tension is not solved. Note, however, that $\Delta H = H_0^L - H_0^{\rm out}$ does prefer small but positive values, that is, and underdensity. We will come back to this in Section 5.4.2.6.

Finally, we include other observables, considering all the combinations discussed in CP Paper I. Table 5.6 presents the relevant results, including the corresponding $\chi^2_{\rm min}$ and the resulting tensions on M_B and H_0, with respect to H0 Paper I and Reid et al. [134], respectively.

5.4.2.2. Curved background FLRW metric

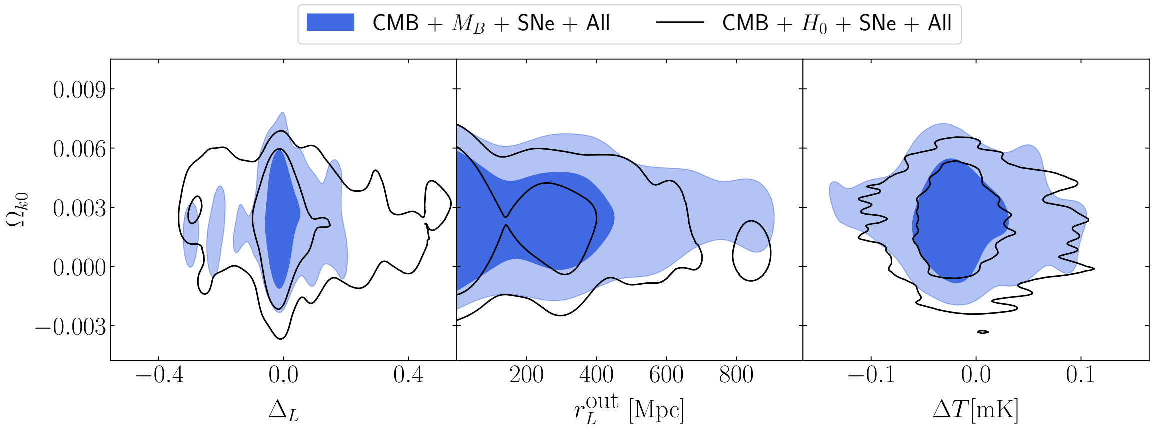

Figure 5.11.: Marginalized constraints on the effective mass density contrast Δ_L, compensating scale $r_L^{\rm out}$, temperature deviation ΔT and background curvature $\Omega_{k,0}$ at 68% and 95% confidence levels.

We also study the case of a non-flat FLRW background. Results for these analyses are shown in Table 5.7 and Figure 5.11. From Table 5.7, we can see that the inclusion of the curvature does not significantly change the overall results. In particular, the data favors a slightly open universe with $\Omega_{k,0} \approx 0.002$, compatible with the flat case at 2σ. In particular, in Figure 5.11 we do not observe a strong correlation between $\Omega_{k,0}$ and the other parameters, in particular ΔT, which remains constrained around zero.

Finally, Figure 5.12 shows the different values obtained for $H_0^{\rm L}$ and M_B for our different analyses, both considering a prior on M_B and H_0. For the sake of the comparison, we have also included the results coming from analyses of the ΛCDM model. We can see how the ΛLTB results follow the ones relative to the ΛCDM model.

5.4.2.3. Model selection

We have seen how the Hubble tension is solved when only low-redshift supernovae are considered but it is no longer solved when all supernovae are included. Here, we will quantify this statement using a Bayesian model comparison between the ΛCDM and ΛLTB models. We perform model

Parameter	Base + BAO + Hz	Base + All
	Prior on M_B (Prior on H_0)	
Ω_{k0}	$0.0024^{+0.0016}_{-0.0016}$ $(0.0022^{+0.0017}_{-0.0017})$	$0.0024^{+0.0017}_{-0.0017}$ $(0.0021^{+0.0018}_{-0.0017})$
M_B [mag]	$-19.372^{+0.016}_{-0.016}$ $(-19.375^{+0.017}_{-0.017})$	$-19.373^{+0.017}_{-0.015}$ $(-19.377^{+0.018}_{-0.015})$
$H_0^{\rm M}$ [km/s/Mpc]	$69.41^{+0.59}_{-0.61}$ $(69.43^{+0.61}_{-0.65})$	$69.38^{+0.62}_{-0.55}$ $(69.30^{+0.60}_{-0.57})$
$H_0^{\rm L}$ [km/s/Mpc]	$69.42^{+0.58}_{-0.59}$ $(69.41^{+0.59}_{-0.62})$	$69.38^{+0.61}_{-0.53}$ $(69.30^{+0.57}_{-0.56})$
$H_0^{\rm R}$ [km/s/Mpc]	$69.42^{+0.56}_{-0.58}$ $(69.43^{+0.58}_{-0.61})$	$69.39^{+0.59}_{-0.52}$ $(69.31^{+0.57}_{-0.55})$
ΔT [mK]	$-0.016^{+0.026}_{-0.039}$ $(0.004^{+0.028}_{-0.060})$	$-0.020^{+0.020}_{-0.032}$ $(-0.014^{+0.016}_{-0.032})$
Tension on H_0	2.7 (2.7)	2.7 (2.8)
Tension on M_B	3.2 (3.2)	3.2 (3.3)
$\chi^2_{\rm min}$	3828.4 (3820.1)	3829.0 (3822.7)

Table 5.7.: As Table 5.6, but for a curved background, $\Omega_{k0} \neq 0$.

selection using the Bayes ratio. Since the ΛCDM model is nested in the ΛLTB model, we can simplify the computation of the Bayes ratio by using the Savage-Dickey density ratio (SDRR) [278]. This technique reduces the Bayes ratio to:

$$B_{01} = \frac{\int \mathcal{P}(\delta_0, z_B, \theta_i) \mathrm{d}\theta_i}{p(\delta_0)p(z_B)}\bigg|_{\delta_0=0, z_B=0}, \tag{5.36}$$

with $\mathcal{P}$ being the posterior of the ΛLTB model, θ_i the ΛCDM background parameters, and p the prior function. Although the SDRR can be safely applied to nested models, one should bear in mind that Equation (5.36) assumes that priors are separable, i.e., $p(\delta_0, z_B, \theta_i) = p(\delta_0)p(z_B)p(\theta_i)$. Here, this assumption is fully satisfied since our analyses use wide flat priors over all parameters.[4] Specifically, we impose $z_B \in [0, 0.5]$ and $\delta_0 \in [-1, 1]$ such that the flat priors result in $p(\delta_0) = 1/2$ and $p(z_B) = 2$. In Equation (5.36) it is $B_{01} \propto \mathcal{E}_0/\mathcal{E}_1$, with 0 representing the nested model, in our case the ΛCDM model, and 1 the more complex model, the ΛLTB model. We qualitatively interpret the ratio B_{01} via the Jeffreys' scale [279]. Specifically, we adopt the conservative version discussed in Trotta [278].

We also use the Akaike information criterion (AIC):

$$\mathrm{AIC} = \chi^2_{\rm min} + 2k\,, \tag{5.37}$$

with k being the number of free parameters. The relative differences $\Delta\mathrm{AIC} \equiv \mathrm{AIC}_{\Lambda\mathrm{LTB}} - \mathrm{AIC}_{\Lambda\mathrm{CDM}}$ are qualitatively interpreted using the calibrated Jeffreys' scale.

Results are shown in Tables 5.8 and 5.9 for the flat and curved ΛCDM background, respectively. Under the assumption of a flat background metric, we find a strong evidence, $B_{01} = -12.5$, in favor of the ΛLTB model when the CMB + M_B + low-z SNe data is considered. This is confirmed

[4] Except for $H_0^{\rm L}$ and M_B, but the priors are still separable.

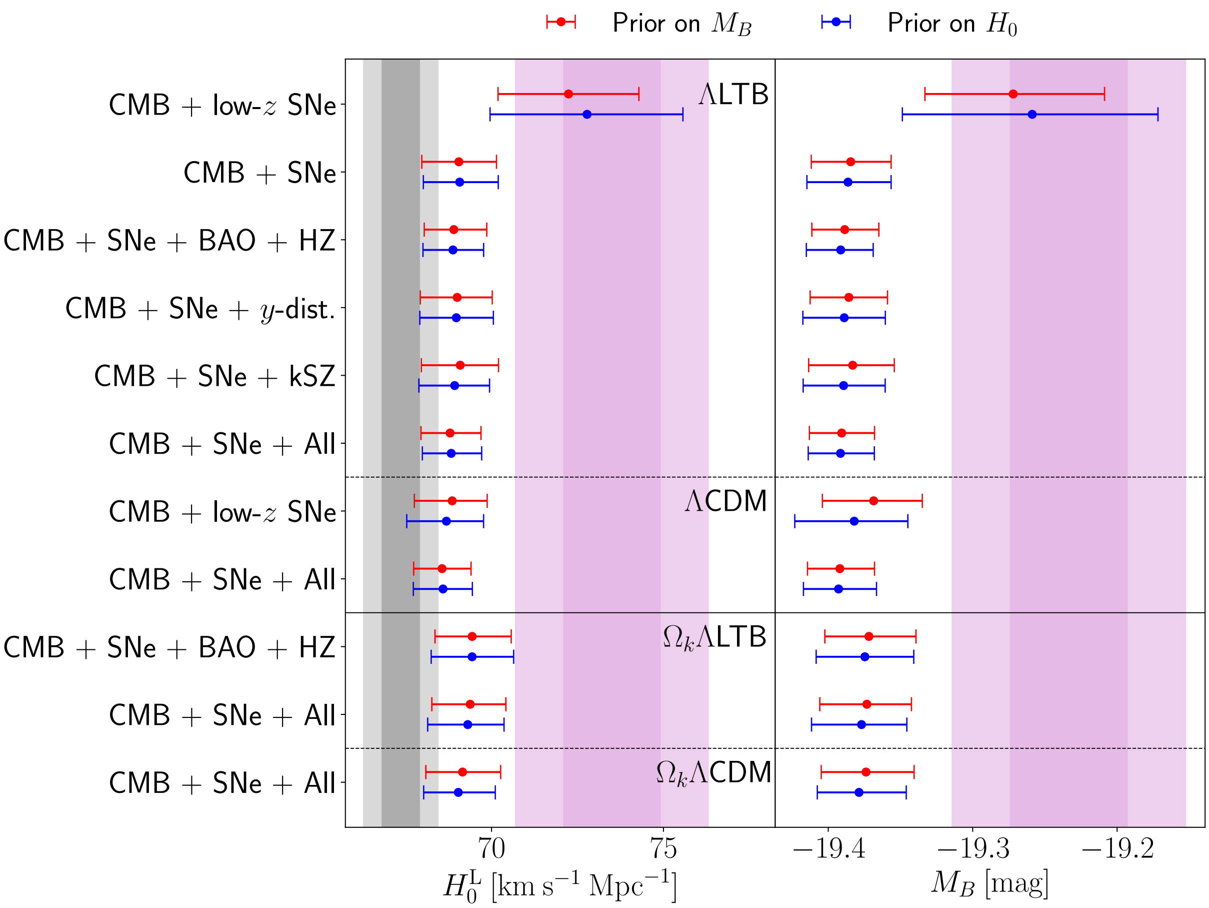

Figure 5.12.: Constraints on H_0^{L} and M_B at 95% confidence level for the cases here considered. The gray area corresponds to the value of the Hubble constant at 68% and 95% confidence level inferred from the CMB observations [233], while the pink areas correspond to the H_0 determination by SH0ES [134] and the corresponding calibration of M_B [H0 Paper I].

Criteria	CMB + M_B + low-z SNe	CMB + H_0 + low-z SNe	CMB + M_B + All	CMB + H_0 + All
$\chi^2_{\Lambda\mathrm{CDM}}$	3014.3	3015.0	3830.0	3825.2
$\Delta\chi^2$	-18.2	-16.7	-1.8	-0.7
ΔAIC	-14.2	-12.7	2.2	3.3
$\ln B_{01}$	-12.5	-17.3	3.0	2.2

Table 5.8.: Results of the model selection analysis for the case of a flat background Universe ($\Delta\chi^2 = \chi^2_{\Lambda\mathrm{LTB}} - \chi^2_{\Lambda\mathrm{CDM}}$).

Criteria	CMB + M_B + All	CMB + H_0 + All
$\chi^2_{\Lambda CDM}$	3828.7	3824.9
$\Delta\chi^2$	0.4	-2.2
ΔAIC	4.4	1.8
$\ln B_{01}$	2.2	2.4

Table 5.9.: Results of the model selection analysis for the case of a curved background Universe ($\Delta\chi^2 = \chi^2_{\Lambda\mathrm{LTB}} - \chi^2_{\Lambda\mathrm{CDM}}$).

by the ΔAIC which shows no support for the ΛCDM model. On the other hand, the inclusion of the full supernova dataset removes the preference for the ΛLTB model. The analysis relative to the combination CMB + M_B + All shows a moderate evidence for the ΛCDM model, $B_{01} = 3.0$, and a substantial support to the same model, $\Delta\mathrm{AIC} = 2.2$. Similar results are obtained by considering a prior on H_0. Finally, as can be seen, from Table 5.9, the introduction of a non-vanishing background curvature does not qualitatively change the results discussed above.

5.4.2.4. Anisotropies

As said earlier, we consider the observer at the center of a spherical structure, a scenario in which observations are perturbed in a spherically symmetric way. As the universe is both radially inhomogeneous and anisotropic, one may argue that an anisotropic perturbation of observations should be considered. To this point, one may consider a more general metric such as the quasi-spherical Szekeres model [280], which features a dipole inhomogeneity instead of a spherical one [281], or simply displace the observer from the origin [108].

Our modeling, however, is justified *a priori* by the fact that we wish to understand if a local underdensity can explain away the Hubble tension. Indeed, this calls for a 9% increase in the local Hubble rate, which means that the observer must be within a deep underdensity of contrast ≈ -0.5, see Eq. (5.34), with subdominant anisotropic corrections. The smaller axis of an underdense ellipsoid grows indeed faster as compared to the longer ones, with the consequence that voids become increasingly spherical as they evolve. If then the observer is misplaced from the center of such a structure, they will develop a peculiar velocity with respect to the CMB of approximately $v = \Delta H \, d_{\mathrm{obs}}$, where $\Delta H \simeq 6$ km/s/Mpc and d_{obs} is the distance from the center [194]. As the observed CMB dipole is $v/c \simeq 1.2 \times 10^{-3}$ [98], this means that $d_{\mathrm{obs}} \lesssim 60$ Mpc, which is small as compared to the size of the inhomogeneity (see Fig. 5.13): in the standard model a source at $z = 0.15$, the maximum redshift considered in the local H_0 determination by SH0ES, is at a distance of ≈ 600 Mpc. We conclude that our modeling is adequate for testing the local-void scenario. On the other hand, it is worth stressing that the local-void scenario fine-tunes the position of the observer by $\approx (60/600)^3 = 1/1000$ chances. In other words, if successful, one trades a one-in-a-million (5σ) inconsistency in data with a one-in-a-thousand fine-tuning.

5.4.2.5. Generalized curvature profile

As discussed in Section 4.3.5.1, the ΛLTB model has three arbitrary functions. We have set two of them, $m(r)$ and $t_{BB}(r)$, using a gauge choice and physical arguments. On the other hand, our particular choice of $k(r)$ is still arbitrary. Here, we study the impact, on the Hubble tension problem, of such an assumption by performing an extra analysis that uses a generalization of Equation (4.28):

$$P_3(x,\alpha) = \begin{cases} 1 & \text{for } 0 \le x < \alpha \\ 1 - \exp\left[\frac{1-\alpha}{x-\alpha}\left(\frac{x-\alpha}{1-\alpha} - 1\right)^3\right] & \text{for } \alpha \le x < 1 \,, \\ 0 & \text{for } 1 \le x \end{cases} \tag{5.38}$$

where $0 < \alpha < 1$ is a new parameter that modifies the smoothness of the transition between the inner and background regions. Sharper profiles are obtained when α approximates unity. Note that our main analysis with Equation (4.28) can be recovered by setting $\alpha = 0$.

Results are shown in Table 5.10, where, for the sake of comparison, we also report the results relative to $\alpha = 0$. The addition of the parameter α leads to an increase in the value of $H_0^{\rm L}$ by 0.64 km s^{-1} Mpc^{-1} as compared with the previous analysis with $\alpha = 0$. This, along with the increment on the error, reduces the Hubble tension to 2.7σ. The tension on M_B decrease to 3.2σ. In other words, we find a small improvement with respect to the analysis, but the ΛLTB cannot fully explain the tension. The assumption of the generalized curvature profile of Equation (5.38) reduces the $\chi^2_{\rm min}$ by 0.3 so that we obtain ΔAIC $= 1.7$ and $B_{01} = 1.9$ in favor of the simplest model with $\alpha = 0$. Namely, weak evidence in favor of the curvature profile given by Equation (4.28) is found.

Parameter	α free	$\alpha = 0$
M_B	$-19.372^{+0.016}_{-0.016}$	$-19.391^{+0.012}_{-0.012}$
$H_0^{\rm M}$	$69.41^{+0.59}_{-0.61}$	$68.77^{+0.40}_{-0.46}$
$H_0^{\rm L}$	$69.42^{+0.58}_{-0.59}$	$68.78^{+0.39}_{-0.44}$
$H_0^{\rm R}$	$69.42^{+0.56}_{-0.58}$	$68.79^{+0.37}_{-0.42}$
$\Delta T[mK]$	$-0.016^{+0.026}_{-0.039}$	$-0.022^{+0.022}_{-0.025}$
Tension H_0	2.7	3.2
Tension M_B	3.2	3.8
$\chi^2_{\rm min}$	3827.9	3828.2

Table 5.10.: 68% confidence level intervals for the relevant parameters. See Section 5.4.2.5 for details.

5.4.2.6. Mapping the local structure of the Universe

While Occam's razor favors the ΛLTB model with $\alpha = 0$, the generalized curvature profile is useful to map the local matter distribution. Figure 5.13 shows the rates of expansion $H_{||}(r,t_0)$ and $H_\perp(r,t_0)$ (right panel), the matter and mass density (top mid panel), and the deviations of $\Omega_{m,0}$ and $\Omega_{k,0}$ from the ΛCDM background (bottom mid panel) as functions of the comoving FLRW coordinate $r^{\rm out}$ for the best fit of the analysis CMB + M_B + All with Equation (5.38) (solid lines). Local fluctuations in the matter density parameters were found by Colgáin et al.

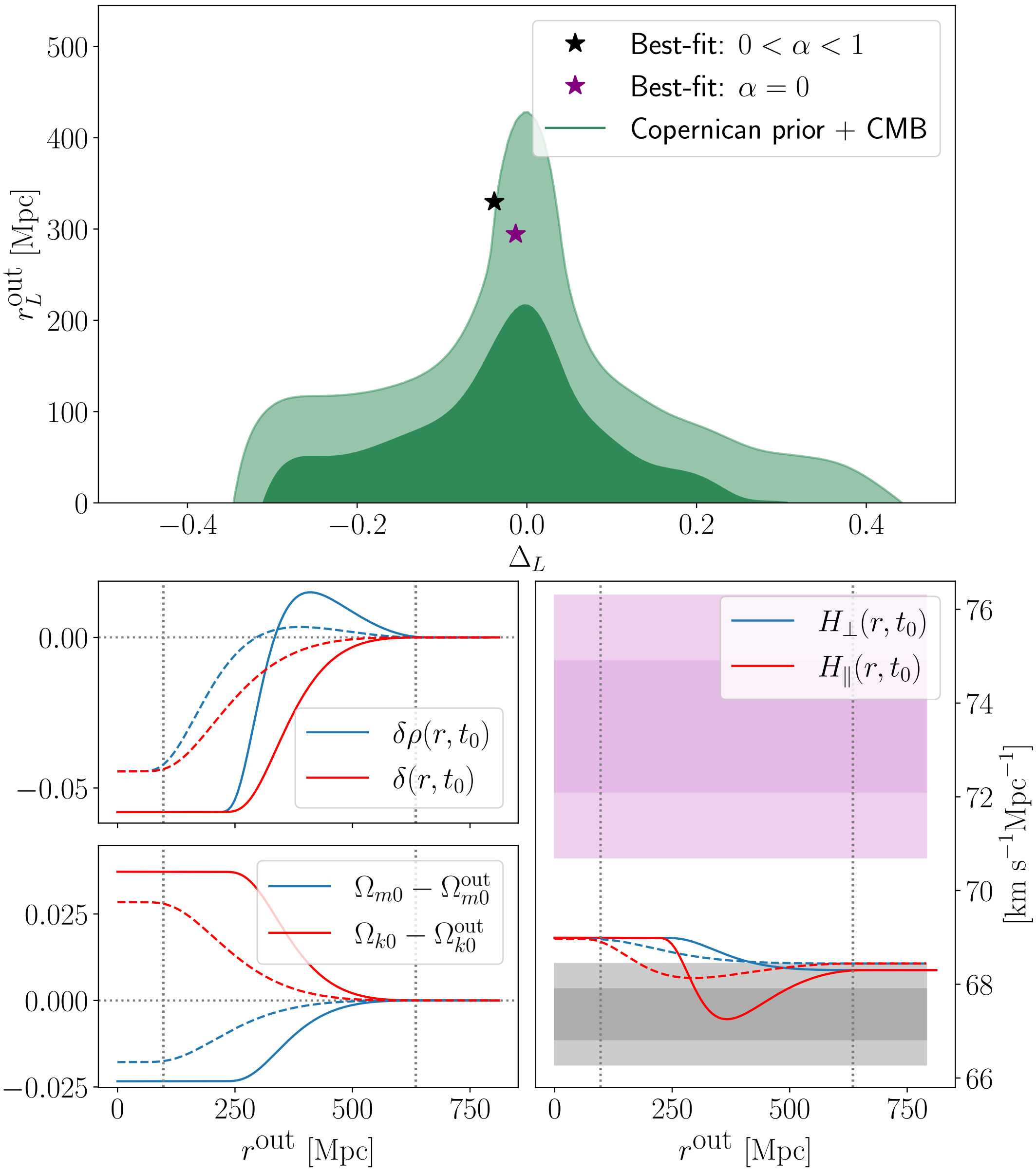

Figure 5.13.: Characterization of our local spacetime from the best fit to all data of the ΛLTB analysis with the generalized profile with $0 < \alpha < 1$ (solid lines) and with $\alpha = 0$ (dashed lines). The panel on the top shows the size $r_L^{\rm out}$ and depth Δ_L of the two best-fit models as compared with the standard model expectation, which is quantified via the Copernican prior convolved with the CMB likelihood [see CP Paper I]. The panels in the left bottom show the matter and mass density contrasts (top) and the deviations of $\Omega_{m,0}$ and $\Omega_{k,0}$ from the ΛCDM background (bottom) as functions of the comoving FLRW coordinate $r^{\rm out}$. The dotted vertical lines mark the redshift range $0.023 < z < 0.15$ that is used to determine H_0. The panel on the right bottom shows the rates of expansion $H_\parallel(r, t_0)$ and $H_\perp(r, t_0)$ a function of $r^{\rm out}$. The purple and gray areas correspond to constraints at 68% and 95% confidence level of the Hubble constant as determined by the SH0ES [134] and Planck collaboration [233], respectively. See Section 5.4.2.6 for details.

[282] when analyzing supernova data. We also display the same quantities considering the best fit of our main analysis with $\alpha = 0$ (dashed lines). The best-fit values are

$$\{\alpha, \Delta_L, r_L^{\rm out}, \Omega_{m,0}^{\rm out}, H_0^{\rm out}\}=\{0.28, -0.038, 330, 0.304, 68.3\} \tag{5.39}$$

for the case of the generalized profile of Equation (5.38), and

$$\{\Delta_L, r_L^{\rm out}, \Omega_{m,0}^{\rm out}, H_0^{\rm out}\} = \{-0.013, 294, 0.302, 68.4\} \tag{5.40}$$

for the case with $\alpha = 0$.

The left panel of Figure 5.13 shows size $r_L^{\rm out}$ and depth Δ_L of the two best-fit models as compared with the standard model expectation, which is quantified via the Copernican prior convolved with the CMB likelihood [CP Paper I]. We can see that the data prefers a shallow void with $\Delta_L \approx -0.04$ and $r_L^{\rm out} \approx 300$ Mpc, which, interestingly, lies on the border of the 95% credible region relative to the standard model expectation.

Even though the analysis including α allows us to map the local distribution of matter in a more general way, the local structure of the Universe could be restricted using a yet more general profile, such as an n-node spline function [226] or a data-driven technique, possibly including anisotropic degrees of freedom. Indeed, while our modeling is adequate to test if a local underdensity can explain away the Hubble tension, it may be important to consider anisotropies when modeling a shallow structure such as the one depicted in Figure 5.13. This is also suggested by recent maps of our cosmological neighborhood [283]. We leave this problem to the future.

5.4.3. Final considerations

In CP Paper II, we pursued a program to test one of the fundamental assumptions of modern cosmology: the Copernican principle. In particular, we modeled the spacetime around us without any prior on the parameters that describe the inhomogeneity, but rather let observations constrain the local structure. Our analysis showed that current cosmological data can tightly constrain radial deviations from the FLRW metric at almost the cosmic variance level. We also showed that typical constraints on the ΛCDM parameters are not weakened if one drops the Copernican hypothesis. Here, we aimed to quantify the impact of the Copernican principle on the Hubble problem: can a non-Copernican structure explain away the Hubble tension?

In order to robustly answer this question, we put care into how to compute the Hubble constant in an inhomogeneous universe, which we parametrize via the ΛLTB model—basically a radial perturbation of an FLRW metric. We adopted three different definitions, which all give basically similar results. Then, in order to quantitatively conclude if the extra geometrical degrees of freedom of the ΛLTB model is favored by the data, we carried out Bayesian model selection via both the Bayes factor and the Akaike information criterion. Finally, we considered both a flat and a curved background FLRW model. Our results show that the ΛLTB model can successfully explain away the H_0 tension and is favored with respect to the ΛCDM model only if one solely considers supernovae in the redshift range that is used to fit the Hubble constant, that is, $0.023 < z < 0.15$. If one considers all the SNe sample then the H_0 tension is not solved and the support for the ΛLTB model vanishes. We have also carried out an analysis that adopts a more general curvature profile. We have found that the inclusion of a new parameter, that sharpens or smooths the transition between the inner inhomogeneity and the background model, does not provide a solution to the Hubble constant problem, only slightly increasing the local expansion rate. Our results are in good agreement with previous studies and improve upon them by considering a more thorough statistical analysis and a more comprehensive set of observations.

Finally, we have used the generalized curvature profile to reconstruct our local spacetime. We have found that the best fit to current cosmological data corresponds to a shallow void with $\Delta_L \approx -0.04$ and $r_L^{\rm out} \approx 300$ Mpc, which, interestingly, lies on the border of the 95% credible region relative to the standard model expectation. A more generic reconstruction of the local matter distribution of the Universe could be achieved using data-driven methods. We leave the study of this topic for future research.

5.5. Future prospects: the beyond homogeneity and isotropy project

In this chapter, we have studied the role of cosmological observations in the issue of testing the Copernican principle. Further, as mentioned earlier, the analyses presented here do correspond to nothing more than the first steps to the development of inhomogeneous precision cosmology. This is particularly noticeable if one notice that, on top of the already mentioned drawbacks of our analysis, our description of the ΛLTB model, as well as the usage of cosmological observation, is limited to the background dynamics. Given that, currently, there is not a satisfactory understanding of the evolution of the large-scale structure on an inhomogeneous background, our analyses do not use perturbation level observables such as redshift space distortions or weak lensing. Subsequently, a better understanding of the evolution of the large-scale structure is a necessary step to place the foundations of the standard paradigm of modern cosmology on more solid grounds.

As a first step, to a better understanding of the evolution of the large-scale structure on an inhomogeneous background, we presented in BEHOMO Paper I the first suite of simulations for the simplest possible early-FLRW cosmologies, i.e., the ΛLTB model. The BEHOMO Paper I paper not only describes the numerical implementation used to produce ΛLTB simulations but also carefully shows that our approach does accurately describe the semi-analytical solutions provided by the `vd2020` code, see Figure 5.14. Within our future prospects, we plan to use the data products presented in BEHOMO Paper I to study the growth of perturbations at the linear and nonlinear level, gravitational lensing, cluster abundances and proprieties, and many other applications which we invite the scientific community to propose. Finally, we would like to stress that the aims of the BEHOMO project are aligned with the objectives of this thesis — both pursue the same grand goal: set up a suitable theoretical and empirical program to push the boundaries of modern cosmology by studying beyond the assumption of large-scale homogeneity and isotropy.

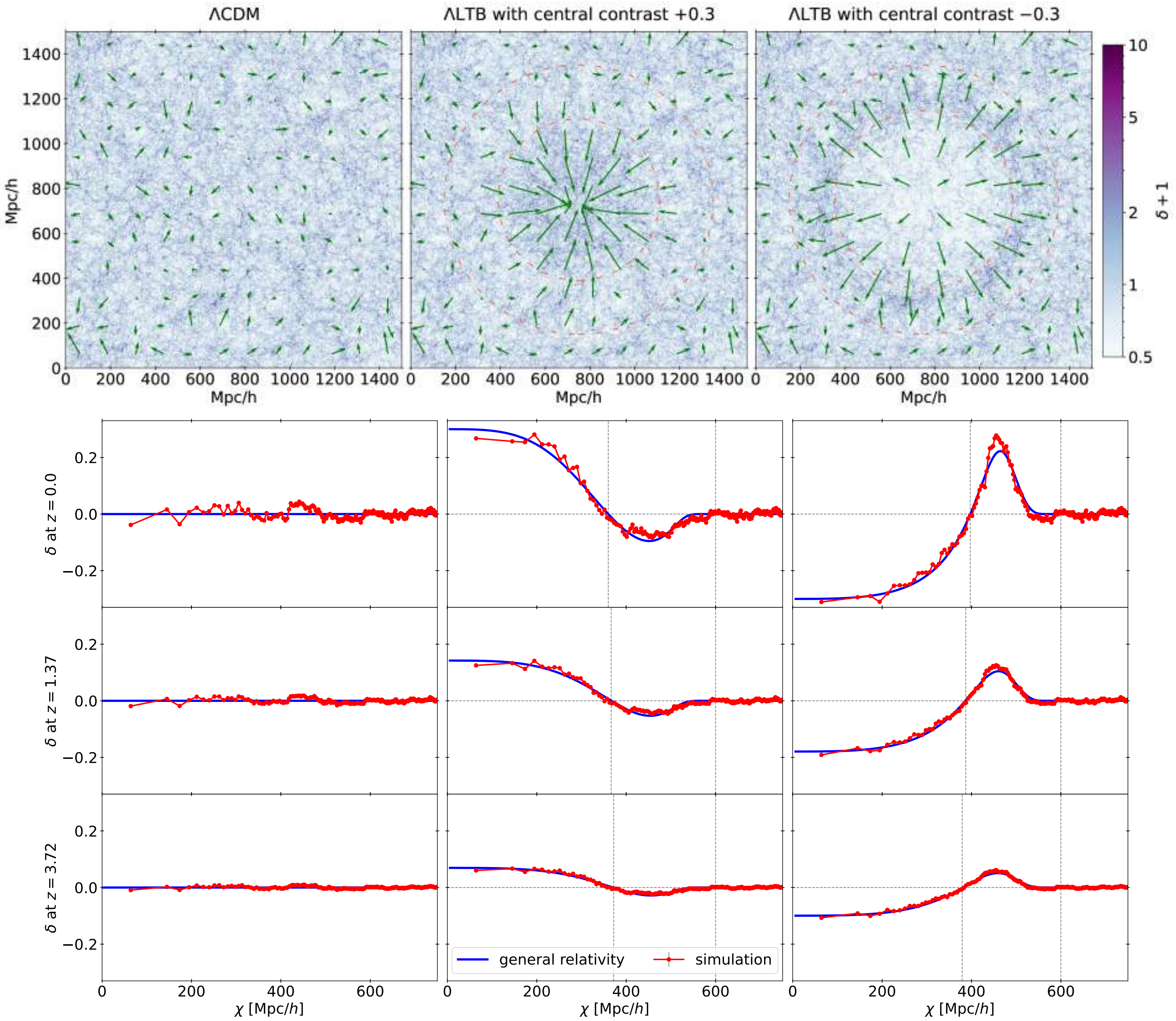

Figure 5.14.: The first row shows the large-scale structure of Box 3 of BEHOMO Paper I at $z = 0$ of the overdense (middle panel) and underdense (right panel) ΛLTB models together with the corresponding ΛCDM model (left panel). The larger thin dashed circle marks the boundary r_B of the ΛLTB inhomogeneity and the smaller one the compensating scale r_L at which $\delta(t_0, r_L) = 0$. The arrows show the velocity field. One can see how the large-scale structure is identical outside the inhomogeneity, but it is distorted by the inhomogeneous bulk flow inside the LTB spherically inhomogeneity. The last three rows show the evolution of the density contrast, from $z = 3.7$ to $z = 0$ as obtained from the simulation and the general relativistic solution obtained as described in Section 4.3.5.2. The larger vertical line marks r_B and the smaller r_L.

Conclusions

The standard paradigm of modern cosmology relies on a series of fundamental assumptions that simplify our understanding of the Universe. Thanks to these simplifications, which contribute to building a suitable empirical and theoretical framework for the study of the cosmos, cosmologists have made a splendid advance in the understanding of our Universe. By analyzing cosmological data, we have been able not only to constrain cosmological parameters with unprecedented precision but also to discriminate between several cosmological models. However, the presence of not-yet resolved theoretical problems and the existence of cosmological tensions could be a hint for physics beyond the standard paradigm; or a breakdown of the fundamental assumptions of the standard paradigm of modern cosmology.

In this context, a crucial step toward improving our understanding of the Universe and firmly establishing the foundations of the standard cosmological paradigm is to relax the fundamental assumptions of modern cosmology. The cosmological community has already begun its journey to promoting and studying physics beyond the standard paradigm and its central hypotheses. Noticeable is the effort made to extend the boundaries of modern cosmology by using a theory of gravity beyond GR and also using dark energy models different from a cosmological constant. Despite this, and the fact that cosmologists have also explored other directions in terms of the extension of the standard paradigm, the hypotheses that establish the symmetry of the Universe have, on the other hand, been less explored. We refer to the Cosmological principle, and more important for our discussion, the Copernican principle. Although we lack observational confirmation that the Copernican principle holds on cosmological scales, cosmologists seem to have settled on the hypothesis that we do not occupy a special place in the Universe and, consequently, we are merely typical observers.

The results of this thesis constitute but the first steps toward a well-established analysis and interpretation of cosmological and astrophysical data within the groundwork of non-Copernican cosmologies. First, by using the latest cosmological data, we have tested the Copernican principle by placing constraints on a spherically inhomogeneous generalization of the standard cosmological model, the ΛLTB model. Later, using a similar approach, we focused on the study of the capability that forthcoming surveys, such as SH0ES, Euclid, DESI, and LSST, will have to test the Copernican principle. Finally, we address the question if the Hubble discrepancy could be explained away by a local inhomogeneity.

Regarding our test of the Copernican principle, we found that, under the assumption of the ΛLTB model, data can tightly constrain radial inhomogeneity around us. Our results also show that since the typical constraints on the standard ΛCDM parameters are not weakened after marginalizing over the local inhomogeneity parameters, relaxing the Copernican hypothesis does not necessarily imply significantly worse constraints on the background parameters. The results of this analysis positively demonstrate that the non-Copernican cosmologies can be used to meaningfully analyzed future and present data.

Additionally, our forecast analysis demonstrates that future surveys will improve the current constraints on the Copernican principle by up to 40%. This improvement will be remarkable at scales $r_B \geq 190$ Mpc, where the inclusion of future data will reduce the constrained area of the space parameters to a factor of < 2 as compared with the area allowed by the Copernican prior. Furthermore, we found that the usage of the data provided by next-generation surveys we will allow us to detect inhomogeneous deviations of the FLRW metric, including Gpc-scale inhomogeneities of contrast -0.1. Finally, our forecast analysis also reveals that given the precision of future surveys a detection of this kind would allow us to rule out the FLRW space-time ($\delta_0 = 0$ and $z_B = 0$) by $\gtrsim 3\sigma$.

On the other hand, to robustly answer the question of whether or not a local void could explain the Hubble discrepancy, we carefully compute the Hubble constant in an inhomogeneous ΛLTB universe. Our results show that the ΛLTB model can successfully explain away the H_0 tension and is favored with respect to the ΛCDM model only if one solely considers the SNe in the Hubble flow used to fit the Hubble constant, that is, $0.023 < z < 0.15$. In contrast, if the whole set of SNe is considered then the H_0 tension is not solved by the ΛLTB model, and the support for the same vanishes. In addition, our analysis using a generalized curvature profile shows that the inclusion of a new parameter, that sharpens or smooths the transition between the inner inhomogeneity and the background model, does not provide a solution to the Hubble constant problem, only slightly increasing the local expansion rate. The same analysis also allows us to reconstruct our local spacetime. We have found that the best fit to current cosmological data corresponds to a shallow void with $\delta_L \approx -0.04$ and $r_L^{\text{out}} \approx 300$ Mpc, which, interestingly, lies on the border of the 95% credible region relative to the standard model expectation.

The results presented in this thesis are nothing but the first steps toward a robust and precise implementation of cosmology beyond the assumption of the Copernican principle. One can consider several routes to take the following steps toward broadening the boundaries of modern cosmology. For instance, in analogy to the matter field, inhomogeneous degrees of freedom could be considered in the radiation component of the Universe. This would not only allows us to generalize the ΛCDM framework, but also assess the effects of an inhomogeneous recombination on the Lithium problem. On the other hand, the arbitrariness introduced by the particular choice of a curvature profile could be overcome by using parametric or data-driven methods in the implementation of the model. This kind of analysis would useful to obtain a more generic reconstruction of the local matter distribution of the Universe and, eventually, could be applied to try to reconstruct the metric of the Universe from data. In addition, another generalization of the analysis presented here could be attained by considering an off-center observer. The introduction of anisotrpic degrees of freedom could be used to study the cosmic dipoles and possible detect a violation to the standard framework of modern cosmology. Last but not least, pursuing the development of perturbations theory in the inhomogeneous background is a crucial step toward a better understanding of physics beyond the Copernican principle. The understanding of the growth of matter perturbations in an inhomogeneous background would be helpful not only to provide a theoretical framework need to use future data, e.g., Euclid weak lensing, but also achieve a fully consistent treatment of observables as the kSZ effect and the y-Compton distortion effect.

The Cepheid calibration: demarginalization technique

From a Bayesian point of view, the SH0ES implementation of the cosmic distance ladder can be effectively summarized by the posterior

$$f(H_0, M_B|\text{SNe}) = \frac{f(H_0)f(M_B)\mathcal{L}(\text{SNe}|H_0, q_0, M_B)}{\mathcal{E}}\,, \tag{A.1}$$

$$f(H_0|\text{SNe}) = \int \mathrm{d}M_B\, f(H_0, M_B|\text{SNe})\,, \tag{A.2}$$

where the last line, posterior on H_0, was obtained by marginalizing over M_B. In the equations above, $f(H_0)$ is an improper flat prior on H_0, $\mathcal{L}$ is the likelihood, $\mathcal{E}$ is the evidence, and SNe represents the standard candles in the range $0.023 \leq z \leq 0.15$. Further, $f(M_B)$ is the informative prior on the absolute magnitude of SNe and is the result of the complicated calibration of the local supernovae via the cosmic distance ladder [see 284, for instance].

The likelihood is given by:

$$\mathcal{L}(\text{SNe}|H_0, q_0, M_B) = |2\pi\Sigma|^{-1/2} e^{-\frac{1}{2}\chi^2(H_0,q_0,M_B)}\,, \tag{A.3}$$

where the χ^2 function is

$$\chi^2 = \{m_{B,i} - m_B^t(z_i)\}\Sigma_{ij}^{-1}\{m_{B,j} - m_B^t(z_j)\}\,, \tag{A.4}$$

Σ is the supernova covariance matrix, $m_{B,i}$ are the observed apparent magnitudes at the redshifts z_i, and m_B^t is the theoretical prediction according to Equation (3.6). Following the methodology of [284], we fix the nuisance parameters that control stretch and color corrections to $\alpha = 0.14$, $\beta = 3.1$, correct the apparent supernova magnitudes with hosts above and below $\log M_{\text{stellar}} \sim 10$ by 0.03 mag fainter and brighter, respectively, and include an intrinsic dispersion of $\sigma_{\text{int}} = 0.1$ mag together with a peculiar velocity error of 250 km/s.

Here, in order to get the calibration prior $f(M_B)$ we solve the integral equation obtained by demanding that Equation (A.2) gives the constraint $H_0 = 73.5 \pm 1.4$ km s^{-1} Mpc^{-1}, the result of the analysis using $q_0 = -0.55$ and $j_0 = 1$ [134]. Assuming a Gaussian distribution for M_B with mean $\bar{M}_B$ and dispersion σ_M – which is also justified *a posteriori* by the fact that M_B is tightly constrained by data – it is possible to marginalize analytically the 2D posterior in Equation (A.2). The result is that H_0 is distributed according to a lognormal distribution with parameters:

$$\mu_{ln}^{dm} = \frac{\ln 10}{5}\left[\bar{M}_B + \frac{\ln 10}{5}\left(\sigma_M^2 + \frac{1}{S_0}\right) - \frac{S_1}{S_0}\right]\,, \tag{A.5}$$

$$\sigma_{ln}^{dm} = \frac{\ln 10}{5}\sqrt{\sigma_M^2 + \frac{1}{S_0}}\,. \tag{A.6}$$

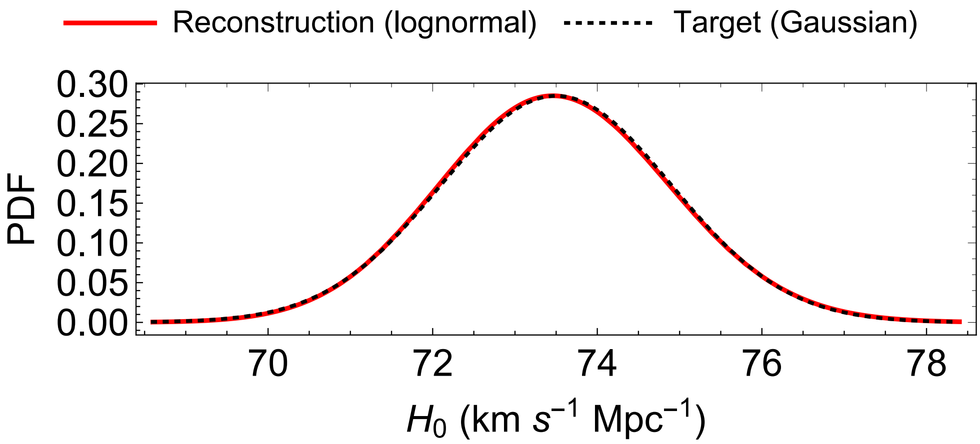

Figure A.1.: Reconstruction of the determination by Reid et al. [134], i.e., $H_0 = 73.5 \pm 1.4\,\mathrm{kms^{-1}Mpc^{-1}}$, using the calibration prior of Equation (A.11). Also shown is a Gaussian with same mean and dispersion. It is evident that the deviation from Gaussianity is negligible.

One can then match first and second moments of the lognormal distribution with $H_0 = 73.5 \pm 1.4\,\mathrm{kms^{-1}Mpc^{-1}}$ so that one has:

$$\mu_{ln}^{Re19} \simeq 4.2971\,, \qquad \sigma_{ln}^{Re19} \simeq 0.019046\,, \tag{A.7}$$

where we used equations the definition of the mean and variance of the lognormal distribution. The calibration prior is then given by:

$$M_B^{dm} = \frac{5}{\ln 10}\mu_{ln}^{Re19} + \frac{S_1}{S_0} - \frac{\ln 10}{5}\left(\sigma_M^2 + \frac{1}{S_0}\right)\,, \tag{A.8}$$

$$\sigma^2_{M_B^{dm}} = \frac{25}{\ln^2 10}\sigma_{ln}^{2\,Re19} - \frac{1}{S_0}\,, \tag{A.9}$$

where the S_0 and S_1 quantities are defined as

$$\begin{aligned} W_i &= m_{B,i} - \tilde{m}_B^t(z_i)\,, \\ V_i &= 1\,, \\ S_0 &= V \cdot \Sigma^{-1} \cdot V^T\,, \\ S_1 &= W \cdot \Sigma^{-1} \cdot V^T\,. \end{aligned} \tag{A.10}$$

with $\tilde{m}_B^t(z_i) \equiv m_B^t - M_B + 5\log_{10} H_0$. Using the previous equations one obtains the calibration prior $f(M_B)$:

$$M_B^{dm} = -19.2334 \pm 0.0404\,\mathrm{mag}\,. \tag{A.11}$$

The reconstructed lognormal distribution on H_0 is very close to a Gaussian as shown in Figure A.1, where the lognormal $f(H_0|\mathrm{SNe})$ is compared with a Gaussian, both with mean and dispersion as given by Reid et al. [134], i.e., $H_0 = 73.5 \pm 1.4$ km s^{-1} Mpc^{-1}.

Impact of large scales inhomo

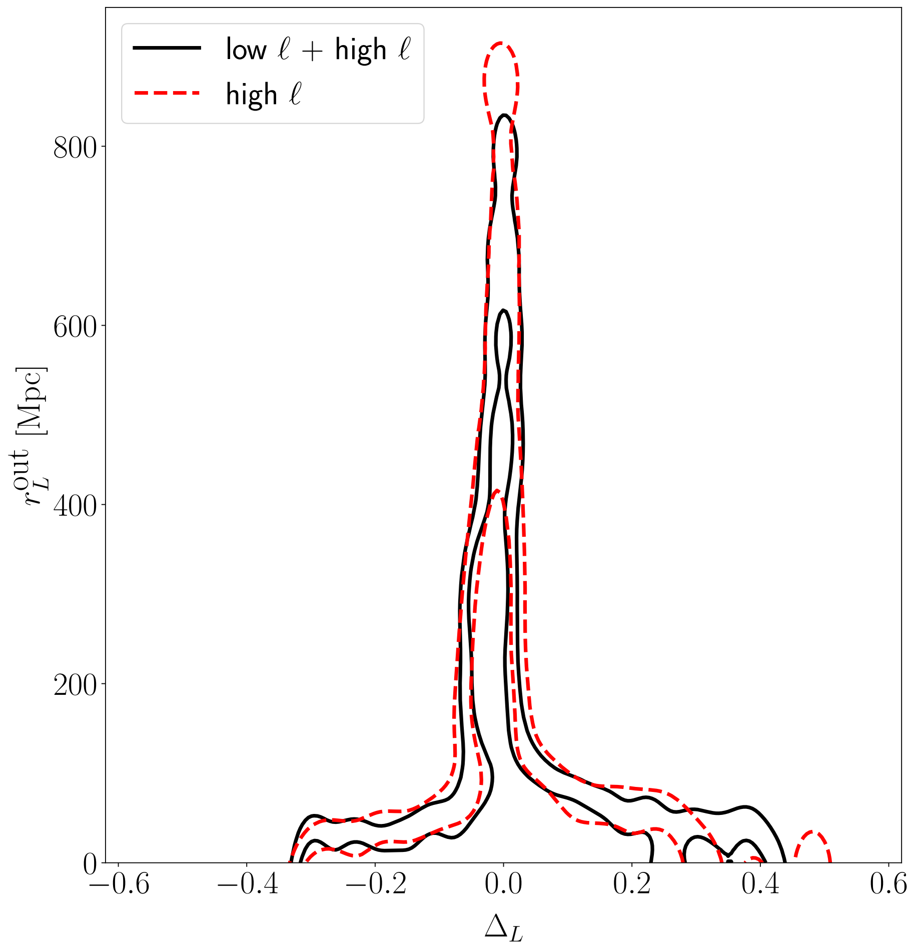

Figure B.1.: Marginalized constraints on the effective density contrast, Δ_L, and the compensating scale, $r_L^{\rm out}$, with/out low-ℓ Planck data. It is straightforward to note that the inclusion of low-ℓ data has a negligible impact on the constraints of the ΛLTB parameters.

As discussed in Section 5.2.1, our analyses rely on the assumption that the ΛLTB model does not change the late-time ISW effect compared to the ΛCDM model. Here, in order to test such an assumption and also assess the impact of the low-ℓ data in our main results, we constrain the

ΛLTB model without assuming low-ℓ Planck data. Figures B.1 and B.2 compare the constraints when using both high- and low-ℓ Planck data with the more conservative case of only including high-ℓ Planck data. We see that the impact on the parameters of the inhomogeneity is minor, see Figure B.1, while the impact on the ΛCDM parameters is, as expected, strong, see Figure B.2. In other words, in the present analysis, the low-ℓ Planck data are effective only for the ΛCDM parameters. A more complete treatment requires the challenging computation of perturbations in an inhomogeneous background.

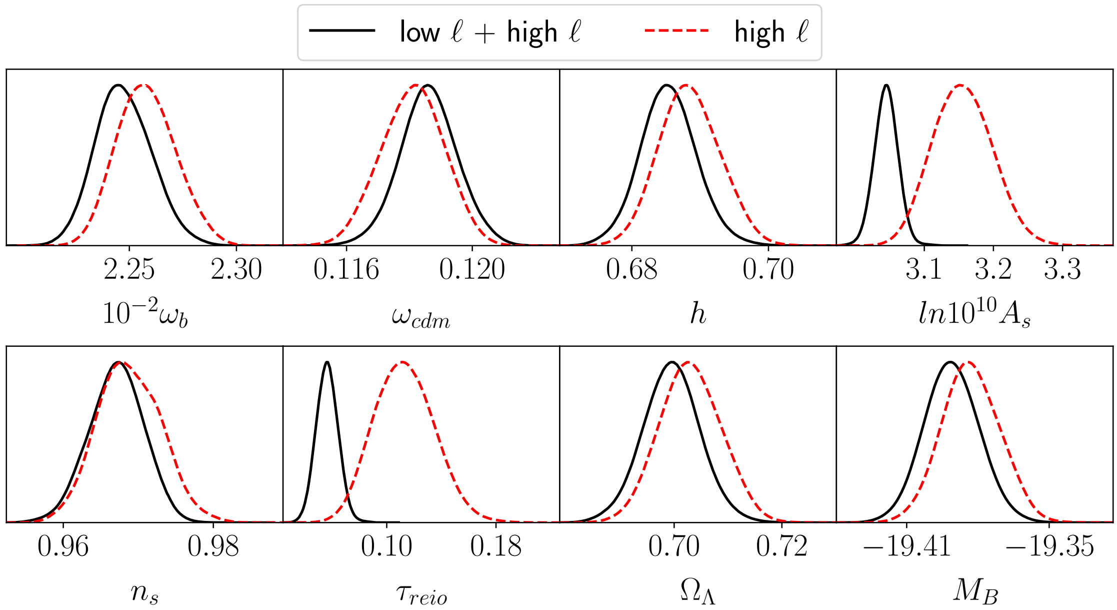

Figure B.2.: Marginalized constraints on the background parameters of the ΛCDM model with/out low-ℓ Planck data. As expected, disregarding low-ℓ data largely impact the ΛCDM-six parameters constraints, mainly, in those related to the early time physics.

Re-scaling data sets

Covariance matrices are fundamental pieces of forecast analyses. However, their production for forthcoming surveys is an open issue when non-standard cosmologies are considered

Consider a given dataset, with x_i being the observed quantity, z_i the corresponding redshift, and C_{ij} the covariance matrix. This dataset can be re-scaled to agree with a particular model via the following steps:

1. We define $R_{ij} = C_{ij}/x_i x_j$, a new matrix that contains the relative uncertainties and correlations from the original covariance matrix.

2. We compute with the theoretical prediction of the new model the fiducial values at the relevant redshifts, such that $x_i^{\rm f} \equiv x^{\rm fid}(z_i)$.

3. Using the above defined quantities, we compute the new correlation matrix as $\tilde{C}_{ij} = x_i^{\rm f} x_j^{\rm f}\, R_{ij}$.

4. We then draw a random realization, $\tilde{x}_i$, of the multivariate-normal distribution $\mathcal{N}(x_i^{\rm f}, \tilde{C}_{ij})$.

Note that this method assumes that relative error and correlations are not changed by a non-standard model. As discussed in this paper, the procedure above is also applied to re-scale real data according to the fiducial models presented on Table 5.3; this ensures that all data are consistently described by a particular fiducial model.

Bibliography

[1] David Camarena, Valerio Marra, Ziad Sakr, and Chris Clarkson. The Copernican principle in light of the latest cosmological data. *Mon. Not. Roy. Astron. Soc.*, 509:1291–1302, 2022. doi: 10.1093/mnras/stab3077. Cited on pages vi, 59, 65, 66, 76, 80, 81, 84, 85, 90, 95, and 96.

[2] David Camarena, Valerio Marra, Ziad Sakr, and Chris Clarkson. A void in the Hubble tension? The end of the line for the Hubble bubble. 5 2022. Cited on pages vi, 32, 59, 76, 84, 85, and 96.

[3] D. Camarena et al. Euclid: Testing the Copernican principle with next-generation surveys. *In preparation*, 2022. Cited on pages vi, 59, 73, and 74.

[4] V. Marra, T. Castro, D. Camarena, S. Borgani, and A. Ragagnin. The BEHOMO project: ΛLTB N-body simulations. 3 2022. Cited on pages vi, 47, 49, 84, 97, and 98.

[5] David Camarena and Valerio Marra. Local determination of the Hubble constant and the deceleration parameter. *Phys. Rev. Res.*, 2(1):013028, 2020. doi: 10.1103/PhysRevResearch.2.013028. Cited on pages vi, vii, 25, 31, 32, 34, 66, 90, and 92.

[6] David Camarena and Valerio Marra. A new method to build the (inverse) distance ladder. *Mon. Not. Roy. Astron. Soc.*, 495(3):2630–2644, 2020. doi: 10.1093/mnras/staa770. Cited on pages vi, vii, 32, 33, 34, 35, and 37.

[7] David Camarena and Valerio Marra. On the use of the local prior on the absolute magnitude of Type Ia supernovae in cosmological inference. *Mon. Not. Roy. Astron. Soc.*, 504:5164–5171, 2021. doi: 10.1093/mnras/stab1200. Cited on pages vi, vii, 27, 35, 36, 37, 38, 62, and 90.

[8] George Alestas, David Camarena, Eleonora Di Valentino, Lavrentios Kazantzidis, Valerio Marra, Savvas Nesseris, and Leandros Perivolaropoulos. Late-transition versus smooth H(z)-deformation models for the resolution of the Hubble crisis. *Phys. Rev. D*, 105(6): 063538, 2022. doi: 10.1103/PhysRevD.105.063538. Cited on pages vi, vii, 27, and 38.

[9] Eleonora Di Valentino et al. Snowmass2021 - Letter of interest cosmology intertwined I: Perspectives for the next decade. *Astropart. Phys.*, 131:102606, 2021. doi: 10.1016/j.astropartphys.2021.102606. Cited on page vii.

[10] Eleonora Di Valentino et al. Snowmass2021 - Letter of interest cosmology intertwined II: The hubble constant tension. *Astropart. Phys.*, 131:102605, 2021. doi: 10.1016/j.astropartphys.2021.102605. Cited on page vii.

[11] Eleonora Di Valentino et al. Cosmology intertwined III: $f\sigma_8$ and S_8. *Astropart. Phys.*, 131: 102604, 2021. doi: 10.1016/j.astropartphys.2021.102604. Cited on page vii.

[12] Eleonora Di Valentino et al. Snowmass2021 - Letter of interest cosmology intertwined IV: The age of the universe and its curvature. *Astropart. Phys.*, 131:102607, 2021. doi: 10.1016/j.astropartphys.2021.102607. Cited on page vii.

[13] Elcio Abdalla et al. Cosmology intertwined: A review of the particle physics, astrophysics, and cosmology associated with the cosmological tensions and anomalies. *JHEAp*, 34:49–211, 2022. doi: 10.1016/j.jheap.2022.04.002. Cited on pages vii, viii, 19, and 23.

[14] S. Nesseris et al. Euclid: Forecast constraints on consistency tests of the ΛCDM model. art. arXiv:2110.11421, October 2021. Cited on pages vii, viii, and 73.

[15] G.F.R. Ellis, R. Maartens, and M.A.H. MacCallum. *Relativistic Cosmology*. Cambridge University Press, 2012. ISBN 9781139642958. URL https://books.google.com.pe/books?id=IgkhAwAAQBAJ. Cited on page 1.

[16] N. Aghanim et al. Planck 2018 results. VI. Cosmological parameters. *Astron. Astrophys.*, 641:A6, 2020. doi: 10.1051/0004-6361/201833910. [Erratum: Astron.Astrophys. 652, C4 (2021)]. Cited on pages 1, 20, 23, 26, and 77.

[17] Adam G. Riess et al. A Comprehensive Measurement of the Local Value of the Hubble Constant with 1 km/s/Mpc Uncertainty from the Hubble Space Telescope and the SH0ES Team. 12 2021. Cited on pages 1, 23, 27, 28, and 32.

[18] G. Lemaître. Un Univers homogène de masse constante et de rayon croissant rendant compte de la vitesse radiale des nébuleuses extra-galactiques. *Annales de la Société Scientifique de Bruxelles*, 47:49–59, 1927. Cited on page 4.

[19] Edwin Hubble. A relation between distance and radial velocity among extra-galactic nebulae. *Proc. Nat. Acad. Sci.*, 15:168–173, 1929. doi: 10.1073/pnas.15.3.168. Cited on page 4.

[20] R. A. Alpher, H. Bethe, and G. Gamow. The origin of chemical elements. *Phys. Rev.*, 73: 803–804, 1948. doi: 10.1103/PhysRev.73.803. Cited on page 4.

[21] Arno A. Penzias and Robert Woodrow Wilson. A Measurement of excess antenna temperature at 4080-Mc/s. *Astrophys. J.*, 142:419–421, 1965. doi: 10.1086/148307. Cited on page 4.

[22] George F. Smoot. COBE observations and results. *AIP Conf. Proc.*, 476(1):1–10, 1999. doi: 10.1063/1.59326. Cited on page 4.

[23] C. L. Bennett, D. Larson, J. L. Weiland, N. Jarosik, G. Hinshaw, N. Odegard, K. M. Smith, R. S. Hill, B. Gold, M. Halpern, E. Komatsu, M. R. Nolta, L. Page, D. N. Spergel, E. Wollack, J. Dunkley, A. Kogut, M. Limon, S. S. Meyer, G. S. Tucker, and E. L. Wright. Nine-year Wilkinson Microwave Anisotropy Probe (WMAP) Observations: Final Maps and Results. *Astrophys. J.*, 208(2):20, October 2013. doi: 10.1088/0067-0049/208/2/20. Cited on page 5.

[24] P. A. R. Ade et al. Planck Early Results. I. The Planck mission. *Astron. Astrophys.*, 536: A1, 2011. doi: 10.1051/0004-6361/201116464. Cited on page 5.

[25] P. A. R. Ade et al. Planck 2013 results. XXIII. Isotropy and statistics of the CMB. *Astron. Astrophys.*, 571:A23, 2014. doi: 10.1051/0004-6361/201321534. Cited on pages 5 and 20.

[26] Y. Akrami et al. Planck 2018 results. VII. Isotropy and Statistics of the CMB. *Astron. Astrophys.*, 641:A7, 2020. doi: 10.1051/0004-6361/201935201. Cited on pages 5 and 20.

[27] P. A. Zyla et al. Review of Particle Physics. *PTEP*, 2020(8):083C01, 2020. doi: 10.1093/ptep/ptaa104. Cited on pages 6 and 19.

[28] Adam G. Riess et al. Observational evidence from supernovae for an accelerating universe and a cosmological constant. *Astron. J.*, 116:1009–1038, 1998. doi: 10.1086/300499. Cited on page 5.

[29] S. Perlmutter et al. Measurements of Omega and Lambda from 42 high redshift supernovae. *Astrophys. J.*, 517:565–586, 1999. doi: 10.1086/307221. Cited on page 5.

[30] David H. Weinberg, Michael J. Mortonson, Daniel J. Eisenstein, Christopher Hirata, Adam G. Riess, and Eduardo Rozo. Observational Probes of Cosmic Acceleration. *Phys. Rept.*, 530:87–255, 2013. doi: 10.1016/j.physrep.2013.05.001. Cited on page 7.

[31] P.P. Coles and P.F. Lucchin. *Cosmology: The Origin and Evolution of Cosmic Structure*. Wiley, 2003. ISBN 9780470852996. URL `https://books.google.com.cu/books?id=BGYcivB1EtMC`. Cited on pages 8 and 18.

[32] H. Bondi and I.W. Roxburgh. *Cosmology*. Dover books on physics. Dover Publications, 2010. ISBN 9780486474830. URL `https://books.google.com.pe/books?id=VrLTOjPJLNIC`. Cited on page 8.

[33] S. Weinberg. *Gravitation and cosmology: principles and applications of the general theory of relativity*. Wiley, 1972. ISBN 9780471925675. URL `https://books.google.com.br/books?id=XLbvAAAAMAAJ`. Cited on page 8.

[34] Morag Scrimgeour et al. The WiggleZ Dark Energy Survey: the transition to large-scale cosmic homogeneity. *Mon. Not. Roy. Astron. Soc.*, 425:116–134, 2012. doi: 10.1111/j.1365-2966.2012.21402.x. Cited on page 9.

[35] Pierre Laurent et al. A 14 h^{-3} Gpc^3 study of cosmic homogeneity using BOSS DR12 quasar sample. *JCAP*, 11:060, 2016. doi: 10.1088/1475-7516/2016/11/060. Cited on page 9.

[36] Pierros Ntelis et al. Exploring cosmic homogeneity with the BOSS DR12 galaxy sample. *JCAP*, 06:019, 2017. doi: 10.1088/1475-7516/2017/06/019. Cited on page 9.

[37] J. Ehlers, P. Geren, and R. K. Sachs. Isotropic solutions of the Einstein-Liouville equations. *J. Math. Phys.*, 9:1344–1349, 1968. doi: 10.1063/1.1664720. Cited on page 9.

[38] Chris Clarkson. Establishing homogeneity of the universe in the shadow of dark energy. *Comptes Rendus Physique*, 13:682–718, 2012. doi: 10.1016/j.crhy.2012.04.005. Cited on pages 9, 10, and 44.

[39] R. Treciokas and G. F. R. Ellis. Isotropic solutions of the Einstein-Boltzmann equations. *Communications in Mathematical Physics*, 23(1):1 – 22, 1971. doi: cmp/1103857548. URL `https://doi.org/`. Cited on page 9.

[40] G.F.R Ellis, R Treciokas, and D.R Matravers. Anisotropic solutions of the einstein-boltzmann equations. ii. some exact properties of the equations. *Annals of Physics*, 150(2): 487–503, 1983. ISSN 0003-4916. doi: https://doi.org/10.1016/0003-4916(83)90024-6. URL https://www.sciencedirect.com/science/article/pii/0003491683900246. Cited on page 9.

[41] Joan Josep Ferrando, Juan Antonio Morales, and Miquel Portilla. Inhomogeneous space-times admitting isotropic radiation: Vorticity-free case. *Phys. Rev. D*, 46:578–584, Jul 1992. doi: 10.1103/PhysRevD.46.578. URL https://link.aps.org/doi/10.1103/PhysRevD.46.578. Cited on page 9.

[42] William R. Stoeger, S. J., Roy Maartens, and G. F. R. Ellis. Proving almost homogeneity of the universe: An Almost Ehlers-Geren-Sachs theorem. *Astrophys. J.*, 443:1, 1995. doi: 10.1086/175496. Cited on page 9.

[43] Christopher A. Clarkson and Richard Barrett. Does the isotropy of the CMB imply a homogeneous universe? Some generalized EGS theorems. *Class. Quant. Grav.*, 16:3781–3794, 1999. doi: 10.1088/0264-9381/16/12/302. Cited on page 9.

[44] Christopher A. Clarkson and A. A. Coley. Magnetic fields and the cosmic microwave background. *Class. Quant. Grav.*, 18:1305–1310, 2001. doi: 10.1088/0264-9381/18/7/312. Cited on page 9.

[45] Chris Clarkson and Roy Maartens. Inhomogeneity and the foundations of concordance cosmology. *Class. Quant. Grav.*, 27:124008, 2010. doi: 10.1088/0264-9381/27/12/124008. Cited on page 9.

[46] Roy Maartens, George F. R. Ellis, and William R. Stoeger, S. J. Limits on anisotropy and inhomogeneity from the cosmic background radiation. *Phys. Rev. D*, 51:1525–1535, 1995. doi: 10.1103/PhysRevD.51.1525. Cited on page 9.

[47] Roy Maartens, George F. R. Ellis, and William R. Stoeger, S. J. Anisotropy and inhomogeneity of the universe from Delta(T) / T. *Astron. Astrophys.*, 309:L7, 1996. Cited on page 9.

[48] Roy Maartens, George F. R. Ellis, and William R. Stoeger. Improved limits on anisotropy and inhomogeneity from the cosmic background radiation. *Phys. Rev. D*, 51:5942–5945, 1995. doi: 10.1103/PhysRevD.51.5942. Cited on page 9.

[49] William R. Stoeger, S. J., Marcelo Araujo, and Tim Gebbie. The limits on cosmological anisotropies and inhomogeneities from COBE data. *Astrophys. J.*, 476:435, 1997. doi: 10.1086/303633. Cited on page 9.

[50] Syksy Rasanen. On the relation between the isotropy of the CMB and the geometry of the universe. *Phys. Rev. D*, 79:123522, 2009. doi: 10.1103/PhysRevD.79.123522. Cited on page 9.

[51] Oliver F. Piattella. Lecture Notes in Cosmology. 2018. Cited on page 12.

[52] David Camarena and Valerio Marra. Cosmological constraints on the radiation released during structure formation. *Eur. Phys. J.*, C76(11):644, 2016. doi: 10.1140/epjc/s10052-016-4517-7. Cited on page 12.

[53] A. Einstein. Kosmologische Betrachtungen zur allgemeinen Relativitätstheorie. *Sitzungsberichte der Königlich Preußischen Akademie der Wissenschaften (Berlin), Seite 142-152.*, 1917. Cited on page 12.

[54] A. S. Eddington. On the Instability of Einstein's Spherical World. *Mon. Not. Roy. Astron. Soc.*, 90:668–678, 1930. Cited on page 13.

[55] Daniel Baumann. Inflation. In *Theoretical Advanced Study Institute in Elementary Particle Physics: Physics of the Large and the Small*, pages 523–686, 2011. doi: 10.1142/9789814327183_0010. Cited on page 14.

[56] Salvatore Capozziello, Rocco D'Agostino, and Orlando Luongo. Extended Gravity Cosmography. *Int. J. Mod. Phys. D*, 28(10):1930016, 2019. doi: 10.1142/S0218271819300167. Cited on page 14.

[57] I.M.H. Etherington. Lx. on the definition of distance in general relativity. *The London, Edinburgh, and Dublin Philosophical Magazine and Journal of Science*, 15(100):761–773, 1933. doi: 10.1080/14786443309462220. URL https://doi.org/10.1080/14786443309462220. Cited on page 15.

[58] L. Amendola and S. Tsujikawa. *Dark Energy: Theory and Observations*. Cambridge University Press, 2010. Cited on page 16.

[59] James M. Bardeen. Gauge Invariant Cosmological Perturbations. *Phys. Rev.*, D22:1882–1905, 1980. doi: 10.1103/PhysRevD.22.1882. Cited on page 16.

[60] Scott Dodelson. *Modern Cosmology*. Academic Press, Elsevier Science, 2003. Cited on page 17.

[61] M. Kowalski et al. Improved Cosmological Constraints from New, Old and Combined Supernova Datasets. *Astrophys. J.*, 686:749–778, 2008. doi: 10.1086/589937. Cited on page 19.

[62] Steven Weinberg. The cosmological constant problem. *Rev. Mod. Phys.*, 61:1–23, Jan 1989. doi: 10.1103/RevModPhys.61.1. URL https://link.aps.org/doi/10.1103/RevModPhys.61.1. Cited on page 19.

[63] Ivaylo Zlatev, Li-Min Wang, and Paul J. Steinhardt. Quintessence, cosmic coincidence, and the cosmological constant. *Phys. Rev. Lett.*, 82:896–899, 1999. doi: 10.1103/PhysRevLett.82.896. Cited on page 19.

[64] Sean G. Ryan, Timothy C. Beers, Keith A. Olive, Brian D. Fields, and John E. Norris. Primordial Lithium and Big Bang Nucleosynthesis. *Astrophys. J.*, 530:L57–L60, 2000. doi: 10.1086/312492. Cited on page 19.

[65] Dominik J. Schwarz, Craig J. Copi, Dragan Huterer, and Glenn D. Starkman. CMB Anomalies after Planck. *Class. Quant. Grav.*, 33(18):184001, 2016. doi: 10.1088/0264-9381/33/18/184001. Cited on page 19.

[66] Cyril Pitrou, Alain Coc, Jean-Philippe Uzan, and Elisabeth Vangioni. Precision big bang nucleosynthesis with improved Helium-4 predictions. *Phys. Rept.*, 754:1–66, 2018. doi: 10.1016/j.physrep.2018.04.005. Cited on page 19.

[67] M. T. Clara and C. J. A. P. Martins. Primordial nucleosynthesis with varying fundamental constants: Improved constraints and a possible solution to the Lithium problem. *Astron. Astrophys.*, 633:L11, 2020. doi: 10.1051/0004-6361/201937211. Cited on page 19.

[68] S. A. Franchino-Viñas and M. E. Mosquera. The cosmological lithium problem, varying constants and the H_0 tension. 7 2021. Cited on page 19.

[69] Jailson Alcaniz, Nicolás Bernal, Antonio Masiero, and Farinaldo S. Queiroz. Light dark matter: A common solution to the lithium and H 0 problems. *Phys. Lett. B*, 812:136008, 2021. doi: 10.1016/j.physletb.2020.136008. Cited on page 19.

[70] Marco Regis and Chris Clarkson. Do primordial Lithium abundances imply there's no Dark Energy? *Gen. Rel. Grav.*, 44:567–579, 2012. doi: 10.1007/s10714-011-1322-3. Cited on pages 19 and 73.

[71] Brian D. Fields. The primordial lithium problem. *Ann. Rev. Nucl. Part. Sci.*, 61:47–68, 2011. doi: 10.1146/annurev-nucl-102010-130445. Cited on page 19.

[72] Patricio Vielva, E. Martinez-Gonzalez, R. B. Barreiro, J. L. Sanz, and L. Cayon. Detection of non-Gaussianity in the WMAP 1 - year data using spherical wavelets. *Astrophys. J.*, 609:22–34, 2004. doi: 10.1086/421007. Cited on page 20.

[73] M. Cruz, E. Martinez-Gonzalez, and P. Vielva. The WMAP cold spot. *Astrophys. Space Sci. Proc.*, page 275, 2010. doi: 10.1007/978-3-642-11250-8_37. Cited on page 20.

[74] M. Cruz, E. Martinez-Gonzalez, P. Vielva, and L. Cayon. Detection of a non-gaussian spot in wmap. *Mon. Not. Roy. Astron. Soc.*, 356:29–40, 2005. doi: 10.1111/j.1365-2966.2004.08419.x. Cited on page 20.

[75] Marcos Cruz, L. Cayon, E. Martinez-Gonzalez, P. Vielva, and J. Jin. The non-gaussian cold spot in the 3-year wmap data. *Astrophys. J.*, 655:11–20, 2007. doi: 10.1086/509703. Cited on page 20.

[76] M. Cruz, M. Tucci, E. Martinez-Gonzalez, and P. Vielva. The non-gaussian cold spot in wmap: significance, morphology and foreground contribution. *Mon. Not. Roy. Astron. Soc.*, 369:57–67, 2006. doi: 10.1111/j.1365-2966.2006.10312.x. Cited on page 20.

[77] András Kovács, Róbert Beck, István Szapudi, István Csabai, Gábor Rácz, and László Dobos. A common explanation of the Hubble tension and anomalous cold spots in the CMB. *Mon. Not. Roy. Astron. Soc.*, 499(1):320–333, 2020. doi: 10.1093/mnras/staa2631. Cited on page 20.

[78] Seshadri Nadathur, Mikko Lavinto, Shaun Hotchkiss, and Syksy Räsänen. Can a supervoid explain the Cold Spot? *Phys. Rev. D*, 90(10):103510, 2014. doi: 10.1103/PhysRevD.90.103510. Cited on page 20.

[79] András Kovács. The part and the whole: voids, supervoids, and their ISW imprint. *Mon. Not. Roy. Astron. Soc.*, 475(2):1777–1790, 2018. doi: 10.1093/mnras/stx3213. Cited on page 20.

[80] Isabella Masina and Alessio Notari. The Cold Spot as a Large Void: Rees-Sciama effect on CMB Power Spectrum and Bispectrum. *JCAP*, 02:019, 2009. doi: 10.1088/1475-7516/2009/02/019. Cited on page 20.

[81] Isabella Masina and Alessio Notari. The Cold Spot as a Large Void: Lensing Effect on CMB Two and Three Point Correlation Functions. *JCAP*, 07:035, 2009. doi: 10.1088/1475-7516/2009/07/035. Cited on page 20.

[82] Benjamin R. Granett, Mark C. Neyrinck, and Istvan Szapudi. An Imprint of Super-Structures on the Microwave Background due to the Integrated Sachs-Wolfe Effect. *Astrophys. J. Lett.*, 683:L99–L102, 2008. doi: 10.1086/591670. Cited on page 20.

[83] Benjamin R. Granett, Mark C. Neyrinck, and Istvan Szapudi. Dark Energy Detected with Supervoids and Superclusters. 5 2008. Cited on page 20.

[84] István Szapudi et al. Detection of a Supervoid Aligned with the Cold Spot of the Cosmic Microwave Background. *Mon. Not. Roy. Astron. Soc.*, 450(1):288–294, 2015. doi: 10.1093/mnras/stv488. Cited on page 20.

[85] A. Kovács et al. The DES view of the Eridanus supervoid and the CMB cold spot. *Mon. Not. Roy. Astron. Soc.*, 510(1):216–229, 2022. doi: 10.1093/mnras/stab3309. Cited on page 20.

[86] Suvodip Mukherjee, Pavan K. Aluri, Santanu Das, Shabbir Shaikh, and Tarun Souradeep. Direction dependence of cosmological parameters due to cosmic hemispherical asymmetry. *JCAP*, 06:042, 2016. doi: 10.1088/1475-7516/2016/06/042. Cited on page 20.

[87] Suvodip Mukherjee and Benjamin D. Wandelt. Making maps of cosmological parameters. *JCAP*, 01:042, 2018. doi: 10.1088/1475-7516/2018/01/042. Cited on page 20.

[88] Shek Yeung and Ming-Chung Chu. Directional variations of cosmological parameters from the Planck CMB data. *Phys. Rev. D*, 105(8):083508, 2022. doi: 10.1103/PhysRevD.105.083508. Cited on page 20.

[89] Benjamin Camacho-Quevedo and Enrique Gaztañaga. A measurement of the scale of homogeneity in the early Universe. *JCAP*, 04(04):044, 2022. doi: 10.1088/1475-7516/2022/04/044. Cited on page 20.

[90] M. Axelsson, Y. Fantaye, F. K. Hansen, A. J. Banday, H. K. Eriksen, and K. M. Gorski. Directional dependence of ΛCDM cosmological parameters. *Astrophys. J. Lett.*, 773:L3, 2013. doi: 10.1088/2041-8205/773/1/L3. Cited on page 20.

[91] Pablo Fosalba and Enrique Gaztanaga. Explaining Cosmological Anisotropy: Evidence for Causal Horizons from CMB data. 11 2020. doi: 10.1093/mnras/stab1193. Cited on page 20.

[92] G. E. Addison, Y. Huang, D. J. Watts, C. L. Bennett, M. Halpern, G. Hinshaw, and J. L. Weiland. Quantifying discordance in the 2015 Planck CMB spectrum. *Astrophys. J.*, 818(2):132, 2016. doi: 10.3847/0004-637X/818/2/132. Cited on page 20.

[93] N. Aghanim et al. Planck intermediate results. LI. Features in the cosmic microwave background temperature power spectrum and shifts in cosmological parameters. *Astron. Astrophys.*, 607:A95, 2017. doi: 10.1051/0004-6361/201629504. Cited on page 20.

[94] N. Aghanim et al. Planck 2018 results. V. CMB power spectra and likelihoods. *Astron. Astrophys.*, 641:A5, 2020. doi: 10.1051/0004-6361/201936386. Cited on page 20.

[95] Eleonora Di Valentino, Alessandro Melchiorri, and Joseph Silk. Planck evidence for a closed Universe and a possible crisis for cosmology. *Nature Astron.*, 4(2):196–203, 2019. doi: 10.1038/s41550-019-0906-9. Cited on pages 21 and 86.

[96] George Efstathiou and Steven Gratton. The evidence for a spatially flat Universe. *Mon. Not. Roy. Astron. Soc.*, 496(1):L91–L95, 2020. doi: 10.1093/mnrasl/slaa093. Cited on pages 21 and 37.

[97] Benjamin Bose and Lucas Lombriser. Easing cosmic tensions with an open and hotter universe. *Phys. Rev. D*, 103(8):L081304, 2021. doi: 10.1103/PhysRevD.103.L081304. Cited on pages 21 and 22.

[98] N. Aghanim et al. Planck 2018 results. I. Overview and the cosmological legacy of Planck. *Astron. Astrophys.*, 641:A1, 2020. doi: 10.1051/0004-6361/201833880. Cited on pages 22, 32, 84, and 93.

[99] Pedro da Silveira Ferreira and Miguel Quartin. First Constraints on the Intrinsic CMB Dipole and Our Velocity with Doppler and Aberration. *Phys. Rev. Lett.*, 127(10):101301, 2021. doi: 10.1103/PhysRevLett.127.101301. Cited on page 22.

[100] Leandros Perivolaropoulos and Foteini Skara. Challenges for ΛCDM: An update. 5 2021. Cited on pages 22 and 23.

[101] Nathan Secrest, Sebastian von Hausegger, Mohamed Rameez, Roya Mohayaee, and Subir Sarkar. A Challenge to the Standard Cosmological Model. 6 2022. Cited on page 22.

[102] J. J. Condon, W. D. Cotton, E. W. Greisen, Q. F. Yin, R. A. Perley, G. B. Taylor, and J. J. Broderick. The NRAO VLA sky survey. *The Astronomical Journal*, 115(5):1693–1716, may 1998. doi: 10.1086/300337. URL `https://doi.org/10.1086/300337`. Cited on page 22.

[103] Federico Marocco, Peter R. M. Eisenhardt, John W. Fowler, J. Davy Kirkpatrick, Aaron M. Meisner, Edward F. Schlafly, S. A. Stanford, Nelson Garcia, Dan Caselden, Michael C. Cushing, Roc M. Cutri, Jacqueline K. Faherty, Christopher R. Gelino, Anthony H. Gonzalez, Thomas H. Jarrett, Renata Koontz, Amanda Mainzer, Elijah J. Marchese, Bahram Mobasher, David J. Schlegel, Daniel Stern, Harry I. Teplitz, and Edward L. Wright. The CatWISE2020 catalog. *The Astrophysical Journal Supplement Series*, 253(1):8, feb 2021. doi: 10.3847/1538-4365/abd805. URL `https://doi.org/10.3847/1538-4365/abd805`. Cited on page 22.

[104] Nathan J. Secrest, Sebastian von Hausegger, Mohamed Rameez, Roya Mohayaee, Subir Sarkar, and Jacques Colin. A Test of the Cosmological Principle with Quasars. 9 2020. Cited on page 22.

[105] Jeremy Darling. The Universe is Brighter in the Direction of Our Motion: Galaxy Counts and Fluxes are Consistent with the CMB Dipole. *Astrophys. J. Lett.*, 931(2):L14, 2022. doi: 10.3847/2041-8213/ac6f08. Cited on page 22.

[106] Neil P. Humphreys, Roy Maartens, and David R. Matravers. Anisotropic observations in universes with nonlinear inhomogeneity. *Astrophys. J.*, 477:47, 1997. doi: 10.1086/303672. Cited on page 23.

[107] Michael Blomqvist and Edvard Mortsell. Supernovae as seen by off-center observers in a local void. *JCAP*, 05:006, 2010. doi: 10.1088/1475-7516/2010/05/006. Cited on page 23.

[108] Havard Alnes and Morad Amarzguioui. CMB anisotropies seen by an off-center observer in a spherically symmetric inhomogeneous Universe. *Phys. Rev. D*, 74:103520, 2006. doi: 10.1103/PhysRevD.74.103520. Cited on pages 23, 64, and 93.

[109] Havard Alnes and Morad Amarzguioui. The supernova Hubble diagram for off-center observers in a spherically symmetric inhomogeneous Universe. *Phys. Rev. D*, 75:023506, 2007. doi: 10.1103/PhysRevD.75.023506. Cited on page 23.

[110] Simon Foreman, Adam Moss, James P. Zibin, and Douglas Scott. Spatial and temporal tuning in void models for acceleration. *Phys. Rev. D*, 82:103532, 2010. doi: 10.1103/PhysRevD.82.103532. Cited on page 23.

[111] Tirthabir Biswas, Alessio Notari, and Wessel Valkenburg. Testing the Void against Cosmological data: fitting CMB, BAO, SN and H0. *JCAP*, 11:030, 2010. doi: 10.1088/1475-7516/2010/11/030. Cited on pages 23, 45, 60, and 63.

[112] A. Kashlinsky, F. Atrio-Barandela, D. Kocevski, and H. Ebeling. A measurement of large-scale peculiar velocities of clusters of galaxies: technical details. *Astrophys. J.*, 691:1479–1493, 2009. doi: 10.1088/0004-637X/691/2/1479. Cited on page 23.

[113] A. Kashlinsky, F. Atrio-Barandela, and H. Ebeling. Measuring bulk motion of X-ray clusters via the kinematic Sunyaev-Zeldovich effect: summarizing the 'dark flow' evidence and its implications. 2 2012. Cited on page 23.

[114] Fernando Atrio-Barandela, Alexander Kashlinsky, Harald Ebeling, Dale J. Fixsen, and Dale Kocevski. Probing the Dark Flow Signal in Wmap 9 -year and Planck Cosmic Microwave Background Maps. *Astrophys. J.*, 810(2):143, 2015. doi: 10.1088/0004-637X/810/2/143. Cited on page 23.

[115] Marika Asgari et al. KiDS-1000 Cosmology: Cosmic shear constraints and comparison between two point statistics. *Astron. Astrophys.*, 645:A104, 2021. doi: 10.1051/0004-6361/202039070. Cited on page 23.

[116] T. M. C. Abbott et al. Dark Energy Survey Year 3 results: Cosmological constraints from galaxy clustering and weak lensing. *Phys. Rev. D*, 105(2):023520, 2022. doi: 10.1103/PhysRevD.105.023520. Cited on page 23.

[117] Eleonora Di Valentino, Olga Mena, Supriya Pan, Luca Visinelli, Weiqiang Yang, Alessandro Melchiorri, David F. Mota, Adam G. Riess, and Joseph Silk. In the realm of the Hubble tension—a review of solutions. *Class. Quant. Grav.*, 38(15):153001, 2021. doi: 10.1088/1361-6382/ac086d. Cited on pages 24 and 25.

[118] Eleonora Di Valentino. A combined analysis of the H_0 late time direct measurements and the impact on the Dark Energy sector. *Mon. Not. Roy. Astron. Soc.*, 502(2):2065–2073, 2021. doi: 10.1093/mnras/stab187. Cited on page 23.

[119] Karsten Jedamzik, Levon Pogosian, and Gong-Bo Zhao. Why reducing the cosmic sound horizon alone can not fully resolve the Hubble tension. *Commun. in Phys.*, 4:123, 2021. doi: 10.1038/s42005-021-00628-x. Cited on pages 25 and 26.

[120] Nils Schöneberg, Guillermo Franco Abellán, Andrea Pérez Sánchez, Samuel J. Witte, Vivian Poulin, and Julien Lesgourgues. The H_0 Olympics: A fair ranking of proposed models. 7 2021. Cited on page 26.

[121] J. Colin Hill, Evan McDonough, Michael W. Toomey, and Stephon Alexander. Early dark energy does not restore cosmological concordance. *Phys. Rev. D*, 102(4):043507, 2020. doi: 10.1103/PhysRevD.102.043507. Cited on page 26.

[122] Giampaolo Benevento, Wayne Hu, and Marco Raveri. Can Late Dark Energy Transitions Raise the Hubble constant? *Phys. Rev. D*, 101(10):103517, 2020. doi: 10.1103/PhysRevD.101.103517. Cited on pages 27 and 37.

[123] Xiangdong Shi, Lawrence M. Widrow, and L. Jonathan Dursi. Measuring hubble's constant in our inhomogeneous universe. *Mon. Not. Roy. Astron. Soc.*, 281:565, 1996. doi: 10.1093/mnras/281.2.565. Cited on page 27.

[124] Yun Wang, David N. Spergel, and Edwin L. Turner. Implications of cosmic microwave background anisotropies for large scale variations in Hubble's constant. *Astrophys. J.*, 498:1, 1998. doi: 10.1086/305539. Cited on page 27.

[125] Xiang-Dong Shi and Michael S. Turner. Expectations for the difference between local and global measurements of the Hubble constant. *Astrophys. J.*, 493:519, 1998. doi: 10.1086/305169. Cited on page 27.

[126] David Camarena and Valerio Marra. The impact of the cosmic variance on H_0 on cosmological analyses. *Phys. Rev.*, D98:023537, 2018. doi: 10.1103/PhysRevD.98.023537. Cited on pages 29 and 30.

[127] Valerio Marra, Luca Amendola, Ignacy Sawicki, and Wessel Valkenburg. Cosmic variance and the measurement of the local Hubble parameter. *Phys. Rev. Lett.*, 110(24):241305, 2013. doi: 10.1103/PhysRevLett.110.241305. Cited on pages 29 and 30.

[128] Io Odderskov, Steen Hannestad, and Troels Haugbølle. On the local variation of the Hubble constant. *JCAP*, 10:028, 2014. doi: 10.1088/1475-7516/2014/10/028. Cited on pages 29 and 30.

[129] Radosław Wojtak, Alexander Knebe, William A. Watson, Ilian T. Iliev, Steffen Heß, David Rapetti, Gustavo Yepes, and Stefan Gottlöber. Cosmic variance of the local Hubble flow in large-scale cosmological simulations. *Mon. Not. Roy. Astron. Soc.*, 438(2):1805–1812, 2014. doi: 10.1093/mnras/stt2321. Cited on pages 29 and 30.

[130] Hayley J. Macpherson, Paul D. Lasky, and Daniel J. Price. The trouble with Hubble: Local versus global expansion rates in inhomogeneous cosmological simulations with numerical relativity. *Astrophys. J. Lett.*, 865(1):L4, 2018. doi: 10.3847/2041-8213/aadf8c. Cited on pages 29 and 30.

[131] Hao-Yi Wu and Dragan Huterer. Sample variance in the local measurements of the Hubble constant. *Mon. Not. Roy. Astron. Soc.*, 471(4):4946–4955, 2017. doi: 10.1093/mnras/stx1967. Cited on pages 29 and 30.

[132] Adam G. Riess et al. A Redetermination of the Hubble Constant with the Hubble Space Telescope from a Differential Distance Ladder. *Astrophys. J.*, 699:539–563, 2009. doi: 10.1088/0004-637X/699/1/539. Cited on page 30.

[133] Matt Visser. Cosmography: Cosmology without the Einstein equations. *Gen. Rel. Grav.*, 37:1541–1548, 2005. doi: 10.1007/s10714-005-0134-8,10.1007/s10714-005-0136-6. Cited on page 31.

[134] M.J. Reid, D.W. Pesce, and A.G. Riess. An Improved Distance to NGC 4258 and its Implications for the Hubble Constant. *Astrophys. J. Lett.*, 886(2):L27, 2019. doi: 10.3847/2041-8213/ab552d. Cited on pages 31, 85, 90, 92, 95, 101, and 102.

[135] Eoin Ó. Colgáin. A hint of matter underdensity at low z? *JCAP*, 09:006, 2019. doi: 10.1088/1475-7516/2019/09/006. Cited on page 32.

[136] G. Efstathiou. A Lockdown Perspective on the Hubble Tension (with comments from the SH0ES team). 7 2020. Cited on page 33.

[137] Antonio J. Cuesta, Licia Verde, Adam Riess, and Raul Jimenez. Calibrating the cosmic distance scale ladder: the role of the sound horizon scale and the local expansion rate as distance anchors. *Mon. Not. Roy. Astron. Soc.*, 448(4):3463–3471, 2015. doi: 10.1093/mnras/stv261. Cited on page 33.

[138] Eric Aubourg et al. Cosmological implications of baryon acoustic oscillation measurements. *Phys. Rev.*, D92(12):123516, 2015. doi: 10.1103/PhysRevD.92.123516. Cited on page 33.

[139] Licia Verde, Jose Luis Bernal, Alan F. Heavens, and Raul Jimenez. The length of the low-redshift standard ruler. *Mon. Not. Roy. Astron. Soc.*, 467(1):731–736, 2017. doi: 10.1093/mnras/stx116. Cited on page 33.

[140] Pablo Lemos, Elizabeth Lee, George Efstathiou, and Steven Gratton. Model independent $H(z)$ reconstruction using the cosmic inverse distance ladder. *Mon. Not. Roy. Astron. Soc.*, 483(4):4803–4810, 2019. doi: 10.1093/mnras/sty3082. Cited on pages 33 and 37.

[141] S. Taubenberger, S. H. Suyu, E. Komatsu, I. Jee, S. Birrer, V. Bonvin, F. Courbin, C. E. Rusu, A. J. Shajib, and K. C. Wong. The Hubble Constant determined through an inverse distance ladder including quasar time delays and Type Ia supernovae. *Astron. Astrophys.*, 628:L7, 2019. doi: 10.1051/0004-6361/201935980. Cited on page 33.

[142] Feeney et al. Prospects for resolving the Hubble constant tension with standard sirens. 2018. Cited on page 33.

[143] E. Macaulay et al. First Cosmological Results using Type Ia Supernovae from the Dark Energy Survey: Measurement of the Hubble Constant. *Mon. Not. Roy. Astron. Soc.*, 486(2):2184–2196, 2019. doi: 10.1093/mnras/stz978. Cited on page 33.

[144] Shadab Alam et al. The clustering of galaxies in the completed SDSS-III Baryon Oscillation Spectroscopic Survey: cosmological analysis of the DR12 galaxy sample. *Mon. Not. Roy. Astron. Soc.*, 470(3):2617–2652, 2017. doi: 10.1093/mnras/stx721. Cited on pages 33, 66, and 78.

[145] G. C. Carvalho, A. Bernui, M. Benetti, J. C. Carvalho, and J. S. Alcaniz. Baryon Acoustic Oscillations from the SDSS DR10 galaxies angular correlation function. *Phys. Rev.*, D93(2):023530, 2016. doi: 10.1103/PhysRevD.93.023530. Cited on page 33.

[146] G. C. Carvalho, A. Bernui, M. Benetti, J. C. Carvalho, and J. S. Alcaniz. Measuring the transverse baryonic acoustic scale from the SDSS DR11 galaxies. 2017. Cited on page 33.

[147] Jailson S. Alcaniz, Gabriela C. Carvalho, Armando Bernui, Joel C. Carvalho, and Micol Benetti. Measuring baryon acoustic oscillations with angular two-point correlation function.

Fundam. Theor. Phys., 187:11–19, 2017. doi: 10.1007/978-3-319-51700-1_2. Cited on page 33.

[148] Ranier Menote and Valerio Marra. Baryon acoustic oscillations in thin redshift shells from BOSS DR12 and eBOSS DR16 galaxies. *Mon. Not. Roy. Astron. Soc.*, 513(2):1600–1608, 2022. doi: 10.1093/mnras/stac847. Cited on page 34.

[149] L. R. Colaço, R. F. L. Holanda, and Rafael C. Nunes. Varying-α in scalar-tensor theory: Implications in light of the supernova absolute magnitude tension and forecast from GW standard sirens. 1 2022. Cited on page 38.

[150] Antonio De Felice, Shinji Mukohyama, and Masroor C. Pookkillath. Addressing H_0 tension by means of VCDM. *Phys. Lett. B*, 816:136201, 2021. doi: 10.1016/j.physletb.2021.136201. Cited on page 38.

[151] Stefano Gariazzo, Eleonora Di Valentino, Olga Mena, and Rafael C. Nunes. Late time interacting cosmologies and the Hubble constant tension. 11 2021. Cited on page 38.

[152] Mattia Atzori Corona, Riccardo Murgia, Matteo Cadeddu, Maria Archidiacono, Stefano Gariazzo, Carlo Giunti, and Steen Hannestad. Pseudoscalar sterile neutrino self-interactions in light of Planck, SPT and ACT data. *JCAP*, 06(06):010, 2022. doi: 10.1088/1475-7516/2022/06/010. Cited on page 38.

[153] Valerio Marra and Leandros Perivolaropoulos. Rapid transition of Geff at zt$\simeq$0.01 as a possible solution of the Hubble and growth tensions. *Phys. Rev. D*, 104(2):L021303, 2021. doi: 10.1103/PhysRevD.104.L021303. Cited on page 39.

[154] Ziad Sakr and Domenico Sapone. Can varying the gravitational constant alleviate the tensions? *JCAP*, 03(03):034, 2022. doi: 10.1088/1475-7516/2022/03/034. Cited on page 39.

[155] Domenico Sapone, Savvas Nesseris, and Carlos A. P. Bengaly. Is there any measurable redshift dependence on the SN Ia absolute magnitude? *Phys. Dark Univ.*, 32:100814, 2021. doi: 10.1016/j.dark.2021.100814. Cited on page 39.

[156] P. Monaco, E. Sefusatti, S. Borgani, M. Crocce, P. Fosalba, R. K. Sheth, and T. Theuns. An accurate tool for the fast generation of dark matter halo catalogs. *Mon. Not. Roy. Astron. Soc.*, 433:2389–2402, 2013. doi: 10.1093/mnras/stt907. Cited on page 39.

[157] Nick Hand, Yu Feng, Florian Beutler, Yin Li, Chirag Modi, Uros Seljak, and Zachary Slepian. nbodykit: an open-source, massively parallel toolkit for large-scale structure. *Astron. J.*, 156(4):160, 2018. doi: 10.3847/1538-3881/aadae0. Cited on page 39.

[158] Michele Moresco et al. Unveiling the Universe with Emerging Cosmological Probes. 1 2022. Cited on pages 39 and 80.

[159] Luca Amendola and Miguel Quartin. Measuring the Hubble function with standard candle clustering. *Mon. Not. Roy. Astron. Soc.*, 504(3):3884–3889, 2021. doi: 10.1093/mnras/stab887. Cited on page 39.

[160] Pengjie Zhang and Albert Stebbins. Confirmation of the Copernican Principle at Gpc Radial Scale and above from the Kinetic Sunyaev Zel'dovich Effect Power Spectrum. *Phys. Rev. Lett.*, 107:041301, 2011. doi: 10.1103/PhysRevLett.107.041301. Cited on pages 41, 45, and 65.

[161] James P. Zibin and Adam Moss. Linear kinetic Sunyaev-Zel'dovich effect and void models for acceleration. *Class. Quant. Grav.*, 28:164005, 2011. doi: 10.1088/0264-9381/28/16/164005. Cited on pages 41 and 45.

[162] Andrzej Krasinski. *Inhomogeneous cosmological models*. Cambridge Univ. Press, Cambridge, UK, 3 2011. ISBN 978-0-511-88754-3, 978-0-521-48180-9, 978-0-521-03017-5. Cited on page 42.

[163] Krzysztof Bolejko, Marie-Noelle Celerier, and Andrzej Krasinski. Inhomogeneous cosmological models: Exact solutions and their applications. *Class. Quant. Grav.*, 28:164002, 2011. doi: 10.1088/0264-9381/28/16/164002. Cited on pages 42, 44, and 66.

[164] P. Szekeres. A Class of Inhomogeneous Cosmological Models. *Commun. Math. Phys.*, 41: 55, 1975. doi: 10.1007/BF01608547. Cited on page 42.

[165] D. A. Szafron. Inhomogeneous cosmologies: New exact solutions and their evolution. *J. Math. Phys.*, 18:1673–1677, 1977. doi: 10.1063/1.523468. Cited on page 42.

[166] R. Kantowski and R. K. Sachs. Some spatially homogeneous anisotropic relativistic cosmological models. *J. Math. Phys.*, 7:443, 1966. doi: 10.1063/1.1704952. Cited on page 42.

[167] Ø. Grøn. Isotropization and homogenization of an anisotropic and inhomogeneous cosmological model during the inflationary era. *Phys. Rev. D*, 32:1586–1587, Sep 1985. doi: 10.1103/PhysRevD.32.1586. URL https://link.aps.org/doi/10.1103/PhysRevD.32.1586. Cited on page 42.

[168] John W. Moffat. Inhomogeneous Cosmology, Inflation and Late-Time Accelerating Universe. 6 2006. Cited on page 42.

[169] Krzysztof Bolejko and Marie-Noëlle Célérier. Szekeres swiss-cheese model and supernova observations. *Phys. Rev. D*, 82:103510, Nov 2010. doi: 10.1103/PhysRevD.82.103510. URL https://link.aps.org/doi/10.1103/PhysRevD.82.103510. Cited on page 42.

[170] Krzysztof Bolejko. Structure formation in the quasispherical szekeres model. *Phys. Rev. D*, 73:123508, Jun 2006. doi: 10.1103/PhysRevD.73.123508. URL https://link.aps.org/doi/10.1103/PhysRevD.73.123508. Cited on page 42.

[171] Krzysztof Bolejko. Evolution of cosmic structures in different environments in the quasispherical szekeres model. *Phys. Rev. D*, 75:043508, Feb 2007. doi: 10.1103/PhysRevD.75.043508. URL https://link.aps.org/doi/10.1103/PhysRevD.75.043508. Cited on page 42.

[172] Ismael Delgado Gaspar and Thomas Buchert. Lagrangian theory of structure formation in relativistic cosmology. VI. Comparison with Szekeres exact solutions. *Phys. Rev. D*, 103 (2):023513, 2021. doi: 10.1103/PhysRevD.103.023513. Cited on page 42.

[173] Roberto A. Sussman, Juan Carlos Hidalgo, Ismael Delgado Gaspar, and Gabriel Germán. Nonspherical Szekeres models in the language of cosmological perturbations. *Phys. Rev. D*, 95(6):064033, 2017. doi: 10.1103/PhysRevD.95.064033. Cited on page 42.

[174] Roberto A. Sussman, I. Delgado Gaspar, and Juan Carlos Hidalgo. Coarse-grained description of cosmic structure from Szekeres models. *JCAP*, 03:012, 2016. doi: 10.1088/1475-7516/2016/06/E03. [Erratum: JCAP 06, E03 (2016)]. Cited on page 42.

[175] Krzysztof Bolejko. The Szekeres Swiss Cheese model and the CMB observations. *Gen. Rel. Grav.*, 41:1737–1755, 2009. doi: 10.1007/s10714-008-0746-x. Cited on page 42.

[176] Andrzej Krasiński and Krzysztof Bolejko. Redshift propagation equations in the $\beta' \neq 0$ szekeres models. *Phys. Rev. D*, 83:083503, Apr 2011. doi: 10.1103/PhysRevD.83.083503. URL `https://link.aps.org/doi/10.1103/PhysRevD.83.083503`. Cited on page 42.

[177] S. M. Koksbang and S. Hannestad. Studying the precision of ray tracing techniques with Szekeres models. *Phys. Rev. D*, 92(2):023532, 2015. doi: 10.1103/PhysRevD.92.023532. [Erratum: Phys.Rev.D 92, 069904 (2015)]. Cited on page 42.

[178] Krzysztof Bolejko, M. Ahsan Nazer, and David L. Wiltshire. Differential cosmic expansion and the Hubble flow anisotropy. *JCAP*, 06:035, 2016. doi: 10.1088/1475-7516/2016/06/035. Cited on page 42.

[179] H. Stephani. Über Lösungen der Einsteinschen Feldgleichungen, die sich in einen fünfdimensionalen flachen Raum einbetten lassen. *Communications in Mathematical Physics*, 4(2):137–142, April 1967. doi: 10.1007/BF01645757. Cited on page 42.

[180] A. Barnes. On shear free normal flows of a perfect fluid. *General Relativity and Gravitation*, 4(2):105–129, March 1973. doi: 10.1007/BF00762798. Cited on page 42.

[181] G. C. McVittie. The Mass-Particle in an Expanding Universe. *Monthly Notices of the Royal Astronomical Society*, 93(5):325–339, 03 1933. ISSN 0035-8711. doi: 10.1093/mnras/93.5.325. URL `https://doi.org/10.1093/mnras/93.5.325`. Cited on page 43.

[182] Oliver F. Piattella. Lensing in the McVittie metric. *Phys. Rev. D*, 93(2):024020, 2016. doi: 10.1103/PhysRevD.93.024020. [Erratum: Phys.Rev.D 93, 129901 (2016)]. Cited on page 43.

[183] G. Lemaitre. The expanding universe. *Gen. Rel. Grav.*, 29:641–680, 1997. doi: 10.1023/A:1018855621348. Cited on page 43.

[184] Richard C. Tolman. Effect of imhomogeneity on cosmological models. *Proc. Nat. Acad. Sci.*, 20:169–176, 1934. doi: 10.1073/pnas.20.3.169. Cited on page 43.

[185] H. Bondi. Spherically symmetrical models in general relativity. *Mon. Not. Roy. Astron. Soc.*, 107:410–425, 1947. doi: 10.1093/mnras/107.5-6.410. Cited on page 43.

[186] Kari Enqvist. Lemaitre-Tolman-Bondi model and accelerating expansion. *Gen. Rel. Grav.*, 40:451–466, 2008. doi: 10.1007/s10714-007-0553-9. Cited on pages 43, 44, 49, and 51.

[187] Marie-Noelle Celerier. Do we really see a cosmological constant in the supernovae data? *Astron. Astrophys.*, 353:63–71, 2000. Cited on page 44.

[188] Andrzej Krasinski. Cosmological models and misunderstandings about them. *Acta Phys. Polon. B*, 42:2263, 2011. doi: 10.5506/APhysPolB.42.2263. Cited on pages 44 and 52.

[189] Kenji Tomita. Analyses of type Ia supernova data in cosmological models with a local void. *Prog. Theor. Phys.*, 106:929–939, 2001. doi: 10.1143/PTP.106.929. Cited on page 44.

[190] Timothy Clifton, Pedro G. Ferreira, and Kate Land. Living in a Void: Testing the Copernican Principle with Distant Supernovae. *Phys. Rev. Lett.*, 101:131302, 2008. doi: 10.1103/PhysRevLett.101.131302. Cited on page 44.

[191] Sean February, Julien Larena, Mathew Smith, and Chris Clarkson. Rendering Dark Energy Void. *Mon. Not. Roy. Astron. Soc.*, 405:2231, 2010. doi: 10.1111/j.1365-2966.2010.16627.x. Cited on page 44.

[192] Tirthabir Biswas, Reza Mansouri, and Alessio Notari. Nonlinear Structure Formation and Apparent Acceleration: An Investigation. *JCAP*, 12:017, 2007. doi: 10.1088/1475-7516/2007/12/017. Cited on page 44.

[193] Daniel J. H. Chung and Antonio Enea Romano. Mapping Luminosity-Redshift Relationship to LTB Cosmology. *Phys. Rev. D*, 74:103507, 2006. doi: 10.1103/PhysRevD.74.103507. Cited on page 44.

[194] Valerio Marra and Alessio Notari. Observational constraints on inhomogeneous cosmological models without dark energy. *Class.Quant.Grav.*, 28:164004, 2011. doi: 10.1088/0264-9381/28/16/164004. Cited on pages 44, 84, and 93.

[195] Havard Alnes, Morad Amarzguioui, and Oyvind Gron. An inhomogeneous alternative to dark energy? *Phys. Rev. D*, 73:083519, 2006. doi: 10.1103/PhysRevD.73.083519. Cited on page 45.

[196] Juan Garcia-Bellido and Troels Haugboelle. Confronting Lemaitre-Tolman-Bondi models with Observational Cosmology. *JCAP*, 04:003, 2008. doi: 10.1088/1475-7516/2008/04/003. Cited on page 45.

[197] Adam Moss, James P. Zibin, and Douglas Scott. Precision Cosmology Defeats Void Models for Acceleration. *Phys. Rev. D*, 83:103515, 2011. doi: 10.1103/PhysRevD.83.103515. Cited on pages 45, 60, and 64.

[198] W. L. Freedman et al. Final results from the Hubble Space Telescope key project to measure the Hubble constant. *Astrophys. J.*, 553:47–72, 2001. doi: 10.1086/320638. Cited on page 45.

[199] Adam G. Riess, Lucas Macri, Stefano Casertano, Hubert Lampeitl, Henry C. Ferguson, Alexei V. Filippenko, Saurabh W. Jha, Weidong Li, and Ryan Chornock. A 3% Solution: Determination of the Hubble Constant with the Hubble Space Telescope and Wide Field Camera 3. *Astrophys. J.*, 730:119, 2011. doi: 10.1088/0004-637X/732/2/129. [Erratum: Astrophys.J. 732, 129 (2011)]. Cited on page 45.

[200] Marie-Noelle Celerier, Krzysztof Bolejko, and Andrzej Krasinski. A (giant) void is not mandatory to explain away dark energy with a Lemaitre – Tolman model. *Astron. Astrophys.*, 518:A21, 2010. doi: 10.1051/0004-6361/200913581. Cited on page 45.

[201] Timothy Clifton, Pedro G. Ferreira, and Joe Zuntz. What the small angle CMB really tells us about the curvature of the Universe. *JCAP*, 07:029, 2009. doi: 10.1088/1475-7516/2009/07/029. Cited on page 45.

[202] E. Shirokoff et al. Improved constraints on cosmic microwave background secondary anisotropies from the complete 2008 South Pole Telescope data. *Astrophys. J.*, 736:61, 2011. doi: 10.1088/0004-637X/736/1/61. Cited on page 45.

[203] Philip Bull, Timothy Clifton, and Pedro G. Ferreira. The kSZ effect as a test of general radial inhomogeneity in LTB cosmology. *Phys. Rev. D*, 85:024002, 2012. doi: 10.1103/PhysRevD.85.024002. Cited on pages 45 and 65.

[204] James P. Zibin. Can decaying modes save void models for acceleration? *Phys. Rev. D*, 84: 123508, 2011. doi: 10.1103/PhysRevD.84.123508. Cited on pages 45 and 64.

[205] G. F. R. Ellis. Relativistic Cosmology: Its Nature, Aims and Problems. *Fundam. Theor. Phys.*, 9:215–288, 1984. doi: 10.1007/978-94-009-6469-3_14. Cited on pages 46, 47, and 48.

[206] Thomas Buchert. Dark Energy from Structure: A Status Report. *Gen. Rel. Grav.*, 40: 467–527, 2008. doi: 10.1007/s10714-007-0554-8. Cited on page 47.

[207] Chris Clarkson, George Ellis, Julien Larena, and Obinna Umeh. Does the growth of structure affect our dynamical models of the universe? The averaging, backreaction and fitting problems in cosmology. *Rept. Prog. Phys.*, 74:112901, 2011. doi: 10.1088/0034-4885/74/11/112901. Cited on page 47.

[208] T. Buchert et al. Is there proof that backreaction of inhomogeneities is irrelevant in cosmology? *Class. Quant. Grav.*, 32:215021, 2015. doi: 10.1088/0264-9381/32/21/215021. Cited on page 47.

[209] Stephen R. Green and Robert M. Wald. How well is our universe described by an FLRW model? *Class. Quant. Grav.*, 31:234003, 2014. doi: 10.1088/0264-9381/31/23/234003. Cited on page 47.

[210] Hayley J. Macpherson, Daniel J. Price, and Paul D. Lasky. Einstein's Universe: Cosmological structure formation in numerical relativity. *Phys. Rev. D*, 99(6):063522, 2019. doi: 10.1103/PhysRevD.99.063522. Cited on page 47.

[211] Roberto A. Sussman. Back-reaction and effective acceleration in generic LTB dust models. *Class. Quant. Grav.*, 28:235002, 2011. doi: 10.1088/0264-9381/28/23/235002. Cited on page 47.

[212] Krzysztof Bolejko, Charles Hellaby, and Alnadhief H. A. Alfedeel. The Metric of the Cosmos from Luminosity and Age Data. *JCAP*, 09:011, 2011. doi: 10.1088/1475-7516/2011/09/011. Cited on page 52.

[213] J. Silk. Large-scale inhomogeneity of the universe: spherically symmetric models. *A&A*, 59(1):53–58, 1977. Cited on page 52.

[214] James P. Zibin. Scalar Perturbations on Lemaitre-Tolman-Bondi Spacetimes. *Phys. Rev. D*, 78:043504, 2008. doi: 10.1103/PhysRevD.78.043504. Cited on page 52.

[215] Sabino Matarrese, Ornella Pantano, and Diego Saez. General-relativistic approach to the nonlinear evolution of collisionless matter. , 47(4):1311–1323, February 1993. doi: 10.1103/PhysRevD.47.1311. Cited on page 54.

[216] Marco Bruni, Sabino Matarrese, and Ornella Pantano. Dynamics of Silent Universes. , 445: 958, June 1995. doi: 10.1086/175755. Cited on page 54.

[217] Valerio Marra and Mikko Paakkonen. Exact spherically-symmetric inhomogeneous model with n perfect fluids. *JCAP*, 01:025, 2012. doi: 10.1088/1475-7516/2012/01/025. Cited on page 54.

[218] Wessel Valkenburg. Complete solutions to the metric of spherically collapsing dust in an expanding spacetime with a cosmological constant. *Gen. Rel. Grav.*, 44:2449–2476, 2012. doi: 10.1007/s10714-012-1405-9. Cited on page 55.

[219] Paul Carter, Florian Beutler, Will J. Percival, Joseph DeRose, Risa H. Wechsler, and Cheng Zhao. The impact of the fiducial cosmology assumption on BAO distance scale measurements. *Mon. Not. Roy. Astron. Soc.*, 494(2):2076–2089, 2020. doi: 10.1093/mnras/staa761. Cited on page 59.

[220] Wessel Valkenburg, Valerio Marra, and Chris Clarkson. Testing the Copernican principle by constraining spatial homogeneity. *Mon. Not. Roy. Astron. Soc.*, 438:L6–L10, 2014. doi: 10.1093/mnrasl/slt140. Cited on pages 60, 61, 67, and 70.

[221] J.P. Zibin, A. Moss, and D. Scott. Can we avoid dark energy? *Phys. Rev. Lett.*, 101: 251303, 2008. doi: 10.1103/PhysRevLett.101.251303. Cited on pages 60 and 63.

[222] Valerio Marra and Mikko Paakkonen. Observational constraints on the LLTB model. *JCAP*, 12:021, 2010. doi: 10.1088/1475-7516/2010/12/021. Cited on page 60.

[223] Diego Blas, Julien Lesgourgues, and Thomas Tram. The Cosmic Linear Anisotropy Solving System (CLASS) II: Approximation schemes. *JCAP*, 07:034, 2011. doi: 10.1088/1475-7516/2011/07/034. Cited on page 61.

[224] Brayan Yamid Del Valle Mazo, Antonio Enea Romano, and Maryi Alejandra Carvajal Quintero. H_0 tension or M overestimation? 2 2022. Cited on page 61.

[225] D.M. Scolnic et al. The Complete Light-curve Sample of Spectroscopically Confirmed SNe Ia from Pan-STARRS1 and Cosmological Constraints from the Combined Pantheon Sample. *Astrophys. J.*, 859(2):101, 2018. doi: 10.3847/1538-4357/aab9bb. Cited on pages 61, 66, and 78.

[226] Matthias Redlich, Krzysztof Bolejko, Sven Meyer, Geraint F. Lewis, and Matthias Bartelmann. Probing spatial homogeneity with LTB models: a detailed discussion. *Astron. Astrophys.*, 570:A63, 2014. doi: 10.1051/0004-6361/201424553. Cited on pages 62, 72, and 96.

[227] George Efstathiou. To H0 or not to H0? *Mon. Not. Roy. Astron. Soc.*, 505(3):3866–3872, 2021. doi: 10.1093/mnras/stab1588. Cited on pages 62 and 85.

[228] Raul Jimenez and Abraham Loeb. Constraining cosmological parameters based on relative galaxy ages. *Astrophys. J.*, 573:37–42, 2002. doi: 10.1086/340549. Cited on page 62.

[229] Juan Garcia-Bellido and Troels Haugboelle. The radial BAO scale and Cosmic Shear, a new observable for Inhomogeneous Cosmologies. *JCAP*, 09:028, 2009. doi: 10.1088/1475-7516/2009/09/028. Cited on page 63.

[230] R.R. Caldwell and A. Stebbins. A Test of the Copernican Principle. *Phys. Rev. Lett.*, 100: 191302, 2008. doi: 10.1103/PhysRevLett.100.191302. Cited on page 64.

[231] Juan Garcia-Bellido and Troels Haugboelle. Looking the void in the eyes - the kSZ effect in LTB models. *JCAP*, 09:016, 2008. doi: 10.1088/1475-7516/2008/09/016. Cited on pages 64 and 65.

[232] James P. Zibin and Adam Moss. Linear kinetic Sunyaev-Zel'dovich effect and void models for acceleration. *Class. Quant. Grav.*, 28:164005, 2011. doi: 10.1088/0264-9381/28/16/164005. Cited on page 65.

[233] N. Aghanim et al. Planck 2018 results. VI. Cosmological parameters. 7 2018. Cited on pages 65, 92, and 95.

[234] Florian Beutler, Chris Blake, Matthew Colless, D.Heath Jones, Lister Staveley-Smith, Lachlan Campbell, Quentin Parker, Will Saunders, and Fred Watson. The 6dF Galaxy Survey: Baryon Acoustic Oscillations and the Local Hubble Constant. *Mon. Not. Roy. Astron. Soc.*, 416:3017–3032, 2011. doi: 10.1111/j.1365-2966.2011.19250.x. Cited on pages 66 and 78.

[235] Ashley J. Ross, Lado Samushia, Cullan Howlett, Will J. Percival, Angela Burden, and Marc Manera. The clustering of the SDSS DR7 main Galaxy sample – I. A 4 per cent distance measure at $z = 0.15$. *Mon. Not. Roy. Astron. Soc.*, 449(1):835–847, 2015. doi: 10.1093/mnras/stv154. Cited on pages 66 and 78.

[236] Michele Moresco, Lucia Pozzetti, Andrea Cimatti, Raul Jimenez, Claudia Maraston, Licia Verde, Daniel Thomas, Annalisa Citro, Rita Tojeiro, and David Wilkinson. A 6% measurement of the Hubble parameter at $z \sim 0.45$: direct evidence of the epoch of cosmic re-acceleration. *JCAP*, 05:014, 2016. doi: 10.1088/1475-7516/2016/05/014. Cited on page 66.

[237] M. Moresco et al. Improved constraints on the expansion rate of the Universe up to z˜1.1 from the spectroscopic evolution of cosmic chronometers. *JCAP*, 08:006, 2012. doi: 10.1088/1475-7516/2012/08/006. Cited on page 66.

[238] Joan Simon, Licia Verde, and Raul Jimenez. Constraints on the redshift dependence of the dark energy potential. *Phys. Rev. D*, 71:123001, 2005. doi: 10.1103/PhysRevD.71.123001. Cited on page 66.

[239] Daniel Stern, Raul Jimenez, Licia Verde, Marc Kamionkowski, and S.Adam Stanford. Cosmic Chronometers: Constraining the Equation of State of Dark Energy. I: H(z) Measurements. *JCAP*, 02:008, 2010. doi: 10.1088/1475-7516/2010/02/008. Cited on page 66.

[240] Cong Zhang, Han Zhang, Shuo Yuan, Tong-Jie Zhang, and Yan-Chun Sun. Four new observational $H(z)$ data from luminous red galaxies in the Sloan Digital Sky Survey data release seven. *Res. Astron. Astrophys.*, 14(10):1221–1233, 2014. doi: 10.1088/1674-4527/14/10/002. Cited on page 66.

[241] Michele Moresco. Raising the bar: new constraints on the Hubble parameter with cosmic chronometers at z $\sim$ 2. *Mon. Not. Roy. Astron. Soc.*, 450(1):L16–L20, 2015. doi: 10.1093/mnrasl/slv037. Cited on page 66.

[242] D.J. Fixsen, E.S. Cheng, J.M. Gales, John C. Mather, R.A. Shafer, and E.L. Wright. The Cosmic Microwave Background spectrum from the full COBE FIRAS data set. *Astrophys. J.*, 473:576, 1996. doi: 10.1086/178173. Cited on pages 66 and 78.

[243] C.L. Reichardt et al. An Improved Measurement of the Secondary Cosmic Microwave Background Anisotropies from the SPT-SZ + SPTpol Surveys. 2 2020. Cited on pages 66 and 78.

[244] Kenji Tomita and Kaiki Taro Inoue. Probing violation of the Copernican principle via the integrated Sachs-Wolfe effect. *Phys. Rev. D*, 79:103505, 2009. doi: 10.1103/PhysRevD.79.103505. Cited on page 66.

[245] Chris Clarkson and Marco Regis. The Cosmic Microwave Background in an Inhomogeneous Universe - why void models of dark energy are only weakly constrained by the CMB. *JCAP*, 02:013, 2011. doi: 10.1088/1475-7516/2011/02/013. Cited on pages 66 and 88.

[246] Erminia Calabrese et al. Precision Epoch of Reionization studies with next-generation CMB experiments. *JCAP*, 08:010, 2014. doi: 10.1088/1475-7516/2014/08/010. Cited on page 66.

[247] Antony Lewis. Cosmological parameters from WMAP 5-year temperature maps. *Phys. Rev. D*, 78:023002, 2008. doi: 10.1103/PhysRevD.78.023002. Cited on page 66.

[248] Andrew Gelman and Donald B. Rubin. Inference from Iterative Simulation Using Multiple Sequences. *Statist. Sci.*, 7:457–472, 1992. doi: 10.1214/ss/1177011136. Cited on page 67.

[249] Antony Lewis. GetDist: a Python package for analysing Monte Carlo samples. 2019. Cited on pages 67 and 79.

[250] A. Euclid Collaboration: Blanchard, S. Camera, C. Carbone, V. F. Cardone, S. Casas, S. Clesse, S. Ilić, M. Kilbinger, T. Kitching, M. Kunz, F. Lacasa, E. Linder, E. Majerotto, K. Markovic, M. Martinelli, V. Pettorino, A. Pourtsidou, Z. Sakr, A. G. Sánchez, D. Sapone, I. Tutusaus, S. Yahia-Cherif, V. Yankelevich, S. Andreon, H. Aussel, A. Balaguera-Antol\'\inez, M. Baldi, S. Bardelli, R. Bender, A. Biviano, D. Bonino, A. Boucaud, E. Bozzo, E. Branchini, S. Brau-Nogue, M. Brescia, J. Brinchmann, C. Burigana, R. Cabanac, V. Capobianco, A. Cappi, J. Carretero, C. S. Carvalho, R. Casas, F. J. Castander, M. Castellano, S. Cavuoti, A. Cimatti, R. Cledassou, C. Colodro-Conde, G. Congedo, C. J. Conselice, L. Conversi, Y. Copin, L. Corcione, J. Coupon, H. M. Courtois, M. Cropper, A. Da Silva, S. de la Torre, D. Di Ferdinando, F. Dubath, F. Ducret, C. A. J. Duncan, X. Dupac, S. Dusini, G. Fabbian, M. Fabricius, S. Farrens, P. Fosalba, S. Fotopoulou, N. Fourmanoit, M. Frailis, E. Franceschi, P. Franzetti, M. Fumana, S. Galeotta, W. Gillard, B. Gillis, C. Giocoli, P. Gómez-Alvarez, J. Graciá-Carpio, F. Grupp, L. Guzzo, H. Hoekstra, F. Hormuth, H. Israel, K. Jahnke, E. Keihanen, S. Kermiche, C. C. Kirkpatrick, R. Kohley, B. Kubik, H. Kurki-Suonio, S. Ligori, P. B. Lilje, I. Lloro, D. Maino, E. Maiorano, O. Marggraf, N. Martinet, F. Marulli, R. Massey, E. Medinaceli, S. Mei, Y. Mellier, B. Metcalf, J. J. Metge, G. Meylan, M. Moresco, L. Moscardini, E. Munari, R. C. Nichol, S. Niemi, A. A. Nucita, C. Padilla, S. Paltani, F. Pasian, W. J. Percival, S. Pires, G. Polenta, M. Poncet, L. Pozzetti, G. D. Racca, F. Raison, A. Renzi, J. Rhodes, E. Romelli, M. Roncarelli, E. Rossetti, R. Saglia, P. Schneider, V. Scottez, A. Secroun, G. Sirri, L. Stanco, J.-L. Starck, F. Sureau, P. Tallada-Cresp\'\i, D. Tavagnacco, A. N. Taylor, M. Tenti, I. Tereno, R. Toledo-Moreo, F. Torradeflot, L. Valenziano, T. Vassallo, G. A. Verdoes Kleijn, M. Viel, Y. Wang, A. Zacchei, J. Zoubian, and E. Zucca. Euclid preparation - VII. Forecast validation for Euclid cosmological probes. , 642:A191, 2020. doi: 10.1051/0004-6361/202038071. URL `https://doi.org/10.1051/0004-6361/202038071`. Cited on pages 74 and 76.

[251] Joachim Harnois-Deraps, Benjamin Giblin, and Benjamin Joachimi. Cosmic Shear Covariance Matrix in wCDM: Cosmology Matters. *Astron. Astrophys.*, 631:A160, 2019. doi: 10.1051/0004-6361/201935912. Cited on page 75.

[252] O. Friedrich et al. Dark Energy Survey year 3 results: covariance modelling and its impact on parameter estimation and quality of fit. *Mon. Not. Roy. Astron. Soc.*, 508(3):3125–3165, 2021. doi: 10.1093/mnras/stab2384. Cited on page 75.

[253] Tassia Ferreira and Valerio Marra. A fast and reliable method for the comparison of covariance matrices. art. arXiv:2107.04211, July 2021. Cited on page 75.

[254] R. Laureijs et al. Euclid Definition Study Report. *arXiv e-prints*, art. arXiv:1110.3193, October 2011. Cited on page 75.

[255] P. Astier et al. Extending the supernova Hubble diagram to z $\sim$ 1.5 with the Euclid space mission. *Astron. Astrophys.*, 572:A80, 2014. doi: 10.1051/0004-6361/201423551. Cited on page 75.

[256] Željko Ivezić et al. LSST: from Science Drivers to Reference Design and Anticipated Data Products. *Astrophys. J.*, 873(2):111, 2019. doi: 10.3847/1538-4357/ab042c. Cited on page 75.

[257] Yan Gong, Asantha Cooray, and Xuelei Chen. Cosmology with Photometric Surveys of Type Ia Supernovae. *Astrophys. J.*, 709:1420–1428, 2010. doi: 10.1088/0004-637X/709/2/1420. Cited on page 75.

[258] Valerio Marra, Miguel Quartin, and Luca Amendola. Accurate weak lensing of standard candles. I. Flexible cosmological fits. *Phys. Rev. D*, 88:063004, 2013. doi: 10.1103/PhysRevD.88.063004. Cited on page 75.

[259] Miguel Quartin, Valerio Marra, and Luca Amendola. Accurate Weak Lensing of Standard Candles. II. Measuring sigma8 with Supernovae. *Phys. Rev. D*, 89(2):023009, 2014. doi: 10.1103/PhysRevD.89.023009. Cited on page 75.

[260] I. Ben-Dayan, M. Gasperini, G. Marozzi, F. Nugier, and G. Veneziano. Average and dispersion of the luminosity-redshift relation in the concordance model. *JCAP*, 06:002, 2013. doi: 10.1088/1475-7516/2013/06/002. Cited on page 75.

[261] J. Jonsson, M. Sullivan, I. Hook, S. Basa, R. Carlberg, A. Conley, D. Fouchez, D. A. Howell, K. Perrett, and C. Pritchet. Constraining dark matter halo properties using lensed SNLS supernovae. *Mon. Not. Roy. Astron. Soc.*, 405:535, 2010. doi: 10.1111/j.1365-2966.2010.16467.x. Cited on page 75.

[262] T. Kronborg et al. Gravitational lensing in the Supernova Legacy Survey (SNLS). *Astron. Astrophys.*, 514:A44, 2010. doi: 10.1051/0004-6361/200913618. Cited on page 75.

[263] L. Pozzetti, C. M. Hirata, J. E. Geach, A. Cimatti, C. Baugh, O. Cucciati, A. Merson, P. Norberg, and D. Shi. Modelling the number density of H emitters for future spectroscopic near-IR space missions. *Astron. Astrophys.*, 590:A3, 2016. doi: 10.1051/0004-6361/201527081. Cited on page 76.

[264] Yun Wang, Chia-Hsun Chuang, and Christopher M. Hirata. Toward More Realistic Forecasting of Dark Energy Constraints from Galaxy Redshift Surveys. *Mon. Not. Roy. Astron. Soc.*, 430:2446, 2013. doi: 10.1093/mnras/stt068. Cited on page 76.

[265] Sylvain de la Torre and Luigi Guzzo. Modelling non-linear redshift-space distortions in the galaxy clustering pattern: systematic errors on the growth rate parameter. *Mon. Not. Roy. Astron. Soc.*, 427:327, 2012. doi: 10.1111/j.1365-2966.2012.21824.x. Cited on page 76.

[266] M. Martinelli et al. Euclid: Forecast constraints on the cosmic distance duality relation with complementary external probes. *Astron. Astrophys.*, 644:A80, 2020. doi: 10.1051/0004-6361/202039078. Cited on page 76.

[267] M. Martinelli et al. Euclid: Constraining dark energy coupled to electromagnetism using astrophysical and laboratory data. *Astron. Astrophys.*, 654:A148, 2021. doi: 10.1051/0004-6361/202141353. Cited on page 76.

[268] Amir Aghamousa et al. The DESI Experiment Part I: Science,Targeting, and Survey Design. *arXiv e-prints*, art. arXiv:1611.00036, October 2016. Cited on page 77.

[269] Andreu Font-Ribera, Patrick McDonald, Nick Mostek, Beth A. Reid, Hee-Jong Seo, and Anže Slosar. DESI and other Dark Energy experiments in the era of neutrino mass measurements. *JCAP*, 05(5):023, May 2014. doi: 10.1088/1475-7516/2014/05/023. Cited on page 77.

[270] Lu Chen, Qing-Guo Huang, and Ke Wang. Distance Priors from Planck Final Release. *JCAP*, 02:028, 2019. doi: 10.1088/1475-7516/2019/02/028. Cited on page 78.

[271] Ashley J. Ross et al. The Completed SDSS-IV extended Baryon Oscillation Spectroscopic Survey: Large-scale structure catalogues for cosmological analysis. *Mon. Not. Roy. Astron. Soc.*, 498(2):2354–2371, 2020. doi: 10.1093/mnras/staa2416. Cited on page 78.

[272] Anand Raichoor et al. The completed SDSS-IV extended Baryon Oscillation Spectroscopic Survey: Large-scale Structure Catalogues and Measurement of the isotropic BAO between redshift 0.6 and 1.1 for the Emission Line Galaxy Sample. *Mon. Not. Roy. Astron. Soc.*, 500(3):3254–3274, 2020. doi: 10.1093/mnras/staa3336. Cited on page 78.

[273] Brad W. Lyke et al. The Sloan Digital Sky Survey Quasar Catalog: Sixteenth Data Release. *Astrophys. J. Suppl.*, 250(1):8, 2020. doi: 10.3847/1538-4365/aba623. Cited on page 78.

[274] Helion du Mas des Bourboux et al. The Completed SDSS-IV Extended Baryon Oscillation Spectroscopic Survey: Baryon Acoustic Oscillations with Lyα Forests. *Astrophys. J.*, 901 (2):153, 2020. doi: 10.3847/1538-4357/abb085. Cited on page 78.

[275] Michele Moresco, Raul Jimenez, Licia Verde, Andrea Cimatti, and Lucia Pozzetti. Setting the Stage for Cosmic Chronometers. II. Impact of Stellar Population Synthesis Models Systematics and Full Covariance Matrix. *Astrophys. J.*, 898(1):82, 2020. doi: 10.3847/1538-4357/ab9eb0. Cited on page 80.

[276] Juan Garcia-Bellido and Troels Haugboelle. Looking the void in the eyes - the kSZ effect in LTB models. *JCAP*, 09:016, 2008. doi: 10.1088/1475-7516/2008/09/016. Cited on page 84.

[277] Will Handley. Curvature tension: evidence for a closed universe. *Phys. Rev. D*, 103(4): L041301, 2021. doi: 10.1103/PhysRevD.103.L041301. Cited on page 86.

[278] Roberto Trotta. Bayes in the sky: Bayesian inference and model selection in cosmology. *Contemp. Phys.*, 49:71–104, 2008. doi: 10.1080/00107510802066753. Cited on page 91.

[279] Harold Jeffreys. Theory of probability. *International series of monographs on physics.*, 1961. Cited on page 91.

[280] P. Szekeres. A class of inhomogeneous cosmological models. *Communications in Mathematical Physics*, 41(1):55–64, February 1975. doi: 10.1007/BF01608547. Cited on page 93.

[281] Krzysztof Bolejko. Evolution of cosmic structures in different environments in the quasispherical Szekeres model. *Phys. Rev. D*, 75:043508, 2007. doi: 10.1103/PhysRevD.75.043508. Cited on page 93.

[282] Eoin Ó. Colgáin, M. M. Sheikh-Jabbari, Rance Solomon, Giada Bargiacchi, Salvatore Capozziello, Maria Giovanna Dainotti, and Dejan Stojkovic. Revealing Intrinsic Flat ΛCDM Biases with Standardizable Candles. 3 2022. Cited on page 96.

[283] Helene M. Courtois, Daniel Pomarede, R. Brent Tully, and Denis Courtois. Cosmography of the Local Universe. *Astron. J.*, 146:69, 2013. doi: 10.1088/0004-6256/146/3/69. Cited on page 96.

[284] Adam G. Riess et al. A 2.4% Determination of the Local Value of the Hubble Constant. *Astrophys. J.*, 826(1):56, 2016. doi: 10.3847/0004-637X/826/1/56. Cited on page 101.